A MEASUREMENT OF RARE ALL-CHARGED DECAYS OF THE D^0 MESON

A Dissertation

Submitted to the Graduate School
of the University of Noter Dame
in Partial Fulfillment of the Requirements
for the Degree of

Doctor of Philosophy

by

Christopher John Kennedy, B.S.

Randal C. Ruchti

Randal C. Ruchti, Director

Department of Physics
Notre Dame, Indiana

April, 1993

AAC5206

A MEASUREMENT OF RARE ALL-CHARGED

DECAYS OF THE D^0 MESON

Abstract

by

Christopher John Kennedy

A measurement of five rare decay of the D^0 meson have been made and are presented here. The data for these mesurements was obtained in Fermilab experiment E687, a photoproduction experiment with mean photon energy of 220 GeV. For the two body states we measure the Branching Ratio ($\pi\pi$)/(Kπ) of 0.046 $\pm$ 0.007 $\pm$ 0.008 (The first error is statistical the second systematic), and a Branching Ratio (KK)/(Kπ) of 0.104 $\pm$ 0.007 $\pm$ 0.0045. A derivative of this gives the Branching Ratio (KK)/($\pi\pi$) of 2.28 $\pm$ 0.38. The fourbody state give the following results: Branching Ratio ($\pi\pi\pi\pi$)/(K$\pi\pi\pi$) of 0.103 $\pm$ 0.011 $\pm$ 0.016; Branching Ratio (KK$\pi\pi$)/ (K$\pi\pi\pi$) of 0.034 $\pm$ 0.004 $\pm$ 0.004; and Branching Ratio (KKKπ)/ (K$\pi\pi\pi$) of 0.0047 $\pm$ 0.0017 $\pm$ 0.0017. Comparisons to previous experiments and the world average are also given.

To My Parents:
Bob and Mary Kennedy.

Mom, that's two dedications
and counting.

Table of Contents

List of Figures.....v
List of Tables.....ix
Chapter 1: Theory..... 1

1.0 General Theory..... 1
1.1 Production Rates..... 1
1.1.1 Vector Meson Dominance..... 1
1.1.2 Photon Gluon Fusion..... 2
1.2 Lifetimes..... 4
1.3 Branching Ratios..... 7
1.3.1 Weak Decays and Cabibbo Theory..... 7
1.3.2 Other Decay Mechanisms..... 12
1.3.3 Phase Space and Form Factors..... 12
1.3.4 Interferance Effects..... 14
1.3.5 Resonances..... 14

Chapter 2: Apparatus..... 16

2.1 The Accelerator..... 16
2.1.1 The Fermilab Proton Accelerator..... 16
2.1.2 The Wideband Beamline..... 18
2.2 Energy Determination..... 21
2.2.1 Microstrip Tagging System..... 21
2.2.2 Recoil Electron Shower Counter..... 21
2.2.3 Beam Gamma Monitor..... 23
2.3 Main Spectrometer..... 23
2.3.1 Charged Particle Tracking..... 23
2.3.1.1 Microstrip System..... 25
2.3.1.2 Multi Wire Proportional Chamber System..... 26
2.3.2 Cerenkov System..... 28
2.3.2.1 C1..... 28
2.3.2.2 C2..... 30
2.3.2.3 C3..... 31
2.3.2.4 Particle Identification..... 32
2.3.3. Electromagnetic Calorimetry..... 33
2.3.3.1 Outer Electromagnetic Calorimeter..... 33
2.3.3.2 Inner Electromagnetic Calorimeter..... 33
2.3.4 Hadron Calorimeter..... 34
2.3.5 The Muon Sysytem..... 36

2.3.6 Triggering System 36
2.3.7 Second Level Trigger 41
2.3.8 Data Acquisition System 41

Chapter 3: Analysis 43

3.1 Pass 1 43
3.1.1 Microstrip Reconstruction 44
3.1.2 PWC Reconstruction 46
3.1.3 Linking 47
3.1.4 Momentum Determination 47
3.1.5 Vertexing 49
3.1.6 Particle Identification 51
3.1.6.1 Cerenkov Identification 51
3.1.6.2 Muon Identification 54
3.1.6.3 Calorimetric Identification 54
3.2 Data Reduction 56
3.2.1 EZ-D analysis 58
3.2.2 Notre Dame Subskim 60
3.3 Monte Carlo Analysis 63
3.4 Branching Ratio Measurements 65
3.4.1 $D^o \to K^+ K^-$ 67
3.4.2 $D^o \to pi^+ pi^-$ 91
3.4.3 $D^o \to K^+ K^- pi^+ pi^-$ 113
3.4.4 $D^o \to pi^+ pi^+ pi^- pi^-$ 123
3.4.5 $D^o \to K^- K^- K^+ pi^+$ 128

Chapter 4: Results and Conclusions 145

Appendix A: The R Cut 153

List of Figures:

1.1 Vector Meson Donminace 2
1.2 Photon Gluon Fusion Model 3
1.3 Associated Production 4
1.4 Spectator Diagrams for Charm Mesons 5
1.5 Weak Decay Mechanisms: (A) and (B) are Cabibbo-Favored; (C) and (D) are Cabibbo-Supressed 8
1.6 KK and $\pi\pi$ decay diagrams 10
1.7 KKKπ decay of the neutral D meson 11
1.8 Other Decay Mechanisms: a) W-exchange, b) Penguin Diagram ; c) W- annihilation, not allowed in neutral D decays 13
1.9 Sub Resonance States of four body decays: (A) D -> rho + rho -> four pions; (B) D -> K star + rho -> Kaon and three pions; (C) D -> phi + rho -> two Kaons and two pions 15
2.1 Fermilab Site 17
2.2 Primary Target 18
2.3 E687 wide band photon beam line 20
2.4 The E687 RESH shower counter 22
2.5 The E687 Spectrometer 24
2.6 The Micro Vertex Detector 25
2.7 Orientation of PWC wires 26
2.8 Side and top view of C1 29
2.9 Top view fo C2 31
2.10 Top view of C3 32
2.11 E687 Hadron calorimeter 34
2.12 The hadron calorimeter pad arrangement 35
2.13 The E687 Muon System 37
2.14 The E687 scintillation counters 38
3.1 Cerenvkov detector identification regions 55
3.2 Confidence level of the secoindary vertex 68
3.3 Low confidence level of primary vertex due to missing track in the secondary vertex 69
3.4 Momentum dependance of Cerenkov Identification 70
3.5 Definitions of the L/sigma measure 71
3.6 Collinear track give high error in secondary vertex position 71
3.7 High L/sigma due to low number of tracks in the primary vertex 72
3.8 Mass plots for systematic study of L/σ cuts, tight Cerenkov definition.. 73
3.9 Mass plots for systematic study of L/σ cuts, loose Cerenkov definition 74
3.10 CL1 cut requires that no tracks from the secondary vertex are consistant with the primary vertex 75
3.11 Many body decays are more likely to have tracks celinear to the D..... 76

3.12 High and low momentum tracks combinations allow a decay product that is collinear with the D 76
3.13 Mass plots for systematic study of CL1 cuts, tight Cerenkov definitions 78
3.14 Mass plots for systematic study of CL1 cuts, loose Cerenkov definitions 79
3.15 CL2 discards events with additional tracks that are consistant with the secondary vertex 77
3.16 Real events may be discarded due to: a) particles from other charm decays, b) unrelated events 80
3.17 Mass plots for systematic study of CL2 cuts, tight Cerenkov definitions 81
3.18 Mass plots for systematic study of CL2 cuts, loose Cerenkov definitions 82
3.19 Mass plots for systematic study of R cuts, tight Cerenkov definitions 85
3.20 Mass plots for systematic study of R cuts, loose Cerenkov definitions 86
3.21 Relative Branching Ratio as a function of L/σ cut for the D -> KK decay 87
3.22 Relative Branching Ratio as a function of CL1 cut for the D -> KK decay 88
3.23 Relative Branching Ratio as a function of CL2 cut for the D -> KK decay 89
3.24 Relative Branching Ratio as a function of R cut for the D -> KK decay 90
3.25 Invariant mass peak from a $K\pi$ decays in Monte Carlo reconstructed as $\pi\pi$ decays 92
3.26 Mass plots for systematic study of L/σ cut for D $\rightarrow\pi\pi$ decay, loose Cerenkov definition 95
3.27 Mass plots for systematic study of L/σ cut for D $\rightarrow\pi\pi$ decay, medium Cerenkov definition 96
3.28 Mass plots for systematic study of L/σ cut for D $\rightarrow\pi\pi$ decay, tight Cerenkov definition 97
3.29 Mass plots for systematic study of CL1 cut for D $\rightarrow\pi\pi$ decay, loose Cerenkov definition 99
3.30 Mass plots for systematic study of CL1 cut for D $\rightarrow\pi\pi$ decay, medium Cerenkov definition 100
3.31 Mass plots for systematic study of CL1 cut for D $\rightarrow\pi\pi$ decay, tight Cerenkov definition 101
3.32 Mass plots for systematic study of CL2 cut for D $\rightarrow\pi\pi$ decay, loose Cerenkov definition 102
3.33 Mass plots for systematic study of CL2 cut for D $\rightarrow\pi\pi$ decay, medium Cerenkov definition 103
3.34 Mass plots for systematic study of CL2 cut for D $\rightarrow\pi\pi$ decay,

tight Cerenkov definition 104
3.35 Mass plots for systematic study of R cut for D ->ππ decay, loose Cerenkov definition 106
3.36 Mass plots for systematic study of R cut for D ->ππ decay, medium Cerenkov definition 107
3.37 Mass plots for systematic study of R cut for D ->ππ decay, tight Cerenkov definition 108
3.38 Relative Branching Ratio as a function of L/σ for the D -> ππ decay tight Cerenkov definitions 109
3.39 Relative Branching Ratio as a function of CL1 cut for the D -> ππ δεχαψ tight Cerenkov definitions 110
3.40 Relative Branching Ratio as a function of CL2 cut for the D -> ππ decay tight Cerenkov definitions 111
3.41 Relative Branching Ratio as a function of R cut for the D -> ππ decay tight Cerenkov definitions 112
3.42 Relative Branching Ratio as a function of L/σ cut for the D -> ππ decay loose Cerenkov definitions 114
3.43 Relative Branching Ratio as a function of CL1 cut for the D -> ππ decay loose Cerenkov definitions 115
3.44 Relative Branching Ratio as a function of CL2 cut for the D -> ππ decay loose Cerenkov definitions 116
3.45 Relative Branching Ratio as a function of R cut for the D -> ππ decay loose Cerenkov definitions 117
3.46 Mass plots for systematic study of L/σ cut for D ->KKππ decay, loose Cerenkov definitions 119
3.47 Mass plots for systematic study of CL2 cut for D ->KKππ decay, loose Cerenkov definitions 120
3.48 Mass plots for systematic study of L/σ cut for D ->KKππ decay, tight Cerenkov definitions 121
3.49 Mass plots for systematic study of CL2 cut for D ->KKππ decay, tight Cerenkov definitions 122
3.50 Relative Branching Ratio as a function of L/σ cut for the D -> KKππ decay loose Cerenkov definitions 124
3.51 Relative Branching Ratio as a function of L/σ cut for the D -> KKππ decay tight Cerenkov definitions 125
3.52 Relative Branching Ratio as a function of CL2 cut for the D -> KKππ decay loose Cerenkov definitions 126
3.53 Relative Branching Ratio as a function of CL2 cut for the D -> KKππ decay tight Cerenkov definitions 127
3.54 Mass plots for systematic study of L/σ cut for D ->ππππ decay, loose Cerenkov definitions 129
3.55 Mass plots for systematic study of CL2 cut for D ->ππππ decay, loose Cerenkov definitions 130
3.56 Mass plots for systematic study of L/σ cut for D ->ππππ decay, tight Cerenkov definitions 131

3.57 Mass plots for systematic study of CL2 cut for D ->ππππ decay, tight Cerenkov definitions 132
3.58 Relative Branching Ratio as a function of L/σ cut for the D -> ππππ decay loose Cerenkov definitions 133
3.59 Relative Branching Ratio as a function of L/σ cut for the D -> ππππ decay tight Cerenkov definitions 134
3.60 Relative Branching Ratio as a function of CL2 cut for the D -> ππππ decay loose Cerenkov definitions 135
3.61 Relative Branching Ratio as a function of CL2 cut for the D -> ππππ decay tight Cerenkov definitions 136
3.62 Mass plots for systematic study of L/σ cut for D ->KKKπ decay, loose Cerenkov definitions 139
3.63 Mass plots for systematic study of CL2 cut for D ->KKKπ decay, loose Cerenkov definitions 140
3.64 Mass plots for systematic study of L/σ cut for D ->KKKπ decay, tight Cerenkov definitions 141
3.65 Mass plots for systematic study of CL2 cut for D ->KKKπ decay, tight Cerenkov definitions 142
3.66 Relative Branching Ratio as a function of L/σ cut for the D -> KKKπ decay loose Cerenkov definitions 143
3.67 Relative Branching Ratio as a function of L/σ cut for the D -> KKKπ decay tight Cerenkov definitions 144
4.1 Comparison of ππ relative branching ratio to previous measurements 146
4.2 Comparison of KK relative branching ratio to previous measurements 147
4.3 Comparison of ππππ relative branching ratio to previous measurements 148
4.4 Comparison of KKππ relative branching ratio to previous measurements 150
4.5 Comparison of ππ / KK relative branching ratio to previous measurements 151
A.1 Invariant Mass plot used for R variable studies 154
A.2 R distribution for background (solid line) and signal (doted line) 155
A.3 Cosine Jackson Theta Distribution for background (silid Line) and signal (dotted line) 157
A.4 Scatter plot of Cosine Jackson Theta versus R for the signal region 158
A.5 Scatter plot of Cosine Jackson Theta versus R for the background region 159
A.6 Single particle momentum distribution for the E687 experiment 163

List of Tables:

1.1 Charm Meson Lifetimes 6
1.2 Branching Ratios for Cabibbo Suppressed Decays 11
3.1 Individual Cerenkov Counter Identification Words 53
3.2 Combined Cerenkov Counter Identifications 54
3.3 Skim One Stream Identifiers 57
3.4 EZ-D Decays 60
3.5 Number of events for decays of interest for the Notre Dame Subskim... 62
3.6 Number of events after first level analysis 62
3.7 Number of events after "washing" 63
3.8 Efficiency of KK decay as a function of significance of detachment cut 72
3.9 Efficiency of KK decay as a function of Isolation of the Primary vertex cut 76
3.10 Efficiency of KK decays as a function of the Isolation of the Secondary vertex cut 80
3.11 Efficiency of KK decay as a function of the R cut 84
3.12 Efficiency of $\pi\pi$ decay as a function of significance of detachment cut 94
3.13 Efficiency of $\pi\pi$ decay as a function of Isolation of the Primary vertex cut 98
3.14 Efficiency of $\pi\pi$ decays as a function of the Isolation of the Secondary vertex cut 105
3.15 Efficiency of $\pi\pi$ decay as a function of the R cut 105
3.16 Efficiency of $KK\pi\pi$ decay as a function of the significance of detachment cut 118
3.17 Efficiency of $KK\pi\pi$ decay as a function of the isolation of the secondary vertex cut 123
3.18 Efficiency of $\pi\pi\pi\pi$ decay as a function of the significance of detachment cut 128
3.19 Efficiency of $\pi\pi\pi\pi$ decay as a function of the isolation of the secondary vertex cut 137
3.20 Efficiency of $KKK\pi$ decay as a function of the significance of detachment cut 137
3.21 Efficiency of $KKK\pi$ decay as a function of the isolation of the secondary vertex cut 138
4.1 Comparison of Branching Ratio Results from this analysis and the World Average 145
4.2 Comparison of $\pi\pi$ Branching Ratio with previous measurements 146
4.3 Comparison of KK Branching Ratio with previous measurements 147
4.4 Comparison of $\pi\pi\pi\pi$ Branching Ratio with previous measurements 148

4.5 Comparison of $KK\pi\pi$ Branching Ratio with previous measurements.... 149
4.6 Comparison of $\pi\pi$ / KK Branching Ratio with previous measurements.....150

CHAPTER 1:

THEORY

1.0 General Theory

Since before the discovery of the J/Psi there have been attempts to predict and then to explain the behavior of the charm quark. These general characteristics can be divided into two main categories, production mechanisms and decay characteristics, with decay characteristics further divided into branching ratios and lifetimes. The analysis in this thesis is primarily concerned with the branching ratios or the physics properties that can be learned from these branching ratios. It is, however, important to examine the theory behind the production rates and lifetimes as well as the branching ratio.

1.1 Production Rates

1.1.1 Vector Meson Dominance

The earliest attempts to explain the photo-production of hadrons is vector meson dominance (VMD)[1]. This theory holds that the photon mixes into virtual hadronic states which have the same quantum numbers as the photon. These states include the rho, omega, phi, and, of interest to us, the J/psi. These virtual vector mesons would then interact hadronically with the target baryon. (Fig 1.1) In this interaction with the target baryon the vector meson's quantum numbers lead to copious production of vector mesons as production products. It was this copious production, which was observed in photo-production, that led to the initial acceptance of the VMD. It was soon discovered that VMD can not be a full

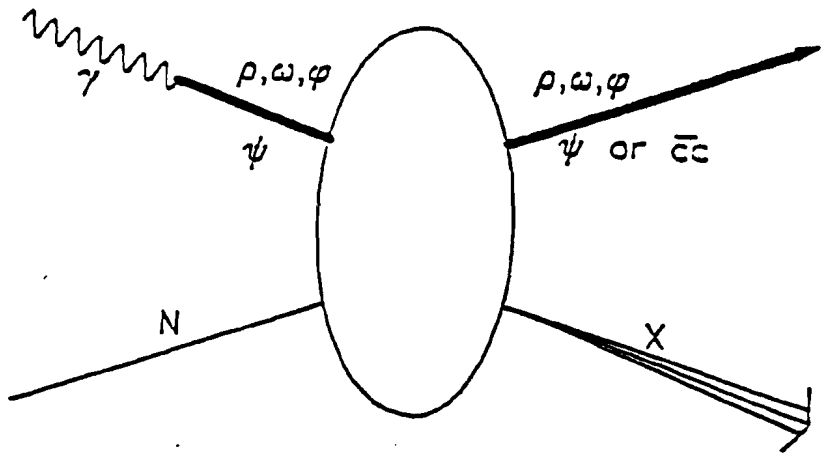

Figure 1.1: Vector Meson Dominance

explanation of the production characteristics. The main production characteristic that the VMD failed to adequately explain was the fact that the charm cross section continues to slowly rise with increasing energy.

1.1.2 Photon Gluon Fusion

The second model for photoproduction is Photon-Gluon Fusion (PGF)[2]. This model holds that the photon creates a virtual c c-bar pair, one of which then interacts with a gluon from the target baryon. (Fig 1.2) Although there can be a variety of higher order processes involving a large number of gluons, the lowest order diagrams are displayed in Fig 1.2. Due to the increased sophistication of the PGF model, as well as the fact that it was developed after the general acceptance of the importance of the quark model, it is able to utilize quantum chromodynamics to calculate production rates. The main advantage of this tool is that PGF gives a production cross section which slowly increases with photon energy, an effect experimentally observed but not adequately predicted or explained by VMD. This energy

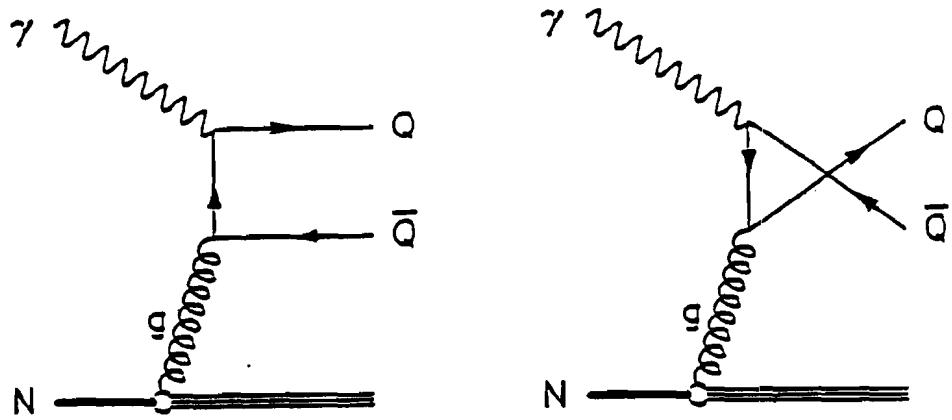

Figure 1.2: Quark Gluon Fusion Model

dependence of the photoproduction cross section becomes important to us in determining the incident photon energy at which to run. This will be discussed more in the beamline discussion.

An additional advantage of Photon Gluon Fusion is that it can be used to describe associated production(fig 1.3). This is seen as primarily a consideration for those people who are looking at charm baryons. The idea behind associated production is that a c $\bar{c}$ pair is created and the charm quark scatters a quark out of the target baryon, leading to the creation of a charm baryon and an anti-charm meson. This is expected to lead to a slight increase in the number of charm baryons in relation to anti-charm baryons, and a very slight decrease in the ratio of charm versus anti-charm mesons. Since these differences are more likely to be observed in a baryon analysis they will not be examined further.

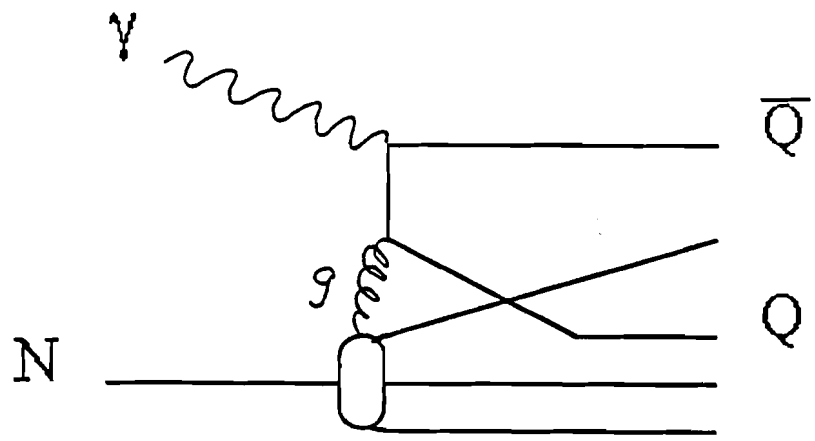

Figure 1.3 Associated Production

1.2 Lifetimes

The most naive model of the decay of charm mesons is the spectator model, called spectator due to the fact that the other quarks in the particle do not interact but simply "watch" the decay. (fig 1.4) The spectator model assumes that the charm (anti-charm) quark decays via W emission and that this process is analogous to muon decay ($\mu \rightarrow e^- \bar{\nu}_e \nu_\mu$). Muon decay is described by

$$\tau_\mu = \frac{1}{\Gamma} = \left(\frac{G_F^2 m_\mu^5}{192\pi^3}\right)^{-1} ,$$

where m_μ is the muon mass and G_F is the fermi coupling constant.

We expect the D lifetime to be described very roughly by

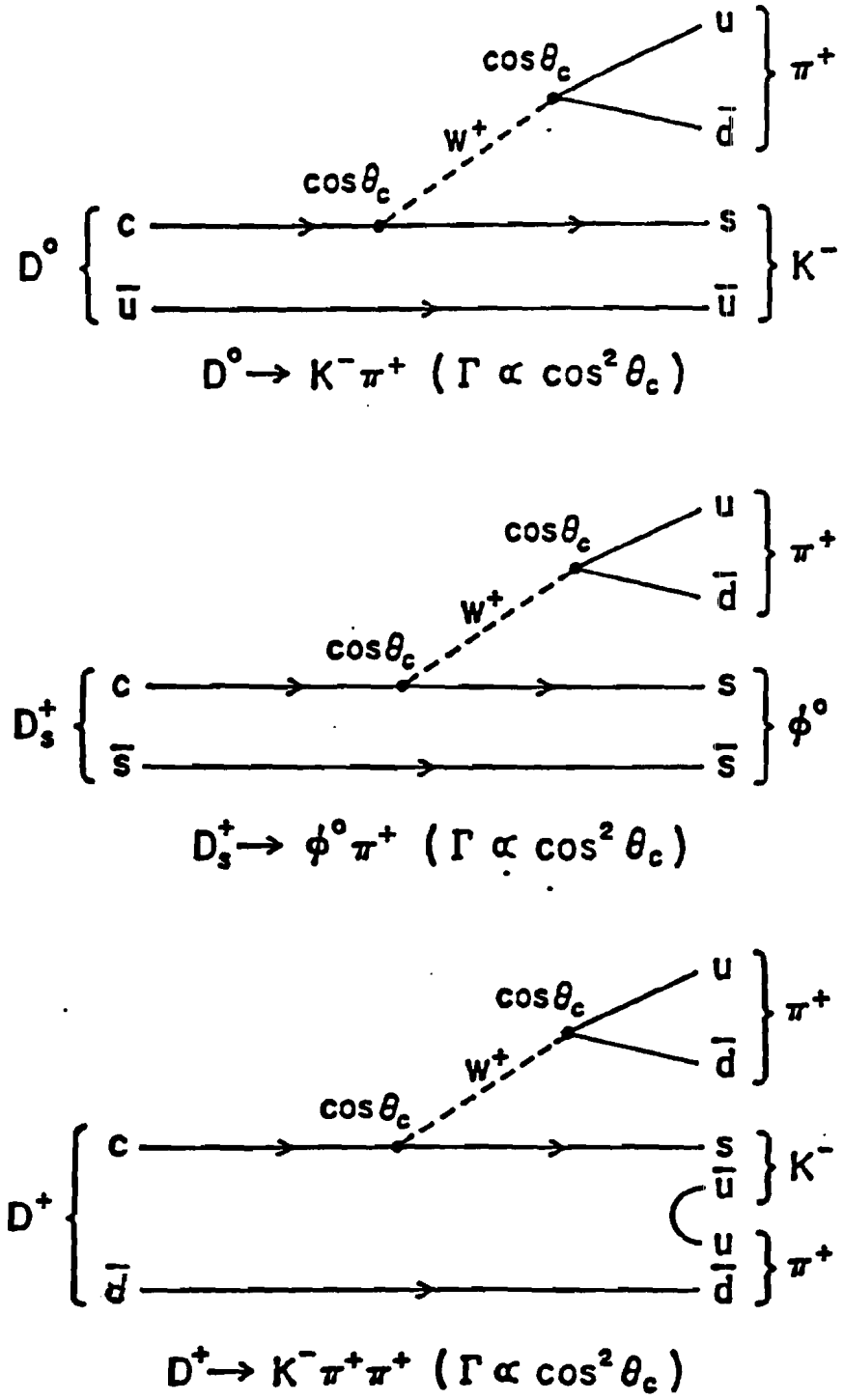

Figure 1.4: Spectator Diagrams for Charm Mesons

$$\tau_c = \frac{1}{\Gamma} = (\text{color factors})\left(\frac{G_F^2 m_c^5}{192\pi^3}\right)^{-1}$$

or the relation to muon lifetime to go as the fifth power of the mass (Sargent's Rule), plus some color terms and phase space factors

$$\tau_{charm} = \frac{1}{2+3}\left(\frac{m_\mu}{m_c}\right)^5 \tau_\mu \quad .$$

This gives a lifetime prediction of

$$\tau_{charm} = 0.7 \times 10^{-12} \text{ seconds}$$

This is derived using a charm quark mass of 1.5 GeV as derived from $K^0 - \overline{K^0}$ mixing [3].

We know from the beginning that the spectator model is not a complete picture due to the absence of exchange and annihilation diagrams as well as final state interactions. If the spectator model represents the dominant decay process we would observe that all of the charm mesons have a similar lifetime. We find however that $t(D^+) >> t(D_S) > t(D^0)$and, as can be seen in table 1.1,[4] there is in fact a difference of a factor of two in the lifetime of the charged to neutral charm mesons. Attempts to explain this discrepancy purely by the existence of W-exchange diagrams for the D^0 lead to helicity problems. This leads us to look at final state interference. where interference occurs because there are two identical particles in the final state. This interference can be destructive due to fermi statistics.

Table 1.1

Meson	Lifefime (psec)
D^+	1.066 ± 0.023
D_S	0.450 ± 0.030
D^0	0.420 ± 0.008

1.3 Branching Ratios

The precision measurement of branching ratios can be a powerful tool to understand a variety of principles. These include but are not limited to Cabibbo suppression, CP violation, higher order interaction, phase space limitations, and new physics.

1.3.1 Weak Decays and Cabibbo theory.

The largest effect in determining the branching ratio is the Cabibbo matrix[5] or Kobayashi-Maskawa (KM) Matrix[6]. These matrices are used to calculate the likelihood that one type of quark will decay into another type of quark via their linking to a W intermediate vector boson. The likelihood of coupling is specified by $\sin\Theta_C$ and $\cos\Theta_C$ where Θ_C is known as the Cabibbo angle.(Fig 1.5) Of interest in our case the relative likelihood that a charm quark will decay into a strange quark versus a down quark. The Cabibbo Matrix is a two by two matrix and was used primarily before the third generation of quarks was discovered [7] and is still used today in cases where the contribution of the third generation is likely to be negligible. The Kobayashi-Maskawa Matrix is a three by three matrix and includes coupling strengths among all three generations of quarks. We will deal primarily with the KM matrix since it is an extension of the Cabibbo matrix. Both matrices are unitary matrices that represent a rotation in two or three dimensions. The KM matrix is generally expressed as follows with $c_i = \cos(\Theta_i)$ and $s_i = \sin(\Theta_i)$:

$$M = \begin{vmatrix} c_1 & c_3 s_1 & s_1 s_3 \\ -c_2 s_1 & c_1 c_2 c_3 - s_2 s_3 e^{i\delta} & c_1 c_2 s_3 + c_3 s_2 e^{i\delta} \\ s_1 s_2 & -c_1 c_3 s_2 - c_2 s_3 e^{i\delta} & -c_1 s_2 s_3 + c_2 c_3 e^{i\delta} \end{vmatrix}$$

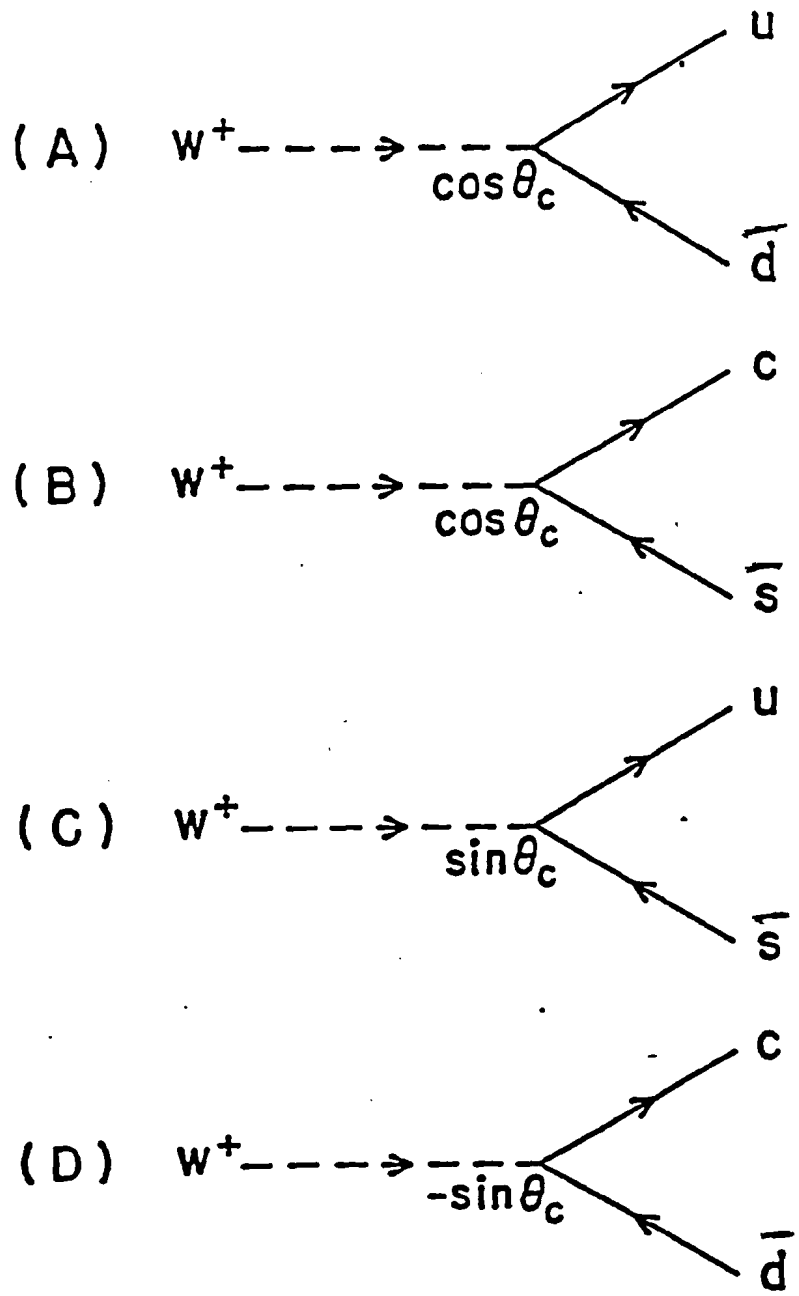

Figure 1.5: Weak Decay Mechanisms: (A) and (B) are Cabibbo-favored; (c) and (D) are Cabibbo-supressed.

One can easily see that if we ignore the existence of the third generation, choosing $\Theta_2 = \Theta_3 = 0$ and setting delta = π we get:

$$M_{Cabibbo} = \begin{vmatrix} \cos\theta_c & \sin\theta_c & 0 \\ -\sin\theta_c & \cos\theta_c & 0 \\ 0 & 0 & 1 \end{vmatrix}$$

which is precisely the Cabibbo Matrix.

This matrix is used to determe the coupling strengths of various weak interactions. From the matrix we get that a coupling between two first generation or two second generation quarks is proportional to $\cos\Theta_c$ and the the coupling between a first and a second generation quark is proportional $\sin\Theta_c$. These cross generational couplings are called Cabibbo suppressed, since Θ_c is about 0.23 to 0.25 radians. Hence we expect the same generation coupling to be much larger than the coupling between different generations. Also, the rate of the decay goes as the second power of the coupling. As we saw above there are at least two couplings associated with each decay. Threfore, we would expect the Cabibbo favored decays to be proportional to $\cos^4(\Theta_c)$ and Cabibbo suppressed decays proportional to $\cos^2(\Theta_c)\sin^2(\Theta_c)$ and Cabibbo double suppressed decays proportional to $\sin^4(\Theta_c)$.

From the above discription and our knowledge of the spectator model we would expect, if the spectator model is the dominant decay process, a similar rate or branching ratio for the decays that we are interested in, $D^0 \to \pi^+ \pi^-$, $D^0 \to K^+ K^-$, $D^0 \to \pi^+ \pi^+ \pi^- \pi^-$, and $D^0 \to K^+ K^- \pi^+ \pi^-$ (fig1.5). Obviously we are also interested in these states for the charge conjugate state, $\overline{D^0}$. This expected equivalence comes from the fact that all of the states listed are Cabibbo suppressed decays and that by the theory outlined above would each be proportional to $\cos^2(\Theta_c)\sin^2(\Theta_c)$. The fact that they do not have simular branching ratios was detected by the Mark II and Mark III experiments. [8,9]

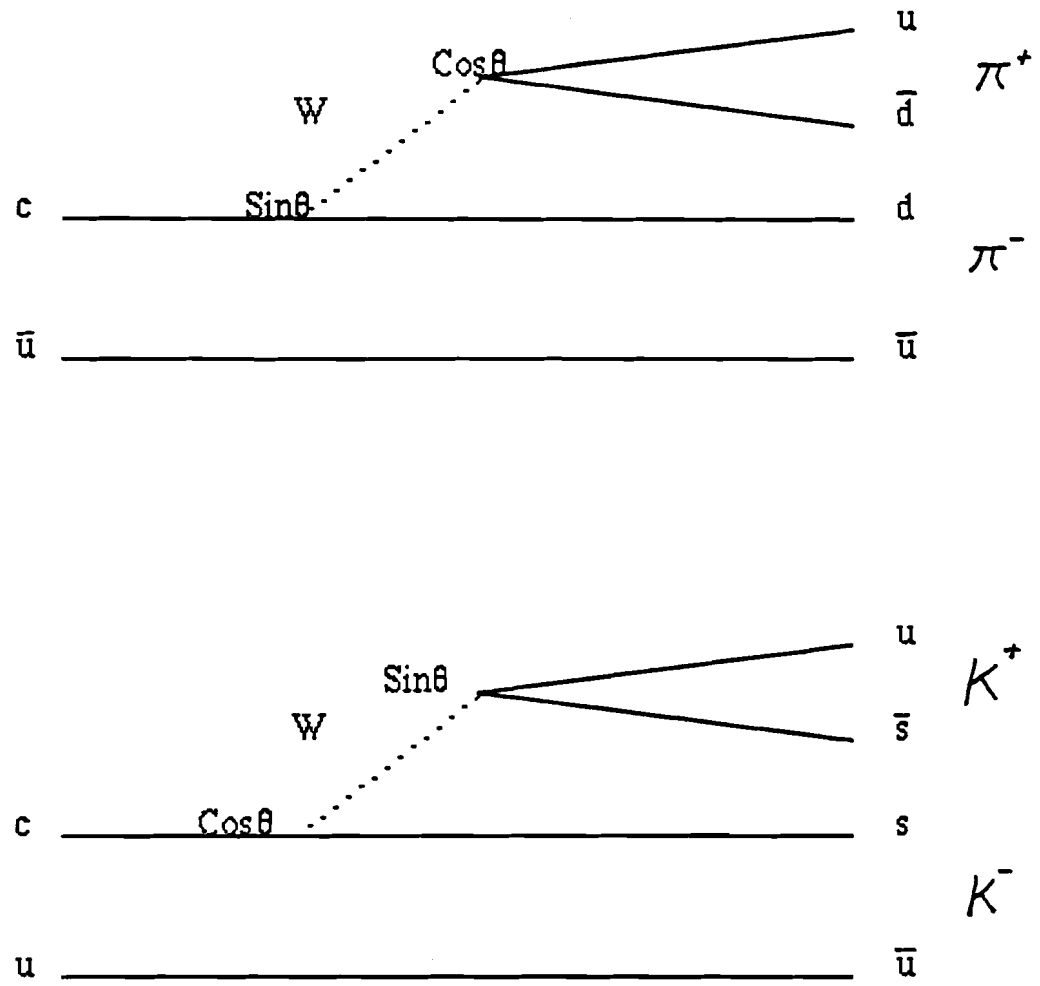

Figure 1.6: Diagrams for the Cabibbo supressed decays of the D0 meson.

$$\frac{\Gamma(D^0 \to K^+K^-)}{\Gamma(D^0 \to K^-\pi^+)} = .119 \pm .018$$

$$\frac{\Gamma(D^0 \to \pi^+\pi^-)}{\Gamma(D^0 \to K^-\pi^+)} = .034 \pm .009$$

The current values of all four branching ratios, in relation to the Cabibbo favored decay modes are presented in table 1.2 [4]

Table 1.2

Decay Mode	Branching Ratio
$D^0 \to \pi^+ \pi^-$	0.045 ± 0.005
$D^0 \to K^+ K^-$	0.113 ± 0.007
$D^0 \to \pi^+\pi^+ \pi^- \pi^-$	0.100 ± 0.011
$D^0 \to K^+ K^- \pi^+ \pi^-$	0.032 ± 0.005

The fact that there is a factor of almost four difference in the branching ratio numbers and that there is no obvious correlation between those states that contain two kaons versus those that contain two pions leads us to suspect that there is much more than just the spectator model acting here. The other state of interest for us, $D^0 \to K^+ K^- K^- \pi^+$, is a Cabibbo allowed state (fig 1.7) but has yet to be measured, presumably due to the lack of available energy in the decay (so called Q value).

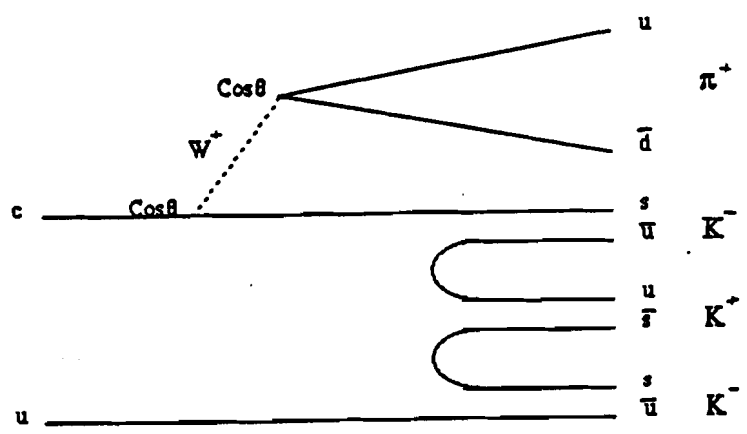

Figure 1.7: KKKπ decay of the neutral D meson

1.3.2 Other Decay Mechanisms

In addition to the simplistic spectator model, which was discussed in relation to the lifetimes of the D mesons, we have several other decay diagrams which also depend mainly on weak decay and Cabibbo theory. These two in particular are W-exchange and Penguin Diagrams. We do not expect to see any contribution from W-annihilation (fig 1.8) mechanisms due to the fact that for a neutral meson there would have to be a neutral annihilation product and no one has yet observed flavor changing neutral currents. Most of the final states at which we are looking can be produced by exchange and penguin diagrams, we can expect to see some difference in the rates due to the possibility of constructive or destructive interference between these diagrams and the simplistic spectator model.[10]

1.3.3 Phase Space and Form Factors

Effects not covered in our simplistic treatment of the spectator model are the ideas of phase space and form factors. The idea of phase space or Q value is especially relevant in our comparison of $D^0 \to KK$ versus $D^0 \to \pi\pi$. Naively in the spectator model we expect these two branching ratios to be the same. In addition, both final states can be produced by means of both W-exchange and penguin diagrams. Phase space arguments contend that since the available energy taken up by the pions is less than that taken up by the kaons, since $m_K > m_\pi$ we expect to have more available Q-value in the $\pi\pi$ decay. This can be manifest either as a greater phase space for the decay or a greater likelihood of creation of q-q bar pairs. If available phase space is the key issue, we would expect a $\pi\pi$ branching ratio that is larger than the KK brancing ratio. Since we do not see this, there is a suggestion that the extra available energy is being manifest in some other manner. In the case of the $\pi\pi$ decay we expect more q-q bar pairs to be produced causing a relatively lower number of higher multiplicity states containing two kaons as opposed to higher multiplicity states containing two pions. We further expect that this difference will be accentuated by the form factor consideration and

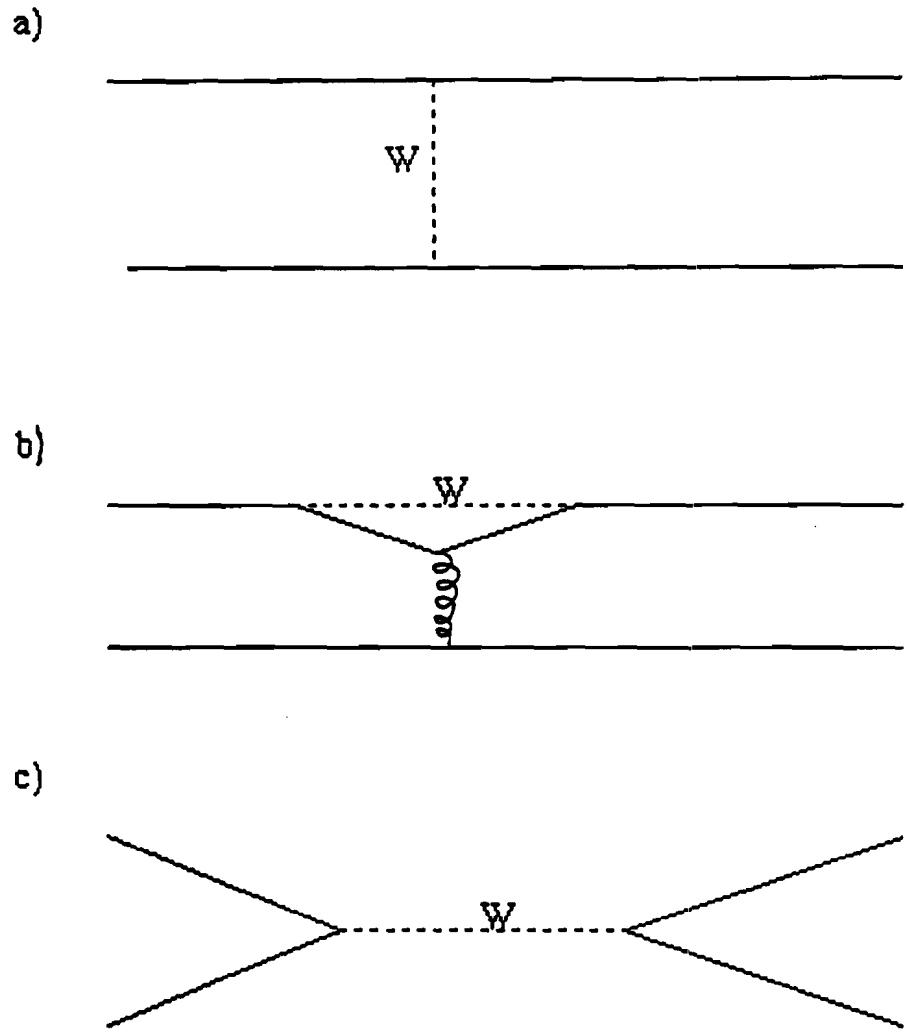

Figure 1.8: Other Decay Mechanisms: (A) W- Exchange; (B) Penguin Diagram; (C) W-Anihilation, not allowed in neutral D decays.

the likelihood of a gluon going to a first generation quark anti-quark pair as opposed to a strange anti-strange pair. We also expect there to be a phase space effect in such states as $KKK\pi$ where the available energy is very small, and therefore the branching ratio is expected to be accordingly small.

1.3.4 Interference effects

Of the two body final states with which we are concerned $K\pi$, KK, and $\pi\pi$: none contain identical quarks or anti-quarks. We do see that several four body states do contain, not only identical quarks, but in many cases identical mesons. In addition to the fermion effect,from the quarks, stated above there are what are considered final state interactions. These will not be considered in any detail here.

1.3.5 Resonances

Due to the difficulty of calculating many body decays, resonance states are of particular interest to theorists. Several examples of this are D^0 -> rho + rho, where each rho decays into a pair of pions. Other prominent resonances include K stars and phis. (fig 1.8)

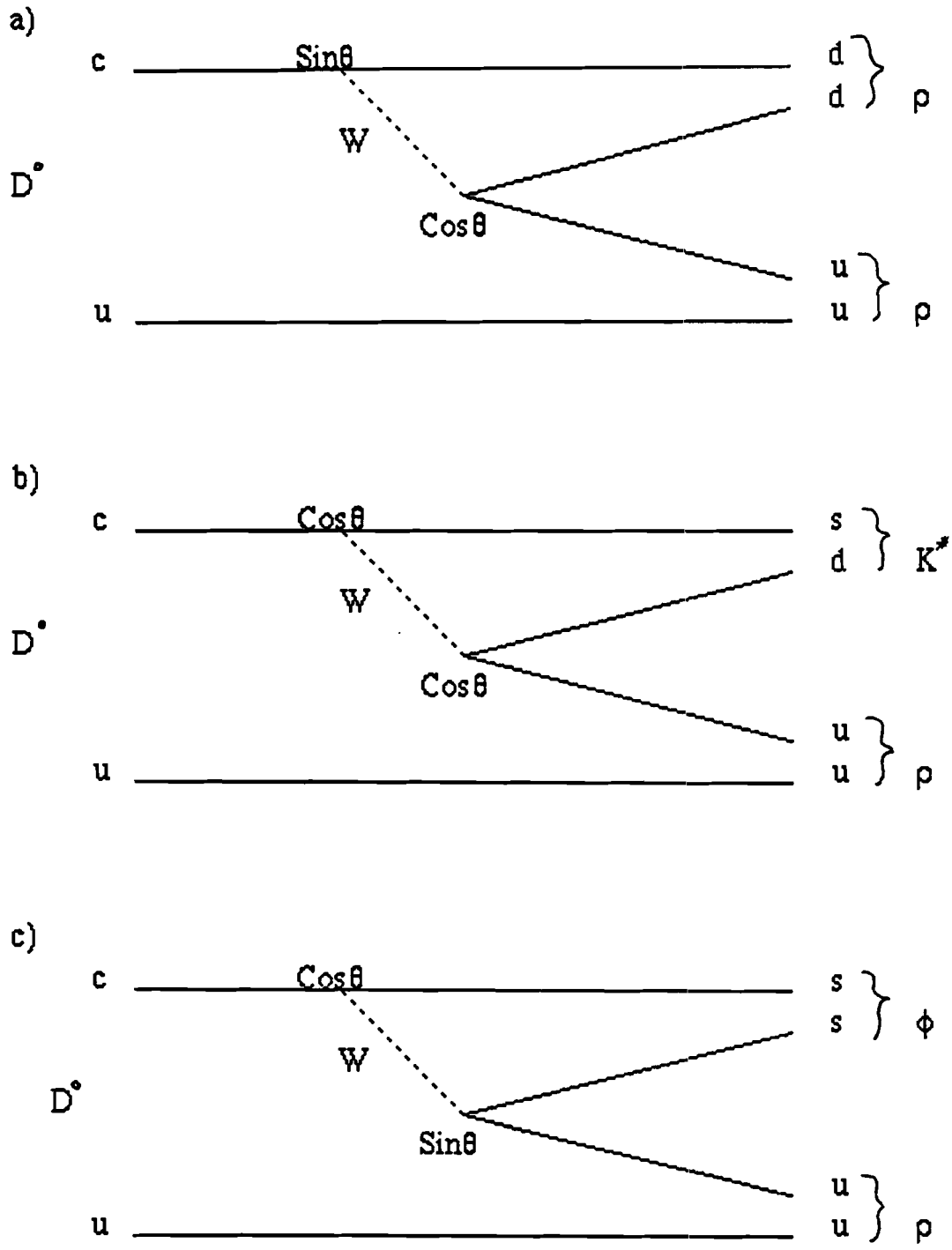

Figure 1.9: Sub-resonance states of four body decays: (A) D -> rho + rho -> four pions; (B) D -> K star + rho -> Kaon and three pions; (C) D -> phi + rho -> two Kaons and Two Pions.

CHAPTER 2:

APPARATUS

The E-687 spectometer is a large acceptance multiparticle detector utilizing a variety of components to achieve the goal of a high statistics search for rare decays of particles containing charm quarks. The spectrometer was proposed in 1982 along with an upgrade of the Broad Band Beamline[11,12]. The upgrade of the beamline was to deliver both higher energy particles and a higher luminosity to the spectrometer. The spectrometer was designed to be able to handle that larger luminosity and to be useful in determining production rates, lifetimes and branching ratios for a wide range of charm particles.

2.1 The Accelerator

The first step in our search for charm particles is the generation of the energy necessary for the creation of these particles. In our experiment this energy comes from 350 GeV photons colliding with a fixed beryllium target. These photons are produced in a two step process. In the first step the Fermilab Proton Accelerator accelerates protons to 800 GeV, and in the second step the Wideband beamline utilizes these protons to create high energy electrons from which photons (of energy up to 350 GeV) are generated by bremsstrahlung.

2.1.1The Fermilab Proton Accelerator.

The Fermilab Proton Accelerator utilizes five separate accelerators to accelerate the protons

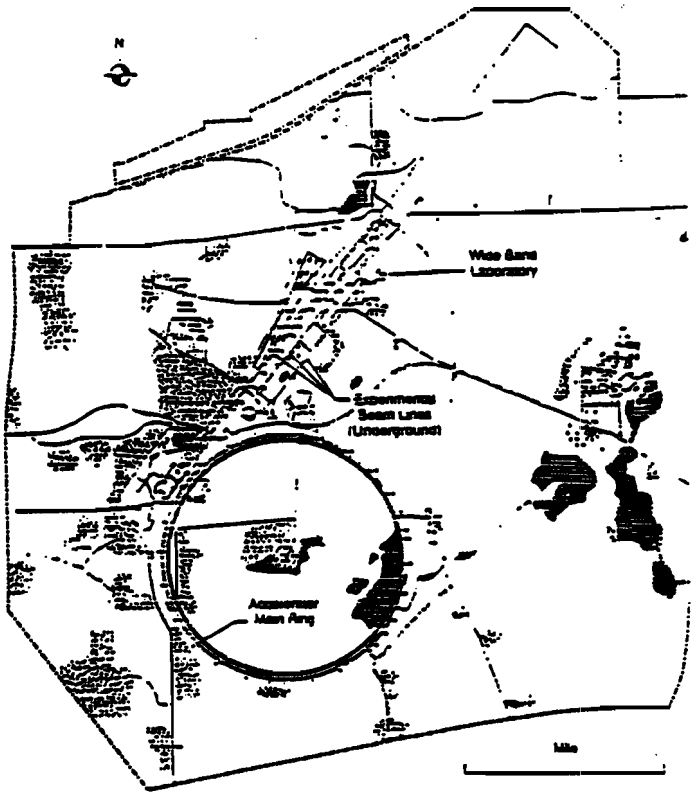

Figure 2.1: Fermilab Site

to 800 GeV(fig 2.1). The first accelerator, a Cockcroft-Walton electrostatic accelerator, accepts negatively charged hydrogen ions at rest and accelerates them to 750,000 eV (.75 MeV). These .75 MeV hydrogen ions are then fed into the linear accelerator (Linac), where they are accelerated to 200 MeV over a distance of 500 feet (150 meters) and sent through a carbon foil. In the carbon foil the two electrons are stripped from the proton of the hydrogen nucleus. This lone proton is fed into a rapid cycling synchrotron, called the Booster. The booster is 500 feet (150 meters) in diameter and accelerates the protons up to 8 GeV. The protons are sent from the booster in bunches to the main ring. Under normal running the main ring will have 12 bunches of protons cycling within it at any given time. The main ring, a synchrotron with a radius if 1km, utilizes 1000 conventional magnets and a station of RF cavaties to accelerate the protons 150 GeV. The Tevatron, also a synchrotron of radius of 1 km but using 1000 superconducting magnets to attain higher magnetic fields, brings the

protons up to 800 GeV. Once the Tevatron has brought the protons to 800 GeV (.8 TeV) they are extracted by means of a kicker magnet and separated to the various beamlines by septum magnets.

2.1.2 The Wideband Beamline

Once the 800 GeV protons are extracted from Tevatron they are sent toward the experimental areas. Since there are generally about 12 fixed target experiments running at any given time the beam must be allocated among them. This allocation takes place in three stages. First the beam is split among the three experimental areas, Proton, Meson, and Neutrino. The Proton portion of the beam is itself then split three way into Proton East (PE), Proton Central (PC), and Proton West (PW). Finally the Proton East beam is split to form PE and PB (Proton Broad Band). The Wide Band , or Broad Band, beam generally receives an allocation of 2e12 protons per spill. It is at this stage that the protons are incident upon a liquid deuterium target.(fig 2.2) The purpose of this target is to create neutral hadronic

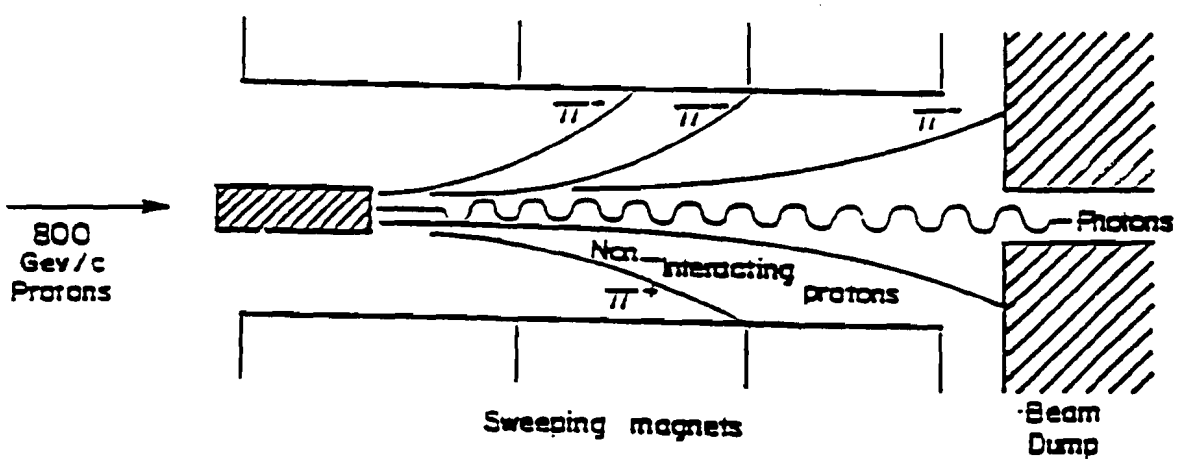

Figure 2.2: Primary Target

particles, primarily π^0 and K^0 mesons. In addition to the neutral particles, charged particles are created. The purpose of the beam line from the primary target is to isolate a high quality electron beam of known energy and then convert it to a photon beam (fig 2.3). Since charged particles are considered to be contamination in our experiment, a large dipole magnet is placed just down stream of the main target to remove the charged particles from the beamline. The K^0 mesons will decay into charged and neutral pions and the neutral pions (both from the decay of kaons and those created in the primary target) will decay into high energy photons. After a sufficient distance, determined to give the majority of pions a chance to decay to photons, a lead converter is placed in the beam. The lead causes the photons to convert into electron positron pairs. After focusing by a quadrupole magnet these pairs are sent through a dipole magnet which directs the electrons into the main beamline. For a portion of our run we operated in double band mode which also included a positron beamline. (All aspects of the electron beamline are mirrored in the positron beam so my explanations will be confined to the electron beam.) Once the electron beam has been established it is sent through another set of dipole magnets designed and calibrated to spread the beam as a function of its momentum. The spread beam is sent through a collimator and another set of dipole magnets designed to accept electron in the 350 +/- 15% GeV energy range. Beam tagging microstrips are located at this point in the beamline. (The beam tagging apparatus will be discussed later.) After the beam is reestablished and refocused, and in the case of double band, recombined with the positron beam, it is sent though a lead radiator, causing the electrons to emit bremsstralung photons. These slowed electrons and their corresponding photons then travel through a strong dipole sweeper magnet. This last element of the beamline causes a separation of electrons by momentum and directs them toward an electromagnetic calorimeter (the RESH counter), which I will discuss later. In the case of the double band the sweepers direct the positron to the opposite side of the beam toward a separate electromagnetic calorimeter (the POSH counter), which is used for momentum determination by means of the positrons. This too will also be discussed later.

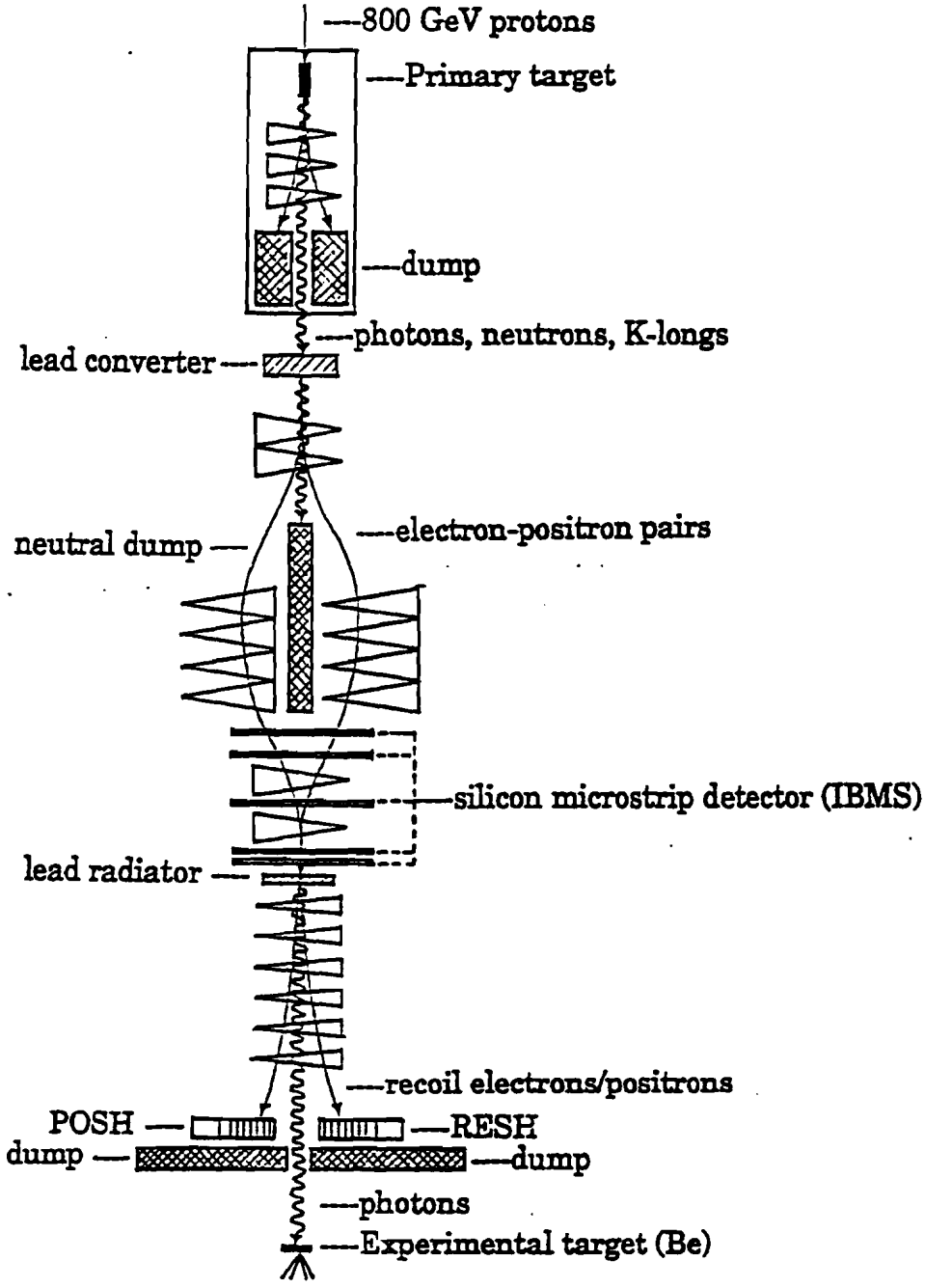

Figure 2.3: E687 wide band photon beam line

2.2 Energy Determination

To determine the energy of the incident photons in our experiment we use three distinct systems; the Microstrip Tagging System, the Recoil Electron Shower Counter (RESH) and the Beam Gamma Monitor.

2.2.1 Microstrop Tagging System.

The Microstrip Tagging System [13] consists of five planes of microstrip detectors situated around the final momentum selecting dipole magnets (pb6d1 and pb6d2). Each plane consists of 256 strips oriented perpendicular to the bend axis of the magnet. The data from these detectors is used to determine the particle path through the two dipole magnets. This gives the initial momentum of the particle and an electron / positron identification. Assuming the particle is only an electron or only a positron will give us the initial energy of the particle.

2.2.2 Recoil Electron Shower Counter.

The Recoil Electron Shower Counter (RESH) (fig 2.4) consists of 15 individual scintillators positioned laterally outward from the nominal beam position in the plane of the sweeper magnet. The RESH measures the momentum of the particle after it has emitted a Bremsstrahlung photon. The momentum determination is used to find the final energy of the electron. The RESH system is also set up so that the pulse height information from the scintillators can be used to calorimetrically determine the energy of the electron.

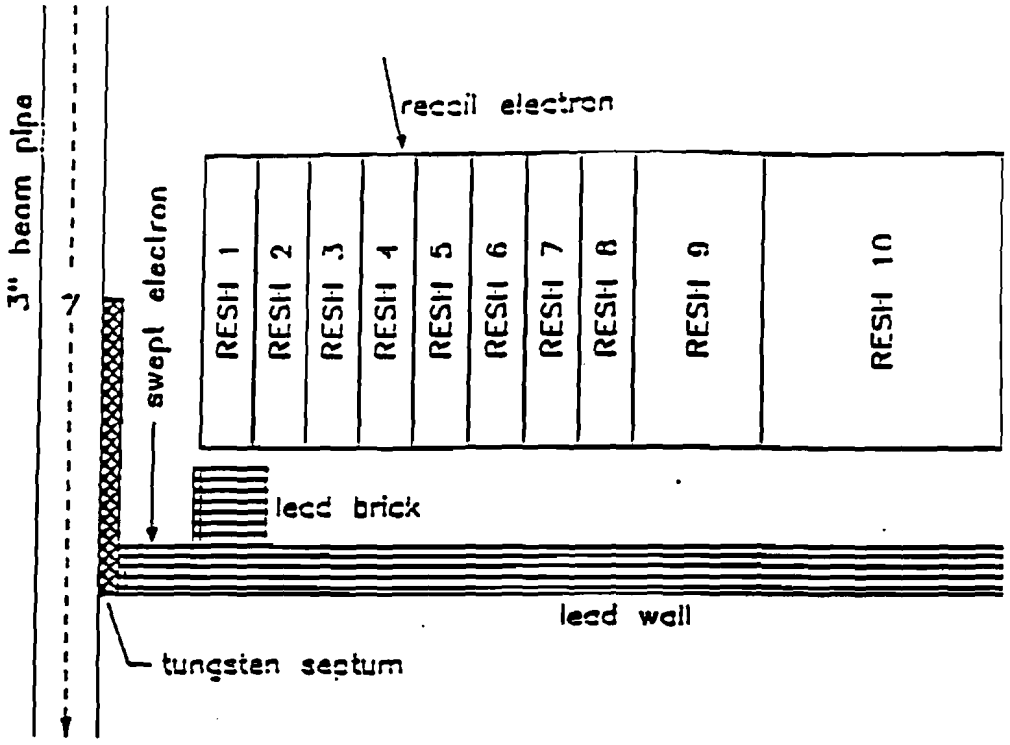

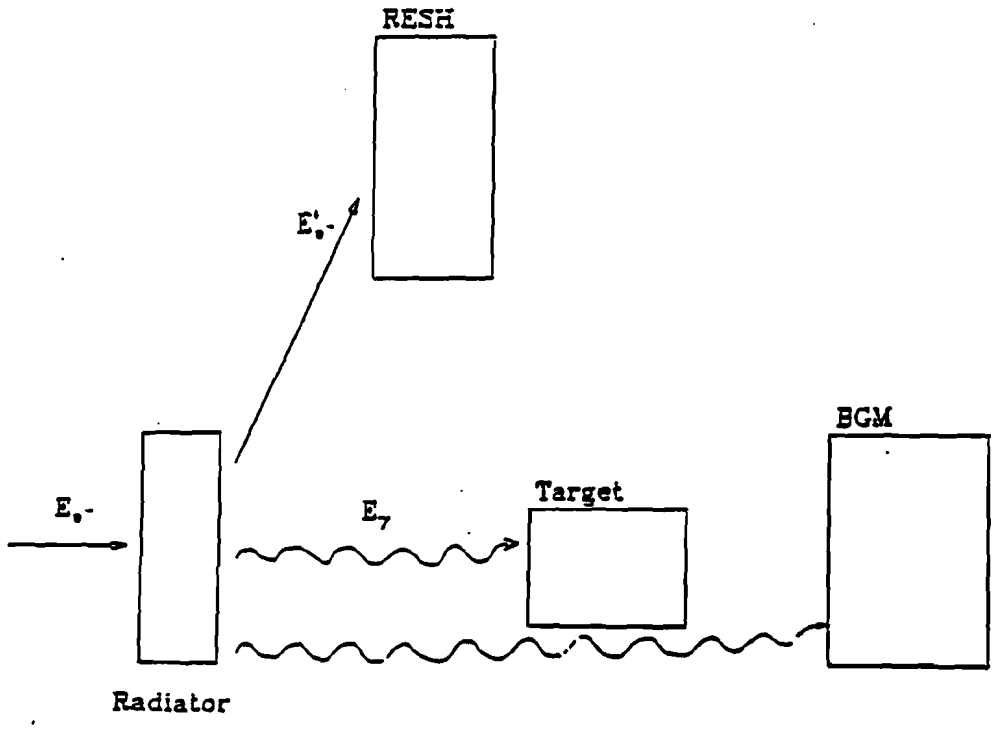

Figure 2.4: The E687 RESH shower counter

2.2.3 Beam Gamma Monitor

The third apparatus used to determine the energy of the incident photon is the Beam Gamma Monitor. In the 1990 portion of the run this consisted of a segmented scintillator calorimeter that was situated in the beam between the hadron calorimeter and the inner muon system. In the 1991 portion of the run, data from the E-683 spectrometer was used for this purpose. This detector was utilized mainly for energy determination in the case of multiple bremsstrahlung events.

2.3 Main Spectrometer

The E-687 spectrometer (fig 2.5) [14]utilizes a variety of subsystems to achieve the goal of charm particle detection. These sub-systems include proportional wire chamber tracking, microstrip tracking, two analyis magnets, a Cerenkov system consisting of three gas threshold Cerenkov detectors, four calorimeters, muon identification, and a variety of scintillation paddle counters that act as an experimental trigger. All of these detectors define an inner acceptance of Θ_x =30 mrad and Θ_y = 50 mrad and an outer acceptance of Θ_x = 100 mrad and Θ_y = 150 mrad.

2.3.1 Charged Particle Tracking

The charged particle tracking is accomplished through the Multi Wire Proportional Chamber (MWPC or PWC) System and the Silicon Microstrip Detector (SMD or SSD) System. The MWPC system is situated downstream of the first bending magnet (M1) and is used primarily for momentum determination and downstream positioning. The SMD system is located upstream of M1 and is used primarily for vertex determination.

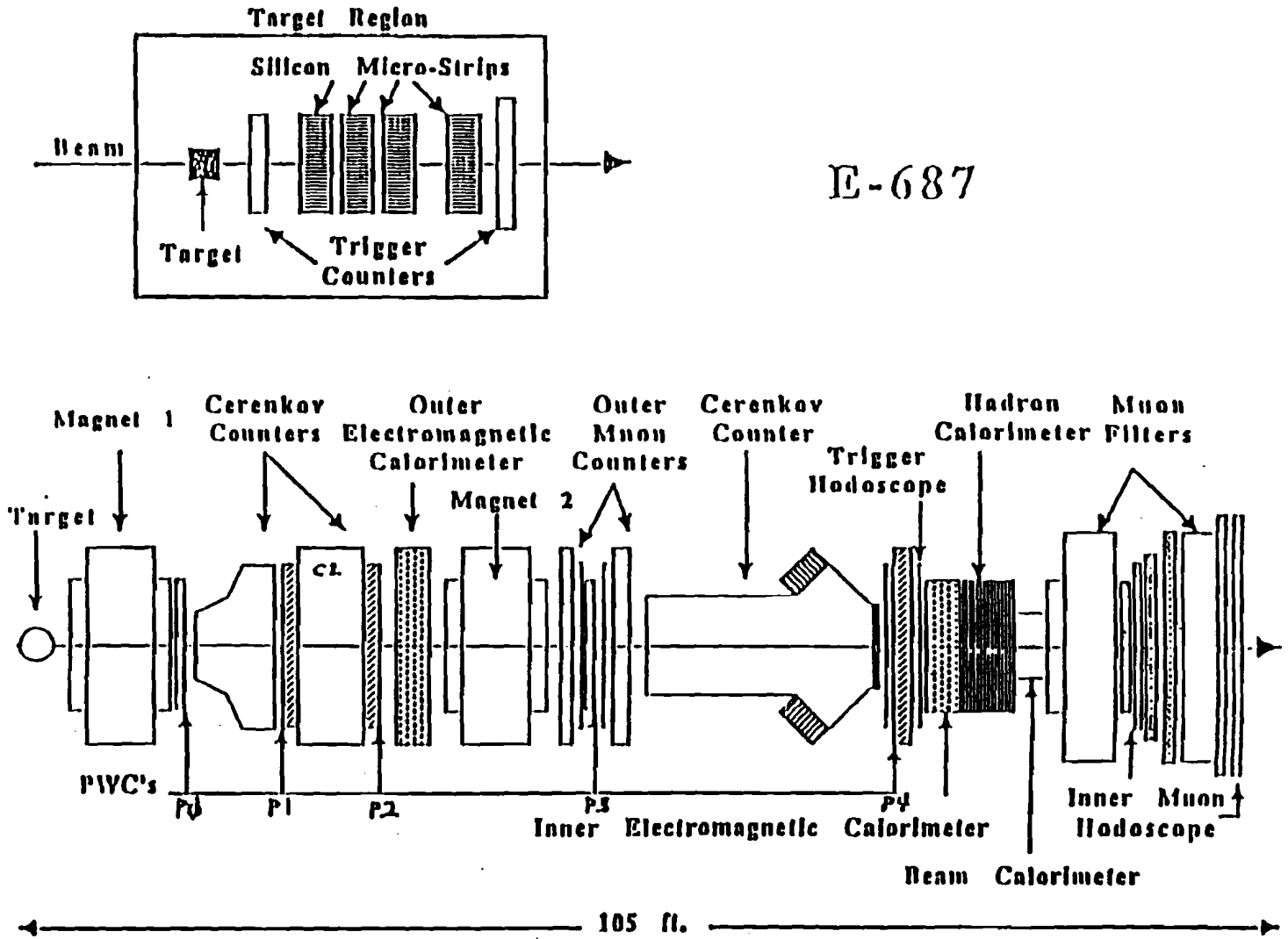

Figure 2.5: The E687 Spectrometer

2.3.1.1 Microstrip system:

The microstrip system consists of 12 planes of detectors, four stations with three planes in each station (fig 2.6). All planes have inner and outer regions. The width of the sense strips in the outer region is twice the width in the inner region for all of the planes. The planes in the first stations have a width of 25 microns for inner strips and 50 microns for the outer strips. The planes in the three downstream stations have strip widths of 50 and 100 microns for the inner and outer regions respectively. Within each station the planes are oriented at -45, -135, and -90 degrees to the horizontal (X) plane respectively.

Data signals from all planes are read out through preamps mounted at the stations and are sent to the counting room where they are fed into LeCroy ADCs. The ADC information is used to cut for pedestals as well as for determining multiple tracks.

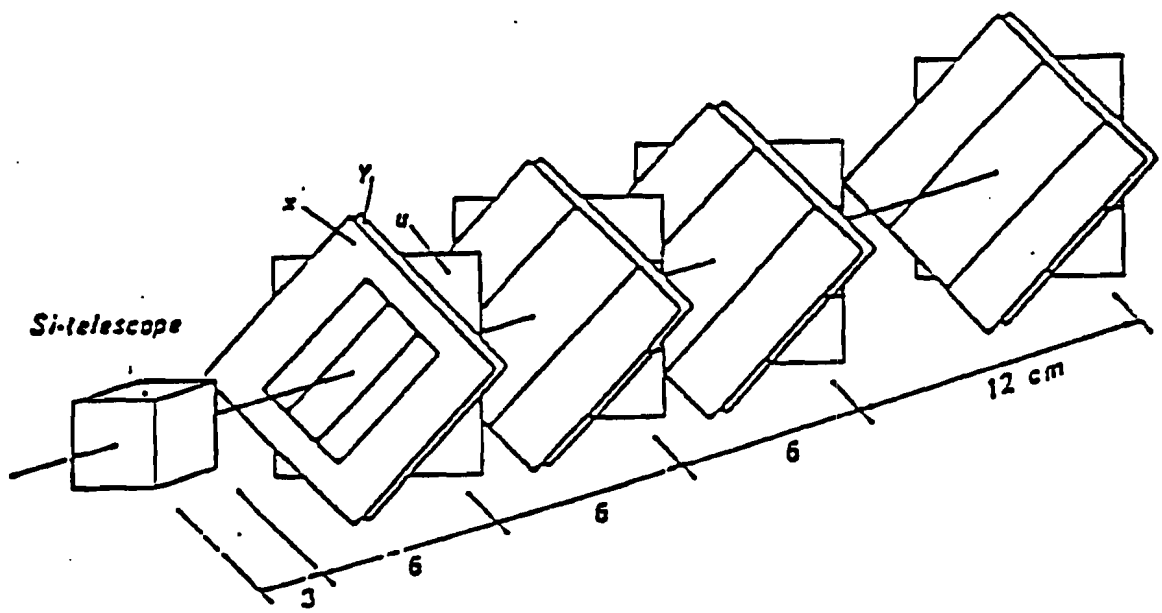

Figure 2.6: The Micro Vertex Detector

2.3.2.2 Multi Wire Proportional Chamber System

The MPWC system consists of 5 chambers of two types, type I and type II. Each chamber has anode sense planes that measure 4 views X,Y,U,V where X and Y are orthogonal and U and V are at 11.6 degrees plus and minus to the Y view (fig 2.7). In addition to the 4 anode sense planes, each chamber has five cathode planes and two ground planes, one each at the most upstream and downstream ends of the chamber.

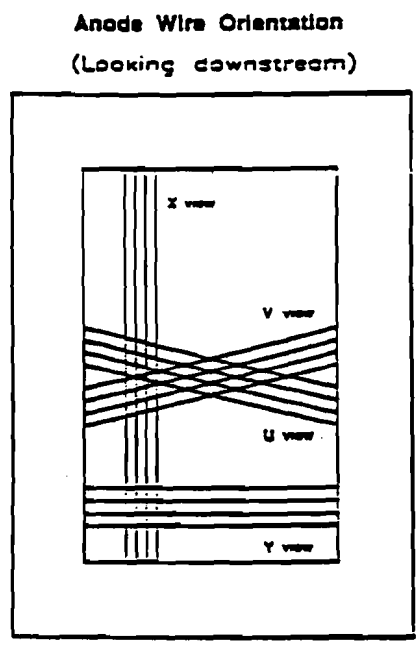

Figure 2.7 Orientation of PWC wires

The type I chambers are the smaller of the two, having an active area of 30 in. x 45 in. with a 2 mm wire spacing and a 0.240 in. half-gap between the anode and cathode planes. Due to the positioning and wire spacing the type I chambers, P0 and P3 have an angular

resolution of 0.49 and 0.13 mrad respectively. The chambers were operated at a cathode voltage of 3.2 -3.6 keV in a 65/35 argon/ethane environment with approximately 1% ethyl alcohol mixture to suppress noise and carbon build up. Due to expected difficulties with the electrostatic stability between the cathodes and the x anode, support wires were installed on the x anode shortly after construction.

The type II chambers all have an active area of 60 in. x 90 inches. There were, however, differences between the type two chambers that were built for the 1987-88 run, P1 and P2, and the chamber built for the 1990 - 1991 run, P4. Chambers P1 and P2 have a wire spacing of 3mm and a half-gap of 0.240 inches. Chamber P4 has a wire spacing of 3.3 mm and a half-gap of 0.2 inches. This difference means that P4 can run at a lower cathode voltage, 2.75 -2.95 keV, compared to P1 and P2, 3.05 - 3.3 keV. P4 is also a significantly quieter chamber which allowed us to run the threshold voltage on the amplifier cards lower and thus increased the efficiency of the chamber. The type II chambers also operate with 65/35 argon/ ethane gas with a 1% ethyl- alcohol mixture. Due to the large size of the type II chambers, it was necessary to add support wires to suppress electrostatic instabilities. These support wires were placed between the ground planes, which are the outermost planes of wires, and the outermost cathode planes, p1 and p5. It was also necessary to put support wires or mylar garlands, depending on the chambers, between the x anode plane and the 4th and 5th cathode planes. Unfortunately these wires and garlands caused a slight decrease in efficiency where they were located but allowed us to increase the overall efficiency of the chamber due to the higher level of electrostatic stability.

The readout of the two chamber types were slightly different. The type I chambers employed 8 channel preamplifier cards while the type II chambers used 16- channel preamps. The signals from both types of chambers were transported to the counting room via 250 to 350 ns Ansley cables into custom build signal shapers and then into Lecroy 4291 TDC (Time to Digital Converter) modules. The Lecroy modules are read into a Lecroy fastbus memory and then into the data acquisition system. The outputs of the Lecroy 4291's were also used

for much of the run in the multiplicity trigger, which measured the number of hits in the PWC's outside of the central, or pair, region. The analysis of the PWC data only utilized the position but not the time information.

2.3.2 The Cerenkov System

The E687 spectrometer has three main particle detection systems: the Muon System, the Calorimeters, and the Cerenkov system. Since the Moun System and Calorimeters figure only peripherally in this analysis I will concentrate on the discussion of the Cerenkov system. The Cerenkov system consists of three separate gas threshold Cerenkov counters. These will be refered to as C1, C2, and C3. The combination of these three counters gives good particle separation over a wide momentum range. All three Cerenkov counters have multiple PMT detection systems which register both pulse height and latch information for each phototube in the detector.

2.3.2.1 C1

The most upstream Cerenkov counter (C1) (fig 2.8) was build by the University of Illinois and is the intermediate counter in terms of velocity threshold. C1 uses He-N_2 at atmospheric pressure which gives a pion momentum threshold of 8.4 GeV/c. The counter is physically situated between the P0 and P1 proportional wire chambers just downstream of the M1 magnet. The C1 is component of the outer part of the spectrometer and is used in identifying both tracks and stubs, or trajectories from particles which do not pass through the second analysis magnet. The path length of the detector is 71 inches in the beam direction. The active area of the counter is 80 inches in the bend direction (y) and 50 inches in the non bend direction (x). This size is matched to contain all of the tracks that will go through all parts of the spectrometer as well as many that will only go through the outer part. The active part of the

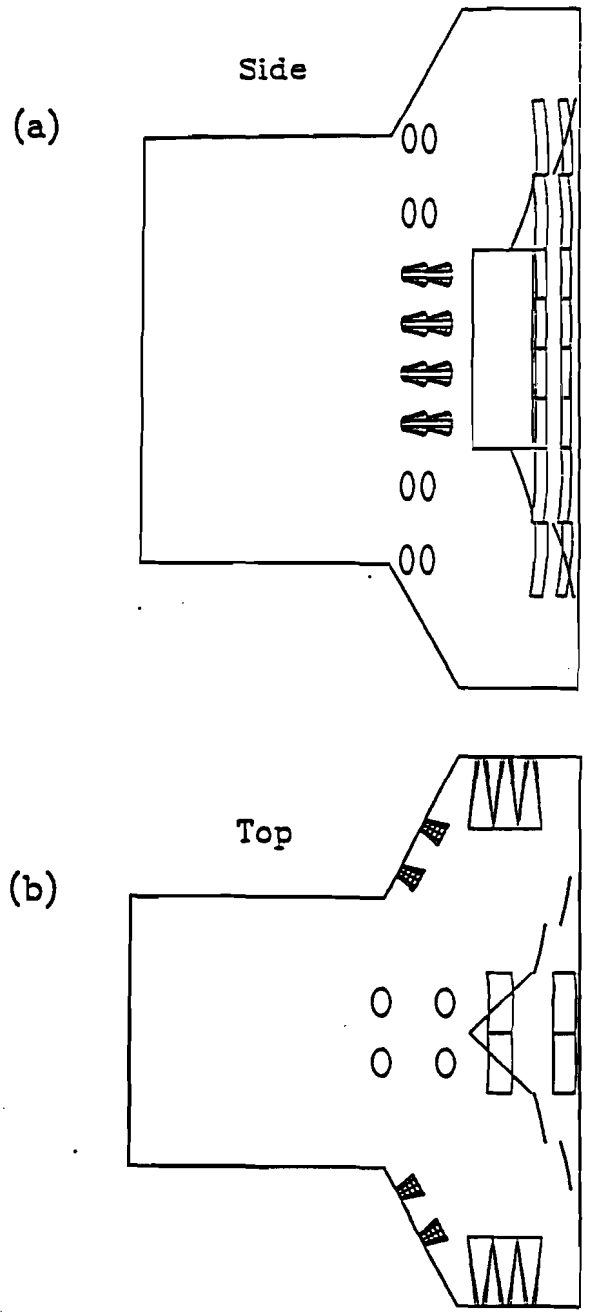

Figure 2.8: Side and Top View of C1

C1 detector is defined by a series of plane and focusing mirrors. The inner part of the active area consists of two thin mirrors, 14x32 inches which are oriented at 45 degrees to the beam (90 degrees to each other) and which reflect the light into 50 photo-multiplier tubes (25 on each side). The photomultiplier tubes are a collection of 2 and 3 inch diameter tubes and utilize light collection cones to improve collection efficiency. The tubes are oriented at 90 degrees to the beam direction to reduce the amount of material in the beam by removing the phototubes and electronics from the fiducial region of the counter and to reduce the amount stray light or scintillation light at the phototubes. The outer portion of the active area consists of 40 focusing mirrors. Each mirror is matched to a photomultiplier tube of 5 inches in diameter or a light collection cone and a photomultiplier tube of 3 inches diameter.

2.3.2.2 C2

The second Cerenkov counter, C2 (fig2.9), uses nitrous oxide as its active medium, giving a pion momentum threshold of 4.5 GeV/c. C2 has the lowest threshold of the three counters. Constructed by the University of Notre Dame, C2 has a path length in the beam direction of 74 inches and has an active area of 100 inches in the bend view (y) and 64 inches in the non bend view (x). C2 is located between P1 and P2 and is upstream of M2 so it is useful in identifying tracks contained both in the inner and outer parts of the spectrometer.

The active area of C2 consists of two segmented plane mirrors oriented 45 degrees to the beam direction and 90 degrees to each other. Each of the two mirrors measures 44x92 inches and is has an adjusted active area due to orientation of the mirrors and trajectory of the particles. The two plane mirrors reflect the light into an array of photomultiplier tubes. The inner portion of the counter consists of fifty-four 2 inch diameter tubes and the outer portion consists of fifty-six 5 inch diameter tubes. Each tube also has a light collection cone attached to improve detection efficiency. As with the inner section of C1, the C2 photomultiplier tubes are oriented at 90 degrees to the beam direction.

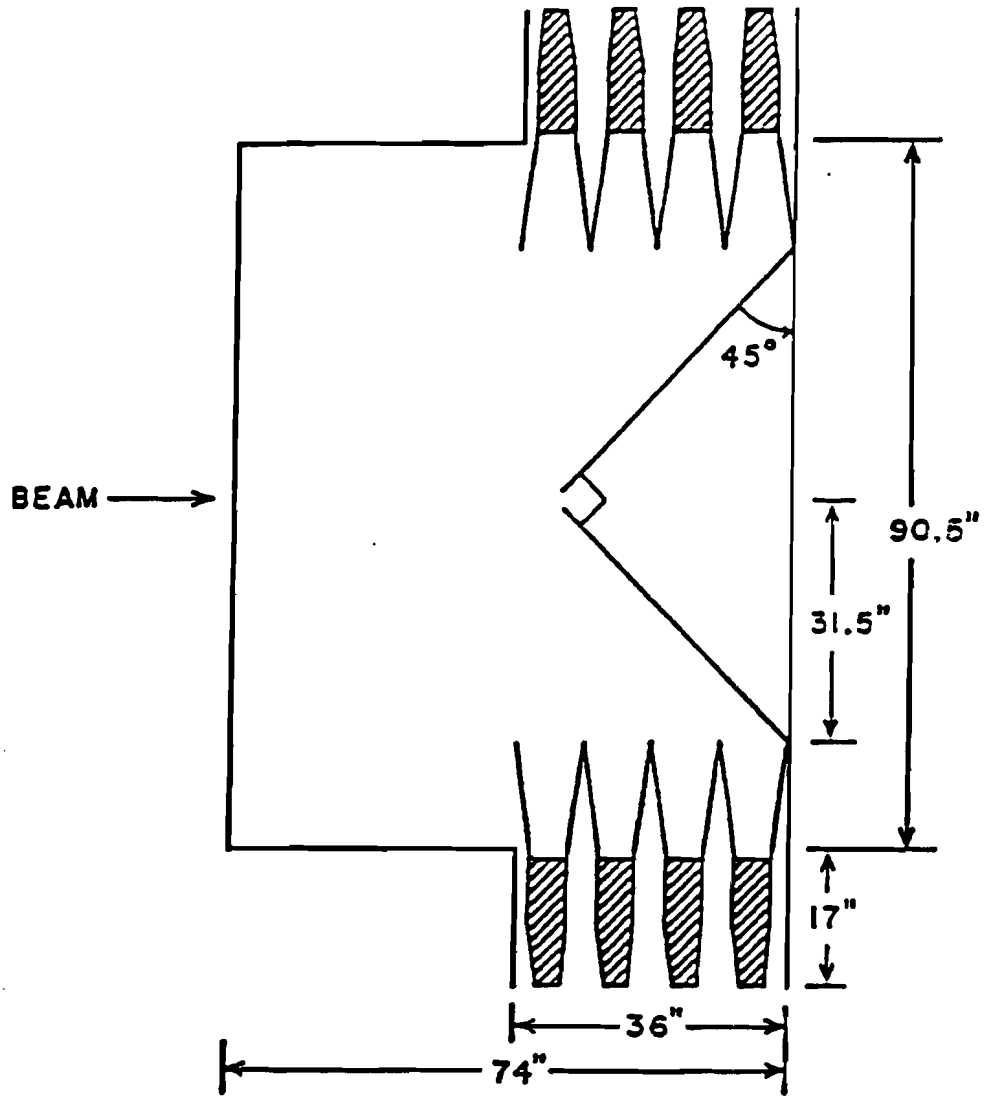

Figure 2.9: Top view of C2

2.3.2.3 C3

The final Cerenkov counter, C3 (fig 2.10), built by Fermilab, is also the most downstream counter. Situated between P3 and P4 and downstream of M2, C3 is useful only in particle identification for those particles which pass through both magnets, generally

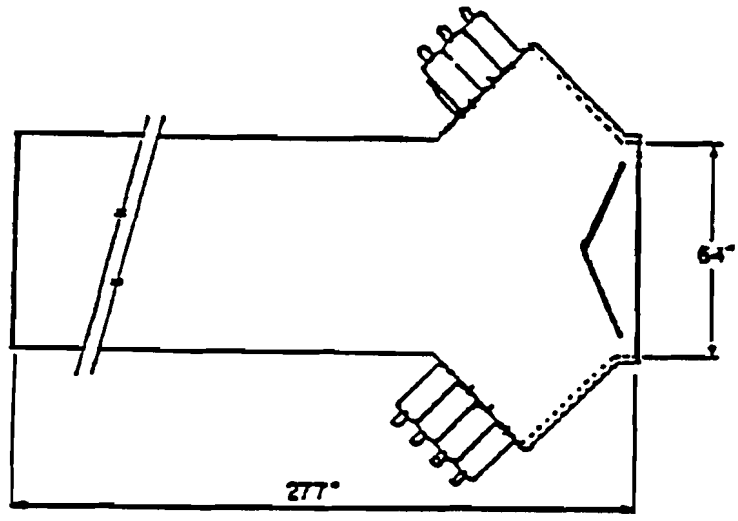

Figure 2.10: Top View of C3

higher momentum particles. Due to this consideration, C3 has the highest pion momentum threshold of 17.2 GeV/c. This high threshold is achieved by using He as the Cerenkov gas. The use of helium presents a variety of difficulties which need to be addressed. In an attempt to reduce poisoning of the photomultiplier tubes by helium diffusion, a nitrogen flush was installed over the face of each of the 100 tubes; due to the low photon yield of Cerenkov light in He, a path length along the beam direction of 277 inches was necessary; focusing mirrors and light collection cones were used to increase the collection efficiency of the tubes. The active area is divided into an inner section of 56 smaller mirrors and tubes and an outer section of 44 larger mirrors and tubes. The active area of the detector measures 79 inches in the bend view (y) and 55 inches in the non bend view (x).

2.3.2.4 Particle Identification

The particle identification utilized both PWC tracking and Cerenkov PMT information. The PWC tracks, or stubs (3 chamber tracks) are projected onto the appropriate cell in each

of the three Cerenkov counters and the presence or absence of light allows the differentiation of electrons, pions, kaons, and protons. Because of the gases in the Cerenkov system, and their respective thresholds, we have good K/π differentiation in the range of 4.5 GeV/c to 60.8 GeV/c, and good K/p differentiation in the range of 15.9 GeV/c to 115.5 GeV/c. For this arrangement of thresholds we have electron/pion separation up to 17.2 Gev/c. In the case of stubs (particles which only pass through the first two Cerenkov counters) we have K/π separation from 4.5 GeV to 23.3 GeV, K/P separation from 15.9 GeV to 44.3 GeV and e/π separation up to 8.5 GeV. Obviously all of these differentiation efficiencies are dependent on the photon detection efficiency of the particular phototubes. We currently do not use the Cerenkov system to try to differentiate between pions and muons.

2.3.3 Electromagnetic Calorimetry

The E687 spectrometer has two electromagnetic calorimeters. The purpose of these calorimeters is twofold. They are used to identify and calculate the energy for electrons, and they are used to reconstruct and provide energy information for photons.

2.3.3.1 Outer Electromagnetic Calorimeter

The outer electromagnetic calorimeter (OE) is matched to the yoke of the second analyzing magnet and is intended to catch those particles which would not pass through the second magnet. It is constructed of scintillator and lead sandwich and the scintillators are read out by photomultiplier tubes.

2.3.3.2 Inner Electromagnetic Calorimeter

The inner electromagnetic calorimeter (IE) was newly built for the 90-91 runs. It is

located between the HxV hodoscope and the hadron calorimeter. It is constructed of scintillating fibers and lead foil for greater energy resolution. The IE scintillation fibers are oriented in the horizontal, vertical, and diagonal direction. The diagonal fibers are used as tie breakers to resolve ambiguities in the positions of showers.

2.3.4 Hadron Calorimeter

The hadron calorimeter (HC) consists of 28 1.75" iron plates interspersed with wire chamber modules which are read out with anode pads (fig 2.11,2.12). The wire chamber modules operate with a 50/50 mixture of argon/ethane. These 28 plates represent 8 interaction lengths. Wire chamber modules are used in conjunction with anode pads to detect showers. A small uranium and scintillator calorimeter is situated at the center of the HC, this is known as the Central Hadron Calorimeter (CHC).

The main purpose of the HC is to provide a hadronic energy trigger for the second level trigger.

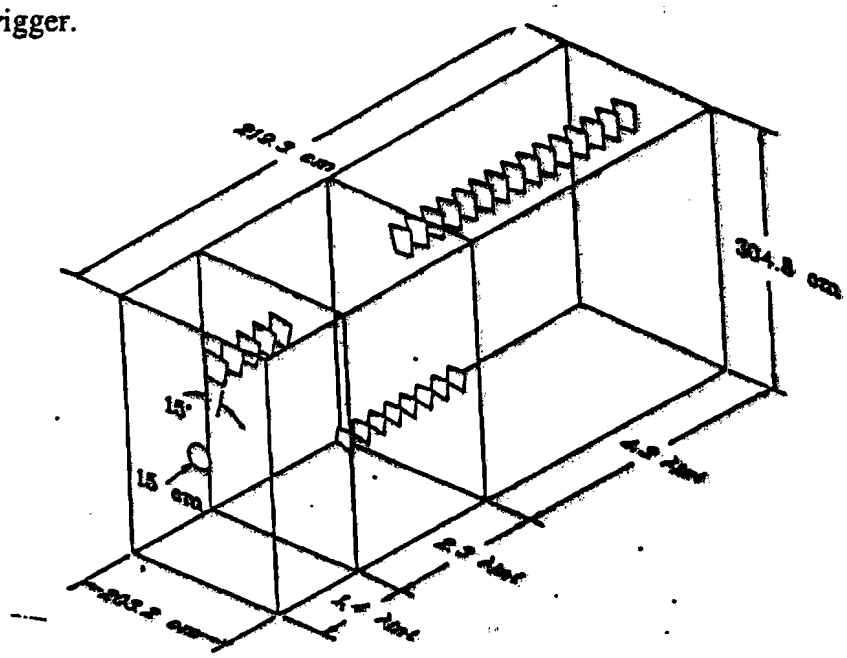

Figure 2.11: E687 Hadron Calorimeter

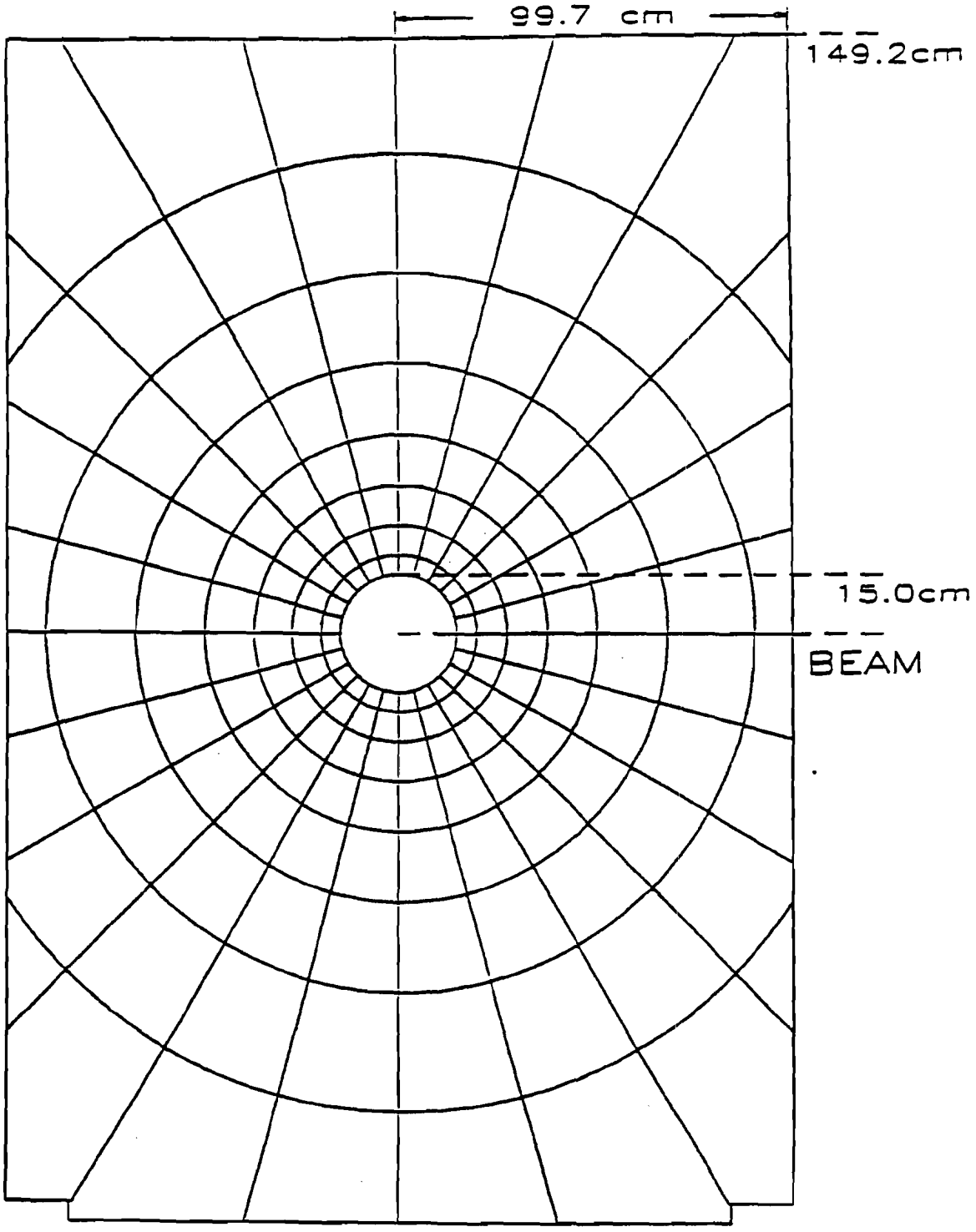

Figure 2.12: The hadron calorimeter pad arrangement

2.3.5. The Muon System

The muon system consists of inner and outer portions (fig 2.13), the outer portion of which is located downstream of M2. The outer muon counter system (OM) utilizes the yoke of M2 as a filter and consists of both scintillator hodoscopes and proportional tubes. The inner portion is located downstream of the hadron calorimeter, central hodoscope calorimeter, and for the part of the run when the beam gamma monitor was used. A muon filter was constructed of concrete blocks. This is in addition to the filtering which occurred in the inner electromagnetic calorimeter and the hadron calorimeter. The inner muon counters (IM) also consisted of both scintillation hodoscopes and proportional tubes. For the portion of the run when the E-683 spectrometer was used in place of the BGM, a hole had to be constructed in both the muon filter and the muon counters. This caused a slight problem with particle spray which was later rectified. The data from the scintillator hodoscopes was used as part of the second level trigger. The information from both the hodoscopes and the proportional tubes was used in data reconstruction for muon identification.

2.3.6 Triggering System

The triggering system consists of two levels, the master gate or first level trigger and the second level trigger. The master gate is designed to be a fast trigger to select events for acceptance into the data acquisition hardware. The second level trigger utilizes the information from the data acquisition hardware to select which events are to be written to tape.

Due to the need for fast response in the master gate, the first level trigger consists entirely of the output of fast scintillation counters(fig 2.14). Although not all of the fast scintillation counters are used in the master gate in data taking mode, all of the counters that

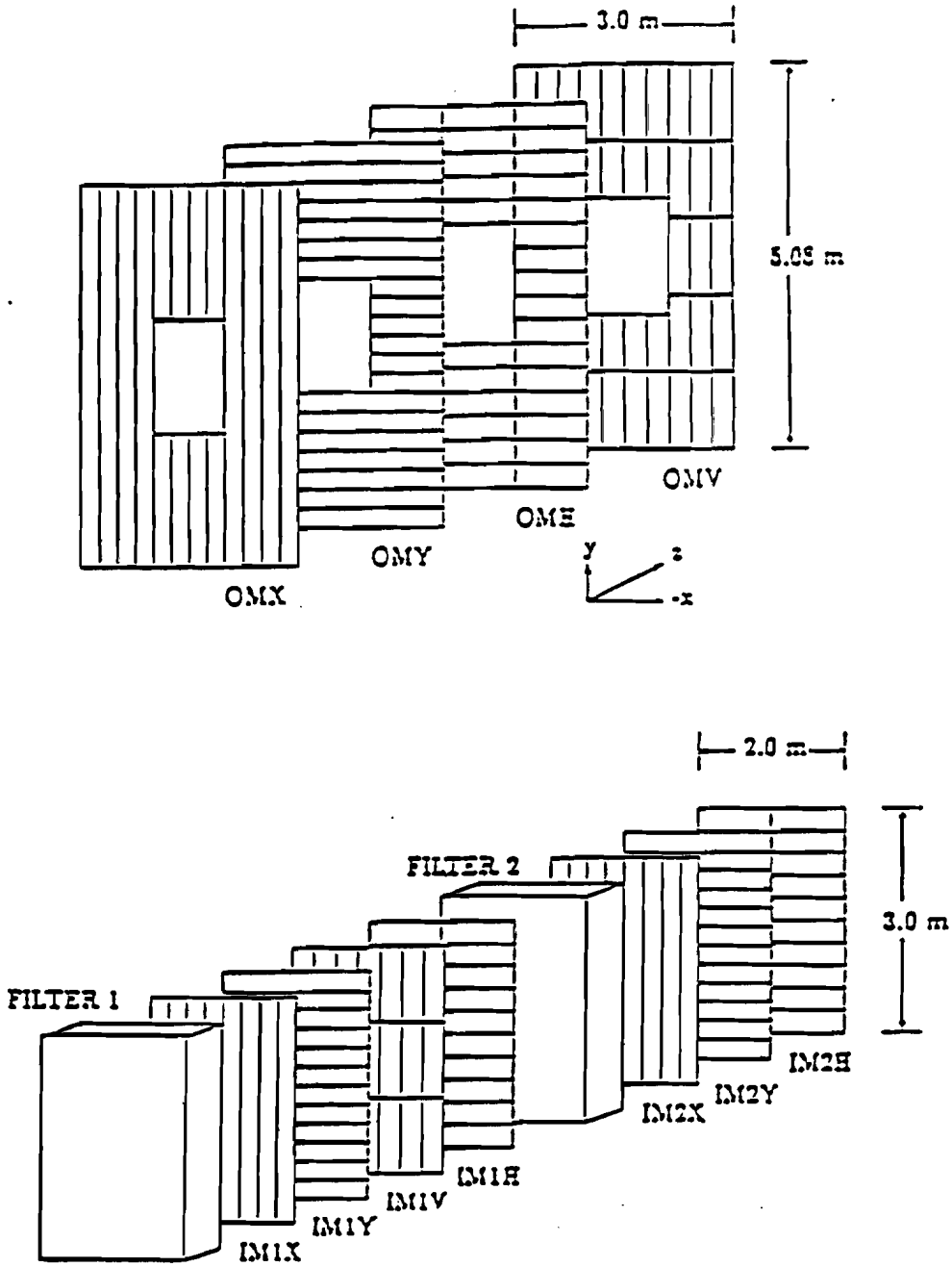

Figure 2.13: The E687 Muon system

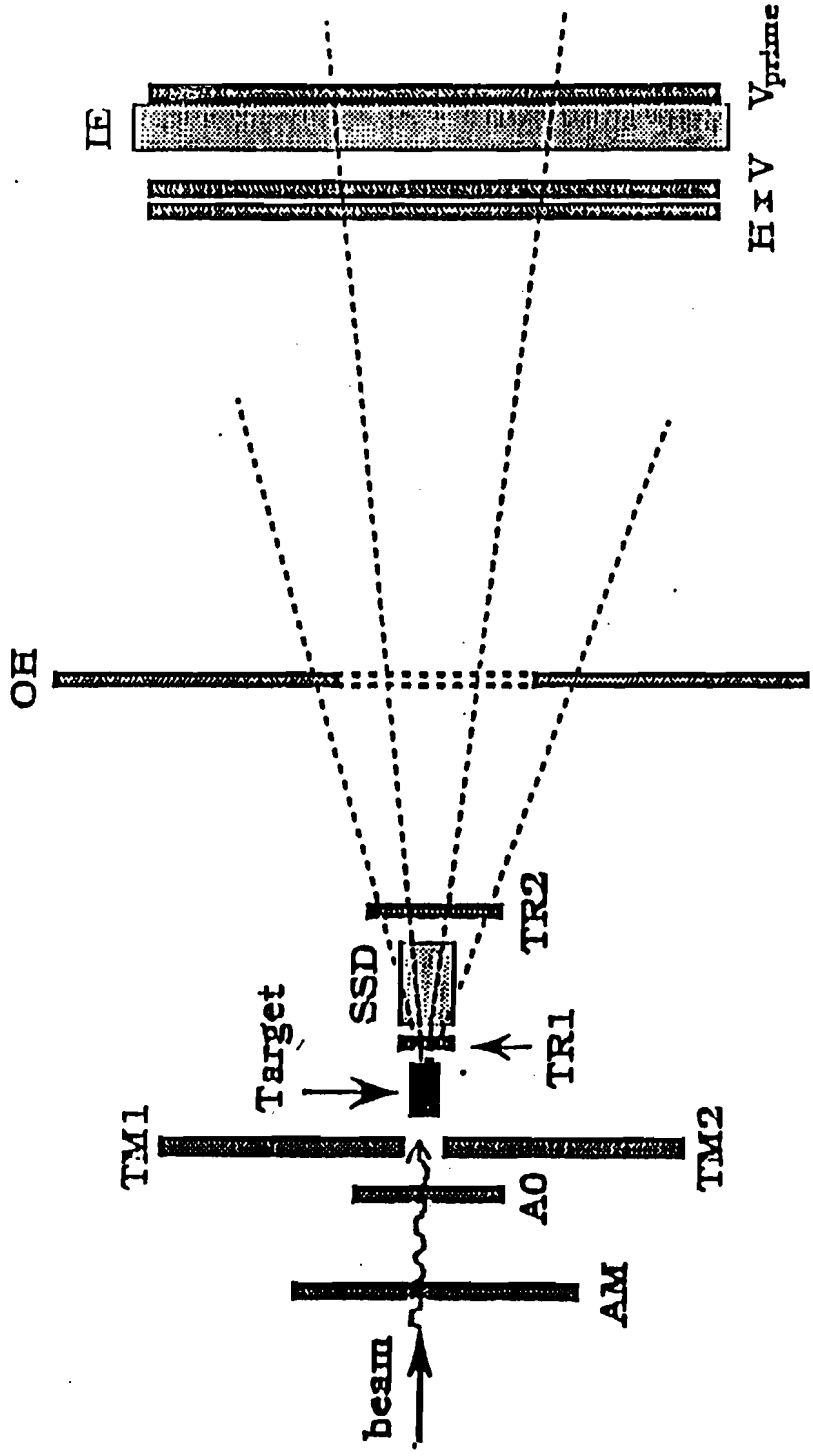

Figure 2.14: E687 scintillation counters

I will discuss are used in the master gate during some type of running.

2.3.6.1 AM

The anti-muon walls are located downstream of the RESH counter and upstream of the target hut. These two walls surround the beam line and cover the majority of the area in the pb6 enclosure which corresponds to the aperture of the experiment. The purpose of these two walls is to provide a veto against upstream muon "halo" that may contaminate the event. These consist of 24 scintillator paddles per wall and the AM is considered to have fired if there is a coincidence between one of the paddles in AM1 and one of the paddles in AM2.

2.3.6.2 A0

The A0 counter is located in the beamline between the RESH and target hut. This is a single scintillation counter used to veto charged particles in the beam.

2.3.6.3 TM1 and TM2

The muon trigger counters (TM1 and TM2) are mounted on the wall of the target hut and are designed to correspond to the aperture of M1. TM1 and TM2 are used primarily to trigger the data acquisition system in muon calibration runs.

2.3.6.4 TR1 and TR2

The trigger counters (TR1 and TR2) are located just upstream and down stream of the silicon strip detectors. These counters are used to insure that there is at least one charged particle track going through microstrip system.

2.3.6.5. OH

The outer hodoscope is a single layer of scintillator paddles mounted on the yoke of analysis magnet M1. These are used to detect particles in the outer portion of the spectrometer.

2.3.6.6 HxV

The HxV (Horizontal and Vertical) counters are a wall of scintillator paddles placed between P4 and the inner electromagnetic calorimeter. The HxV counters are organized into four quadrants with a gap to allow electron positron pairs to pass through without triggering. A valid signal from the HxV array occurs when there is a coincidence of one H and one V counter in a specific quadrant. The HxV signals, as used by the master gate can either be 1-body signals or 2-body signals. The 1-body signals indicate that there was a coincidence in at least 1 quadrant. The 2 body signal indicates that there were coincidences in at least two different quadrants.

2.3.6.7 V'

The V' (Vertical prime) counters are a rather late addition to the spectrometer and are mounted behind the IE calorimeter. The purpose for the V prime counters is that, with the HxV, there were often misfires due to scattered or higher Pt pair electrons. The selection criterion for the HxV' trigger is the same as for HxV with V' replacing V. V' also has a gap to allow electron positron pairs that may pass through the IE to pass without triggering the system.

2.3.6.8 Master Gate

The master gate, as stated above, is comprised of a coincidence of several of these counters. In normal running the master gate is:

MG = (TR1.TR2).((HxV)2body + (HxV)1body.OH).(A0+AM1.AM2)

The master gate trigger rate is roughly 4×10^5 per spill with a photon flux of 1.5×10^8 (where the photons are required to have momentum $p > 133$ GeV/c) incident on the target.

2.3.7 Second Level Trigger

The second level trigger utilizes latch information to make more specific events selections. The primary latch information that is used is the total and transverse energy information from the hadron calorimeter. Other information that was used in various general second level triggers included PWC multiplicity, and RESH requirements. Specific triggers included the use of muon latches and a prescaled Master Gate.

2.3.8 Data Acquisition System

After events pass the second level trigger, all of the relevant information from the ADCs, TDCs, and latches are fed into Lecroy 1892 fastbus memories and CAMAC memories. At this point the PAN-DA [15] data acquisition system developed by the Fermilab Online and Data Acquisition Software Groups takes control of the data. The PAN-DA system was developed in response to the anticipated data rate of a few megabytes per second. To handle the higher rates the system utilizes CAMAC and FASTBUS smart crate controllers (SSC and FSSC) as well as the Struck General Purpose Master (GPM). The information from

the FASTBUS and CAMAC memories are routed by the GPM to a VME crate of Fermilab ACP parallel processing computers. A Motorola MVME133A-20 based processor board coordinates the data flow in the ACP system. The data is reorganized into the desired form for writing out to tape. To write the data to tape it is first sent to a CIPRICO RIMFIRE 3510 tape controller. The RIMFIRE is capable of supporting up to seven 8mm tape drives. E687 had 4 drives, each with a data recording rate of 245,000 bytes per second, for a combined rate of approximately one megabyte per second. Due to transfer rate bottle necks between the Lecroy ADCs and the FASTBUS memories we never achieved a sustained data rate of over 0.5 megabytes per second so for the majority of the run we only used two 8mm tape drives.

In addition to the main system described above there are several additional software systems. The Run Control task serves both to receive control information from the host machine and also to coordinate the data acquisition activity within the VME crate. The Data Hoist task identifies events for real time processing and delivers them to the appropriate machine.

CHAPTER 3:

ANALYSIS

The analysis of the data consists primarily of three processes; data reconstruction, data reduction and final analysis. The first of these is performed to translate the assorted latch, ADC and TDC information that was obtained from the spectrometer into useful physics information such as particle identification, momentum, charge, or energy. For the E687 experiment this initial reconstruction was referred to as Pass 1 and the initial part of the data reduction was referred to as Skim 1. Both Pass 1 and Skim 1 were performed at Fermilab on a RISC cluster from the Fall of 1991 to the fall of 1992. These were both a cooperative effort of the entire collaboration with individuals running shift. Portions of the output of the Skim 1 were distributed to the various institutions where further reduction and final analysis were performed.

3.1 Pass 1

The initial reconstruction (Pass1) was performed on the majority of the 5×10^{8} recorded events. These events were contained on approximately 1000 8mm tapes. Skim 1 included a level of data reduction in that it eliminated obviously bad or unusable events. Examples of such events would be those with missing blocks of data, too many PWC hits, or too few tracks. The desired events were then written out to approximately 2000 8mm tapes with a loss of about 10% in the number of events.

As stated above there were several aspects involved in data reconstruction and they will be described below.

3.1.1 Microstrip Reconstruction

The microstrip information was used primarily for vertexing with some confirmation of track momentum when the PWC tracking, which will be discussed later, was added. Due to the needed precision of the vertex for analysis it is necessary to have good tracking information out of the microstrips. The basic algorithm for the microstrips (MICRORICO) looks at the four planes in each of the three different views, or projections, of the microstrips and fits straight tracks to the points. Microrico then combines the three projections to form a 3-D space track. Since there is no magnetic field, this is a fairly straightforward task of combining hits from two projections and looking for a confirming track in the third. In reality, thought still straightforward, the task is a bit more involved. In finding the projection of tracks there are two difficulties; first is the variable pitch of the microstrips, and second is missing or double tracks. The variable pitch is manifest in two ways; difference by station and for a given station different pitch for inner and outer regions. The first station has an inner region of 25um and an outer region of 50 um, the other three stations have a inner region of 50um and an outer region of 100um. The problem of variable pitch is handled by making the weighting of the hits proportional to 1/pitch. The problems associated with missing and double hits are handled in a variety of ways. The first requirement is that 3 or 4 stations in each projection must have a hit. Clean up algorithms are employed later to account for Coulomb scattering or wide angle tracks with fewer than 3 hits in a projection. Double hits are first handled when coordinates are determined. If two adjacent channels are on and have an energy that is consistent with 1 minimum ionizing particle (mip) then this combination is considered as 1 hit with it's location as the mid-point between the two channels. If three channels have energy that is consistent with 2 mips it is considered to be two hits. The two hits can be assigned in one of two ways. If there is a large disparity in the energy of the two outside channels, the location of one hit is considered to be the higher energy outside channel and the other hit is considered to be at the mid-point between the middle channel and the other

outside channel. If the two outer channels do not show much energy difference the position of the hits are taken as the mid-points between the inner channel and the outer channels. Two and three adjacent hits that have energies consistent with two and three mips respectively are considered to be two or three hits. Groupings of 4 or more hits are not considered when looking for projections, but may be used later as confirming hits. The next means of eliminating multiple hits comes at the stage where three dimensional space tracks are made from the projections. All space tracks are required to have a χ^2 per degree of freedom of less than eight, which was determined empirically. The algorithm attempts to reduce the number of grouped tracks, possibly due to multiple adjacent hits, on the basis of the lowest χ^2. This method is also used to reduce tracks that share one or two projections.

The efficiency of the microstrip algorithm was found to be 96% overall and 99% at 10 GeV and 90% at 2.5 GeV by use of Monte Carlo simulation. In addition there were found to be less than 2.7% spurious tracks in the microstrip analysis. This initial microstrip analysis is independent of the PWC reconstruction; the resulting tracks are later correlated with the PWC system for the purposes of momentum determination as well as increasing the efficiency of both the microstrip and PWC tracking routines.

The resolution of the microstrip track at a the z position of the center of the target was calculated to be:

$$\sigma_x = 11\mu m \sqrt{1 + \left(\frac{17.5\text{GeV}}{p}\right)^2}$$

$$\sigma_y = 7.7\mu m \sqrt{1 + \left(\frac{25\text{GeV}}{p}\right)^2}$$

This is in good agreement with vertexing studies of the data.

3.1.2 PWC Analysis:

Since the PWC are used for tracking there are some obvious similarities to the microstrip tracking routines. There are however several important differences. The first, and major, difference is that the PWC are on either side of a magnet, M2, which means that there are deflections expected in several of the projections because of the magnetic field. In our case three of the four views have such a deflection. The fact that there are 4 views in the chambers is a second important difference. The extra view gives an additional level of redundancy which is needed due to the fact that the wire chamber channels are less efficient and more likely to have noise than the microstrip channels.

The PWC tracking is performed by matching each hit in the first chamber (P0) with a corresponding hit in the third chamber (P2) and looking at the second chamber (P1) for a confirming hit. If there are hits in all three of these chambers this resulting segment is refered to as a stub. In the case of the x-projection, or non-bend view, the stub is simply projected downstream of the M2 Magnet and confirming hits are looked for in P3 and P4. If confirming hits are found this 'stub' is refered to as a track. In the case of the bend view, the stub is projected to the bend center of M2 and this spatial point is then matched with hits in P4 and confirming hits are looked for in P3. The above description is for cases where there are no missing hits. There are a variety of methods that are used under the assumption of missing hits in P1, P2, P3, and P4. At this point in the analysis all track and stub projections must have a hit in P0. The projections are then taken in pairs and confirming projections and hits are searched for. Once a three dimensional space track is found, a χ^2 of the track is taken for a preliminary cut. The momentum of the track is also calculated and used in an iterative process to find more hits or projections associated with the track. A final χ^2 cut is applied to the track which is also used to arbitrate between multiply used hits or tracks. A final hit analysis of the track is made. Each space track must have hits on at least 15 of the 20 possible planes and cannot be missing more than 2 hits from any one chamber. Additional tracking analysis is

done after the linking stage which mainly involves projecting unlinked microstrip tracks into the bend center of M1 and using this as a space point instead of P0.

Overall the efficiency of the PWC tracking algorithm was found by Monte Carlo to be 98% with less than 0.5% spurious hits.

3.1.3 Linking

Since there are two different systems for tracking it is expected that improvements will be realized overall through combining the information from the two systems[16]. As we will see later the PWC tracks are associated with momentum determination and particle ID while the microstrip tracks are associated with high resolution vertexing. The first step in the linking process is to calculate the 2-dimensional miss distance and slope at the bend center of the M1 analysis magnet. Three chamber tracks (stubs) are only used to calculate the miss distance in the nonbend view. Any tracks that are within a minimum miss distance are refit for all 32 planes (12 for the microstrips and 20 for the PWC's). While there is no multiple Coulomb scattering correction at this stage of the analysis, nevertheless the χ^2 is adjusted for expected multiple scattering effects. This χ^2 is used to arbitrate between multiple links of PWC tracks, i.e. the connection of one PWC track to several microstrip tracks or one microstrip track to several PWC tracks. Each PWC track can be used only once but each microstrip track may be used more than once. This is mainly due to the prevalence of such things as imbedded pairs, which are electron positron pairs that are colinear until they reach the M1 magnet. Monte carlo calculations indicate a linking efficiency of 90% between the PWC and microstrip (SSD) systems.

3.1.4 Momentum Determination

Momentum determination is handled in similar but distinct ways for the two types of PWC tracks. The easier of the two is the case of 5-chamber tracks. Since these measured tracks have segments on either side of M2, the bend of the particle in M2 is found and this bend is used for the momentum determination. After a momentum has been found for M2 and the MPWC track has been linked to a Microstrip track, a consistency check is performed using the deflection in M1. For three chamber stubs that are linked, the bend through M1 is calculated and this is used to calculate the momentum of the track. Unlinked track momenta are found through a variety of algorithms. The main strategy in determining the momenta of unlinked stubs or confirming the momenta of unlinked tracks is to project a line from the intersection of the track at the bend center of M1 to some vertex. The most desirable situation is where there is one SSD vertex, in which case this vertex is used as the end point of the track. If there are multiple SSD vertices the stub is projected back in the non-bend view and the criterion of closest approach is used to arbitrate between possible vertices. If no SSD vertices are available, or none fit the criterion, a main spectrometer vertex, found from PWC tracks, is used for track projection. If there are no usable main spectrometer vertices then the center if the target is used as the vertex position for momentum determination,

The momentum resolution for the experiment is calculated as:

$$\frac{\sigma_p}{p} = 3.4\% \left(\frac{p}{100\text{GeV}}\right) \sqrt{1 + \left(\frac{17\text{GeV}}{p}\right)^2} \qquad \text{using M1}$$

$$\frac{\sigma_p}{p} = 1.4\% \left(\frac{p}{100\text{GeV}}\right) \sqrt{1 + \left(\frac{23\text{GeV}}{p}\right)^2} \qquad \text{using M2}$$

The proportionality of sigma to p^2 is due primarily to the granularity of the PWC system. The large MCS effect for M2 is due to the longer lever arm and additional material that a particle must traverse to be measured in M2. Despite the MCS effects, the resolution of tracks that reach M2 is better over almost all momentum ranges. Studies of the momentum resolution

have shown that M1 and M2 momentum resolutions are understood to within 10 percent with systematic differences being to within 0.5 percent.

3.1.5 Vertexing

There are several different types of vertexing that are used in the E-687 analysis. The two main types of vertexing also tend to differentiate between analysis techniques. The first type is what is considered a global vertex approach. The first step in the global vertexing algorithm [17] is to take all of the available tracks and form a single vertex. Individual tracks are then removed and the effect on the χ^2 is examined. The process is iterated until there is no significant improvement in the chi squared per degree of freedom. At this point the χ^2 is compared to a minimum acceptable χ^2. If the vertex passes this cut the process is restarted using the tracks that were thrown away to see if another vertex can be formed. This process is iterated until either all of the tracks are used in vertices or the remaining unused tracks cannot make a vertex with a low enough χ^2. This global vertex approach can be used with either Microstrip tracks or PWC tracks to find SSD vertices or main spectrometer vertices respectively. Other than their use in momentum determination of unlinked stubs, this thesis analysis does not utilize the results from the global vertex routine.

The second type of vertexing used is a "candidate driven" vertex analysis [18]. This type of analysis chooses a specific final state which is of interest. It then finds all particle combinations in an event which are consistent with that final state. For each specific combination a vertex is found using the candidate particles. The total momentum of the combined particle is found and defined as a new track. This new track is used to seed another vertex. Similar to the global vertex algorithm, all unused tracks are combined with the new track to determine a vertex. Then tracks are removed iteratively to generate the best χ^2 for the primary vertex. It is also possible to use the results of this vertex to further seed another vertex. While not implemented for this dissertation, this process is being actively considered

for b analysis. The result of the candidate driven analysis is a large number or potential primary-secondary vertex combinations. These combinations are then scrutinized using a variety of measures. The most powerful of these is the significance of detachment cut, known variously as the L/sigma or elsig cut. This cut is based on the linear separation of the vertices divided by the error of the longitudinal individual positions of the two added in quadrature. This elsig number also identifies that the secondary vertex is downstream of the primary vertex. The next measure is the confidence level of the primary and secondary vertices. This number is calculated by looking at the χ^2 and figuring what the confidence level is that all of the tracks actually come from that vertex. In this analysis these quantities are labeled CLP and CLD for confidence level of the primary and confidence level of the downstream vertex. This analysis uses a 1% CLP and CLD cut and other than for systematic studies the CLP and CLD cuts were not used. The last two intrinsic cuts that are used in the candidate driven vertex analysis are the isolation cuts. These cuts are known as CL1 and CL2. The CL1 cut is the confidence level that one of the tracks from the secondary vertex is consistent with being part of the primary vertex. The CL2 cut is calculated by finding the confidence level that any track that is not in the primary or secondary vertex is consistent with being in the secondary vertex. Since both of these are calculations of a situation which is undesirable if true we therefore insist that the confidence level be below a certain level. The CL1 cut serves to eliminate combinatoric background that may exist from particles in a single vertex which may pass the elsig cut for vertex separation. The CL2 cut addresses an entirely different problem which is charm background. Since the candidate driven vertexing routine starts from a hypothesis that there is at least a certain content to the down stream vertex, there is no effort made in the initial vertexing process to look for additional tracks that are consistent with that vertex or to look for the vertex with the largest number of tracks as the global vertex fit does. This strategy, although it has several advantages, leaves us open to background from such states as $D_S \to K\pi\pi$ which may be reconstructed as $D^0 \to K\pi$. For background due to misidentification of charm there are real vertex separations and the elsig, confidence level and CL1 cuts will

not eliminate this background. However the CL2 cut can be used in conjunction with particle ID cuts to eliminate shifts due to both loss of a particle and/or misidentifaction. We will look at the particle ID process in the next section. Wheter the background is from missing particle or misidentified the knowledge that there exists another particle which is consistent with the secondary vertex is invaluable to eliminate long lived, or charm, background and this technique has been used extensively in this analysis.

3.1.6 Particle Identification.

The Pass 1 analysis has three components to particle identification; these are Cerenkov, muon, calorimetric identification. Since the Cerenkov ID is the only identification that is used in this analysis, I will be brief in the discussion of the muon and calorimetric identification.

3.1.6.1 Cerenkov Identification.

The Cerenkov system consists of three gas threshold Cerenkov counters. For details of the physical characteristics of the counters the reader is refered to the equipment section of this dissertation. The Cerenkov counter thresholds are selected to give good particle identification among electrons, pions, kaons, and protons over a wide range of momenta. Muons and pions are close enough in mass that the Cerenkov system is not used to differentiate them. The way that threshold Cerenkov counters work is that when a particle passes through the activating gas the medium will emit Cerenkov light if the particle speed exceeds the local speed of light. The exact determination of the threshold momentum is given by:

$$p_t = \frac{m}{\sqrt{n^2-1}}$$

This leads to two useful characteristics of the Cerenkov counters, For a given particle, the medium will emit Cerenkov light at a lower particle velocity and therefore lower momentum, in a manner which is inversely proportional to the square root of the difference of the index of refraction squared from one, and for a given medium, lighter particle will cause the medium to emit light at lower momenta and heavier particle will cause the medium to emit light at relatively higher momenta.

The first step in the Cerenkov analysis [19] is to examine each cell in the three counters to generate an on or off code for the cells. This code is determined by looking at the phototube pulse height as recorded by the ADC modules and determining if the ADC value is significantly above the pedestal value for that particular ADC channel. Once the Cerenkov cells have all been set on or off the algorithm then takes each main spectrometer track and projects it through each Cerenkov counter to determine which cells correspond to the track. Once the principle cell is determined, the measured momentum is used to make a hypothesis about the light yield in the principle and adjacent cells. If light is detected in any of the appropriate cells the track is called "on" whereas it is called "off" if light was anticipated and no light was detected. If a condition exists that a track cannot be called definitely on or off it is called "confused". The main sources of confusion include the kinematic case of the threshold regions for a particle or the geometric cases of light falling on boundaries between cells or two tracks being associated with a single cell. Once each track is called "on", "off", or "confused" the track momentum is compared to the momentum threshold to get a Cerenkov word for that particular detector. The Cerenkov word is a four bit word with the four bits corresponding to the electron, pion, kaon and proton and a value of one in the bit position corresponding to Cerenkov information consistent with that particle hypothesis. The bits are arranged starting with the least significant bit as follows:

Bit 1 : electron
Bit 2 : pion
Bit 3 : kaon
Bit 4 : proton

A confused signal is assigned a value of 15 (all bits on) for the word at this point of the analysis. Since one of the major sources of confusion is the threshold region of the particles the algorithm is constructed in such a way to allow the tracks to be treated differently in the threshold region, which is defined as threshold to 1.08 x threshold. Table 3.1,below, shows the possible values of the specific cerenkov words.

Table 3.1

Track Momentum Region	Track off	Track on	Confused
$0 < p < P_{pi}$	1110	0001	1111
$P_{pi} < p < 1.08xP_{pi}$	1110	0011	1111
$1.08xP_{pi} < p < P_k$	1100	0011	1111
$P_k < p < 1.08xP_k$	1100	0111	1111
$1.08xPk < p < P_p$	1000	0111	1111
$P_p < p < 1.08xP_p$	1000	1111	1111
$p > 1.08xP_p$	0000	1111	1111

Once a Cerenkov word is found for each of the three detectors and they are logically ANDED together. The attached figures show the threshold regions and combined particle identification for the various particles and cerenkov counters. Once the three Cerenkov words are ANDED together the final word is called the ISTAT word and the codes are as presented in Table 3.2 below.

Table 3.2

ISTATP	Identification
0	Inconsistent information
1	electron definite
2	pion definite
3	electron, pion ambiguous
4	kaon definite
6	kaon, pion ambiguous
7	electron, pion, kaon ambiguous
8	proton definite
12	kaon, proton ambiguous
14	pion, kaon, proton ambiguous
15	electron, pion, kaon, proton ambiguous

These codes are used for particle identification for the remainder of the analysis.

3.1.6.2 Muon Identification.

As stated in the equipment section, the muon system consists of inner and outer muon detectors[20] . The muon analysis consists of projecting PWC tracks through the various muon filters (steel or concrete absorbers) and looking for corresponding hits in the muon scintillators or muon proportional tubes. In this run there were seven layers of muon detectors of which 5 needed to be hit to confirm a muon identification. The inner muon detectors were placed behind a wall of concrete downstream of the hadron calorimeter. The outer muon system used the M2 magnet yoke and OE calorimeter as the muon filter.

3.1.6.3 Calorimetric Identification

The inner and outer electromagnetic calorimeters as well as the hadronic calorimeters are used for electron and photon identification. The most obvious use of the electromagnetic calorimeters is for the reconstruction of neutral pions from photons. Additionally they can

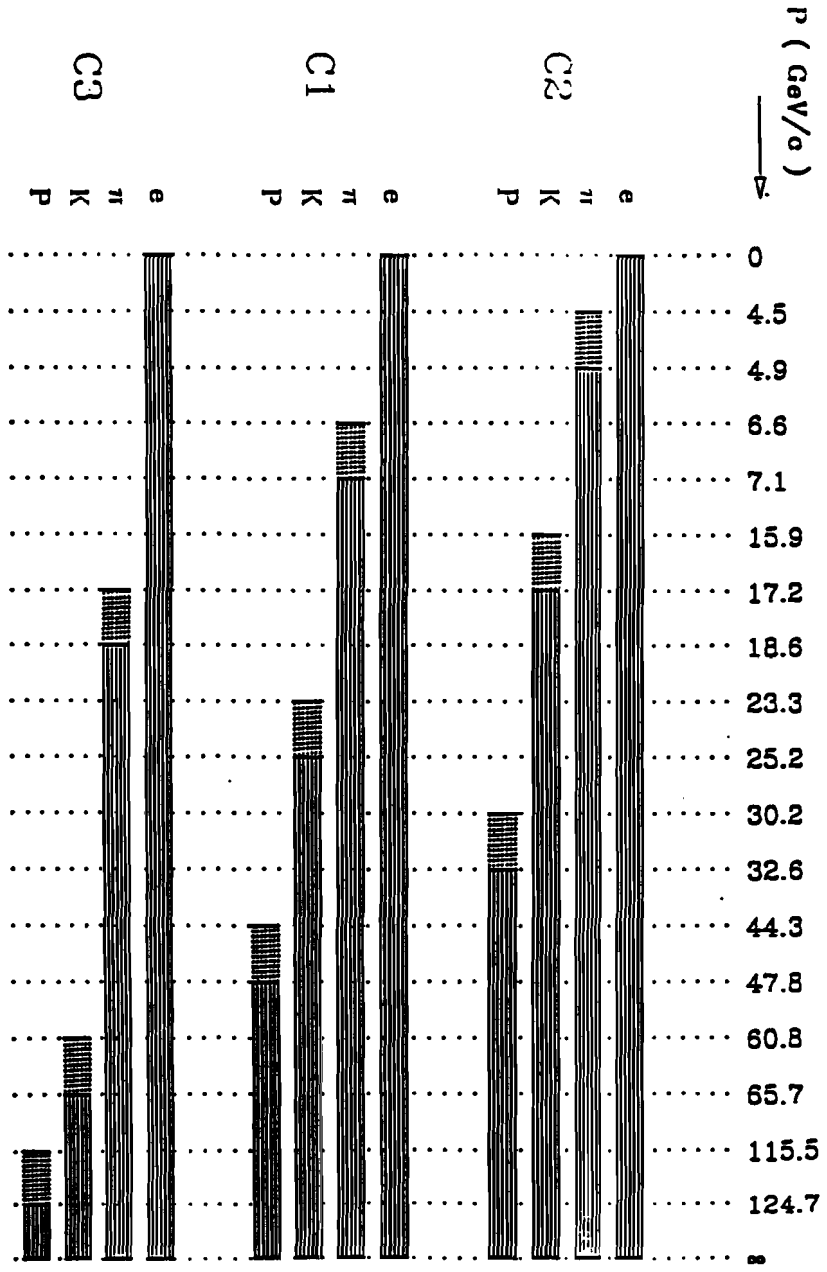

Figure 3.1: Cerenkov detector identification regions

be used for electron / pion separation either through shower profile or E/p measurements.

3.2 Data Reduction

Data reduction proceeds in two steps. The first is the selection of relevant events and the second is the selection of relevant information that those events contain. As stated above, the Pass 1 process began with approximately 1000 data tapes representing a raw data set in excess of 500 million events. The output of the pass 1 process resulted in 2000 data tapes, containing full reconstruction of the initial data set. At this stage some events were removed because of defects. The slight reduction in the number of events was due primarily to the discarding of obviously bad events, those with either too many or too few tracks to be able to be reconstructed or those with missing critical data blocks. The Skim 1 process began with these 2000 data tapes and processed them to three data streams that represented various data reduction strategies. The first skim was operated under the premise that all events with physics potential would be kept and all possibly relevant data associated with these events would be kept. This skim represented approximately a 60% reduction in number and size of the data set. The second skim was operated under the theory that all relevant events should be kept but that the raw information need not be kept if data summary blocks were generated and kept. This skim caused a reduction to 40% of the original event numbers but represented a reduction by a factor of 10 in the physical size of the data. The last skim stream imposed very precise definitions on the prospective physics needed to keep an event but once an event was selected to be kept all of the information about the event was kept in the form of miniADC blocks. This strategy resulted in a factor of 20 reduction in the number of events and a factor of 30-50 reduction in the physical size of the data set. The analysis in this dissertation was generated from the second skim stream. There were a variety of physics topics which were selected to be included in the second or QT skim stream, as indicated in the following table

Table 3.3

Skim Bit	Stream
1	Semi-Leptonic Skim
2	1% pre scale skim
3	Master Gate Prescale Skim
4	Pair Trigger Skim
5	Vertex Skim
6	Vertex Skim (2nd Bit)
7	Cascade Skim
8	K short Skim
9	EZ-D Skim (All)
10	EZ-D Skim D^* Selection
11	EZ-D Skim Cabibbo Allowed Decays
12	EZ-D Reserved but not used
13	Lambda Skim
14	Kink Skim
15	Baryon Skim
16	Proton, Kaon, Pion Skim
17	Lepton Skim
18	Muon Skim
19	Diffractive Skim
20	
21	Topological Skim
22	Topological Skim
23	
24	
25	Kaon Lepton Skim
26	Phi Skim
27	Phi Skim
28	Phi Skim
29	Phi Skim
30	Phi Skim

As stated above, the first skim (MOM or parent skim) contains all of the skimmed events and the DST2 block, the EZD block, the cascade block, the MiniADC block, the OE and IE reconstructed blocks, the Muon block, and the reconstructed Cerenkov block. The second or QT skim contains all skimmed events but only the DST2 block, the EZD block, the cascade block, and the reconstructed muon block. The third, or tiny, skim only has the Cabibbo favored decays (called golden modes) from the EZD analysis (skimbit 11), the phi skim (skimbit 28), the cascade skim (skimbit 7), and the kaon lepton skim (skimbit 25). It contains all of the data blocks which the QT skim has as well as the miniADC block. This thesis analysis used the data from the QT skim and specifically used those events from the EZ-D analysis.

3.2.1 EZ-D analysis

The EZ-D analysis is a package that was developed by the high energy group at the University of Illinois[21]. This analysis looks for events which are consistent with having D^0, D^+, or D_S invariant masses and decay modes. The EZ-D analysis looks for all charged final states that include electrons, muons, pions and kaons. The EZ-D analysis began as an outgrowth of the skim-a-dee analysis that was created for the analysis of the 1987-88 run of E-687. The main addition was the inclusion of the electron and muon states, but these states are not considered in the analysis presented here. Rather, I will confine the discussion to the states containing kaons and pions. Due to the large number of decay modes contained within EZD it was inefficient to approach the modes in the standard software analysis manner of nested do loops. A novel approach was developed to reduce the combinatorics and computing time. This approach involved two nested do loops. The first loop selects the tracks to use and the second loop assigns the identification of the particles. Both loops utilize that fact that track

selection and particle identification are on/off operations, which leads to an obvious use of binary counting. The track assignments are accomplished by means of the following do loop index:

```
do ICOM= 3,(2**NT)-1
```

This gives an equal number of bits as tracks and in counting uniquely selects track combinations. At this point there is a preliminary analysis that looks at the total charge of the event, requiring it to be -1, 0, or 1, and the number of tracks in the event, less than or equal to 6. If these two conditions are met a second do loop is executed:

```
do LCOM = 0, (2**NBDY) - 1
```

where NBDY is the number of tracks in the state that is being examined and a 1 in the bit represents a kaon identification. Several steps are taken at this point to reduce the combinatoric background; first, only linked tracks are used to construct the D mesons and second, any particles that are identified as kaons are required to meet the KP7 Cerenkov requirement. The KP7 requirement specifies that kaons are required to be either kaon definite, kaon proton ambiguous or kaon, pion ambiguous if the momentum of the particle is greater than the than 60 GeV which corresponds to the kaon threshold for the C3 Cerenkov counter and thus the limit of kaon pion separation. There are also vertex requirements at this point in the analysis. There is a general vertex separation, or elsig, requirement of ≥ 2 and a confidence level requirement on both the primary and secondary vertices of 0.1%. Since, however, the use of the D^* to D^0 + pion decay is so prevalent and useful, due to the small excess energy of the extra or tagging pion, the EZ-D analysis treats this as a special case of the D^0 decay as follows. Once a D^0 candidate is identified to be within the right mass range, all tracks that are not used to make the D^0, linked or unlinked, are used to calculate an

invariant mass for the D^*. The mass difference between the D^* and the D^o is calculated and if it is less than a specified cut, 160 MeV/c^2, the requirement on the primary vertex is eliminated except that the secondary vertex must still be downstream of the primary. If the conditions of a D* are met, then skim bit 10 is set in addition to the skimbit 9 which is set whenever a charm meson candidate is found. When any charm candidate is found, D^o or D^*, there is a specific EZ-D block which is created. This block contains a variety of information. Most important to this analysis is the NDFTYP block which lists, by number or mnemonic, the number of decays of each type that are found in each specific event. The decays for the D^0 are as follows:

Table 3.4

Type	Number	Mnemonic	Decay
2-body	2	IKPI	$D^0 \to K^-\pi^+$
	10	I2PI	$D^0 \to \pi^+\pi^-$
	11	I2K	$D^0 \to K^+K^-$
4-body	3	IK3PI	$D^0 \to K^-\pi^+\pi^+\pi^-$
	12	I4PI	$D^0 \to \pi^+\pi^+\pi^-\pi^-$
	13	I2K2PI	$D^0 \to K^+K^-\pi^+\pi^-$
	14	I2K2PIWS	$D^0 \to K^-K^-\pi^+\pi^+$
	15	I3KPI	$D^0 \to K^+K^-K^-\pi^+$
	16	I4K	$D^0 \to K^+K^+K^-K^-$

Obviously there are codes and mnemonics for $D^\pm$ and D_S as well as for those states which contain electrons and muons in the final state. Since they do not apply to this thesis analysis they will not be discussed.

3.2.2 Notre Dame Subskim

The result of the data reconstruction and reduction was two sets of data tapes that were

delivered to Notre Dame; the QT stream, which was all skimmed events but with only the data summary information, and the Tiny stream, which only included select events with obvious physics opportunities but with the miniADC block for the ability to do more diverse analysis. Since there were several people at Notre Dame who were interested in accessing the information on the QT tapes, a sub-skim of the QT tapes was instituted. For the 1990 running period there were 81 tapes in the QT skims; these tapes were put through a 3-way skimmer with the three streams as follows:

Stream 1	Neutral D meson decays	Skim bit 9 plus EZ-D block selections
Stream 2	Charged D meson Decays	Skim bit 9 plus EZ-D block selections
Stream 3	Charmed Baryon Decays	Skim bits 7,13,15,16

These streams represented 20%, 10% and 15% skims respectively and were written out to 27, 20 and 21 tapes respectively, although not all of the tapes were completely full. The 1991 data came on 76 tapes and represented a slight reorganization of the skim strategy. The Stream 3 was split into 2 streams. The new Stream 3 comprised the skim bits 7,15,and 16 which were the lambda c to protons, kaons, pion skim, the baryon skim, and the cascade skim. This new Stream 3 represented approximately a 7 percent skim. The new Stream 4 was a lambda skim, skimbit 13, and also represented about a seven percent skim. The skim ratio of the first two streams did not change appreciably for the 91 data with respect to the 90 data. The data from the 91 sub skim was written to 15, 12, 5, and 4 tapes for streams one, two, three, and four respectively. The forty two tapes from stream one were then put through an additional skim to split off the various decay states of interest. This selection was made on the basis of the EZ-D block and the split was to $\pi\pi$, kk, four π, and a final stream which included both the two k-two pion state and the three kaon-one pion state. This output was to nine tapes each for the $\pi\pi$ and four π modes and four tapes each for the kk and kk$\pi\pi$ and kkkπ combined modes. Totals are as follows:

Table 3.5

Tape #	# $\pi\pi$	# $\pi\pi\pi\pi$	# KK	# $KK\pi\pi$, $KKK\pi$
1	935000	1068000	769000	711000
2	940000	1107000	379000	352000
3	795000	920000	662000	598000
4	459000	538000	782000	675000
5	780000	989000		
6	795000	979000		
7	698000	879000		
8	595000	739000		
9	538000	684000		
Total	6536730	7902475	2591516	1696205

The $k\pi$ and $k3\pi$ states were not separately skimmed at this stage since each state was included individually in roughly 40% of the stream 1 skim tape.

The next stage in the data reduction was the initial analysis cuts. Studies were performed to evaluate cut possibilities. Several of these were selected which were shown to significantly reduce background while still maintaining the majority of usable signal events. The cuts that were found to be most effective in this regard were a "loose" elsig, or significance-of-detachment cut, a total charge cut and a use of the standard Cerenkov particle definitions. The elsig cut that was used was a cut of 4 if there was no tagging pion from a D^* that gave a mass difference of less than 160 MeV, and a cut of 2 if there was such a tagging pion. At this stage there was no cut on the correlation of the sign of the tagging pion. The total charge cut simply required that the sum of the charges of the tracks used to reconstruct the D^0 actually totalled to zero. The definition used was that a pion was not identified as being a definite heavy particle with a Cerenkov id of 4, 8 or 12, and that a kaon had an id of 4, 7, or 12. The effect of these two cuts were as follows:

Table 3.6

State	Total after cuts	% kept after cuts
pipi	483000	7.3%
pipipipi	614000	7.8%
kk	73000	2.8%
kkpipi	98000	5.8%
kkkpi	20000	1.2%

Since the kkππ and kkkπ states were separated at this time the percent that was kept is the ratio to the previous skim that had both kkππ and kkkπ included in it.

The next stage in the data reduction process was to split the larger signals into 90 and 91 data and to run a screening or washing program to remove multiple entries of a given event. The run, spill and event number were written to a file and each new event was compared to the file to see if there is a match with a previous event. In the case of matches the duplicates were discarded. In an attempt to reduce the possibility of error due to a corrupted or incorrect header block, the number of tracks, which is stored in a separate 'track' block, was also compared in cases of apparent duplication. The 90 and 91 data are separated on the basis of run number. Due to the relatively small size of the kkππ and kkkπ samples they were not separated on the basis of 90/91 run at this point in time. The stream 1 tapes were skimmed at this point to extract the kπ and k3π consistent events, the standard elsig, cerenkov and total charge cuts were applied as well as the 90/91 separation and washing to get the following results. (table 3.7)

Table 3.7

State	#90	#91	total	%kept
pipi	200000	239000	439000	90.7%
kpi	111000	144000	255000	
kk	28000	38000	66000	90.7%
pipipipi	249000	310000	559000	91.1%
kpipipi	158000	203000	361090	
kkpipi			89000	90.9%
kkkpi			18000	90.9%

3.3 Monte Carlo Analysis

Since this analysis is looking for branching ratios of less well known states in comparison to better known states it is important to understand the acceptance and efficiency

of each final state which we are examining. Since it is a difficult process to solve the efficiency and acceptance analytically, the E687 collaboration uses a well known elementary particle physics technique known as the Monte Carlo simulation. The idea behind the Monte Carlo simulation is that if the properties of each of several detectors and detector systems are known in isolation, the combined properties of the system can be found by 'walking' a particle through the entire detector. All 'random' or probabilistic aspects of the experiments are handled through the use of random number generators. The main difficulty with Monte Carlo simulations is that there must be a trade between accuracy and computing time. This is, of course, due to that fact that a higher degree of segmentation implies a greater number of steps for the simulation to calculate. This problem was addressed by the E687 Monte Carlo simulation, known as Rogue[22], which opted for a minimalistic state of detector activation for charm meson analysis. What this means is that since the analysis of most charm mesons do not use calorimetric information, the calorimeters are not simulated. Likewise, since the muon system is only used peripherally, at best, by most charm meson analysis the muon filters are handled in a bulk manner. In addition, since the Rogue Monte Carlo was initially designed for branching ratio and lifetime measurements it does not simulate far upstream beam transport mechanisms.

The Rogue Monte Carlo was structured around simulation parameters which are fed into the code by means of a CHAT file. The CHAT file can be constructed by hand or by means of an interactive interogation program. The event generation was handled by a program called GENERIC which took the input parameters and calculated an incident photon spectrum and interaction position. The Generic program would then calculate the lifetime of the particle and assign the final decay state. Generally the CHAT file only designates one of the charm decays in an event. GENERIC also has the ability to add backward jets or other additional particles to the event.

There are two versions of ROGUE. In the first version, an entire event sample would be generated before it was sent to ROGUE, the spectrometer simulation program. In the new

ROGUE each individual event is immediately fed from the event generator to the spectrometer simulation. As stated above, the Monte Carlo simulation calculates the event decay and then steps the event through the spectrometer. ROGUE does this by calculation ofthe four momenta of each of the decay products, as well for any particles from the primary vertex, and traces them through the spectrometer.

The tracing of the particles through the magnetic field of the spectrometer was accomplished by means of a TURTLE tracing routine. The microstrip channels, including charge sharing between strips and charge distributions within a strip were simulated based on the location of the track in relation to the channels. For the PWC system the wire number of the hit was determined and corrected for adjacencies, typically a 4-6% effect, and channel efficiencies of typically 80-90%.

The Cerenkov system was simulated by calculation of the photon yield of a particle based on its ID and momentum. The photons were then traced to the phototube cell to get the ADC count for that channel. The ROGUE simulation does not calculate Cerenkov misidentification due to spurious light sources or out of time tracks. The OH and HxV counter were simulated using experimentally calculated efficiencies. The TR1 and TR2 hodoscopes were assumed to have 100% efficiency. The master gate definitions that were used were the same as for actual experimental running as was the second level trigger. Since such things as the second level trigger, spectrometer geometry and detector efficiency changed during the data run, run periods were defined and could be selected, although ROGUE was setup to produce the appropriate distribution over the possible run periods.

3.4 Branching Ratio Measurements.

When measuring the likelihood of occurrance of an event decay one can either attempt to determine an absolute likelihood, or branching ratio, with respect to the total intial state, or can measure the likelihood of the decay occuring in respect to some bench mark

process, and hence a relative branching ratio. Since it is difficult to measure the total number of D^0 mesons produced and since our spectrometer has large but not complete acceptance, the likelihood of reconstructing double charm events is fairly small. We would have a difficult time measuring absolute branching ratios. Therefore it makes more sense to measure the branching ratio relative to a well known state. Since I am looking at two and four body non-leptonic decays of the D^0 meson it is most reasonable to measure the states in relation to another two or four body non-leptonic decay state of the D^0 meson. From the earlier discussion of theory we know that the $D^0 \to k^- \pi^+$ and $D^0 \to k^- \pi^+ \pi^+ \pi^-$ are Cabbibo favored and were know from an examination of the literature that these are well measured states. Hence these would be a good choice for a comparative measurement. The equation for calculation of the relative branching ratio is given as follows:

$$BR \frac{D^0 \to X_1}{D^0 \to X_2} = \frac{\text{Yield } X_1}{\text{Yield } X_2} \frac{\text{Efficiency } X_2}{\text{Efficiency } X_1}$$

where the efficiency of reconstruction is given by:

$$\text{EFFICIENCY } X_1 = \frac{\text{Yield } X_{1\,MC}}{\#\text{ GENERATED } X_1}$$

which gives a final equation for relative branching ratio of:

$$BR \frac{D^0 \to X_1}{D^0 \to X_2} = \frac{\text{Yield } X_1}{\text{Yield } X_2} \frac{\text{Yield } X_{2\,MC}}{\text{Yield } X_{1\,MC}} \frac{\#\text{ GENERATED } X_{1\,MC}}{\#\text{ GENERATED } X_{2\,MC}}$$

This measure will be used extensively in the next few sections.

3.4.1 $D^0 \to K^+ K^-$

The $D^0 \to K^+ K^-$ decay is of interest as a Cabibbo suppressed decay. It has a distinctive signature due to the relatively small number of kaons that generally exist in reconstructed spectrometer events. Also, we know from the literature that this state has one of the higher expected relative branching ratios for a Cabibbo supressed decay at 0.113 ± 0.007[4]. The two factors make this decay topology an excellent candidate for measurement as well as for discussing the cuts that will be employed in the latter part of this analysis. The analysis program that was used to select the event sample imposed a few cuts on the data already: these are an elsig cut of 4; and confidence level cut on the primary and secondary vertex of 1%; a requirement that the sum of the charges be equal to zero; and the kaons fit the Cerenkov id requirements of being either kaon consistent, kaon / pion ambiguous, our pion / kaon / proton ambiguous if the momentum of the kaon was greater than 65 GeV. We know from Monte Carlo simulations that these cuts preserve about 7.3% of the signal. According to these same Monte Carlo simulation the combined effect of the experimental master gate, the second level trigger and the pass 1 and skim 1 procedures was to retain 40% of the signal.

The first step in the analysis is to examine the effect of various possible cuts on the strength of signal and the size of the background. Depending on the analysis one may wish to select cuts on the basis of their effects on a measure of signal-to-noise or significance of signal, which is defined as the ratio of the Yield to the error in the yield. Other criteria when examining cuts include the χ^2/DOF of the fit, and comparisons to such "known" factors as the position or width of the invariant mass peak. Also visual inspection of the fits aids in selecting the 'best' or most accurate fit.

This analysis looked primarily at the significance of signal. This is due to the fact that for a branching ratio measurement, unlike a lifetime or resonance measurement, all relevant aspects of the background are parameterized by the fit, and hence background under a signal will not adversely affect the analysis. After a systematic study it was decided that the

appropriate cuts to apply were a significance of detachment cut of 8, an isolation cut on the primary of less than 0.05, an isolation cut on the secondary vertex of less than 0.01, a momentum ratio cut of between 0.15 and 0.85 and a Cerenkov definition for a kaon of kaon definite or kaon / proton ambiguous (ISTATP = 4 or 12).The actual meaning and effect of these cuts will now be discussed.

The CLP and CLD cuts are selections based on the confidence level of the primary and secondary verticies. The confidence levels are based on the χ^2/DOF results of the vertex fits. For this analysis these are both set to 1% so these cuts are satisfied unless there is no intersection of the tracks within a reasonable error estimation. Events that fail to pass the CLD cut are those which contain sets of tracks that, for pairs, simply fail to approach each other or for more than two tracks if there is not a common intersection point (fig. 3.2). The

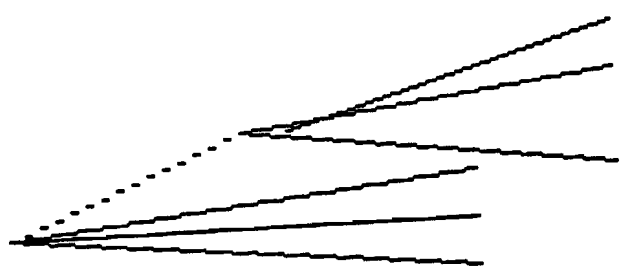

Figure 3.2 Confidence level of secondary vertex

CLP cut tends to remove those combination of tracks in the secondary that, though they have a common vertex, are missing enough actual secindary vertex tracks that they simply do not point back to the actual primary vertex. Since a point back vector is the only vector that cannot be removed when the primary vertex is being created, a highly incorrect point back vertex will cause a high χ^2/DOF and thus a low confidence level (fig 3.3).

The two main aspects of the E687 spectrometer which enable us to reduce the high levels of background to find existing charm signals are the precision tracking, which includes both momentum and vertex determination, and particle identification, which is mainly

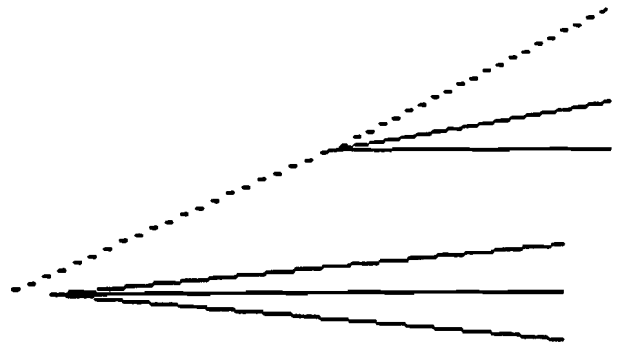

Figure 3.3: Low confidence level of primary vertex due to missing track in the secondary vertex

accomplished through our Cerenkov system. The CLP and CLD cuts are very dependant on the vertexing information. The vertex and tracking position will be very important in many other of the cuts to be discussed.

At this point, however, I will make a quick discussion of the gains that are achieved through the Cerenkov identification. The discussion of the particle identification algorithm earlier in this chapter introduced the ISTATP variable. This is, as stated earlier, a four bit word with each word corresponding to one of the four particles for which the system was designed to detect, the electron, pion, kaon, and proton. Using binary counting, the word can then be expressed as a value between 0 and 15, with each value representing a specific state of cerenkov identification consistancy. The are generally two levels of Cerenkov identification cuts that are made. The first level consistancy cuts are standard throughout the E687 analysis. For kaons, first level consistancy is that a track must be either kaon consistant (ISTATP equal four), kaon / pion ambiguous (ISTATP equals seven),when the momentum of the kaon is above 60.8 GeV/c or kaon / proton ambiguous (ISTATP equals twelve). Since we get a large kinematic reflection in the KK invariant mass distribution from $D^0 \rightarrow K^- \pi^+$ with a misidentified pion when the pion is identified as an ISTATP of seven, the KK analysis employed a tighter Cernekov id cut which did not includes the kaon / pion ambiguous condition. This, unfortumately, has the effect of elimination of all kaons with a momentum greater than 60.8 GeV/c. As can be seen by the following figure (fig. 3.4) the Cerenkov

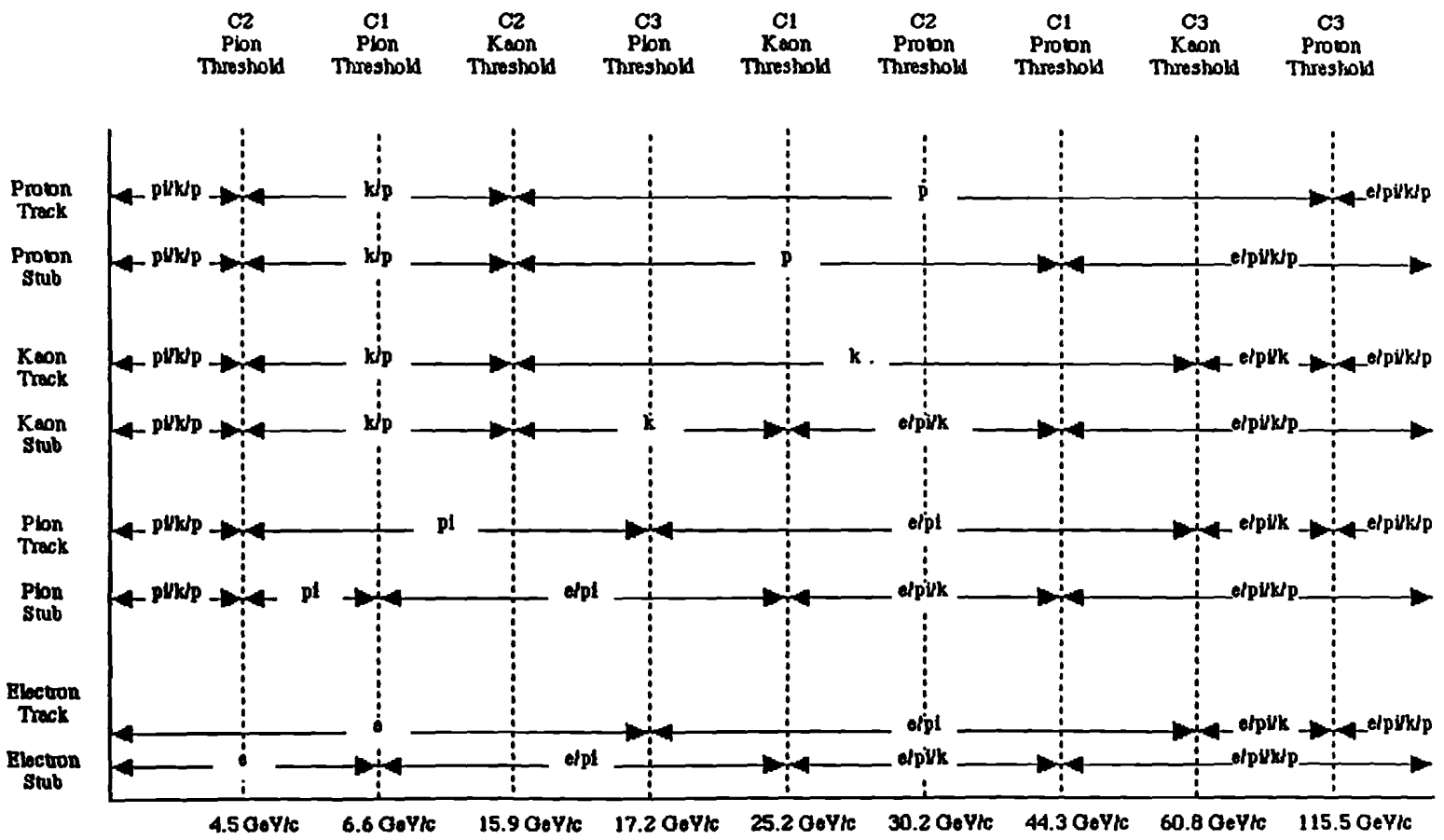

Figure 3.4: Momentum dependance of the Cerenkov identification

definition is highly dependent on the momentum of the particle to be identified. This momentum dependence of the Cerenkov cuts tends to have effects on most other cuts, including the intrinsic "quality" of vertex cuts. These effects are not shown here. All studies of cuts, however, will include the cuts with the loose and tight kaon definition.

The significance of detachment cut, also known as the L/σ or elsig cut (fig 3.5), is a measure of two vertex related quantities in conjunction with each other. First, this cut

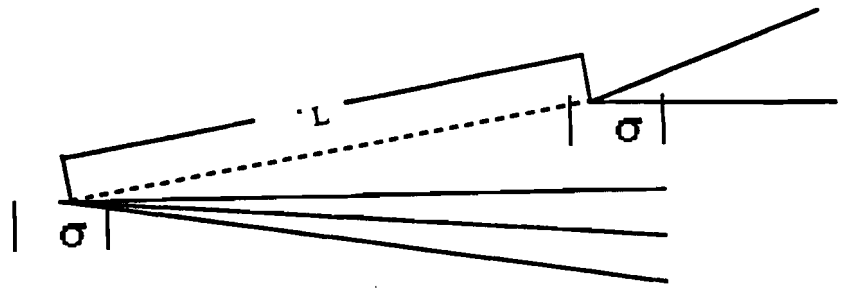

Figure 3.5: Definition of the L/sigma measure

selects particles with finite vertex separation; secondly it selects for particles with well defined vertices. The selection of events with large vertex separation is not considered an absolute lifetime cut due to the the fact that there is no correction made for the momentum, and hence the Lorentz boost of the particle. Since the vertex separation is divided by the joint error in the vertices, a large separation with poor vertex definition may fail while a smaller vertex separation with very good vertex definition might pass. Since charm particles have a long lifetime they generally have a large elsig value. This cut is used mainly to eliminate noncharm combinatoric background. The cut is not as efficient in eliminating misidentified charm backgrounds or backgrounds due to low momentum non-primary vertex tracks intersecting primary vertex tracks (fig. 3.6). Obviously charm events with short decay

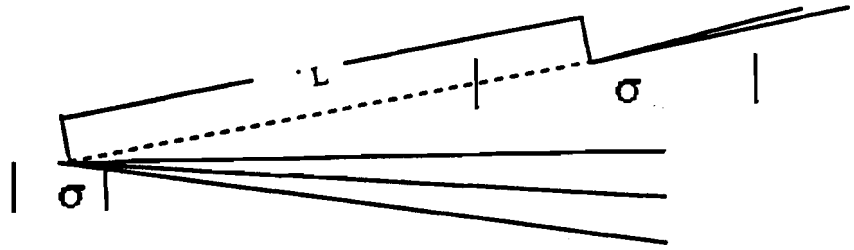

Figure 3.6: Collinear tracks give high error in secondary vertex position.

lengths will be elimnated as well as those with poorly defined vertices, possibly due to low numbers of primary vertex tracks (fig. 3.7). The efficiencies for the cuts on the elsig variable

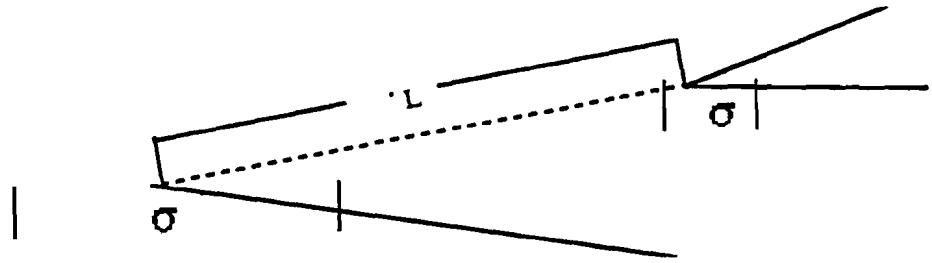

Figure 3.7: High L/sigma due to low number of tracks on the primary vertex

are presented in Table 3.8. These efficiencies, as are the rest of the efficiencies quote in this chapter, were calculated by generating a Monte Carlo sample and running that sample through the analysis routines. The number of Monte Carlo events that were reconstructed and survived the selection criterion was then compared to the number that was generated to achieve an efficiency. All of these numbers already include software cuts from the master gate and second level triggers, the Pass 1 and Skim 1 at Fermi lab, as well is the preliminary event selections described in this and the preceding sections. The cuts are considered alone and with the cuts used for final analysis for both the tight and loose Cerenkov id cuts.

Table 3.8

Cut on elsig	Efficiency with just primary analysis cuts	Efficiency with final analysis cuts	Efficiency with just primary cuts and tight ISTATP definitions	Efficiency with final analysis cuts and tight ISTATP definitions
$L/\sigma > 4$	7.29%	4.27%	5.86%	3.56%
$L/\sigma > 5$	6.43%	4.04%	5.12%	3.32%
$L/\sigma > 6$	4.64%	3.76%	4.46%	3.07%
$L/\sigma > 7$	4.98%	3.45%	3.89%	2.79%
$L/\sigma > 8$	4.42%	3.18%	3.44%	2.55%
$L/\sigma > 9$	3.94%	2.91%	3.04%	2.32%
$L/\sigma > 10$	3.54%	2.67%	2.73%	2.11%
$L/\sigma > 12$	2.86%	2.22%	2.16%	1.72%
$L/\sigma > 14$	2.29%	1.82%	1.71%	1.39%

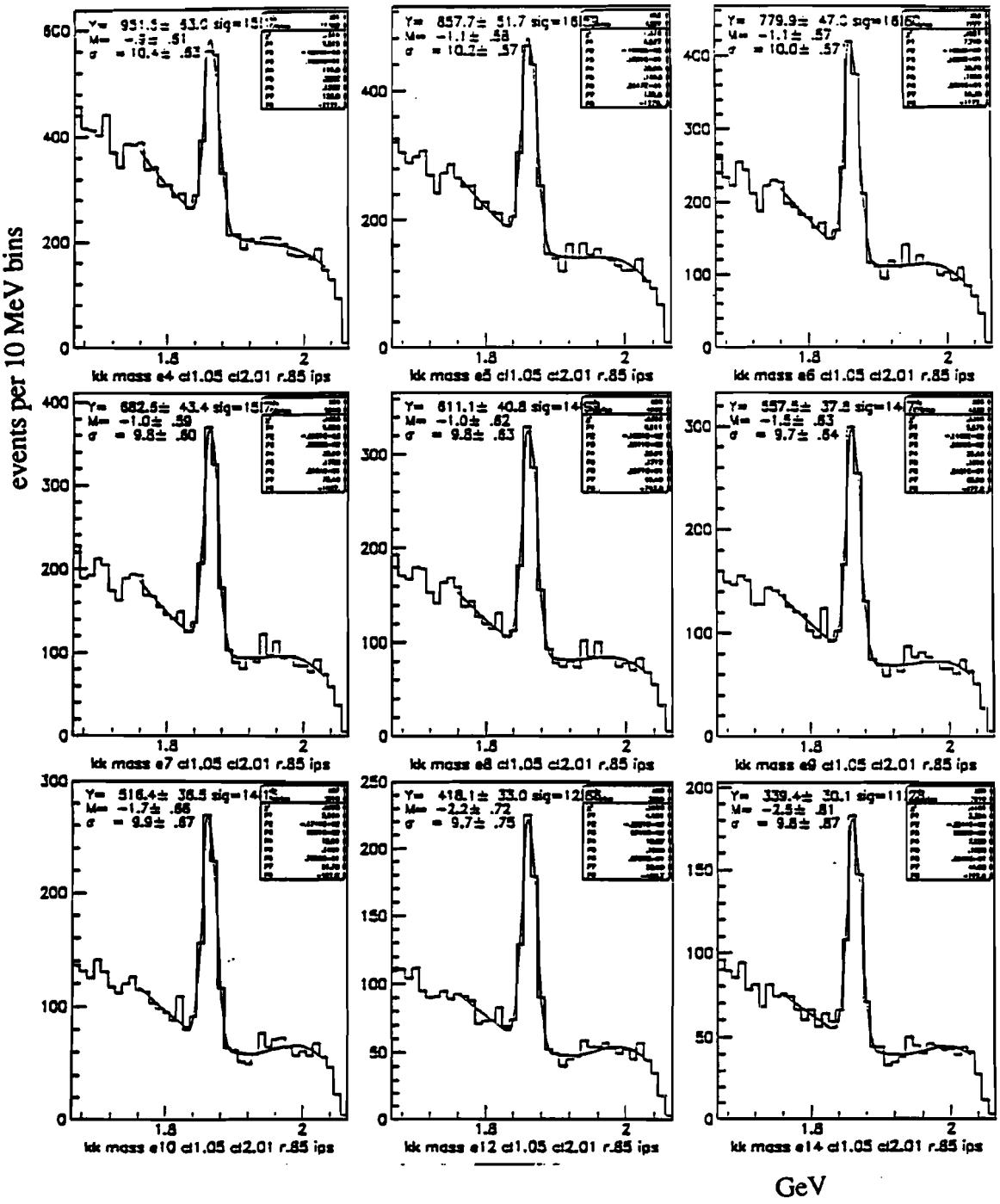

Figure 3.8: Mass plots for systematic study of L/σ cuts, tight Cerenkov definition

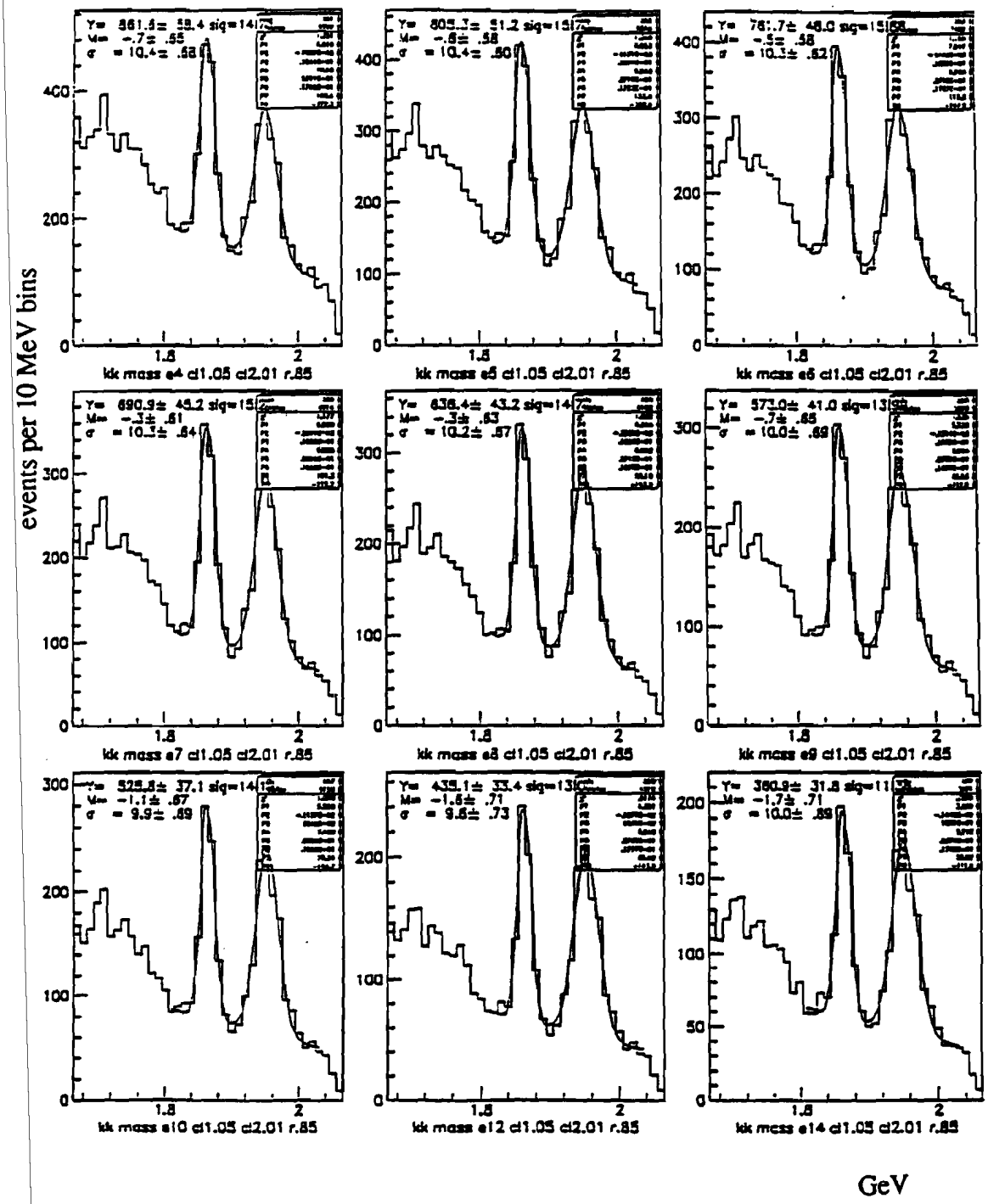

Figure 3.9: Mass plots for systematic study of L/σ cuts, loose Cerenkov defintion

The signals from these elsig studies with the tight Cerenkov definitions are presented in figure 3.8 and the signals from the elsig studies with the loose Cerenkov definitions are presented in fig. 3.9. The second peak that is seen in the mass plots with the loose Cerenkov definitions is from a misidentification of a pion from the $K\pi$ deacy of the D^0 as a kaon. This identification can take place because the loose Cerenkov defintion includes the ISTATP = 7 defintion which is π / K /p ambiguous, therefore a real pion with an ISTATP definition of 7 will be treated as a kaon in this decay. The tight Cerenkov definitions do not completely eliminate this effect, a reflection peak can be clearly seen in for some of the tighter cuts that are presented in the systematic studies. This effect of these definitions on the yield and branching ratios will be discussed more later.

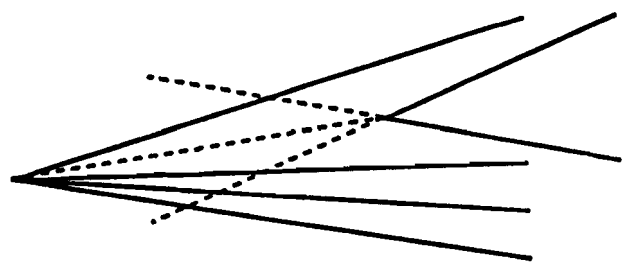

Figure 3.10: CL1 cut requires that no tracks from the secondary are consistant with the primary vertex

The isolation cut on the primary vertex requires that the confidence level that any track from the secondary vertex is consistent with the primary vertex is less than the cut value (fig 3.10). This cut is most effective for two body states such as $D^0 \to K^+ K^-$ or $D^0 \to \pi^+ \pi^-$ where it is less likely that one of the decay secondaries will be collinear with the parent particle than it is for a mode with more than two decay products (fig 3.11). Hence this cut is useful in eliminating charm background events with multiple decay products. Additionally, this cut is good at eliminating combinatoric background from events with a secondary vertex that is created by the intersection of a high momentum primary vertex particle with a low

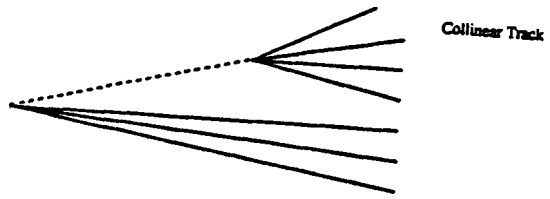

Figure 3.11: Many body decays are more likely to have track collinear to the D momentum non-primary vertex particle (fig 3.12). As we shall see in the discussion of the R -cut below, the background events are much more likely to have this momentum

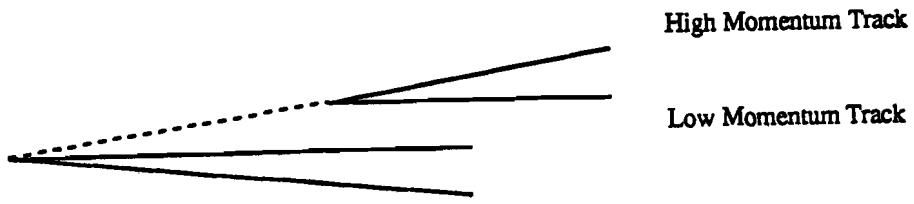

Figure 3.12 High and low momentum track combinations allow a decay product that is collinear with the D

asymmetry than are charm signals. The two body topologies that this cut eliminates are any where the two particle decays have a small opening angle in the lab reference frame. In the case of an event having a small opening angle the particles are nearly colinear with the parent particle and therefore will point back to the primary vertex. The efficiency of the CL1 cut is given in table 3.9.

Table 3.9

Cut on CL1 value.	Efficiency with only initial analysis cuts	Efficiency with standard cuts and loose ISTATP definitions	Efficiency with standard cuts and medium ISTATP definitions	Efficiency with standard cuts and tight ISTATP definitions
CL1 < 1	7.29%	3.41%	5.86%	2.72%
CL1 < .8	7.14%	3.40%	5.76%	2.71%
CL1 < .6	6.96%	3.38%	5.63%	2.70%
CL1 < .5	6.84%	3.37%	5.54%	2.69%
CL1 < .4	6.70%	3.35%	5.44%	2.68%
CL1 < .2	6.23%	3.31%	5.07%	2.65%
CL1 < .1	5.80%	3.25%	4.74%	2.61%
CL1 < .05	5.39%	3.18%	4.43%	2.55%
CL1 < .01	4.53%	2.98%	3.73%	2.40%

As one can see from the the actual data signals used to study the effects of these cuts there is a decrease in the background by more than a factor of two with very little degradation of the signal (fig. 3.13 for tight Cerenkov definitions and fig. 3.14 for loose Cerenkov Defintions). The CL1 cut was varried from a value of 1, which corresponds to no cut to a value of 0.01.

The CL2 cut requires that only tracks that are identified as being in the in the primary or secondary vertices are consistent with being in the secondary vertex. The CL2 measure is accomplished by taking each candiate track, among those not already in a vertex, and combining them with the tracks that are assigned to the secondary vertex. After a vertex is found the χ^2/DOF is calculated and used to find the confidence level that the particular track is from the same vertex as the charm candidate. The confidence level is compared to the confidence level for all other candidate particles and the highest confidence level value is assigned as the CL2 value. The cut is primarily designed to eliminate charm backgrounds that are produced when a real charm vertex is reconstructed less one, or more of its tracks (fig. 3.15). This background has been discussed briefly in the discussion of the CLP cut. The CLP

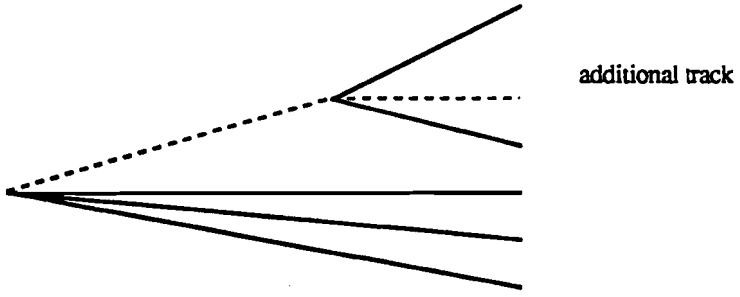

Figure 3.15 CL2 discards events with additional tracks that are consistant with the secondary vertex.

cut is limited in reducing this form of charm background to those missing particles with a high enough transverse momentum to significantly alter the point-back direction of the reconstructed charm particle. That is, a soft pion will not change the momentum of the charm particle

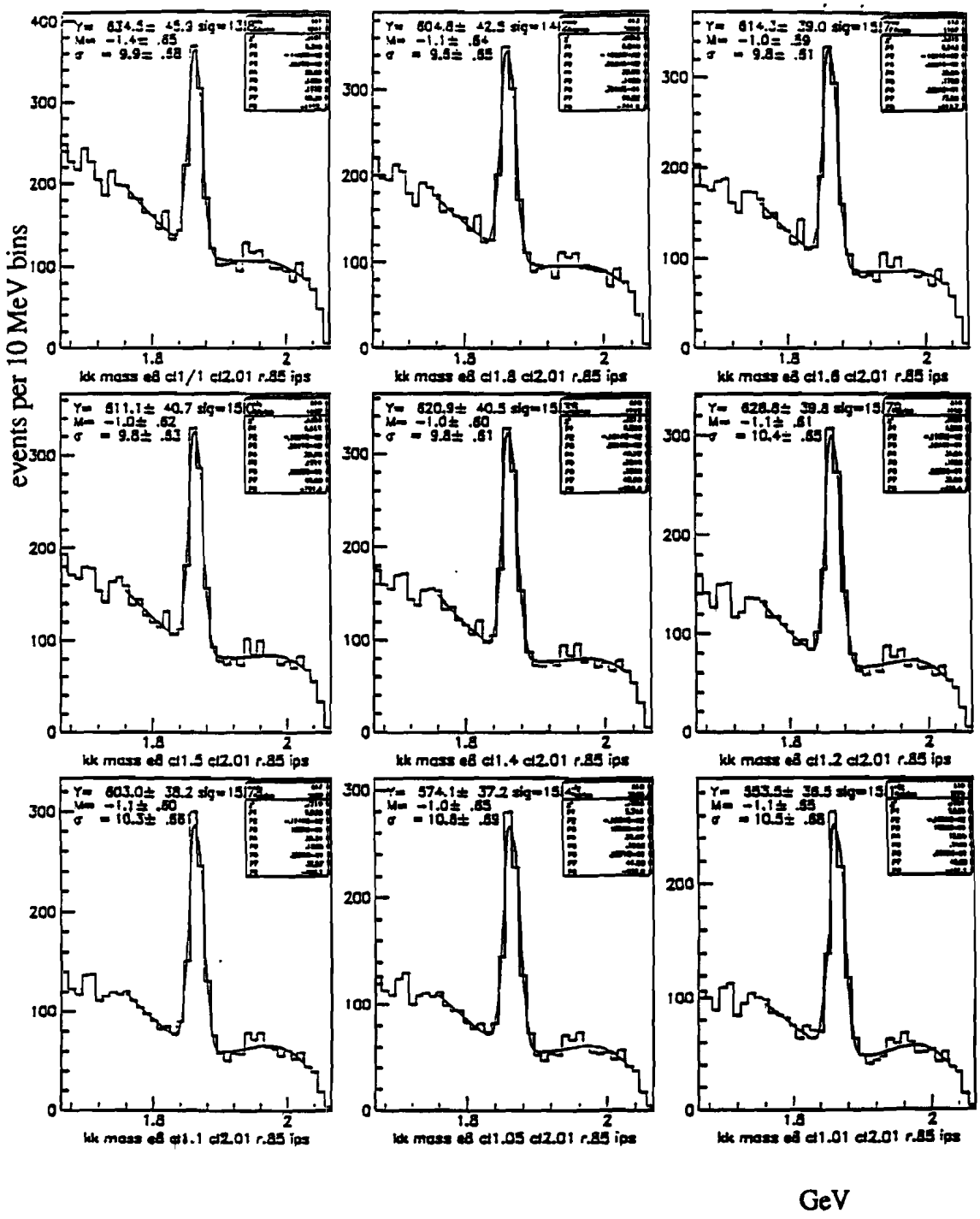

Figure 3.13: Mass plots for systematic study of CL1 cuts, tight Cerenkov defintion

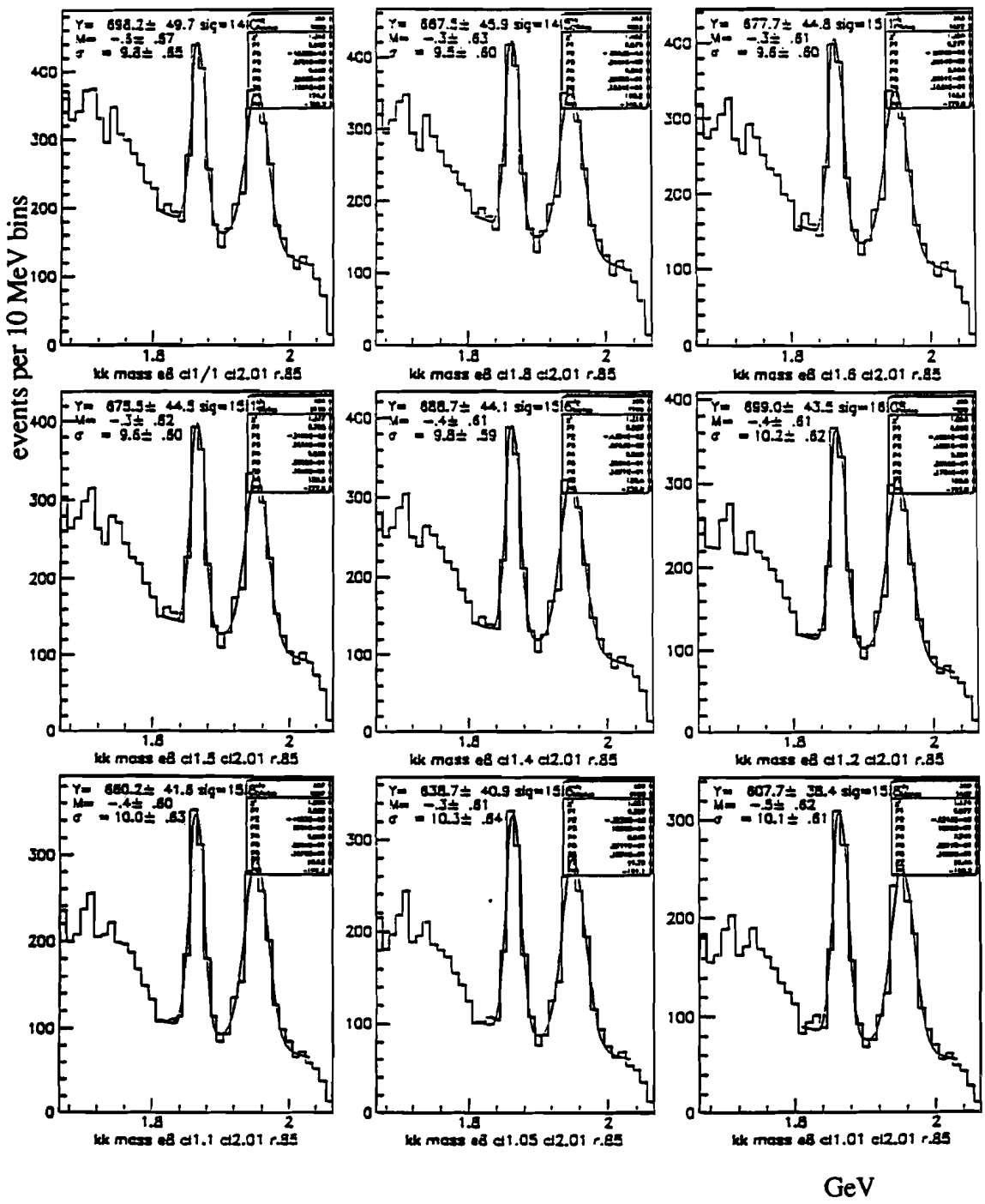

Figure 3.14 Mass plots for systematic study of CL1 cuts, loose Cerenkov definition

enough to decrease the significance of the primary vertex, especially if there are relatively tracks coming from the primary. The CL2 cut is, however, not dependent on the momentum other than the momentum dependent portion of the error in track parameters. The most likely signal that this cut will eliminate comes from the case of unrelated tracks or tracks from a second charm vertex which overlap with the origional charm vertex(fig. 3.16). Given the

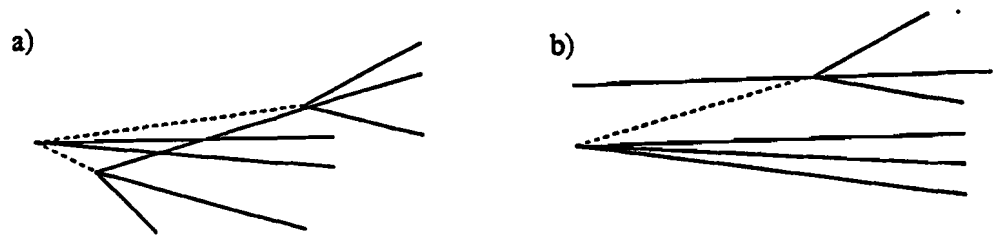

Figure 3.16: Real events may be discarded due to: a) particles from other charm decays, b) unrelated events

precision with which the microstrip system can position the tracks this is actually a very good cut to eliminate background without appreciable signal reduction.

Table 3.10

Cut in CL2	Efficiency with only preliminary analysis cuts	efficiency with standard analysis cuts and loose ISTATP definitions	efficiency with standard analysis cuts and medium ISTATP definitions	efficiency with standard analysis cuts and tight ISTATP definitions
CL2< 1	7.29%	3.74%	5.86%	3.00%
CL2< 0.5	6.98%	3.58%	5.60%	2.88%
CL2< 0.1	6.58%	3.40%	5.29%	2.73%
CL2< 0.05	6.42%	3.32%	5.15%	2.66%
CL2< 0.01	6.07%	3.18%	4.87%	2.55%
CL2< 0.001	5.69%	3.03%	4.57%	2.43%
CL2< 0.0001	5.43%	2.90%	4.35%	2.32%
CL2< $1x10^{-4}$	5.21%	2.79%	4.17%	2.23%
CL2< $1x10^{-5}$	5.03%	2.71%	4.04%	2.18%

The data results, as studied over the range of CL2 values presented in the table, shows similar

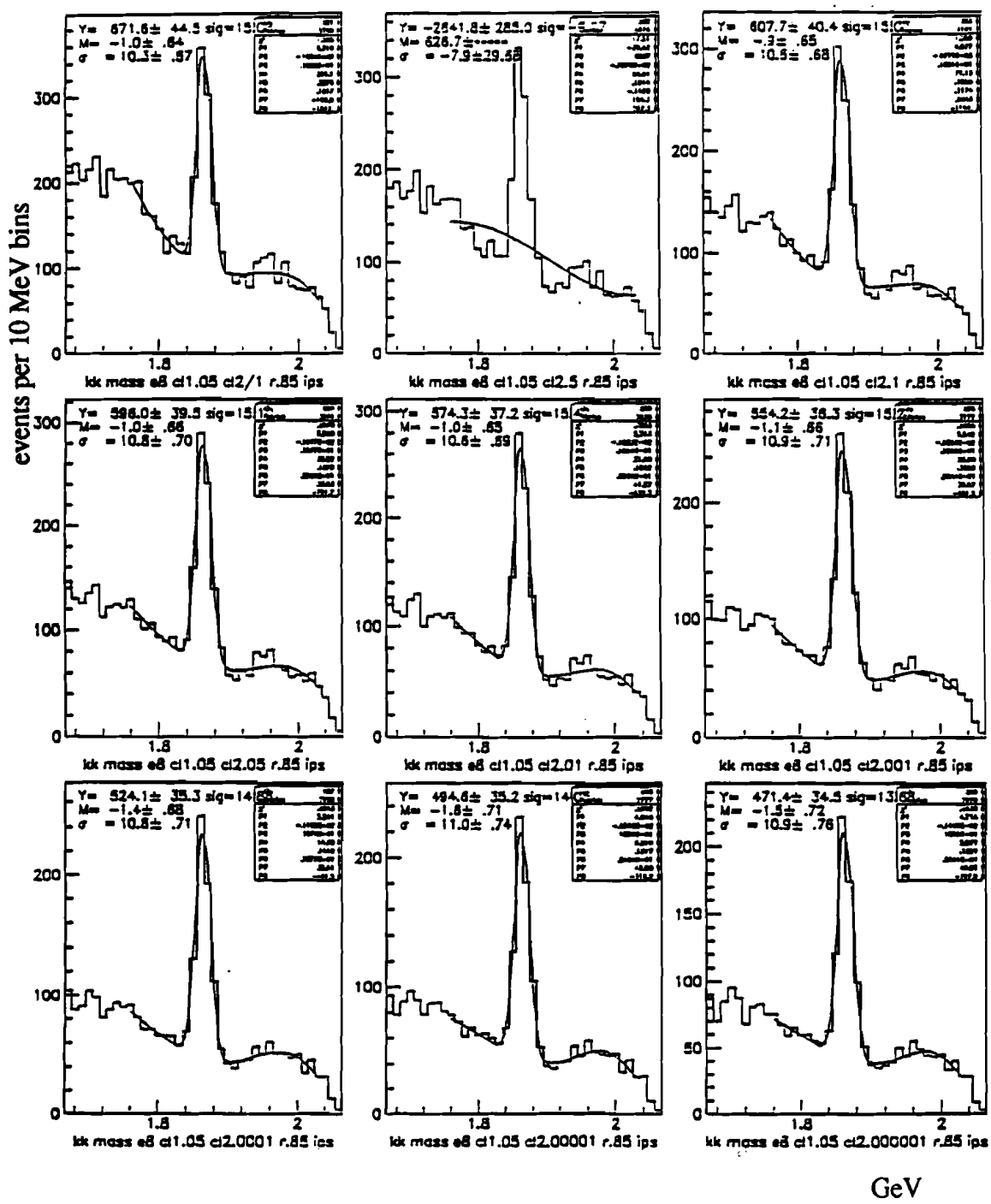

Figure 3.17 Mass plots forthe systematic study of CL2 cuts, tight Cerenkov definition

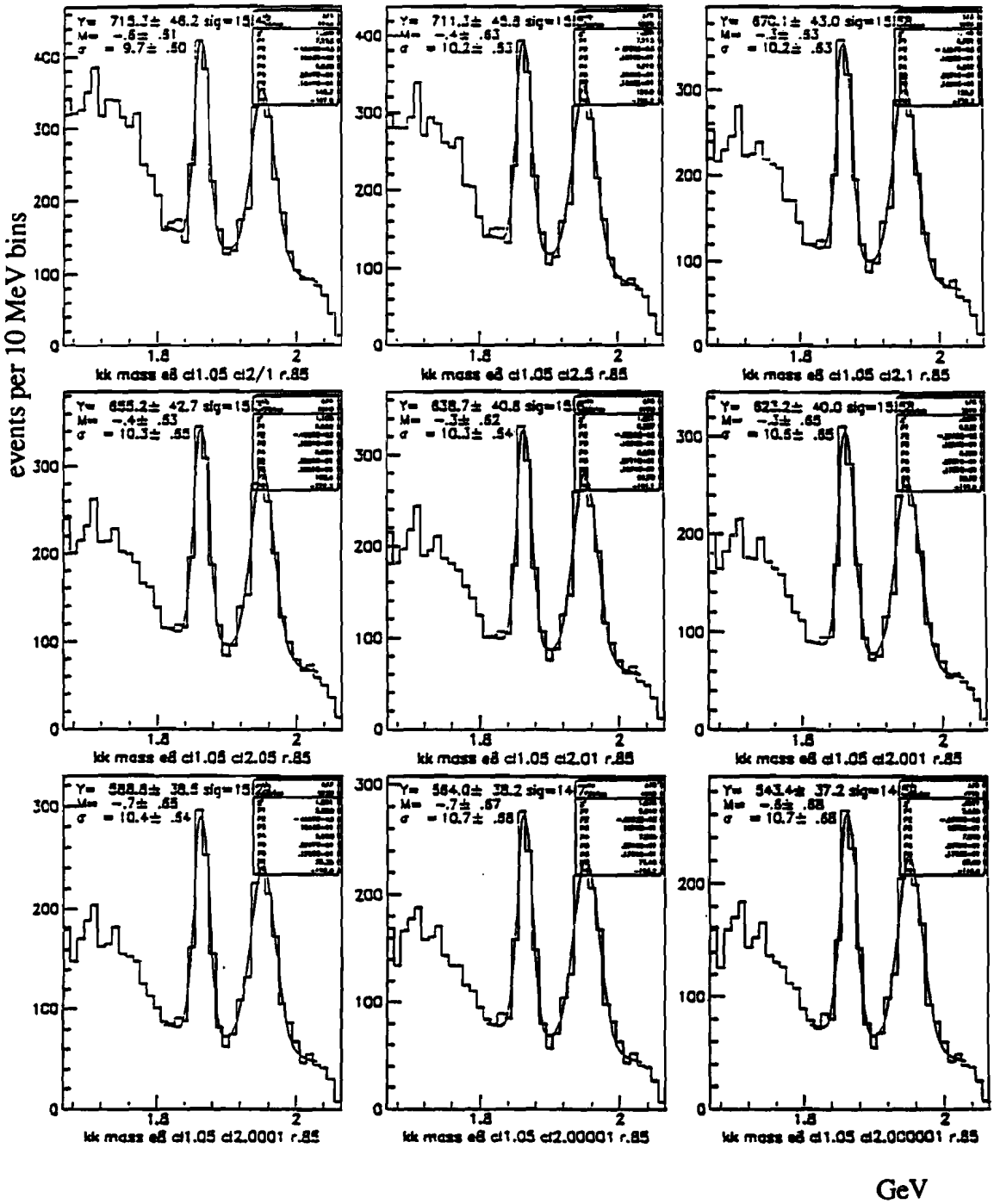

Figure 3.18: Mass plots for the systematic studies of CL2 cuts, loose Cerenkov definition

behavior to the Monte Carlo efficiency predictions for both the tight (fig. 3.17) and loose (fig. 3.18) Cerenkov cuts. In addition, we can see that there is a reduction in the background by more than a factor of two while more than two thirds of the signal is retained.

The R or ratio of momentum measure is, as outlined in Appendix A, a linear transformation of the cosine theta jackson measure. The R measure, is expressed as follows:

$$R = \frac{P_1}{P_1 + P_2} ,$$

where P_1 and P_2 are the magnitudes of the momenta of the two secondaries of the two body decay candidate. Due to the obvious symmetry that exists for measuring R with respect to the momentum of an arbitrary particle we express a cut value of v to mean,

$$1 - v < R < v .$$

Thus we see that an R cut of 0.85 is actually a requirement that the first particle have at least 15% of the momentum but no more than 85% of the momentum. As stated in the Appendix, the reason that this cut works is that when a pseudoscalar meson decays into two other pseudoscalars the decay is isotropic in the rest frame. By taking a measurement of the cosine of one of the particles with respect to the incident beam direction we get a flat distribution to within experimental acceptances. Since the R measure is highly correlated with this distribution it is also flat once corrected for experimental acceptances. By contrast combinatorial background is highly peaked at high and low values of R due to the combinatorics of the momentum distribution and mechanisms of the invariant mass determination which are outlined in Appendix A. The Monte Carlo calculated efficiencies

for the R cut are presented below (table 3.11), once again, the efficiency of the cut is given with and without the other analysis cuts and with the loose and tight Cerenkov cuts.

Table 3.11

Cut in R	Efficiency with preliminary analysis cuts	Efficiency with final analysi cut and loose ISTATP definitions	Efficiency with final analysi cut and medium ISTATP definitions	Efficiency with final analysi cut and tight ISTATP definitions
R= 1	7.29%	3.38%	5.86%	2.67%
R= 0.95	7.29%	3.38%	5.86%	2.67%
R= 0.90	7.17%	3.36%	5.82%	2.66%
R= 0.85	6.57%	3.18%	5.44%	2.55%
R= 0.80	5.81%	2.84%	4.88%	2.32%
R= 0.75	4.94%	2.45%	4.25%	2.04%
R= 0.70	4.03%	2.00%	3.57%	1.74%
R= 0.65	3.08%	1.57%	2.82%	1.42%
R= 0.60	2.11%	1.10%	1.98%	1.03%

As can be seen in the figures (fig 3.19, tight Cerenkov definitions and fig 3.20, loose Cerenkov definitions) for the range of this cut, the non-charm background is reduced by a factor of three going from no R cut (R = 1) to an R cut of 0.85 and with a decrease in real signal of less than 10 percent. Beyond this point the gains in background reduction are offset by losses to the signal. The study with the loose Cerenkov cuts also confirms that the R cut does very little to reduce the misidentified charm background.

As stated above, the cuts for the final analysis were: the 1% CLP and CLD cuts from the reconstruction routines, elsig greater than 8, CL1 less than 0.05, CL2 less than 0.01, and $0.15 \leq R \leq 0.85$. These cuts, when compared with the $D^0 \rightarrow K^- \pi^+$, and Monte Carlo simulation of both states, gave a relative branching ratio of $.104 \pm .0075$. To get a measure of the systematic error I used the signal from the cut studies that were reported on above to calculate the relative branching ratio. The calculated branching ratio was then plotted as a function of the cuts to get an estimate of any systematic error that might be introduced. The error from the elsig cut is estimated as .0025 (fig 3.21), the error from the CL1 cut is estimated

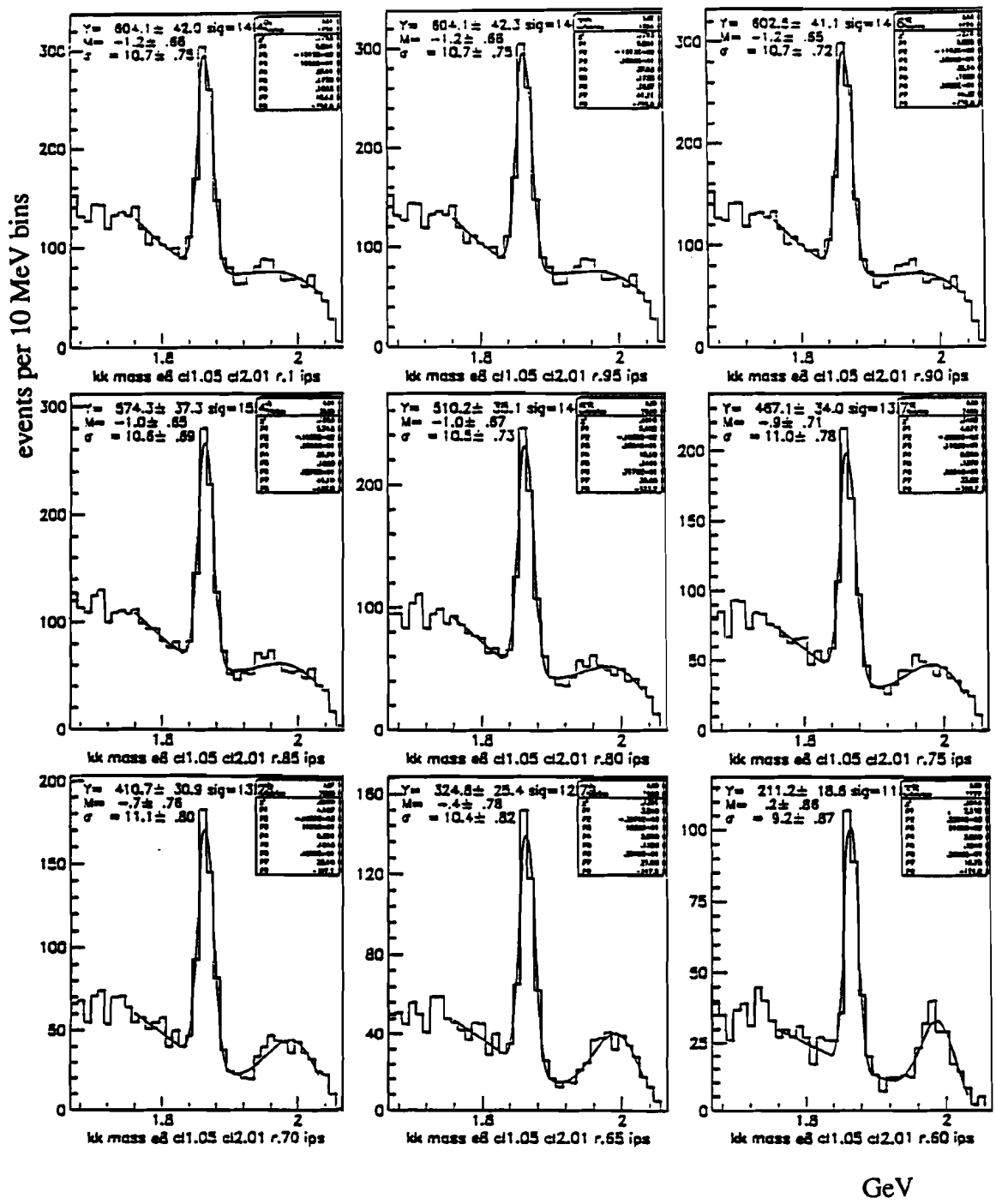

Figure 3.19: Mass plots for the systematic study of the R cut, tight Cerenkov definition

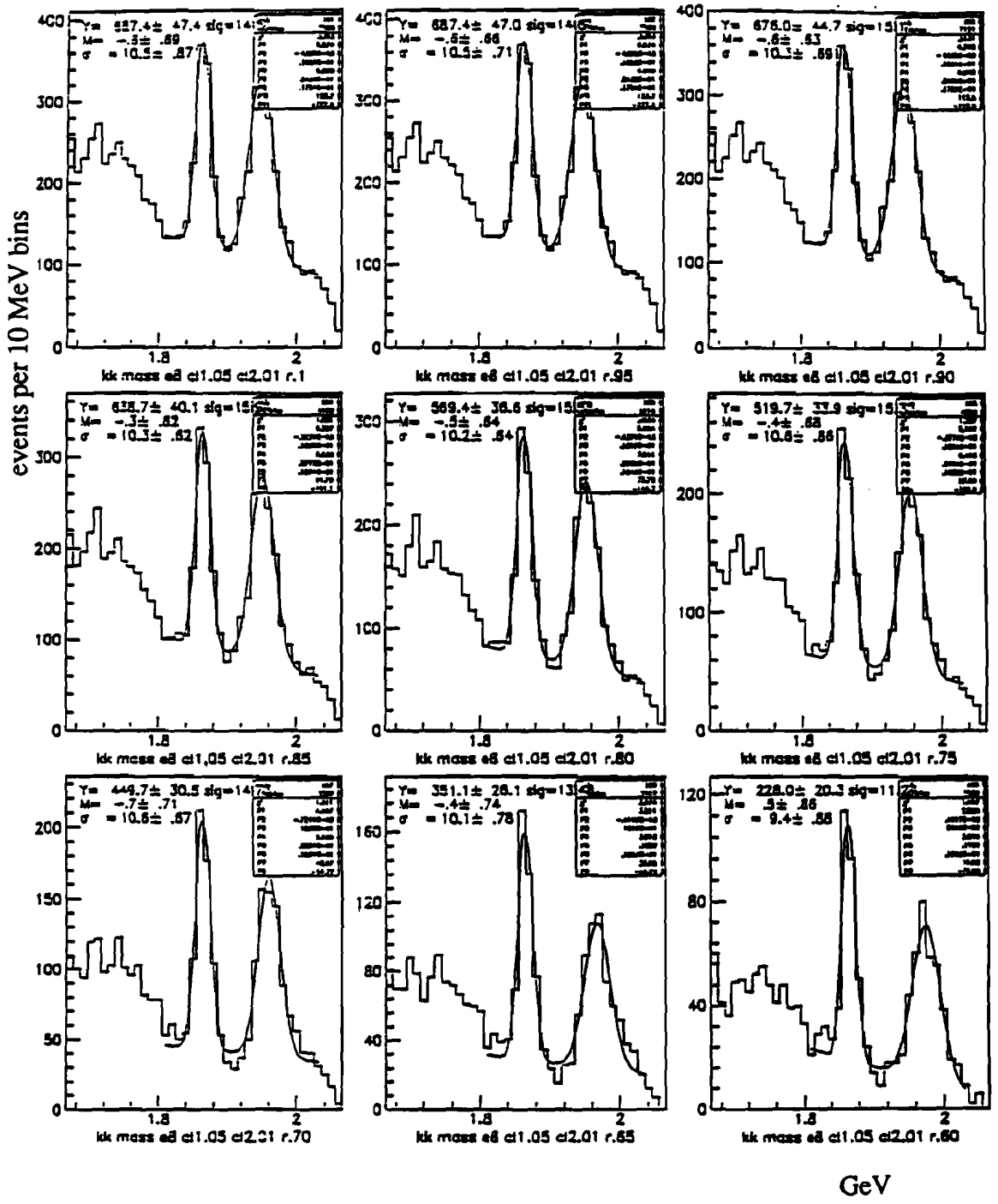

Figure 3.20: Mass plots for the systematic study of the R cut, loose Cerenkov definition

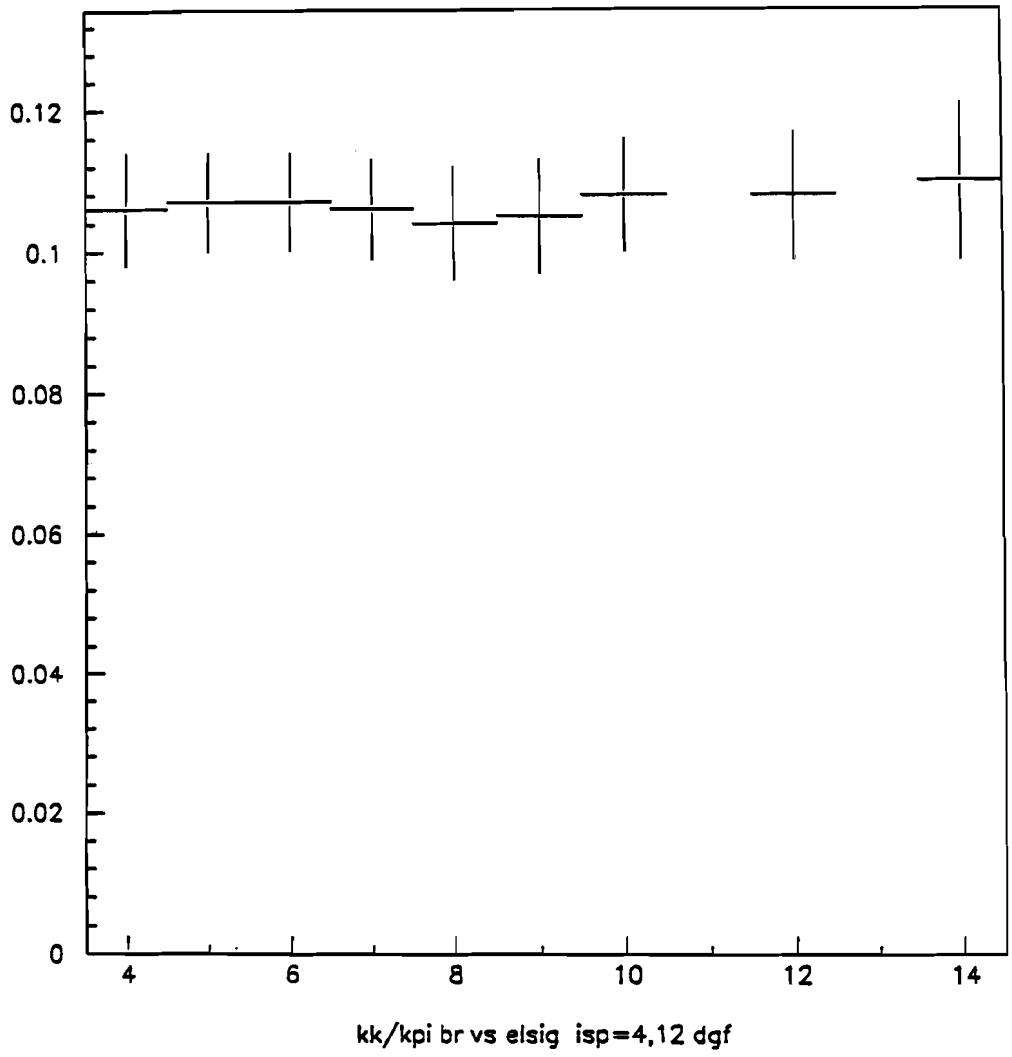

Figure 3.21: Relative Branching ratio as a function of L/σcut for the D -> KK decay

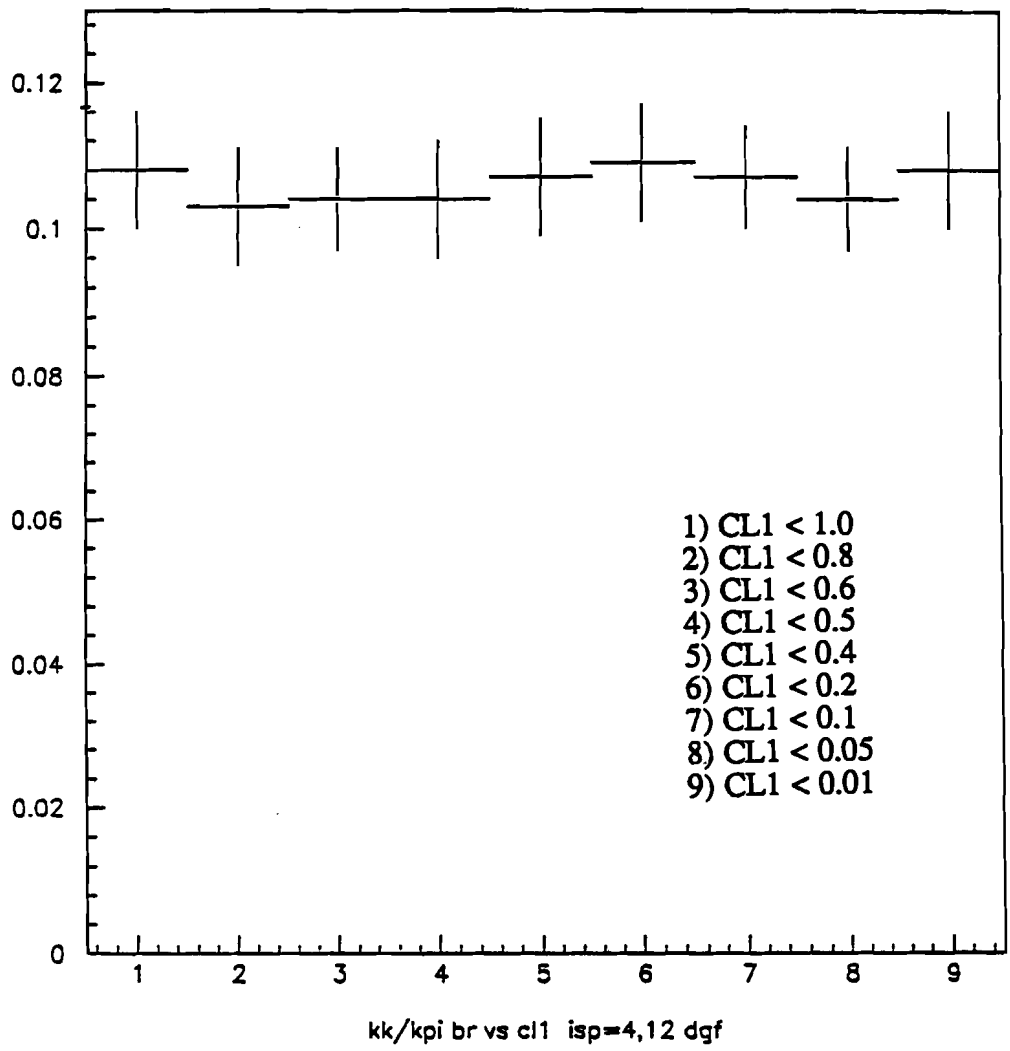

Figure 3.22: Relative Branching ratio as a function of CL1 cut for the D -> KK decay

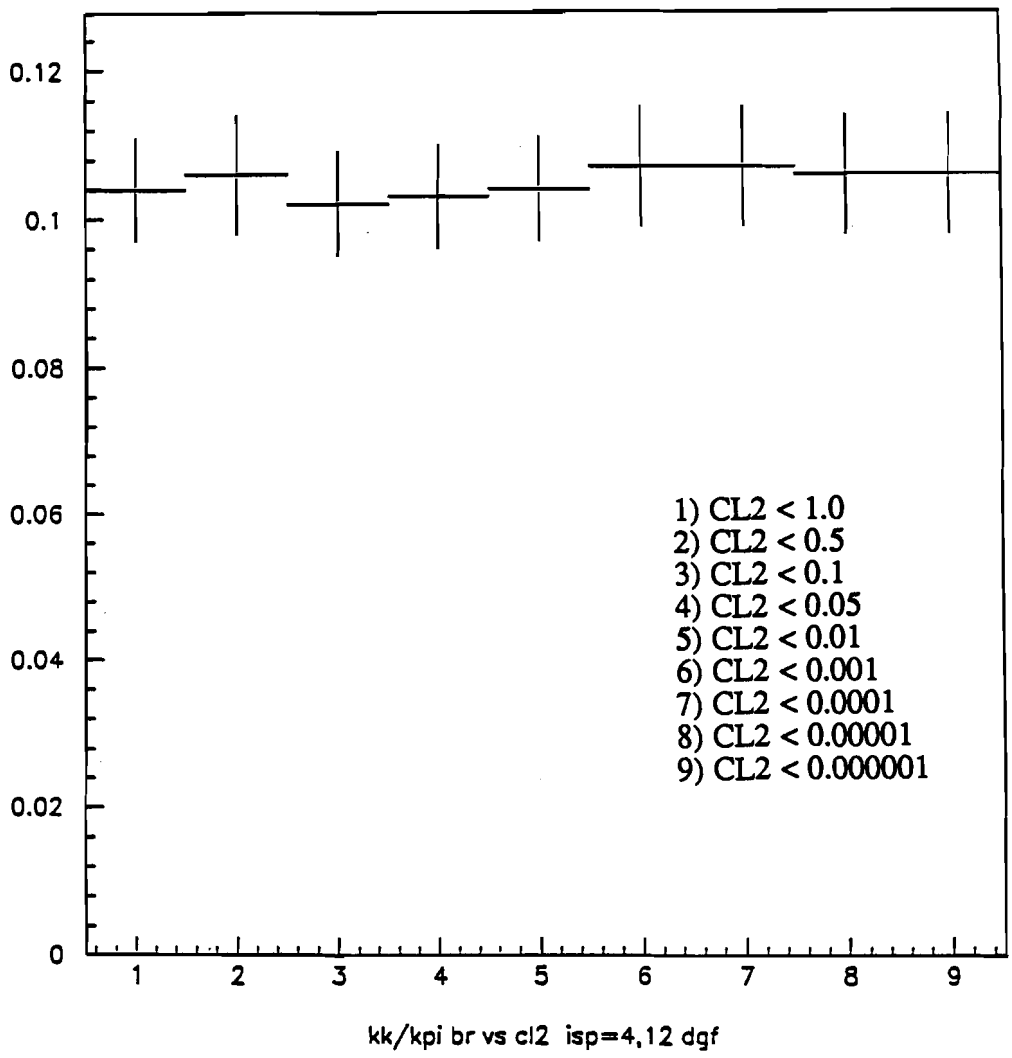

Figure 3.23: Relative Branching ratio as a function ofCL2 cut for the D -> KK decay

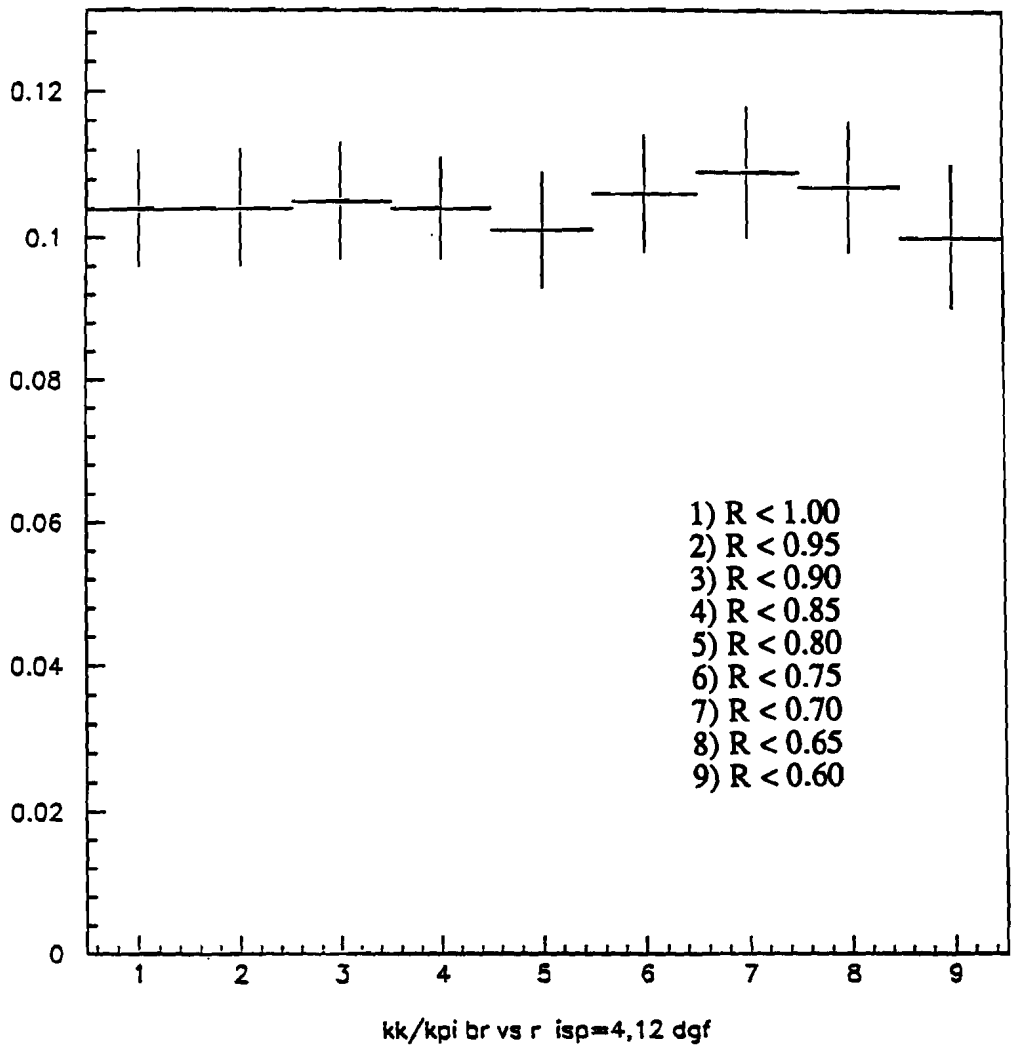

Figure 3.24: Relative Branching ratio as a function of R cut for the D -> KK decay

to be .0025 (fig 3.22), from the cl2 cut .002 (fig 3.23) and from the R cut .002 (fig 3.24) for a systematic error when added in quadrature of .0045. Then I investigated the effect of the Cerenkov cut by finding the yield and branching ratio of the state with the looser Cerenkov cut, namely, that a particle is called a kaon if it is kaon consistent, kaon / proton ambiguous, or kaon / proton / pion ambiguous. As discussed above, this resulted in a rather large reflection peak on the high mass side, seen in the various studies of the loose Cerenkov cuts. The result of this measurement is a branching ratio of .090 ± .0061 or a difference of 1.5 combined standard deviations from the tighter Cerenkov cut value. Estimating an error of .01 from this measurement and adding in quadrature we get a new systematic error of .011 for final value of .104 ± .0075 ± .011

3.4.2 $D^0 \to \pi^+ \pi^-$

The $D^0 \to \pi\pi$ is probably the most difficult of the branching ratio measurements performed in this analysis. The reasons for the difficulty are that it is a relatively small branching ratio, about half of the kk or four π, it sits atop a very large combinatoric background, and it is affected strongly by the misidentification of the kaon from the $D^0 \to k\pi$ as a pion. The misidentification of the kaon, though expected to shift the nominal invariant mass down by 88 MeV (fig 3.25), still presents several problems. Due to experimental resolution and simple kinematics the upper edge of the resultant kinematic reflection peak can be modeled by a Gaussian distribution. This distribution has a width of 25 MeV. This width and the displacement of the peak indicate that although we can expect to find very few $k\pi$ misidentified events in the $\pi\pi$ region this peak dominates the lower mass background for all but the tightest Cerenkov cuts, for which it is still present. This reflection peak, however, contributes very little to the high mass background. This highly asymmetric background causes particular difficulties in fitting the mass and width of the signal mass peak. It is for this reason in particular that I looked at the systematics of four different branching ratio

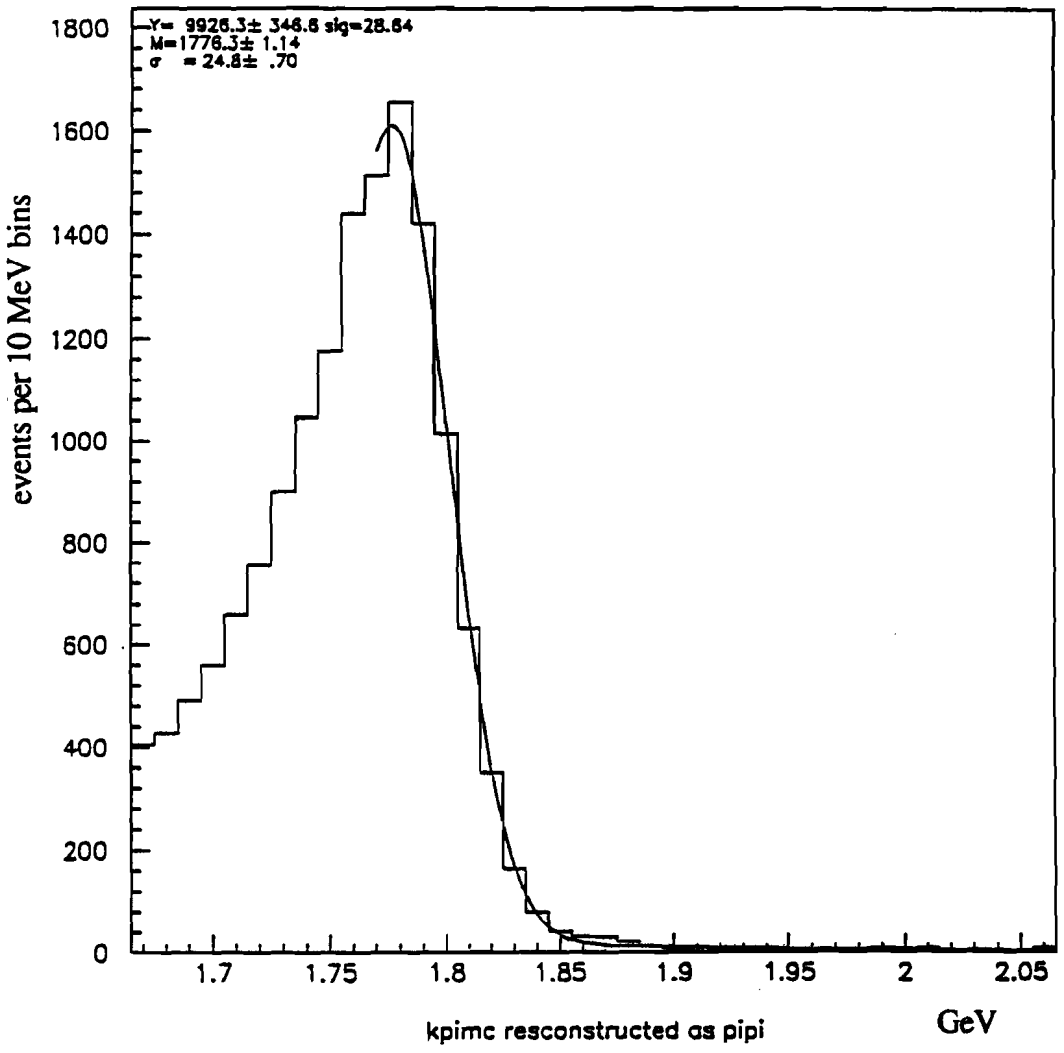

Figure 3.25: Invariant mass peak for Kπ decays in Monte Carlo reconstructed as ππ decays

calculations for the $D^0 \rightarrow \pi\pi$ decay mode. A discussion of the four different branching ratio calculations follows a discussion of the cuts used.

The first level of cuts are, of course, those imposed in the reconstruction program. As with the KK decay, these include elsig value greater than 4; CLP is greater than 1%, and CLD is greater than 1%. Beyond the reconstruction cuts ,the first calculation assumes a state where the pion is defined as being either pion definite or electron/pion ambiguous (ISTATP equals 2, or 3), and all of the fit parameters are left variable. Despite the fact that the Cerenkov cuts significantly reduce the reflection peak, a double Gaussian was fit over a quadratic background with one of the Gaussians acting as a background to handle any remaining reflection peak was still used. In addition to the Cerenkov cuts I also imposed a significance of detachment cut of eight, a primary vertex isolation cut of less than 0.05, a secondary vertex isolation cut of less than 0.01 and a $0.15 < R < 0.85$. The three sets of cuts will be discussed later.

Most of the cuts are simular to cuts imposed for the study of the KK decay mode. However we expect there to be slightly higher transverse momentum at the vertex due to the higher Q of the decay. This should increase the vertexing efficiencies due to a larger opening angle. In reality, however, this difference is rather small. The Cerenkov identification portion of this analysis contained three sets instead of the two which were used for the KK anlysis. The cuts were made on the basis of elimination of general combinatoric background as well as reduction of the charm reflection peak which was discussed earlier. The loosest Cerenkov identication was simply that a pion not be kaon definite, proton definite, or kaon proton ambiguous (ISTATP is not equal to 4,8,12). This was a very broad cut that did not eliminate any momentum regions from consideration but also left a great deal of the $k\pi$ reflection peak intact. This is the standard E687 pion definition which is understood over a broad range of kinematic and resolution cuts. The second definition eliminates the kaon pion ambuguous definition, the ISTATP equal 7, and eliminates any electron definite as well any of the confused or inconsistant values, ISTATP equal 0,1,15. We therefore have a pion labled

either pion definite, electron / pion ambiguous, or pion / kaon / proton ambiguous (i.e. not electron). This definition has allowed values of the ISTATP of 2,3, and 14. This keeps five chamber tracks up to 60.8 GeV, and keeps 3 chamber stubs up to 23.3 GeV. The final Cerenkov identification scheme is the one that only includes pion definte or electron / pion ambiguous (ISTATP equals 2 or 3). This very effectively reduces the $D^0 \rightarrow K\pi$ reflection peak but also eliminates all pions below the c2 pion threshold of 4.5 GeV. Direct comparisons of the effects of the different Cerenkov definitions will not be done at this point but the tables showing the efficiency effects of the other cuts will include entries for the tight and loose Cerenkov definitons in conjunction with the standard cuts.

The elsig cut is the same as for the KK decay. Since the main difficulty is in fitting the charm background, which the elsig does not reduce at a greater rate than signal, a very restrictive elsig cut is not needed. A tight elsig cut was however useful in parameterizing the reflection peak. It was this parameterization, along with the parameterization from the R cut study which was used to set the width of the Gaussian of the high side of the reflection peak. The efficiencies of this cut are given in Table 3.12.

Table 3.12

Cut on elsig	Efficiency with reconstruction cuts	Efficiency with analysis cuts and loose ISTATP definitions	Efficiency with analysis cuts and tight ISTATP definitions
elsig.gt.4	11.3%	5.9%	2.5%
elsig.gt.6	10.1%	5.6%	2.3%
elsig.gt.8	9.1%	5.2%	2.2%
elsig.gt.9	8.3%	4.9%	2.0%
elsig.gt.10	7.5%	4.6%	1.8%
elsig.gt.11	6.7%	4.2%	1.6%
elsig.gt.12	6.1%	3.9%	1.5%
elsig.gt.14	5.1%	3.4%	1.3%
elsig.gt.16	4.3%	2.8%	1.0%

As can be seen in the signals presented (figs. 3.26, 3.27, 3.28) for the loose, intermediate, and tight cerenkov cuts. The range of elsig cuts from 4 to 14 reduces the combinatoric background

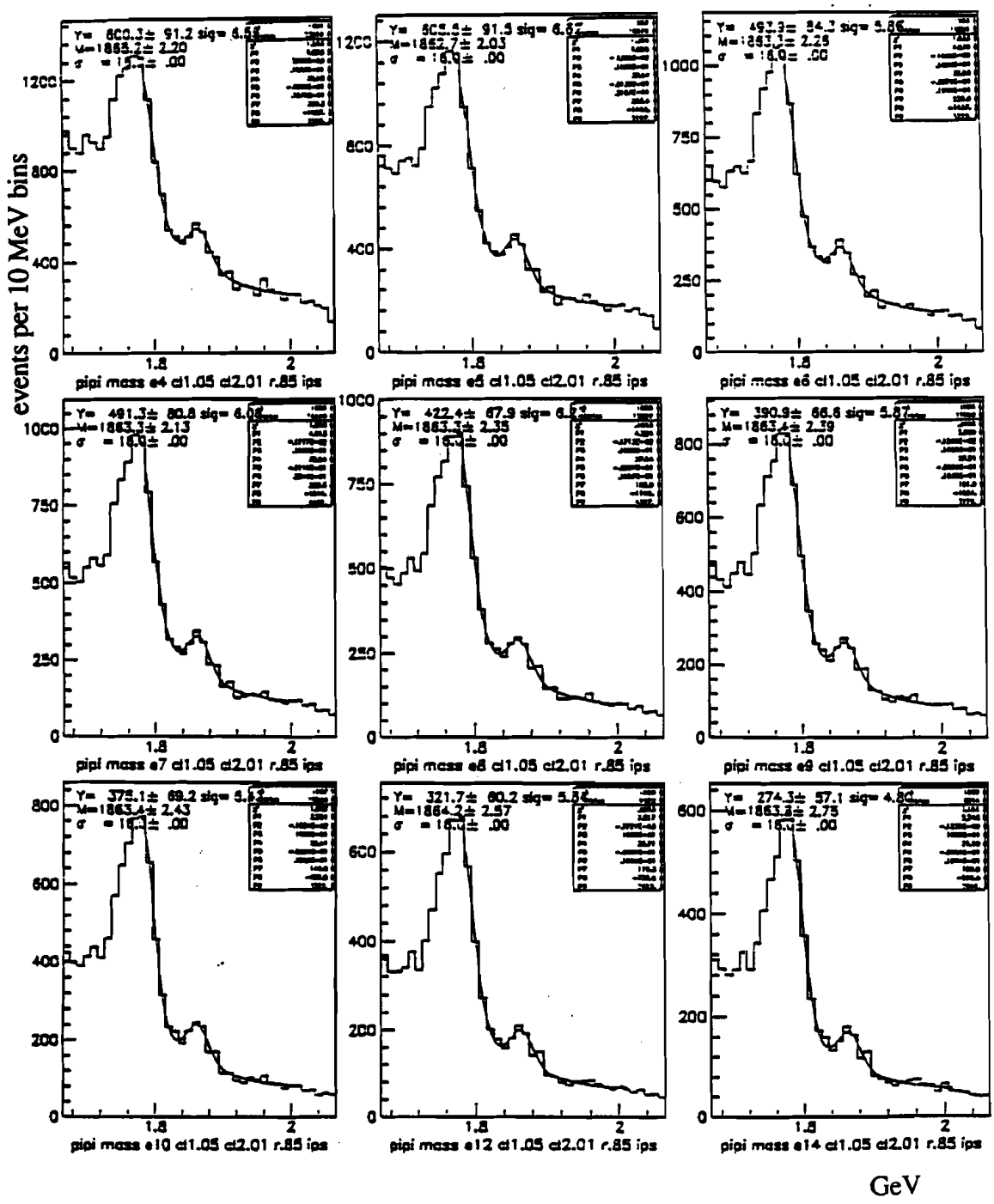

Figure 3.26: Mass plots for the systematic study of L/σ for the D ->ππ decay, loose Cerenkov definition

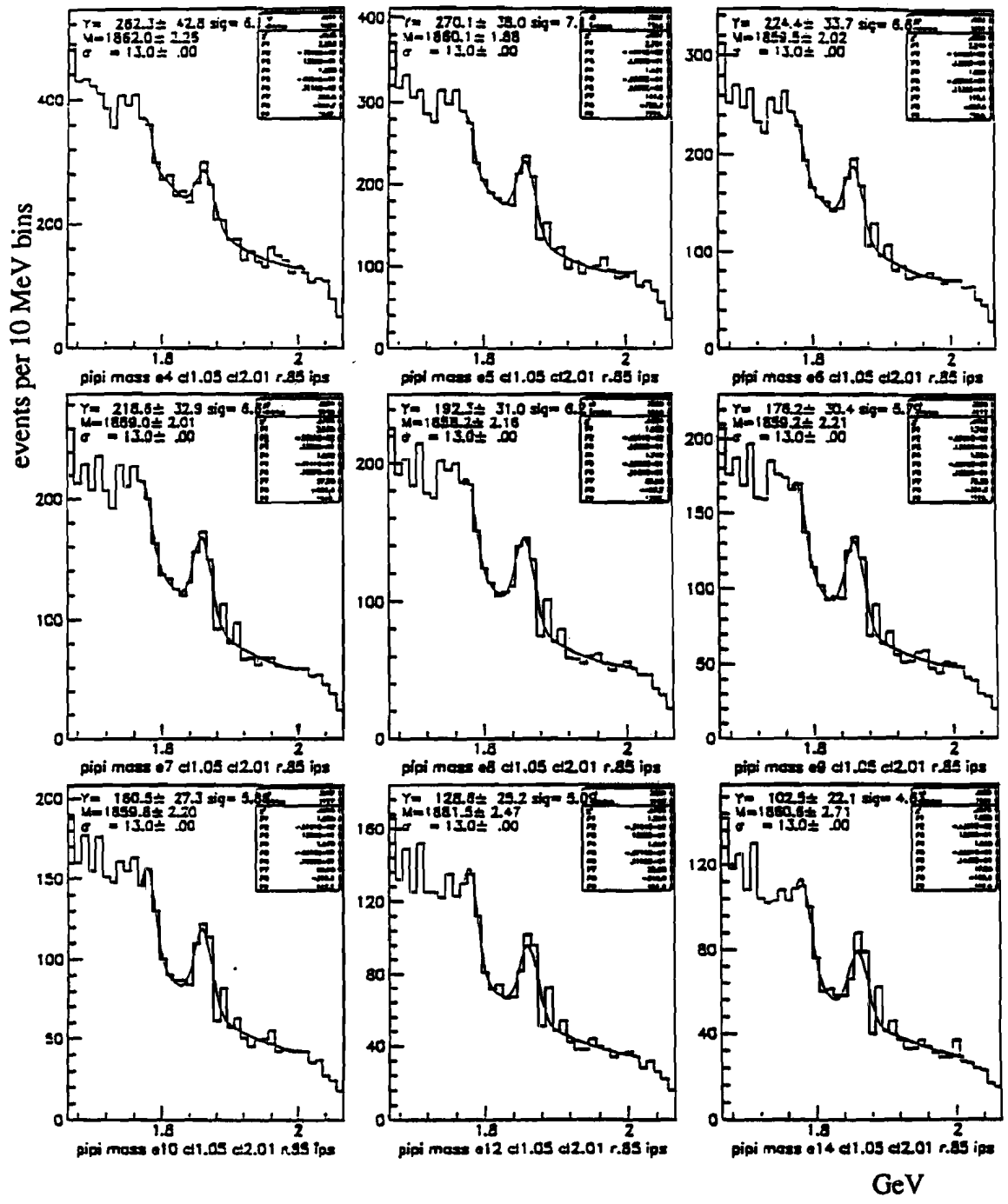

Figure 3.27: Mass plots for the systematic study of L/σ for the D ->ππ decay, medium Cerenkov definition

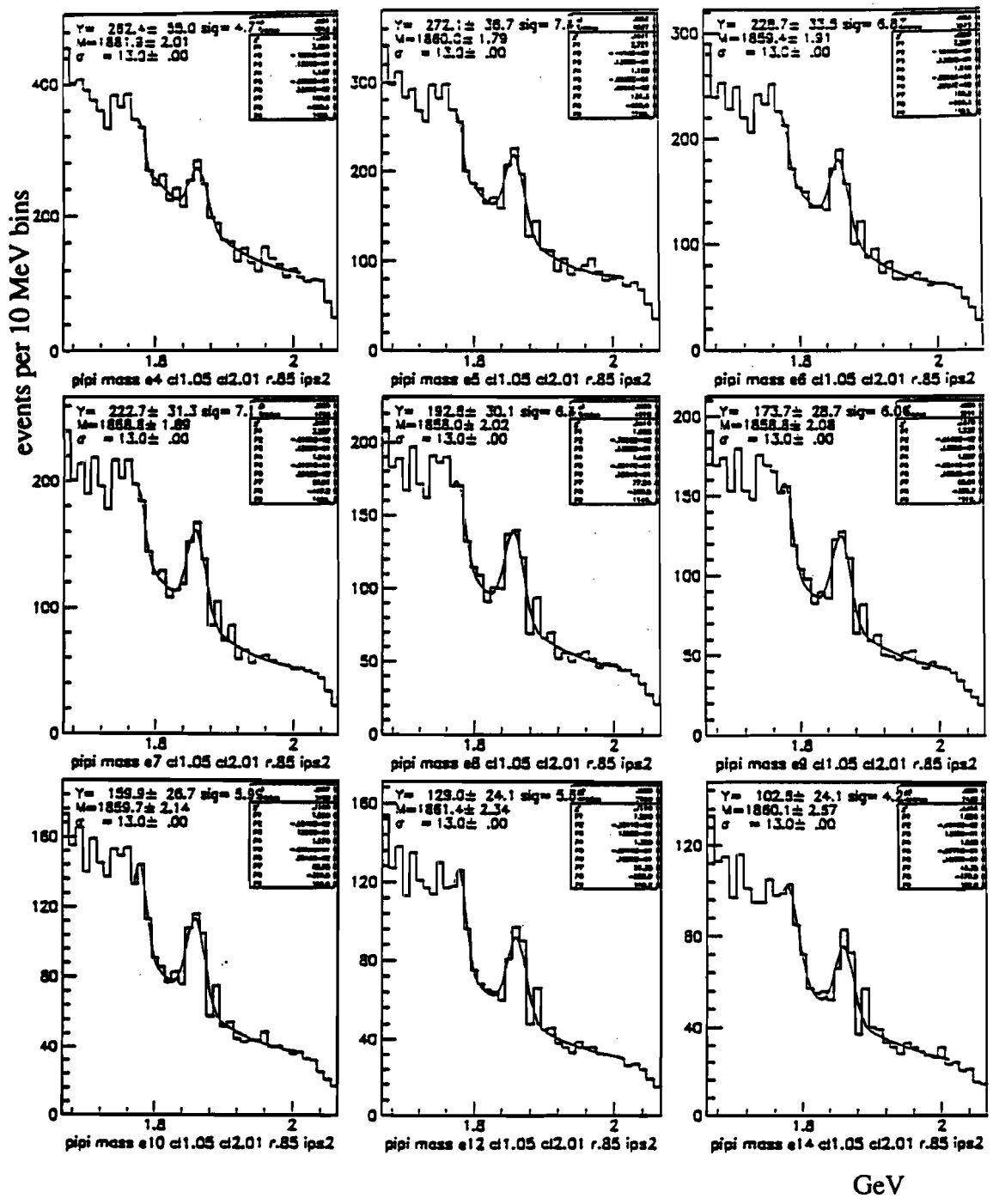

Figure 3.28: Mass plots for the systematic study of L/σ for the D ->ππ decay, tight Cerenkov definition

by a factor of four while reducing the signal by a little more than a factor of 2.

The CL1 cut is identical to that used in the KK analysis. The efficiencies are presented in Table 3.13.

Table 3.13

Cut on CL1	Efficiency with reconstruction cuts	Efficiency with analysis cuts and loose ISTATP definitions	Efficiency with analysis cuts and tight ISTATP definitions
CL1.lt.1	11.3%	5.2%	1.99%
CL1.lt.0.5	10.3%	5.0%	1.93%
CL1.lt.0.1	8.6%	4.7%	1.85%
CL1.lt.0.05	8.0%	4.6%	1.82%
CL1.lt.0.01	6.7%	4.3%	1.75%
CL1.lt.0.005	6.4%	4.2%	1.70%
CL1.lt.0.001	5.6%	3.9%	1.62%
CL1.lt.0.0005	5.3%	3.8%	1.58%
CL1.lt.0.0001	4.7%	3.6%	1.49%

The signals from the CL1 study can be seen for the three different Cerenkov cuts (fig 3.29 3.30, 3.31). Over the tested range of CL1 value the background is reduce by a factor of 2.5, but the signal is actually reduced very little, less than 25%.

The CL2 cut efficiencies are presented below. The cuts upon CL2 were chosen to maximize the significance of signal. The effects of the CL2 cut on the signal and backround for the loose, intermediate and tight cerenkov definitions can be seen in the attached figures(3.32, 3.33, and 3.34).

The R cut was once again effective in improving the signal to noise significantly. Similar effect can be seen for the two looser Cerenkov samples (fig 3.35, 3.36, 3.37). The efficiencies for the R cut are presented in Table 3.15. Most of the combinatoric background is eliminated by the 0.85 cut so we shall stay there for the maximum significance of signal.

A value of 0.0457 ± 0.0089 for the relative branching ratio was calculated for the cuts

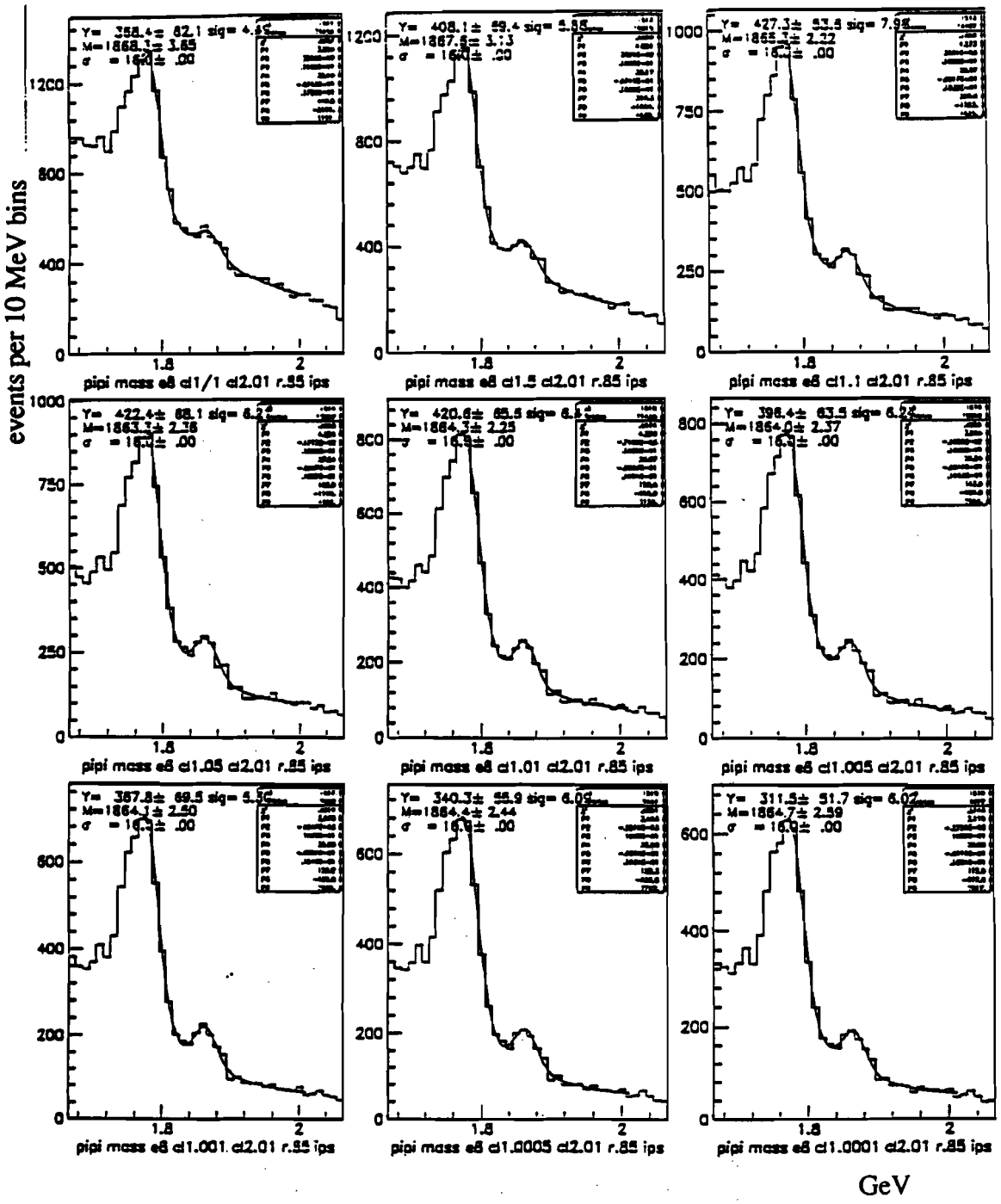

Figure 3.29: Mass plots for the systematic study of CL1 for the D -> $\pi\pi$ decay, loose Cerenkov definition

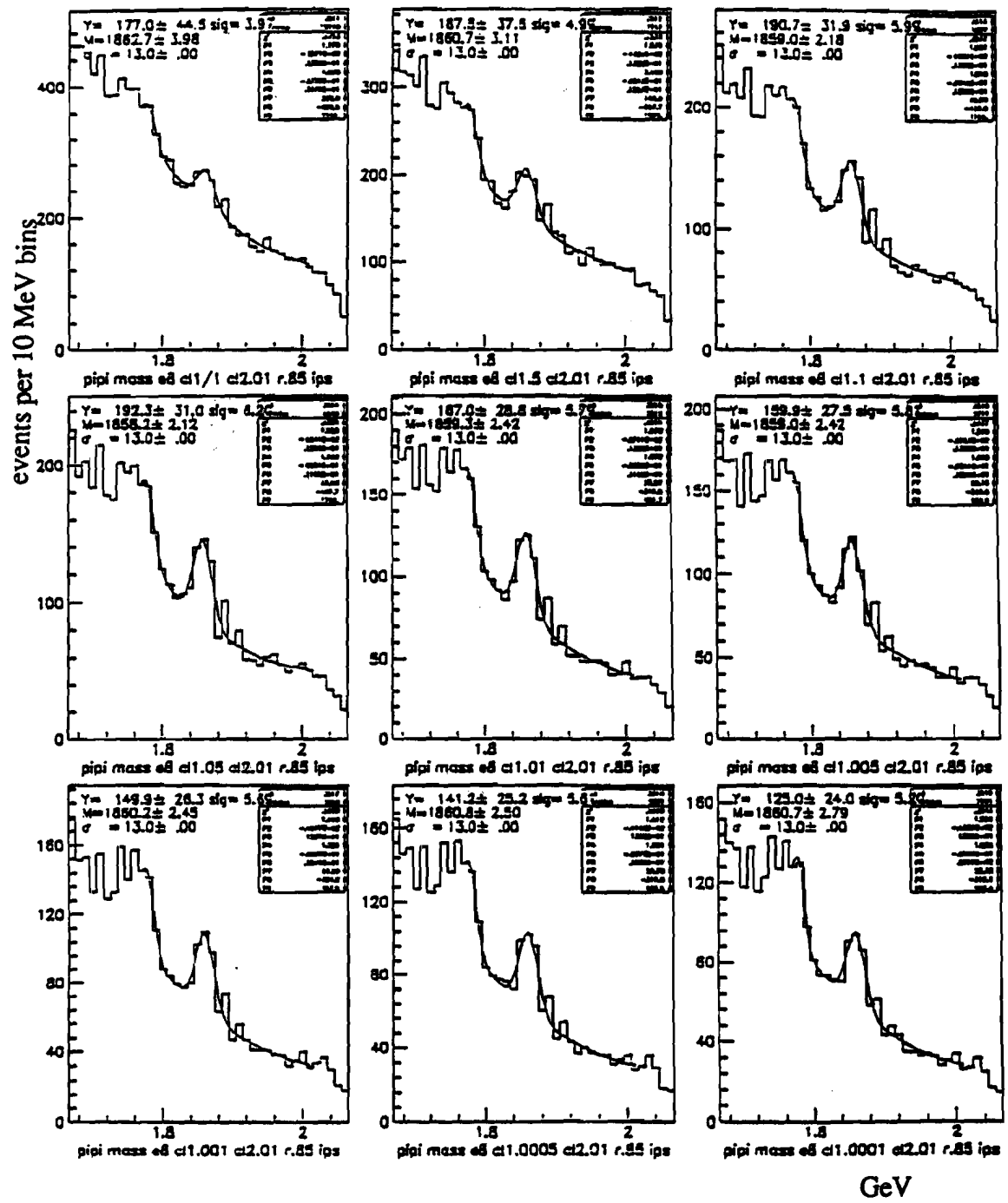

Figure 3.30: Mass plots for the systematic study of CL1 for the D -> $\pi\pi$ decay, medium Cerenkov definition

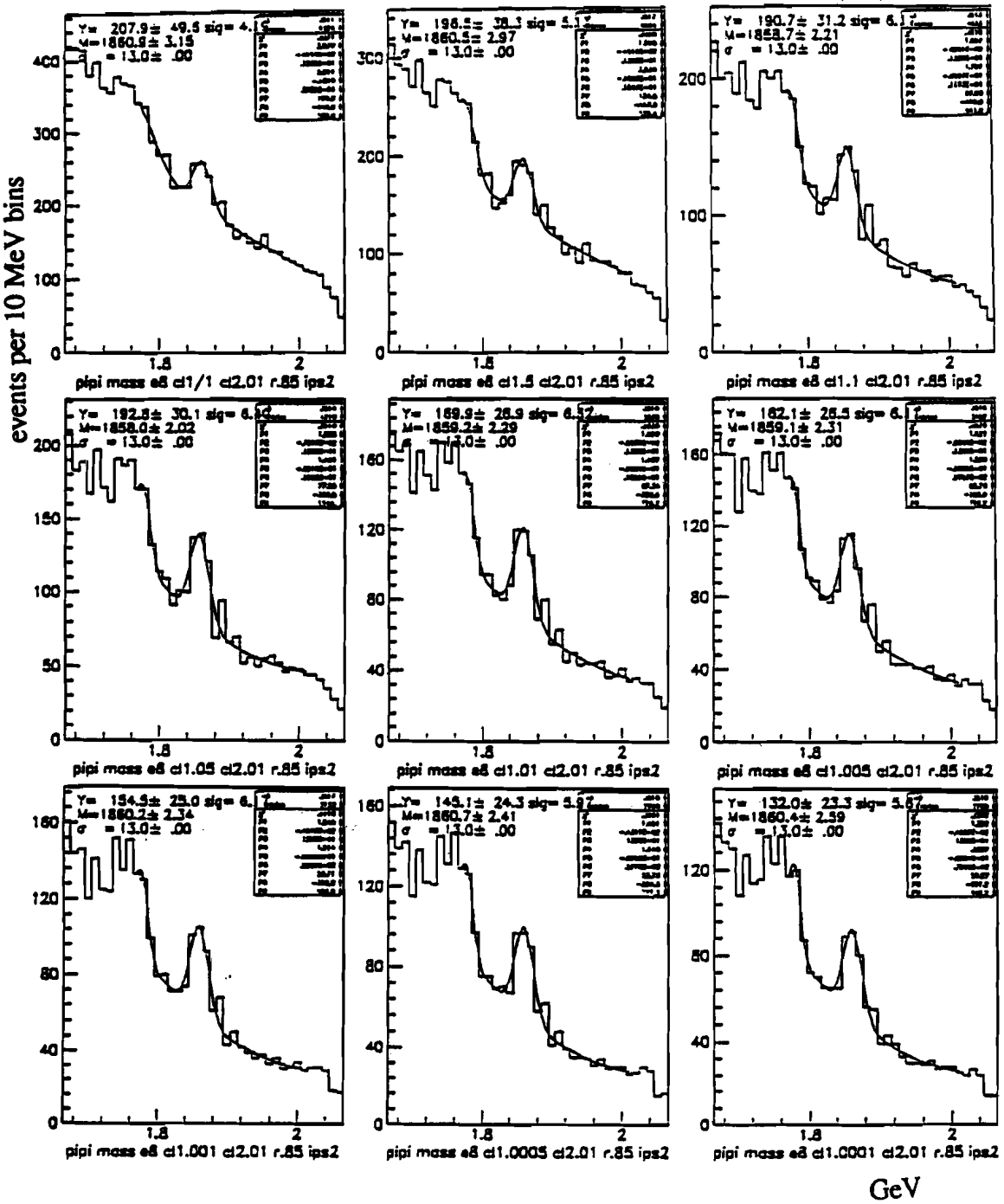

Figure 3.31: Mass plots for the systematic study of CL1 for the D -> ππ decay, tight Cerenkov definition

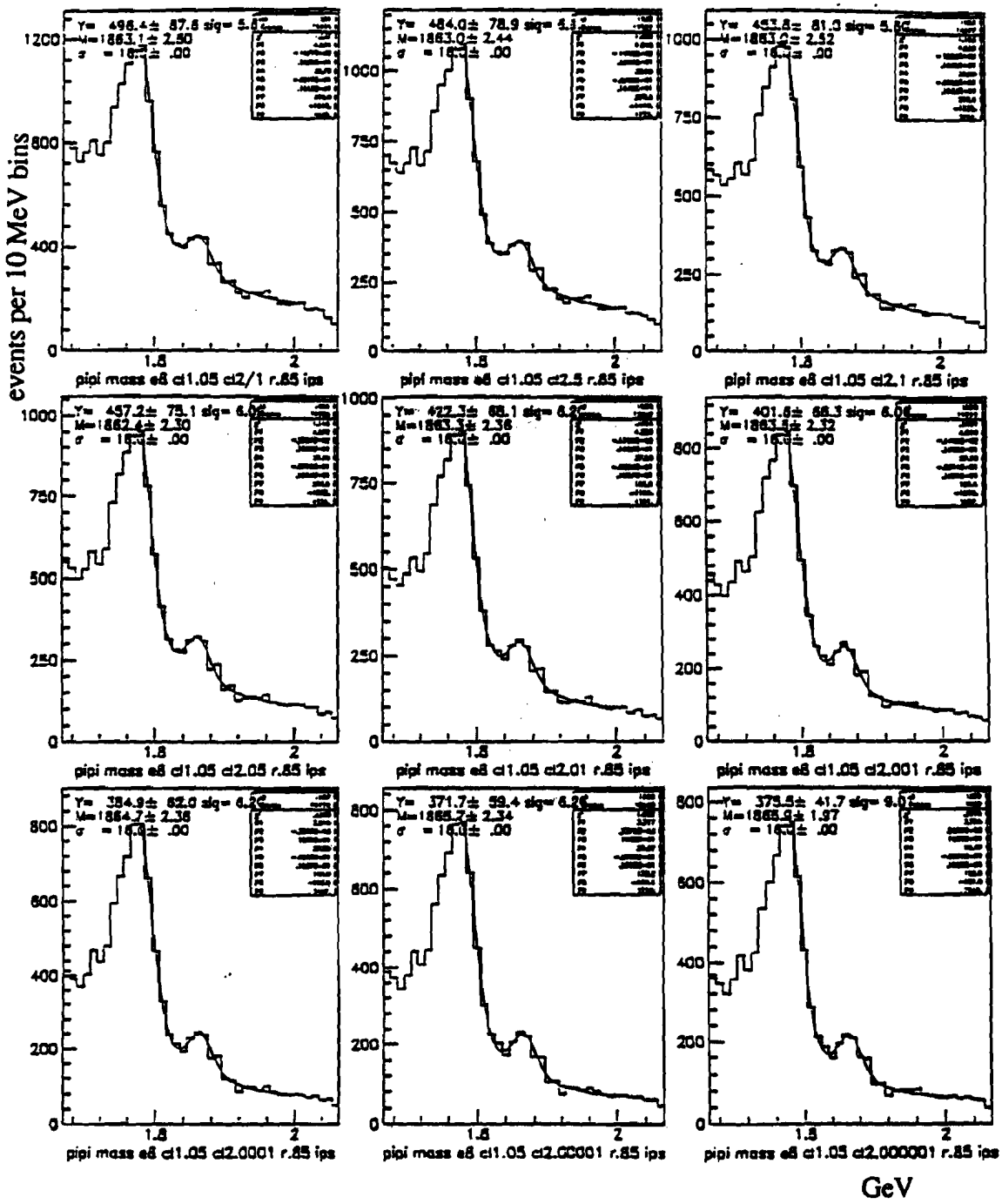

Figure 3.32: Mass plots for the systematic study of CL2 for the D -> ππ decay, loose Cerenkov definition

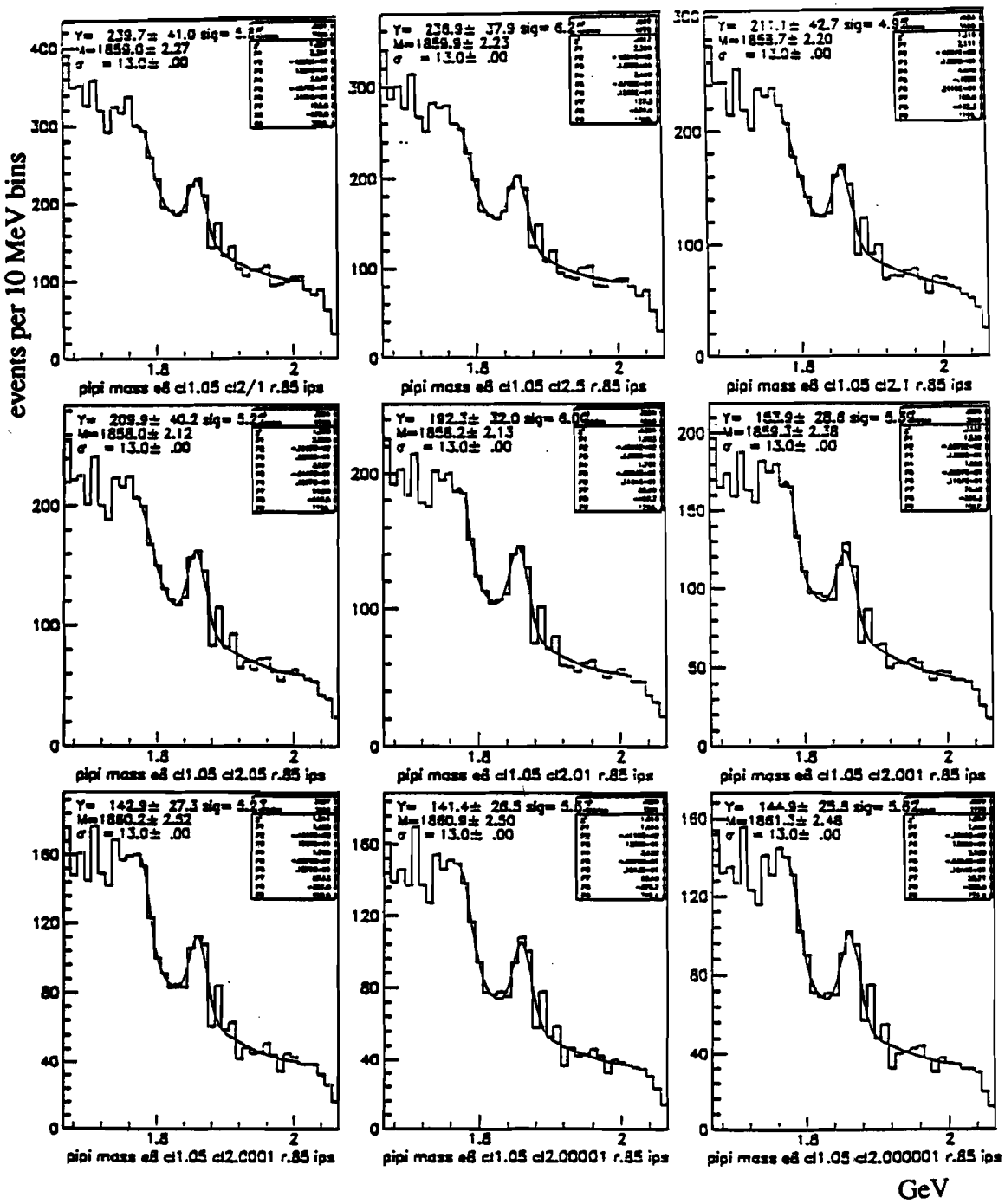

Figure 3.33: Mass plots for the systematic study of CL2 for the D -> ππ decay, medium Cerenkov definition

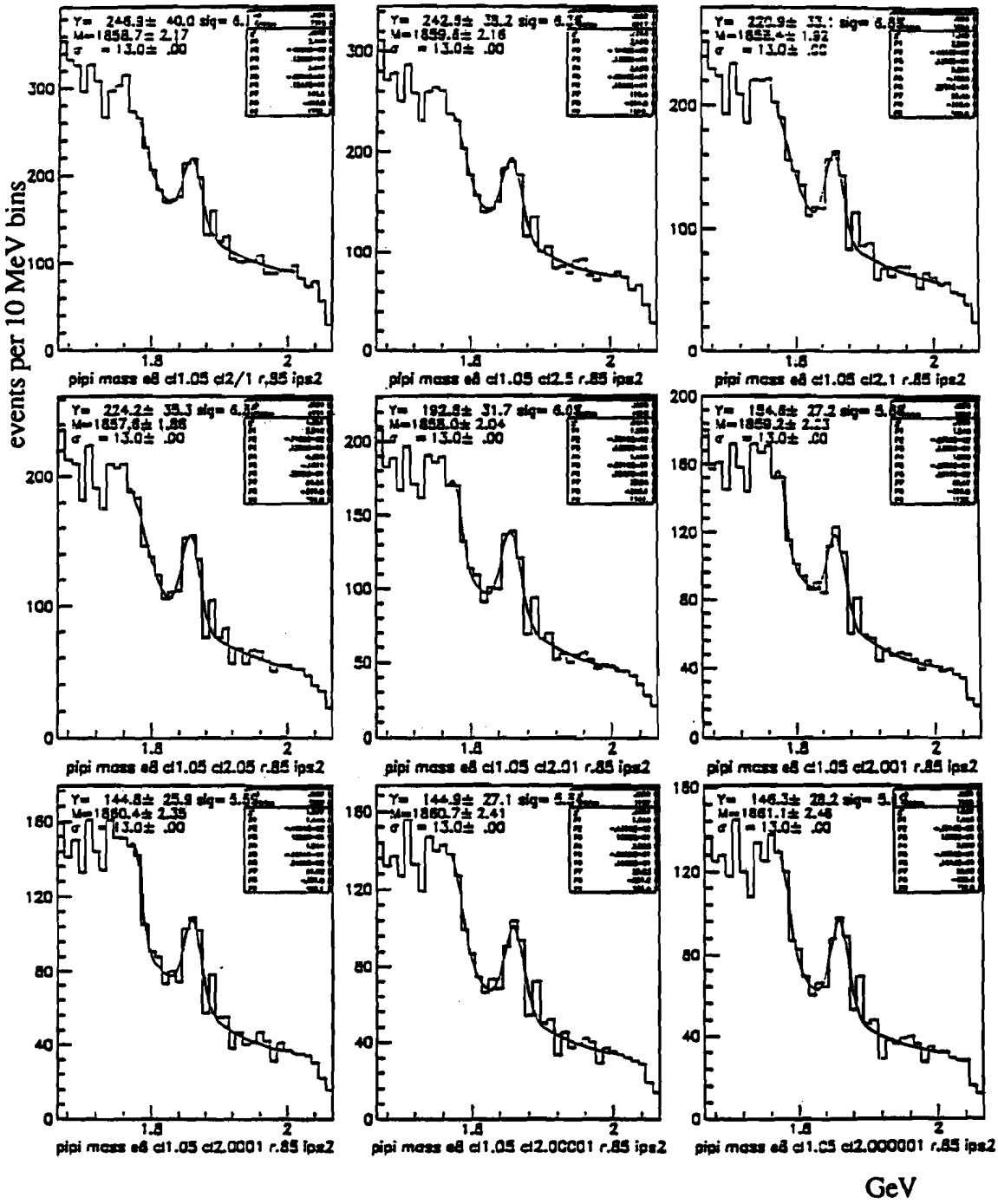

Figure 3.34: Mass plots for the systematic study of CL2 for the D -> $\pi\pi$ decay, tight Cerenkov definition

Table 3.14

Cut on CL2	Efficiency with reconstruction cuts	Efficiency with analysis cuts and loose ISTATP definitions	Efficiency with analysis cuts and tight ISTATP definitions
CL2.lt. 1	11.3%	5.2%	2.05%
CL2.lt.0.1	10.9%	5.0%	4.00%
CL2.lt 0.05	10.4%	4.8%	1.91%
CL2.lt.0.01	10.2%	4.7%	1.89%
CL2.lt.0.005	9.8%	4.6%	1.82%
CL2.lt.0.001	9.4%	4.4%	1.75%
CL2<1×10^{-3}	9.0%	4.3%	1.70%
CL2<1×10^{-4}	8.7%	4.2%	1.65%
CL2<1×10^{-5}	8.4%	4.1%	1.61%

Table 3.15

Cut	Lone eff	eff with cuts	eff w/ isp1
r.= 1	11.3%	5.6%	1.99%
r.= 0.95	11.0%	5.4%	1.98%
r.= 0.90	10.1%	5.1%	1.96%
r.= 0.85	9.0%	4.6%	1.82%
r.= 0.80	7.8%	4.0%	1.66%
r.= 0.75	6.6%	3.4%	1.46%
r.= 0.70	5.3%	2.9%	1.22%
r.= 0.65	4.4%	2.1%	0.95%
r.= 0.60	2.7%	1.4%	0.66%

as outlined above and the tight Cerenkov definitions. As can be seen by the attached plots (fig 3.38, 3.39, 3.40, 3.41) this result is relatively independent of the values of the cuts. We expect a systematic error of about .004 for each of the cuts and when added in quadrature this gives a combined systematic error of .008. The next step in the analysis was to investigate the effect of the Cerenkov cuts on the analysis in the branching ratio. Since I ran into a great deal of difficulty fitting many of the mass plots for the looser Cerenkov cuts, it was decided that it was necessary to fix the width of the signal Gaussian. Since there is some variation already in the widths of the mass peaks for the tight Cerenkov cuts a value of the fixed width needed to be established. The value that was chosen was the nominal value from the Monte Carlo simulation. There has been some indication that the true width of signal is 10-15%

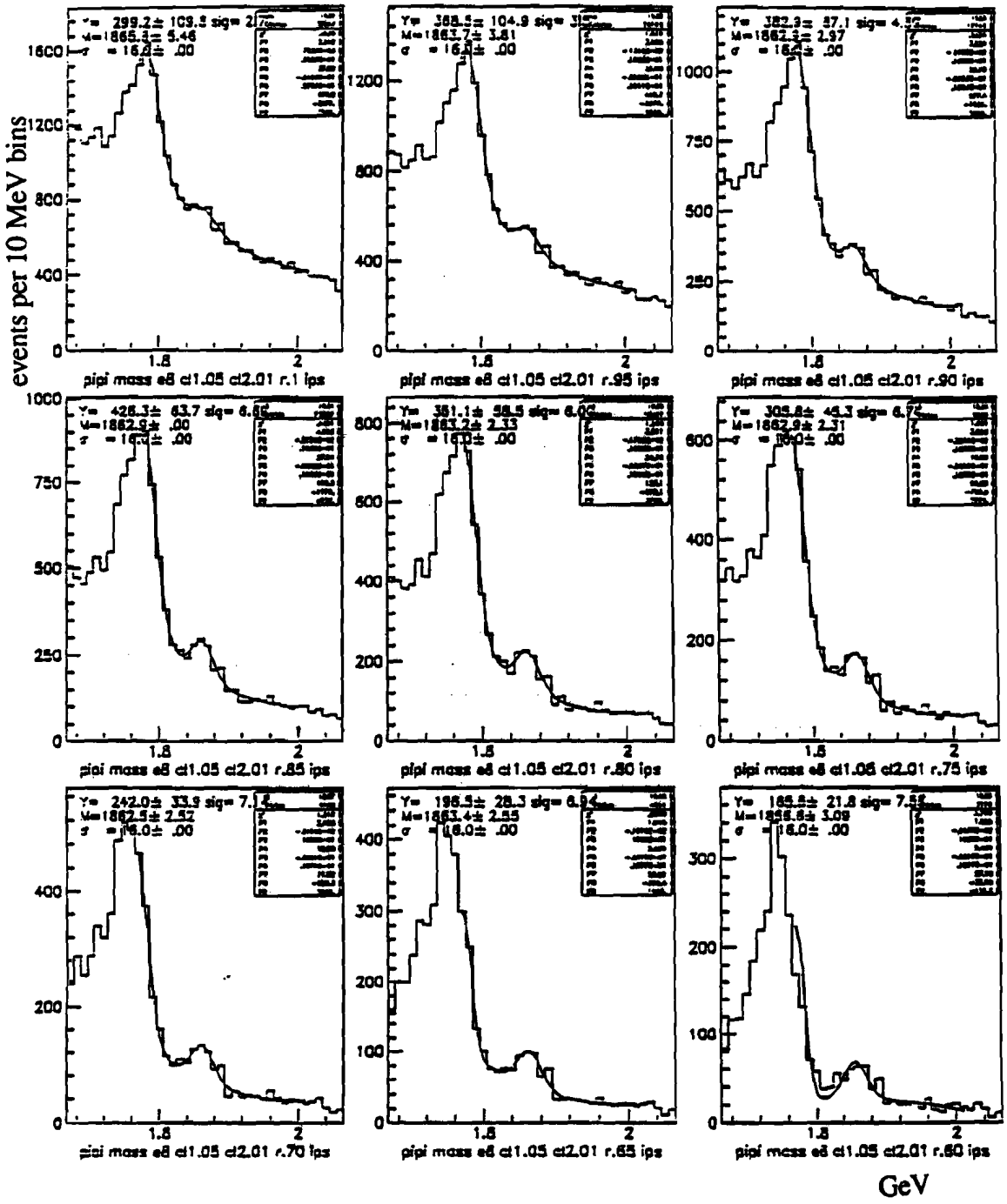

Figure 3.35: Mass plots for the systematic study of R for the D -> $\pi\pi$ decay, loose Cerenkov definition

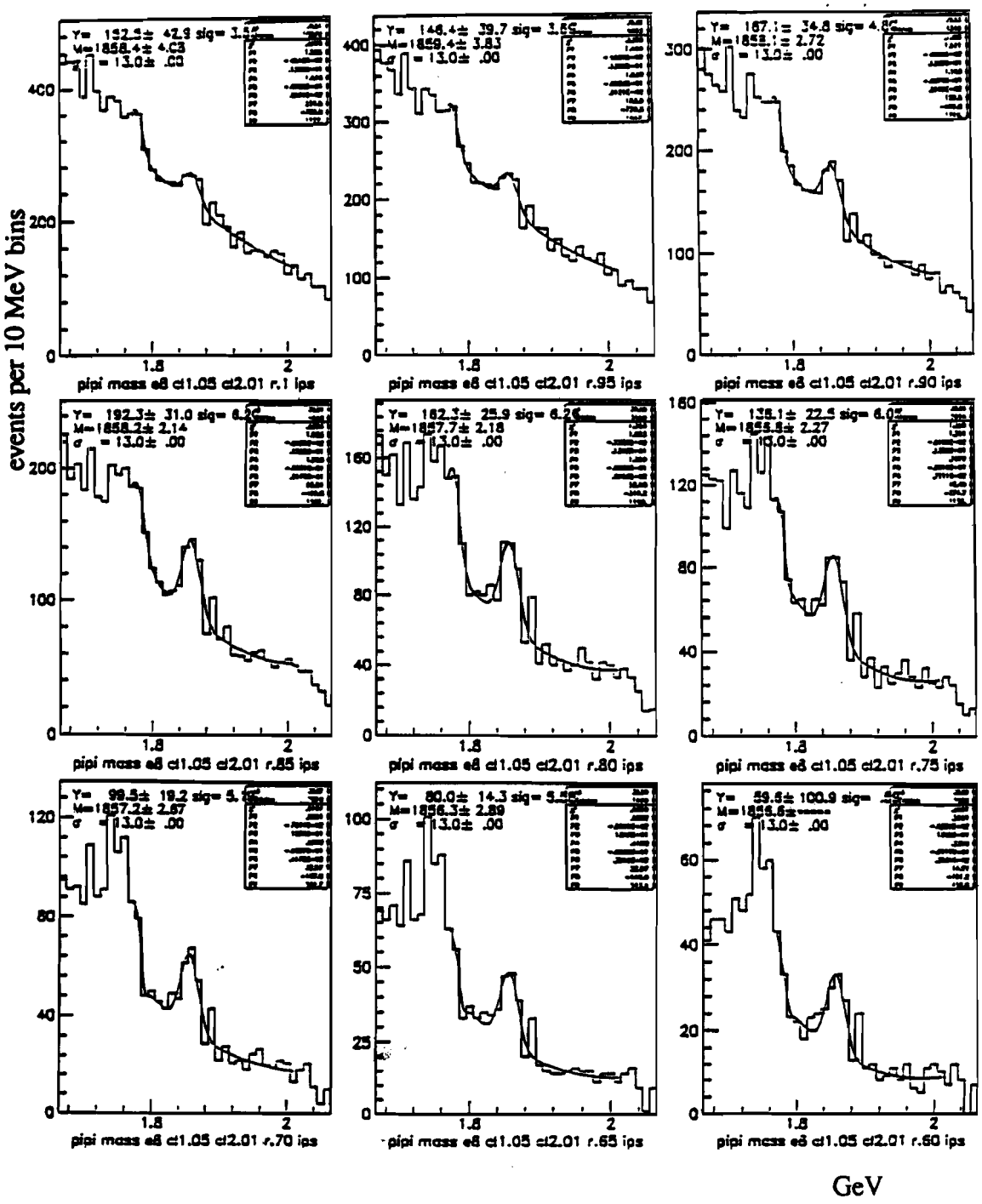

Figure 3.36: Mass plots for the systematic study of R for the D -> $\pi\pi$ decay, medium Cerenkov definition

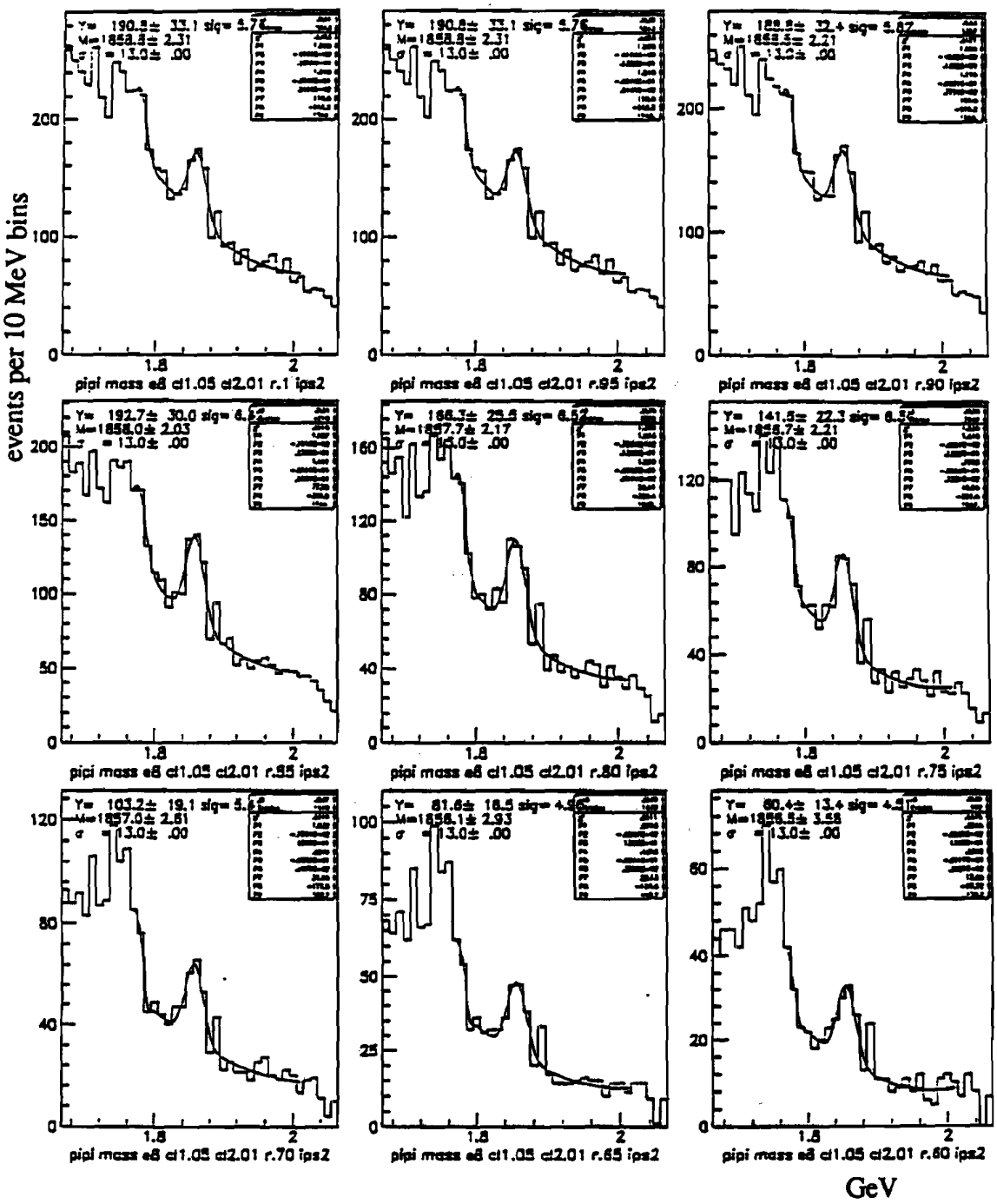

Figure 3.37: Mass plots for the systematic study of R for the D -> ππ decay, tight Cerenkov definition

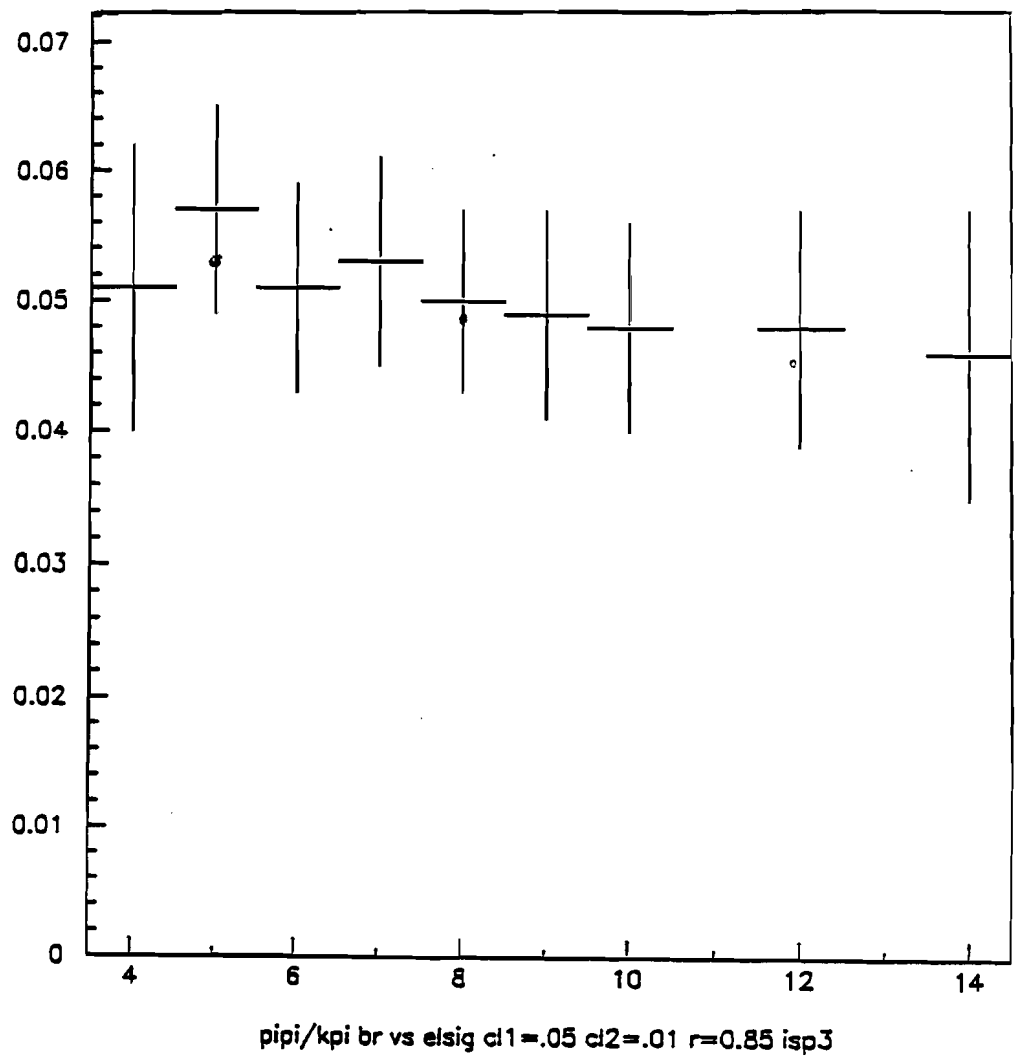

Figure 3.38: Relative branching ratio as a function of L/σ for the D -> ππ decay, tight Cerenkov definitions

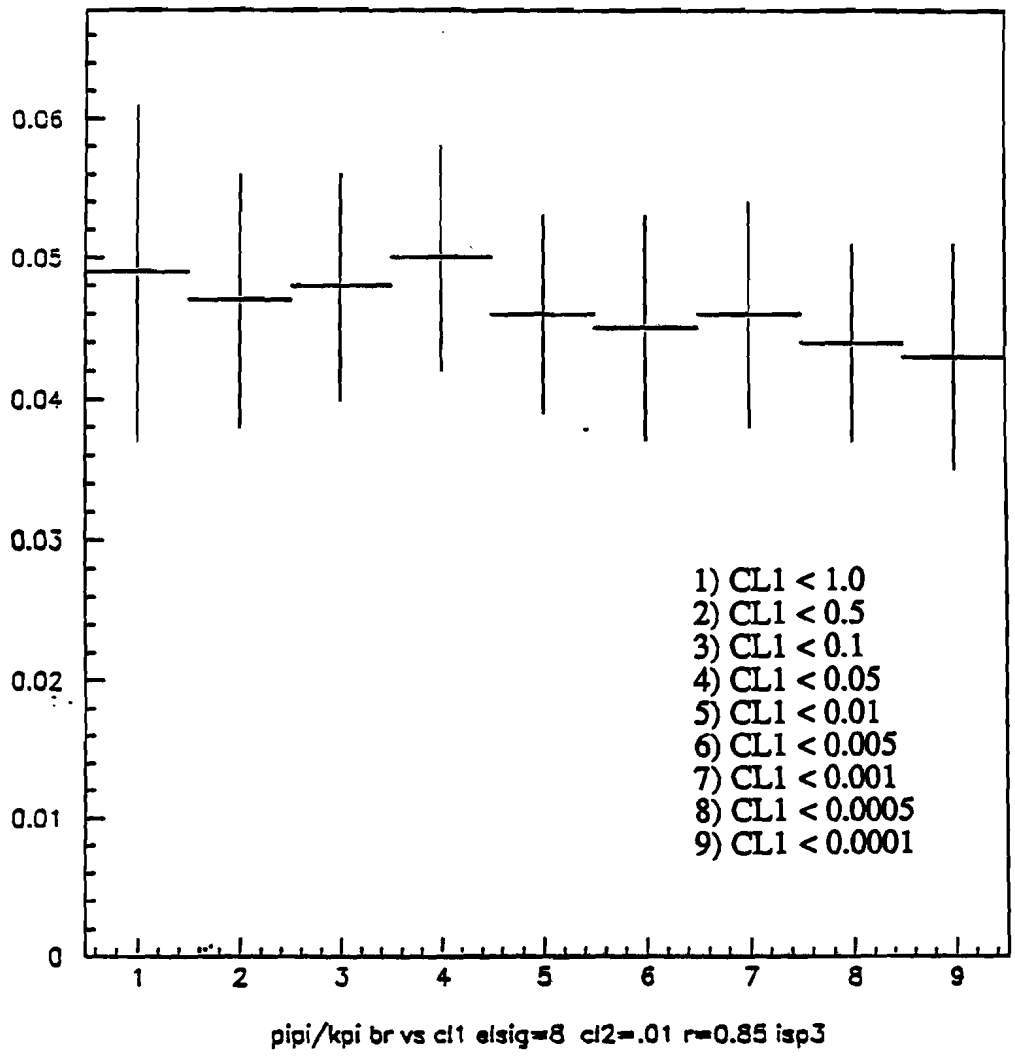

Figure 3.39: Relative branching ratio as a function of CL1 for the D -> $\pi\pi$ decay, tight Cerenkov definitions

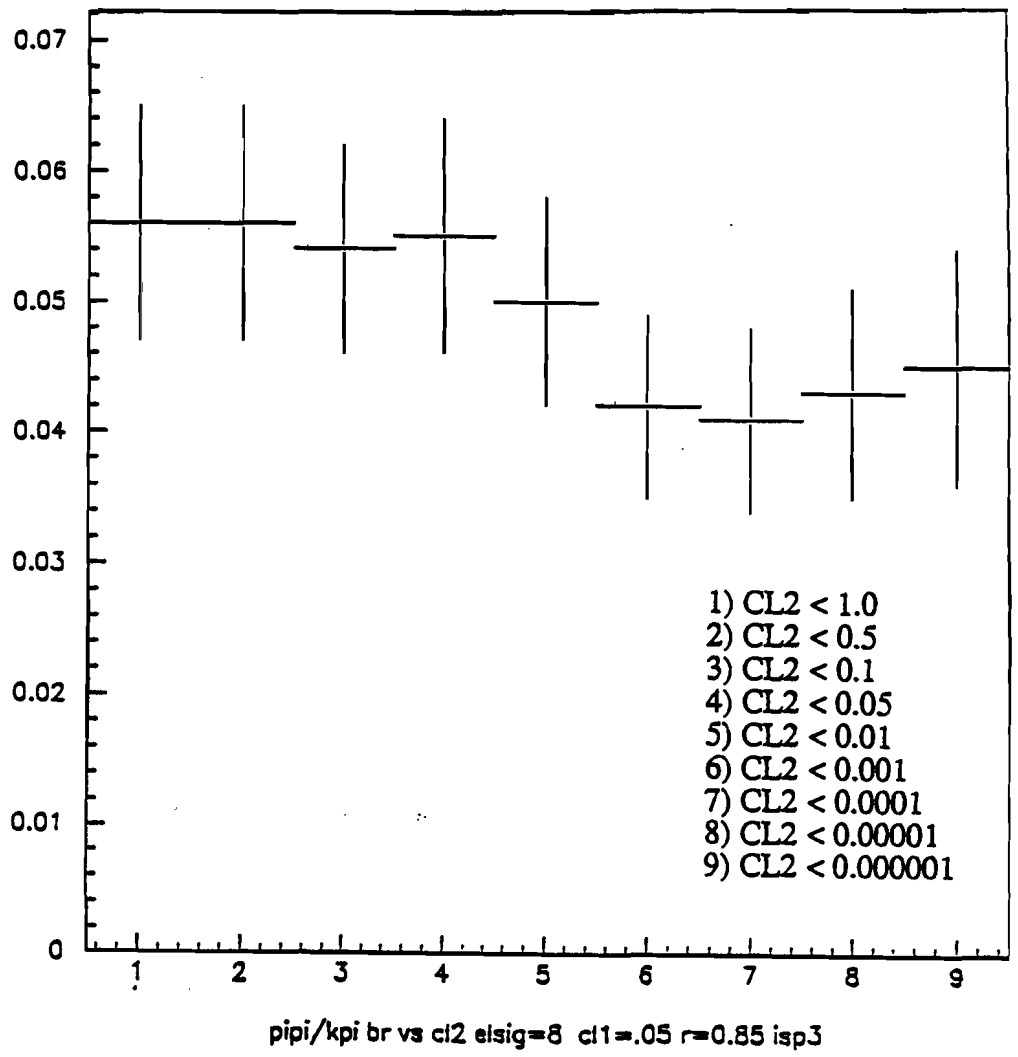

Figure 3.40: Relative branching ratio as a function of CL2 for the D -> $\pi\pi$ decay, tight Cerenkov definitions

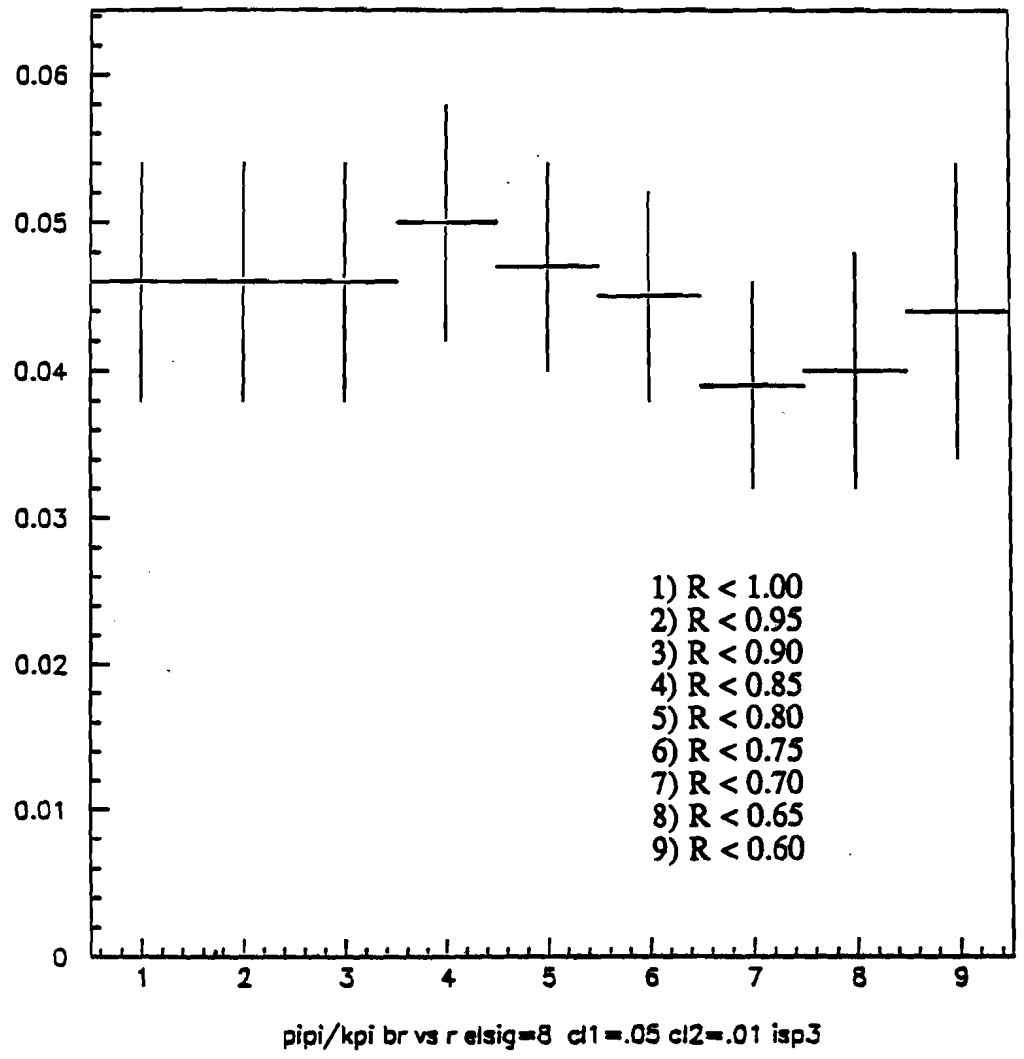

Figure 3.41: Relative branching ratio as a function of R for the D ->ππ decay, tight Cerenkov definitions

narrower than the Monte Carlo simulation but since this is primarily to determine the effect of the cuts this was not judged to be a major effect. The widths that were chosen were 13 MeV for the tighter Cerenkov cuts and 16 MeV for the loose Cerenkov cuts. There also has been some concern in the collaboration about the accuracy of the Monte Carlo modelingof the tight Cerenkov definitions. We can see from comparison of the plots (fig 3.42, 3.43, 3.44, 3.45) that the loosest cuts are systematically lower than the two tighter cuts. This is not an effect that is outside of the statistical error and actually can be estimated at .002. This additional systematic error will not appreciably change the total systematic error of the measurement.

3.4.4 $D^0 \to K^+ K^- \pi^+ \pi^-$

The next decay topologies to be discussed are four body modes. Here the R-cut can no longer be used since the difference between background and signal in momentum distribution is reduced due to the larger number of decay products. One would initially expect that, due to the larger number of tracks used to create the secondary vertex, the likelihood of a random incorrect vertex being created is lessened. This does not hold, however, when the fact that the greater number of decay particles means a lower amount of available energy in the rest frame, which corresponds to smaller opening angles in the lab frame. This smaller opening angle degrades the vertexing ability of the microstrip algorithm. This smaller opening angle, as well as the larger number of tracks significantly decreases the effectiveness of the CL1 cut. The effectiveness of the CL1 cut is further weakened by the fact that in the two body state the only events that are likely to have decay tracks that point back to the primary vertex are those with colinear tracks, which would have a large error in secondary vertex position and could be eliminated by the elsig cut, or eliminated by the R cut. The four body states have a greater likelihood of having a secondary that is almost colinear with the D^0 direction. For this reason it was found that the CL1 cut was not useful here. In addition, there were concerns about the accuracy of the Cerenkov identification as modeled in the

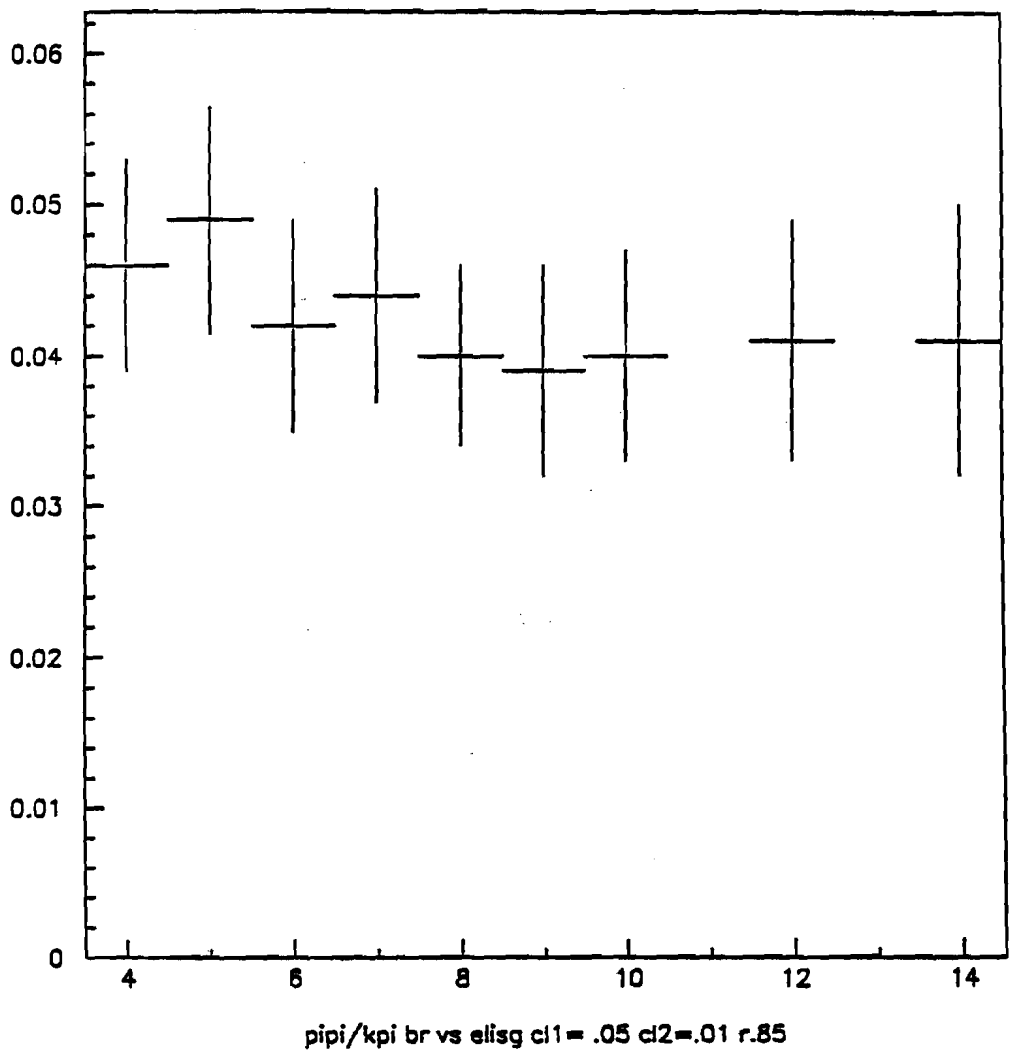

Figure 3.42: Relative branching ratio as a function of L/σ for the D -> ππ decay, loose Cerenkov definitions

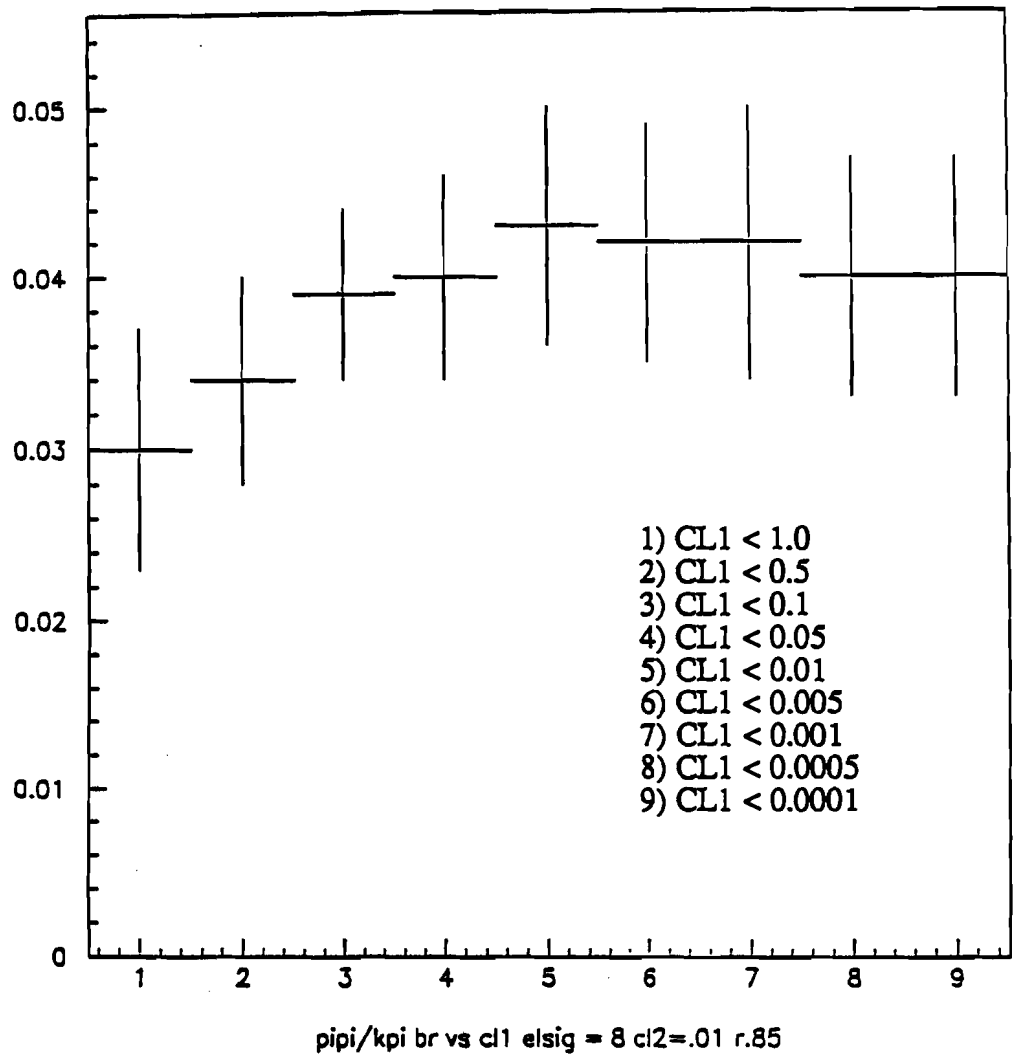

Figure 3.43: Relative branching ratio as a function of CL1 for the D -> $\pi\pi$ decay, loose Cerenkov definitions

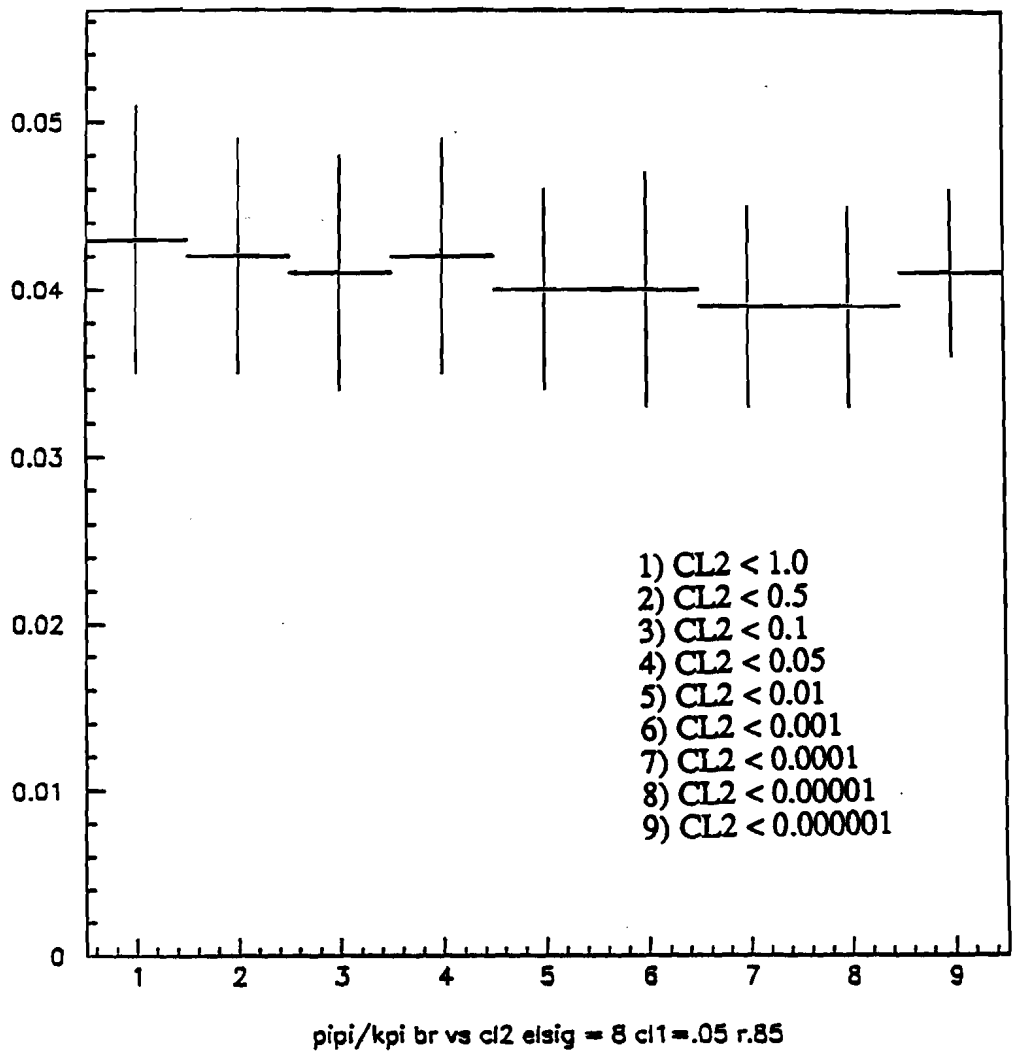

Figure 3.44: Relative branching ratio as a function of CL2 for the D -> $\pi\pi$ decay, loose Cerenkov definitions

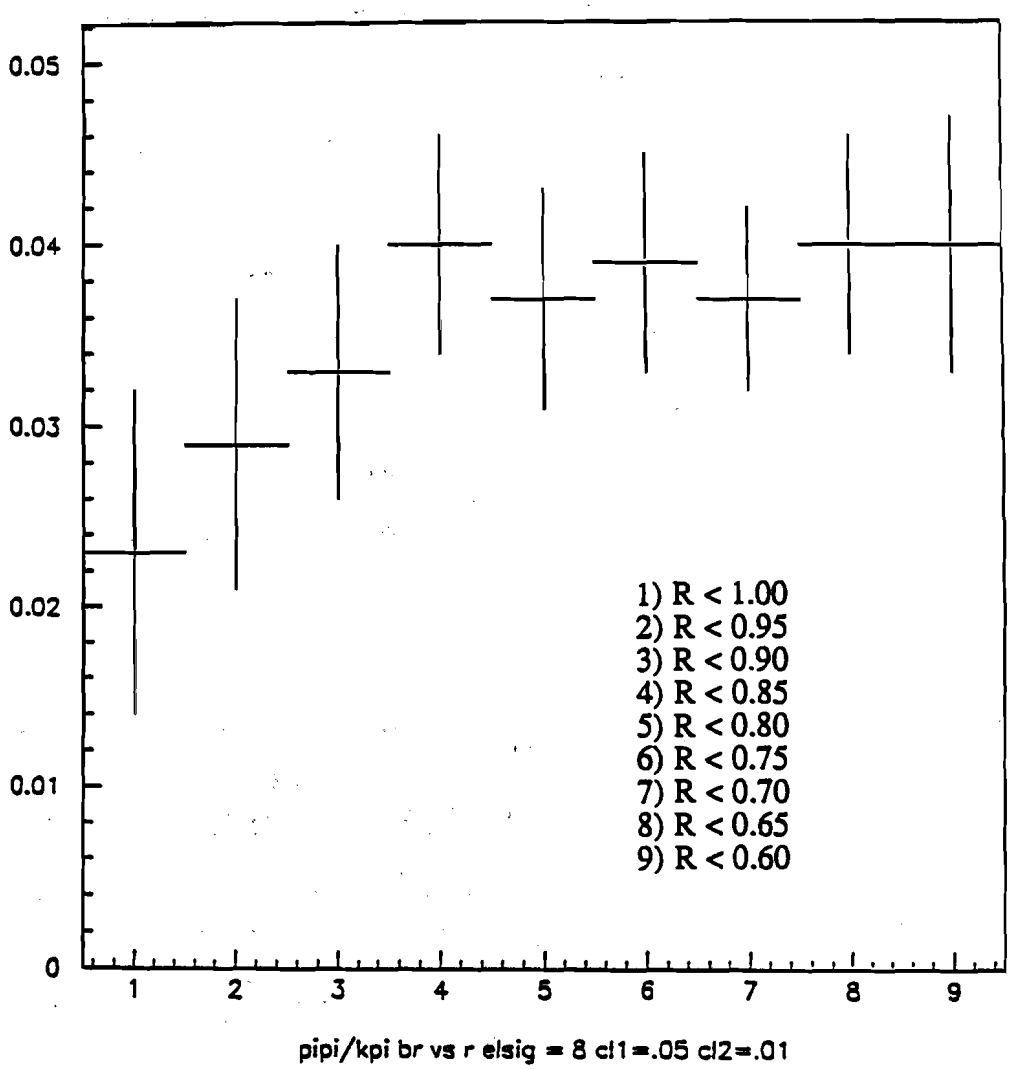

Figure 3.45: Relative branching ratio as a function of R for the D -> $\pi\pi$ decay, loose Cerenkov definitions

Monte Carlo. For this reason the looser Cerenkov cuts were used in all cases except the KKKπ state and there the effect was accounted for in the systematic error calculation.

The 2K 2π decay of the D^0 meson, although having a small branching ratio, has very little combinatoric background due to the existence of the two kaons in the final state. Once again there exists a reflection peak, this time from the Cabibbo favored K$\pi\pi\pi$ decay mode. Given the kinematics of the 2 kaon, 2 pion decay, the reflection peak is fairly small and rather isolated with its low edge almost a full 130 MeV higher than the nominal D^0 mass. This allows us to fit a background without serious concerns about the reflection peak. Again the cuts that were utilized were elsig, and isolation of the secondary vertex. The efficiencies of the cuts as determined by Monte Carlo are displayed in Table 3.16 and Table 3.17. The results include cuts from the reconstruction program as well as well as analysis cuts with loose, medium, and tight Cerenkov identification. The raw results of the signal studies for the elsig and CL2 cut are presented for both the loose (fig 3.46, 3.47) and the tight (fig. 3,48, 3.49) definitions are presented.

Table 3.16

cut on elsig	Efficiency with reconstructin cuts	Efficiency with analysis cuts and loose ISTATP definitions	Efficiency with analysis cuts and medium ISTATP definitions	Efficiency with analysis cuts and tight ISTATP definitions
elsig>4	6.6%	4.5%	3.7%	2.14%
elsig>5	5.6%	3.9%	3.2%	1.92%
elsig>6	5.0%	3.5%	2.8%	1.68%
elsig>7	4.4%	3.1%	2.5%	1.48%
elsig>8	3.9%	2.7%	1.2%	1.32%
elsig>9	3.4%	2.4%	1.9%	1.17%
elsig>10	3.0%	2.1%	1.7%	1.03%
elsig>12	2.4%	1.6%	1.3%	0.81%
elsig>14	1.9%	1.2%	0.9%	0.61%

When an elsig cut of 8 and a CL2 cut of 0.001 were applied to the loose Cerenkov sample I observed a signal of 240.3 $\pm$ 29.4 events. Once adjusted for the efficiency of the cuts and compared to the k$\pi\pi\pi$ decay of the D^0 meson, I calculated a relative

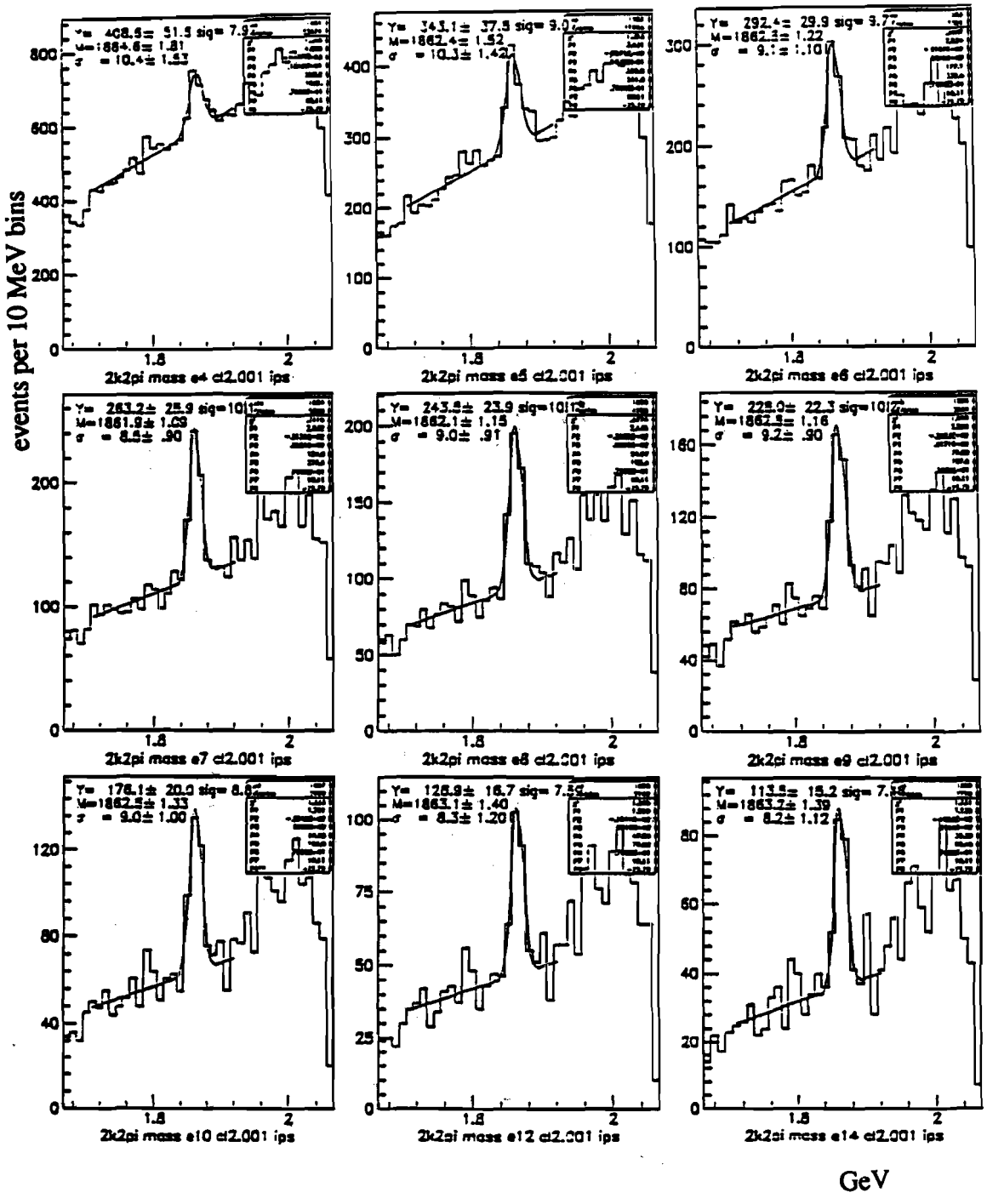

Figure 3.46: Mass plots for systematic study of L/σ for D -> KKππ decay loose Cerenkov definitions

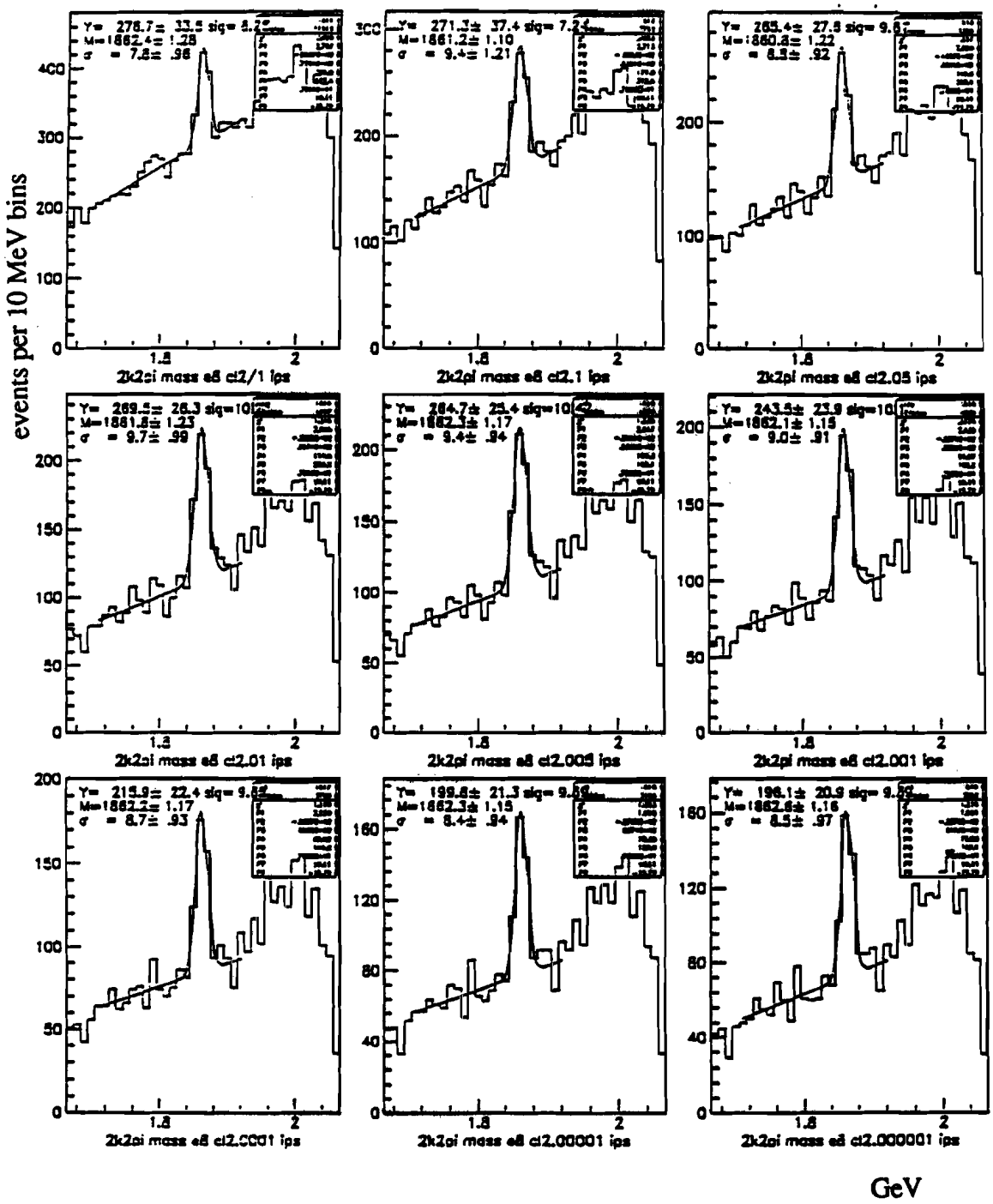

Figure 3.47: Mass plots for systematic study of CL2 for D -> KKππ decay loose Cerenkov definitions

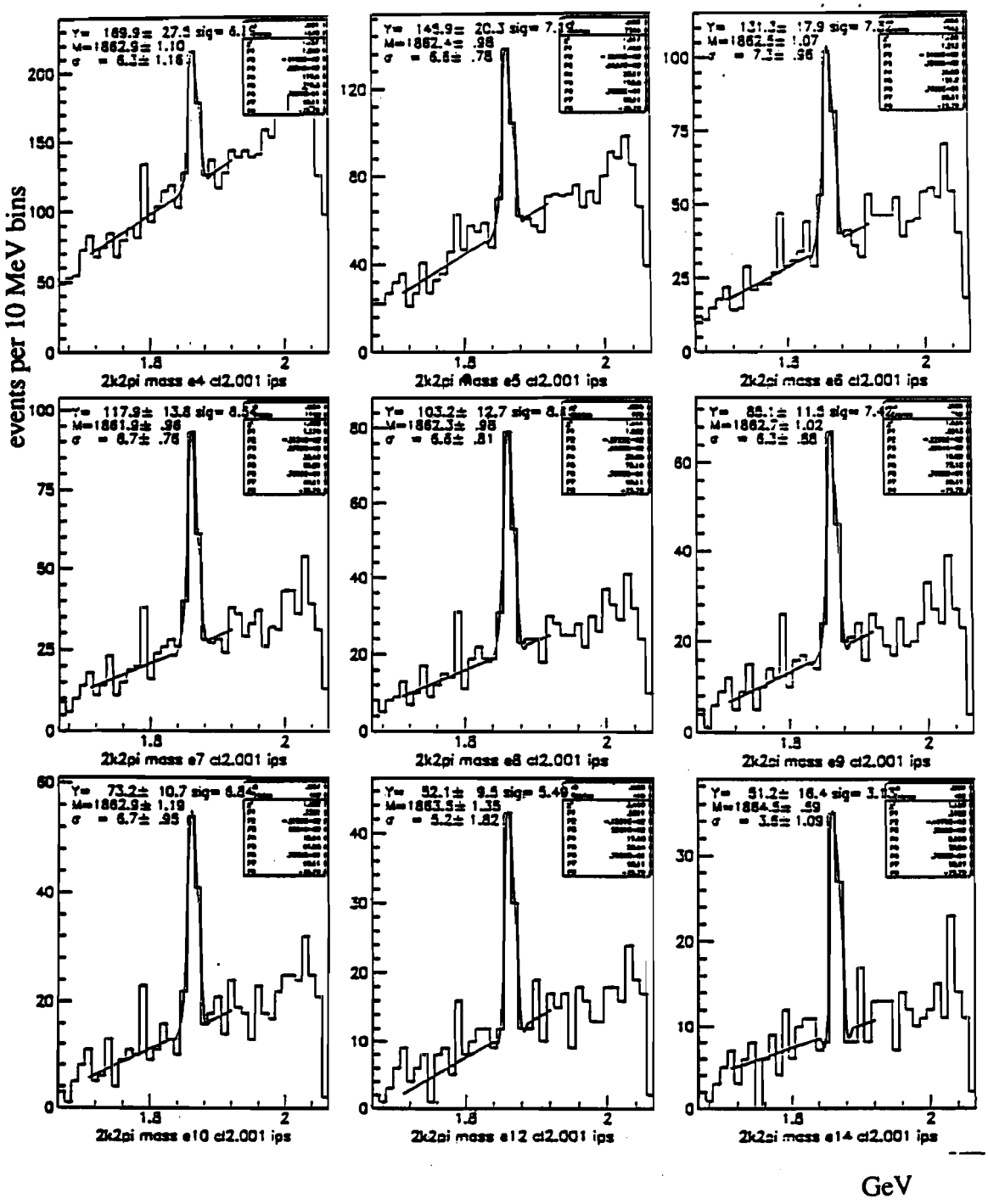

Figure 3.48: Mass plots for systematic study of L/σ for D -> KKππ decay tight Cerenkov definitions

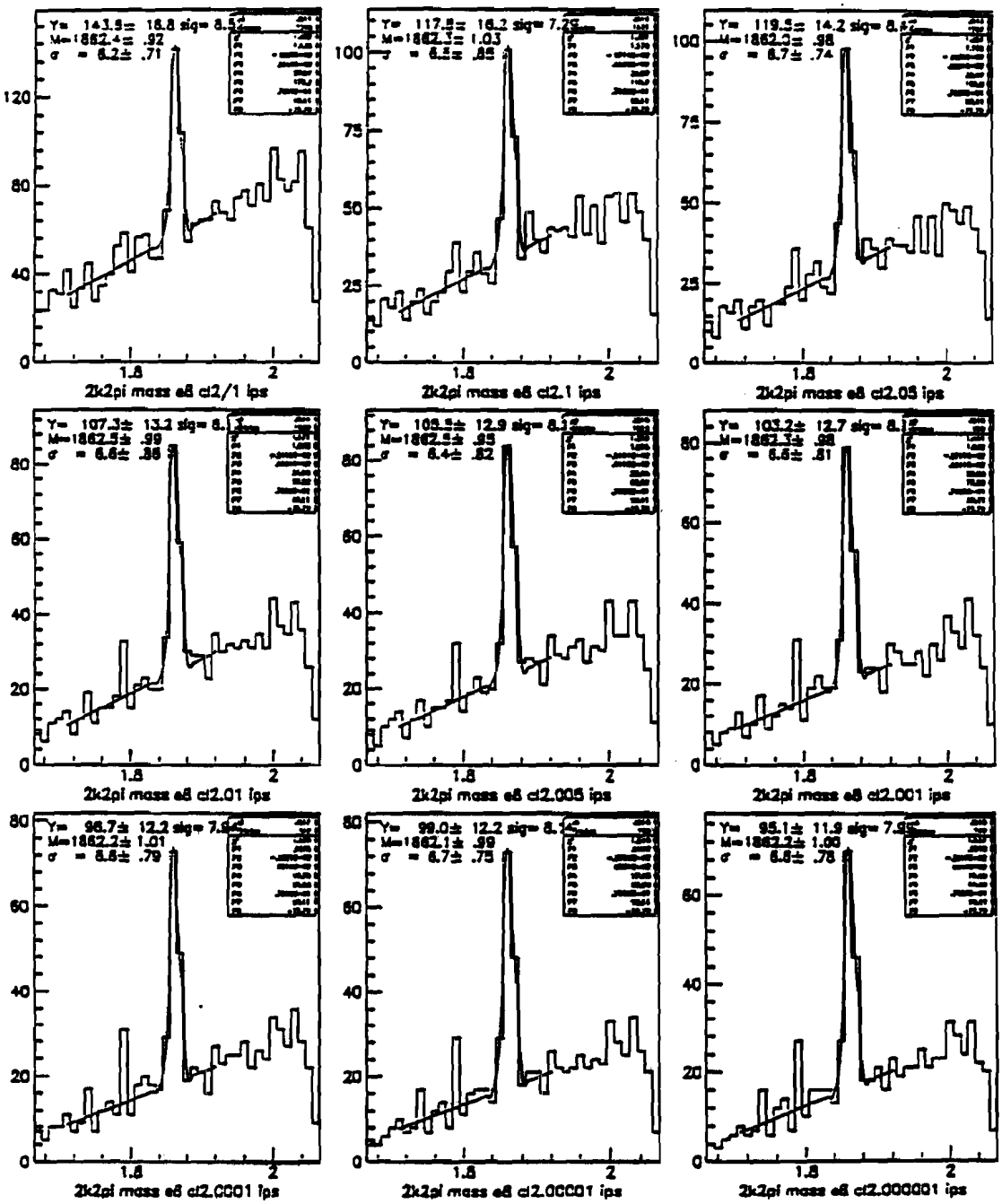

Figure 3.49: Mass plots for systematic study of CL2 for D -> KK$\pi\pi$ decay tight Cerenkov definitions

Table 3.17

cut on CL2	Efficiency with reconsttruction cuts	Efficiency with analysis cuts and loose ISTATP definitions	Efficiency with analysis cuts and medium ISTATP definitions	Efficiency with analysis cuts and tight ISTATP definitions
CL2< 1	6.6%	3.9%	3.10%	1.90%
CL2<0.1	5.5%	3.2%	2.62%	1.62%
CL2<0.05	5.3%	3.1%	2.52%	1.55%
CL2<0.01	4.9%	2.9%	2.34%	1.44%
CL2<0.005	4.8%	2.8%	2.28%	1.40%
CL2<0.001	4.5%	2.7%	2.16%	1.32%
CL2<0.0001	4.2%	2.5%	2.06%	1.27%
CL2<1×10^{-4}	4.0%	2.4%	1.98%	1.22%
CL2<1×10^{-5}	3.9%	2.4%	1.92%	1.19%

branching ratio of 0.034 ± 0.004. I then looked at the variation of the branching ratio as a function of both the elsig and CL2 cut to assess the systematic error. The systematic error from the elsig cut is judged to be 0.0025 (fig 3.50) and the error from the cl2 cut is estimated to be 0.002 (fig 3.51). Comparing these to the branching ratios for the tight Cerenkov cuts (fig 3.52, fig 3.53) we get a systematic error of .003 giving a total systematic error of .004.

3.4.3 $D^0 \to \pi^+ \pi^+ \pi^- \pi^-$

The four π decay mode is similar to the $\pi\,\pi$ decay mode in that to find the signal we must overcome a large combinatoric background and a prominent reflection peak from the Cabibbo favored decay: $D^0 \to K^- \pi^+ \pi^+ \pi^-$. We can attempt to deal with this reflection either by attempting to fit it with a Gaussian peak or to reduce it with tight Cerenkov cuts. Early analysis indicated that since some of the specific distributions of the Cerenkov cuts were not adequately understood and that cutting too tight on the Cerenkov identification could introduce undesirable levels of systematic error. Therefore to compensate we introduced tighter isolation cuts on the secondary vertex in an attempt to further define the MeV of

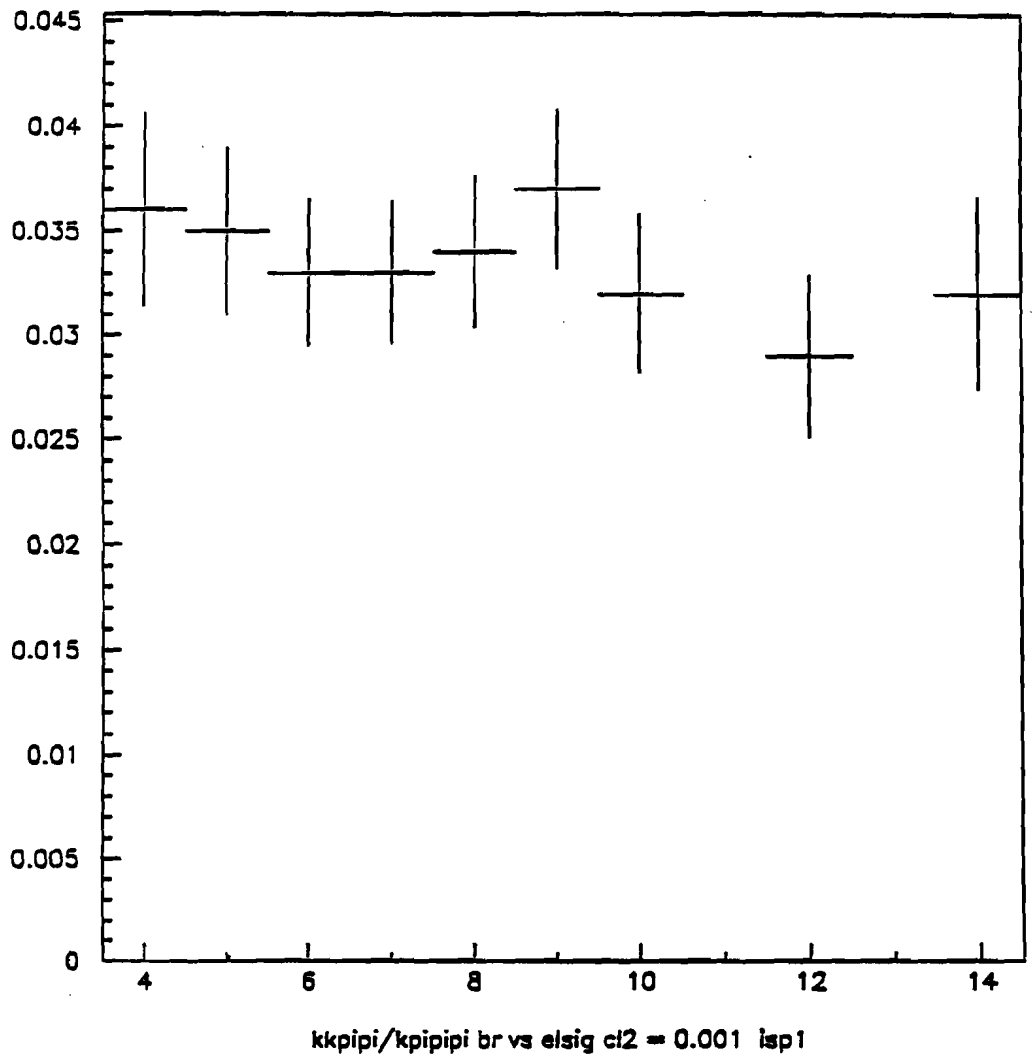

Figure 3.50: Relative branching ratio as a function of L/σ cut for the D -> KKππ decay, loose Cerenkov definition

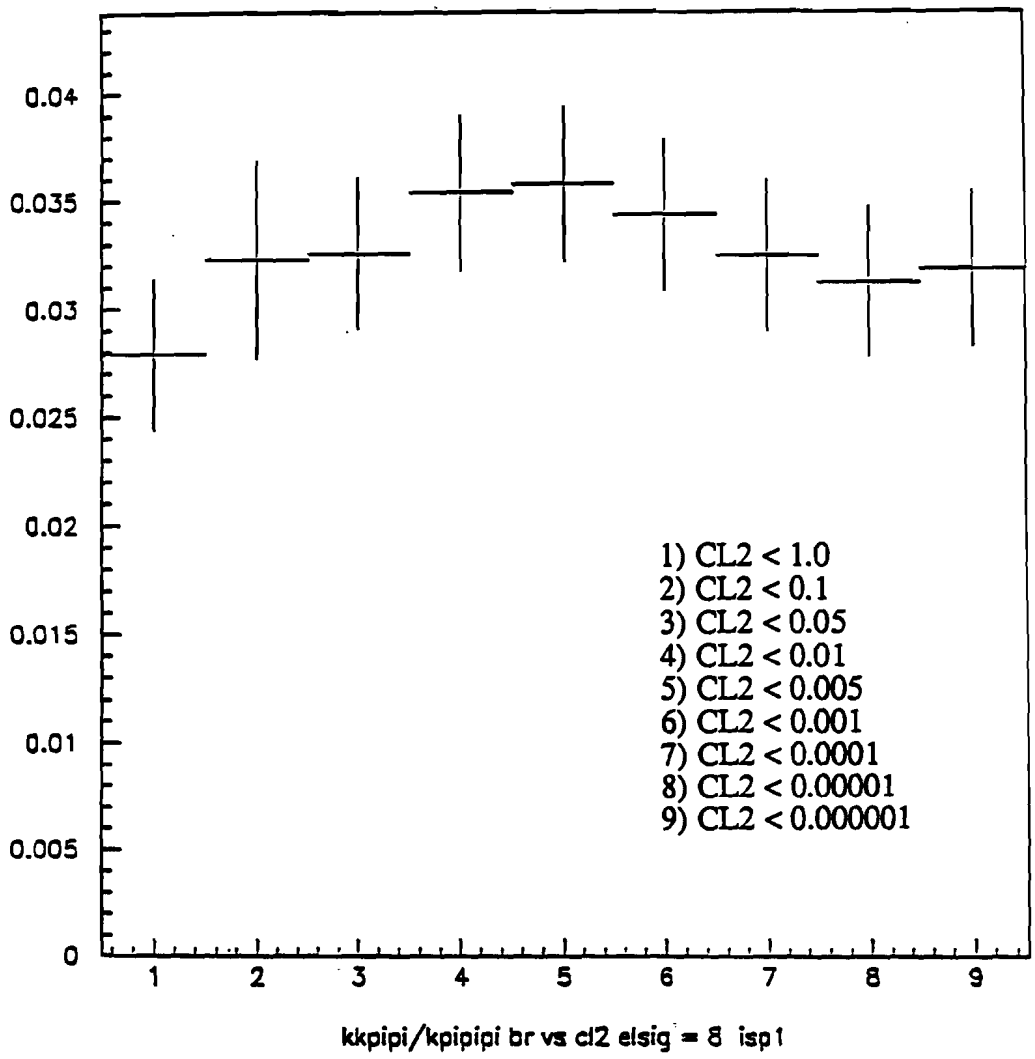

Figure 3.51: Relative branching ratio as a function of CL2 cut for the D -> KK$\pi\pi$ decay, loose Cerenkov definition

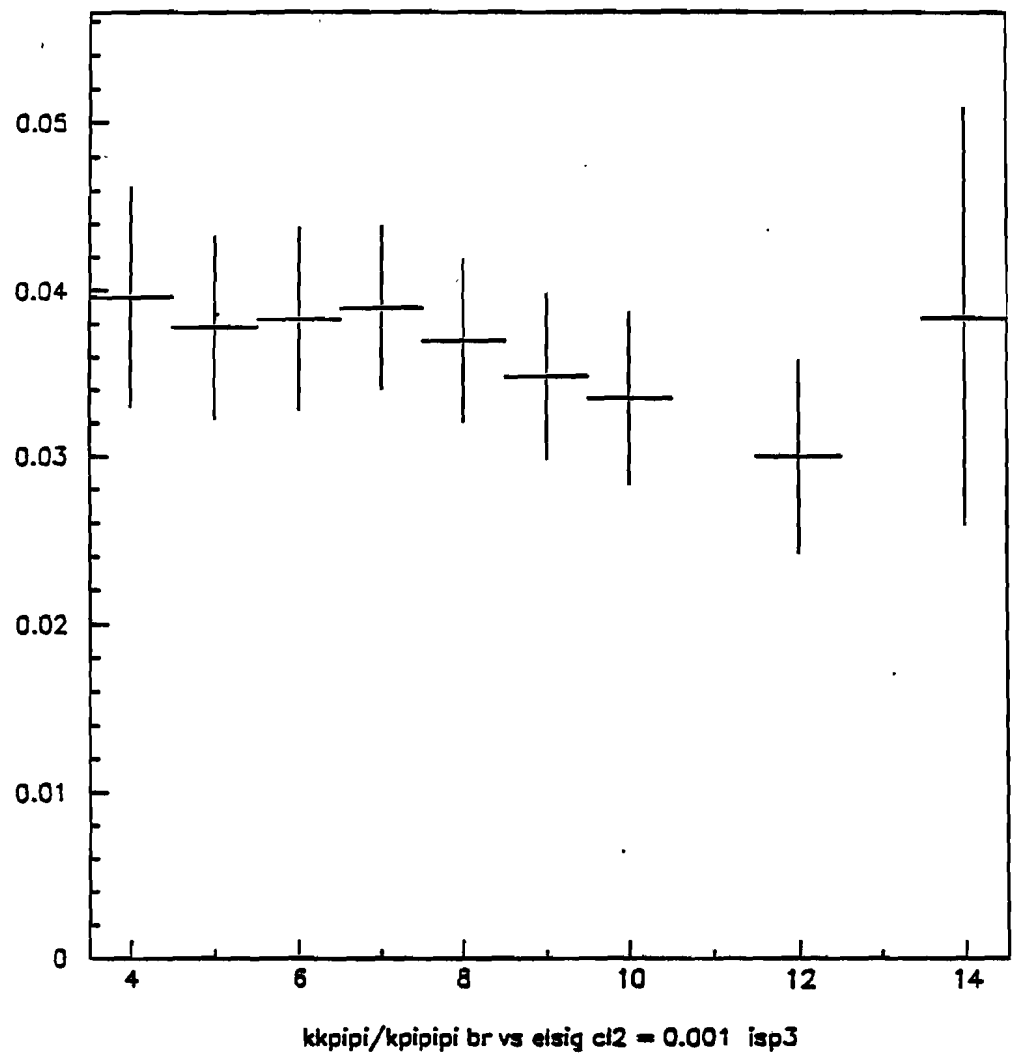

Figure 3.52: Relative branching ratio as a function of L/σ cut for the D -> KKππ decay, tight Cerenkov definition

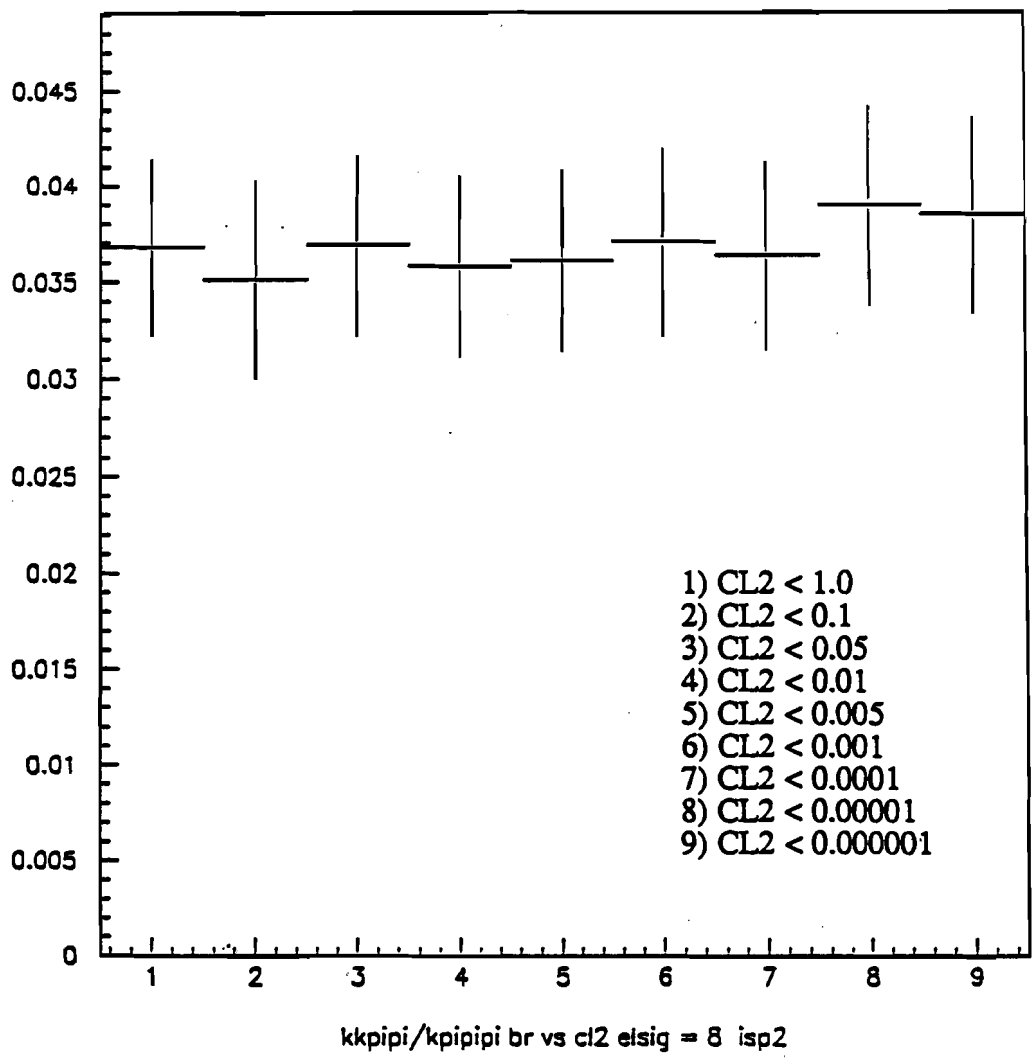

Figure 3.53: Relative branching ratio as a function of CL2 cut for the D -> KK$\pi\pi$ decay, tight Cerenkov definition

reflection peak to aid in its fitting. The final selection of cuts was a significance of detachment cut of greater than 10 and a CL2 cut of 0.005. The efficiencies of these cuts for tight and loose Cerenkov cuts are presented in table 3.18 and the mass plots from the systemic studies are shown (fig. 3.54, 3.55, 3.56, 3.57). The calculation using the loose Cerenkov identification and the above cut gave a branching ratio of 0.103±.0114 for a yield of 156 events. In addition to this calculation we examined the effect of the elsig (fig 3.58, 3.59) and the cl2 (fig 3.60, 3.61) cuts on the systematic errors. These systematic errors were studied for both the loose and tight Cerenkov cuts. We estimated a systematic error from the elsig cut of approximately .008, the systematic error from the CL2 cut of .006 and the systematic error from the Cerenkov cuts of .012 for a combined systematic error of 0.016.

Table 3.18

cut on elsig	Efficiency with reconsttruction cuts	Efficiency with analysis cuts and loose ISTATP definition	Efficiency with analysis cuts and medium ISTATP definition	Efficiency with analysis cuts and tight ISTATP definition
elsig> 4	9.57%	7.13%%	3.85%	2.03%
elsig> 5	7.71%	5.72%	3.03%	1.61%
elsig> 6	6.32%	4.71%	2.48%	1.34%
elsig> 7	5.75%	4.31%	2.25%	1.22%
elsig> 8	5.29%	3.93%	2.05%	1.11%
elsig> 9	4.86%	3.62%	1.86%	1.02%
elsig> 10	4.50%	3.34%	1.71%	0.93%
elsig> 12	3.77%	2.83%	1.42%	0.79%
elsig> 14	3.21%	2.42%	1.20%	0.66%

3.4.5 $D^0 \to K^- K^- K^+ \pi^+$

This state is particularly interesting for a variety of reasons: it has not been measured before and it is on the very edge of the measurable region. Since the D^0 has an invariant mass of 1864.5 MeV, the kaon a mass of 493.6 MeV and the pion a mass of 139.6 MeV one can easily calculate that the available energy or Q value to be 244.1 MeV. This is to be contrasted with the Q value for the $K\pi$ state of 1231.3 MeV or even the $K\pi\pi\pi$ decay which has 952.1

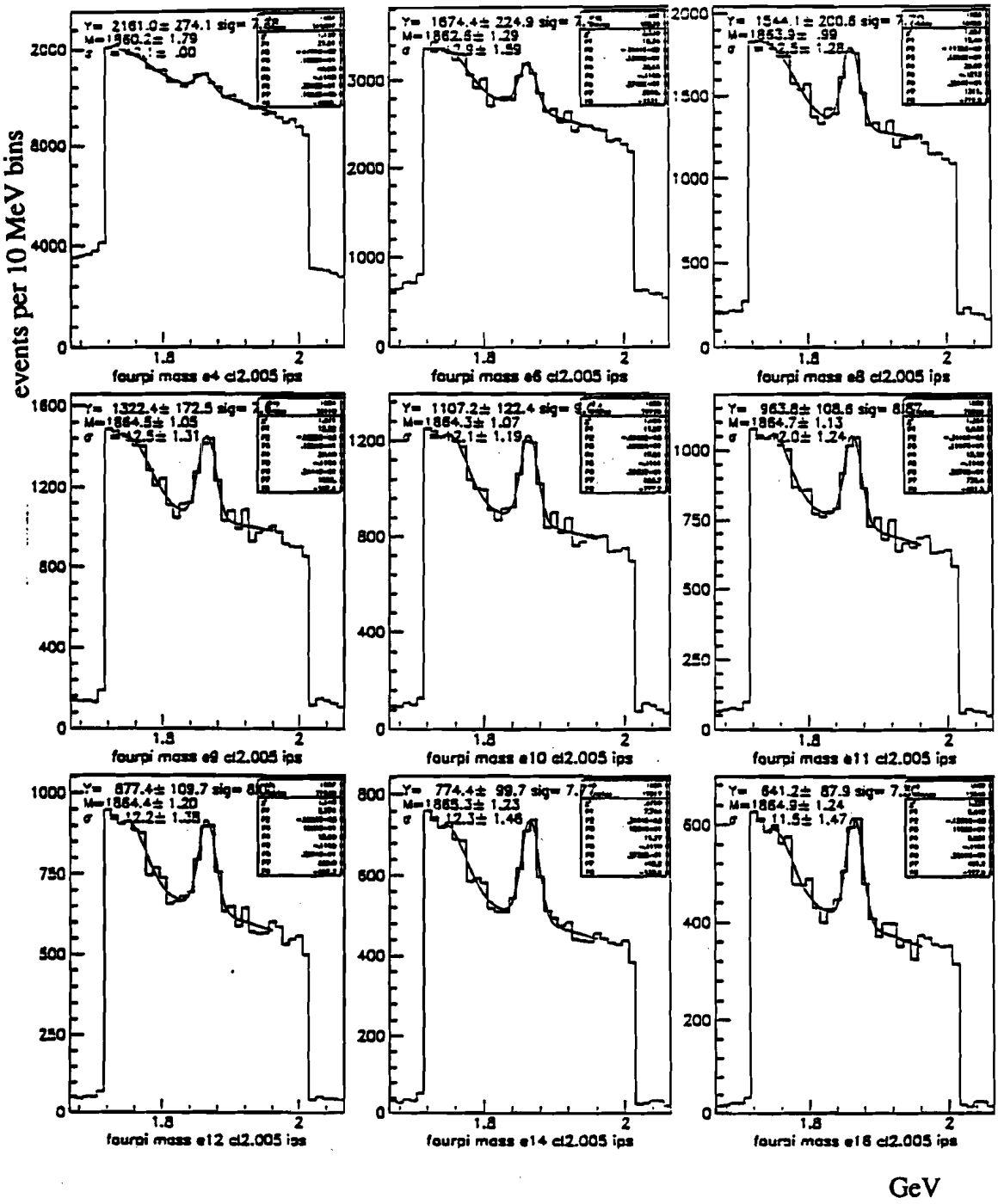

Figure 3.54: Mass plots for systematic study of L/σ for D -> ππππ decay loose Cerenkov definition

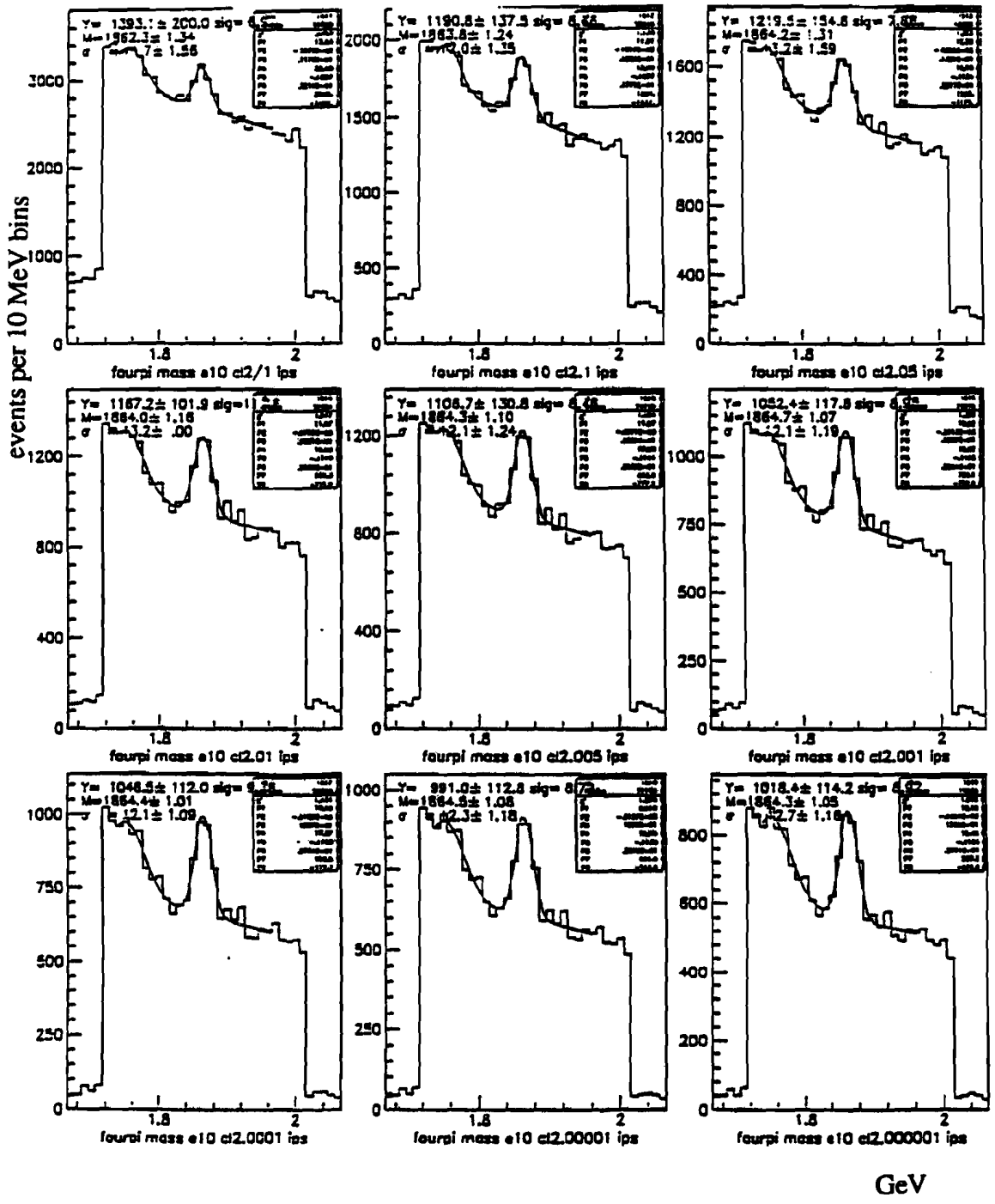

Figure 3.55: Mass plots for systematic study of CL2 for D -> ππππ decay loose Cerenkov definition

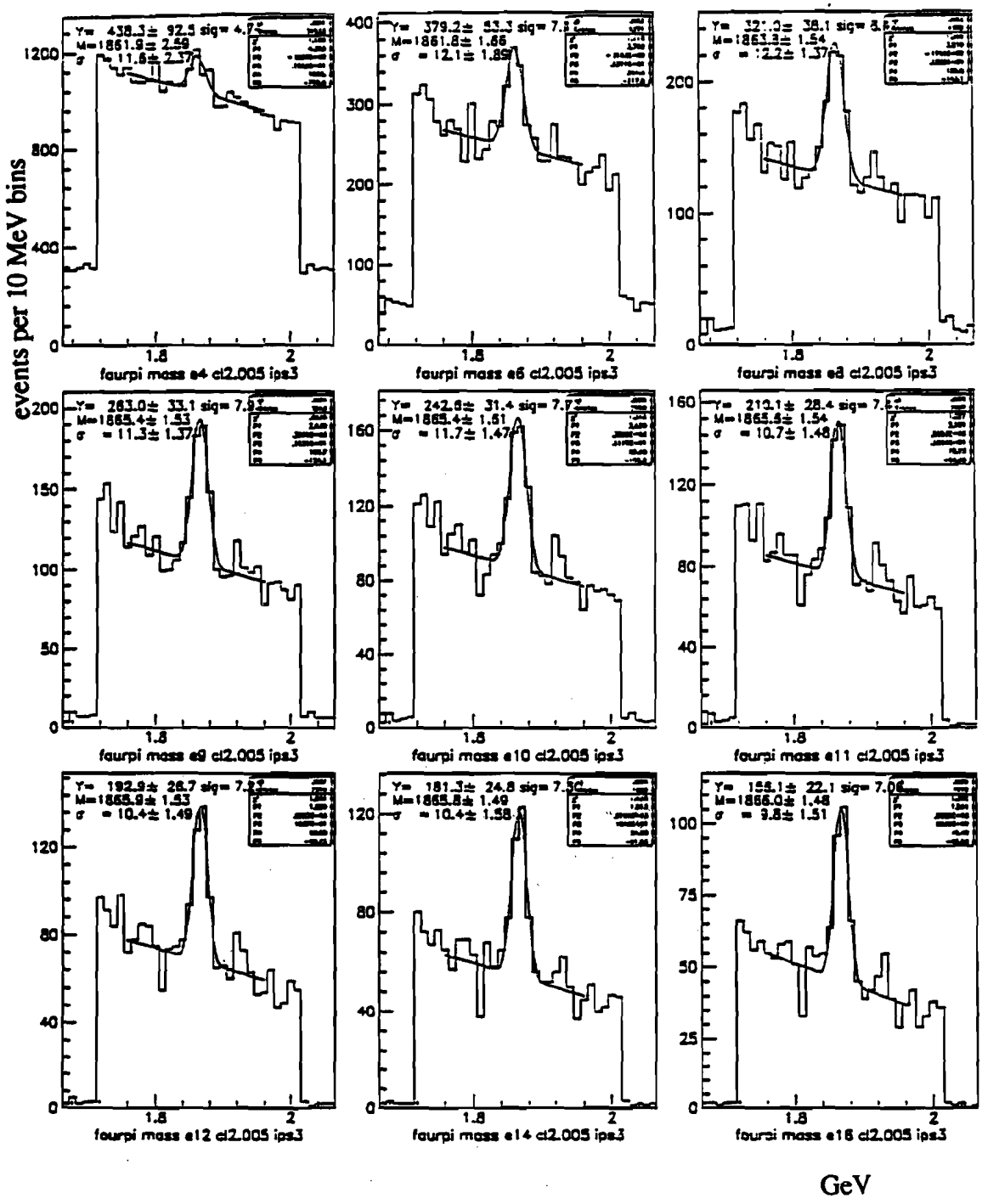

Figure 3.56: Mass plots for systematic study of L/σ for D -> ππππ decay tight Cerenkov definition

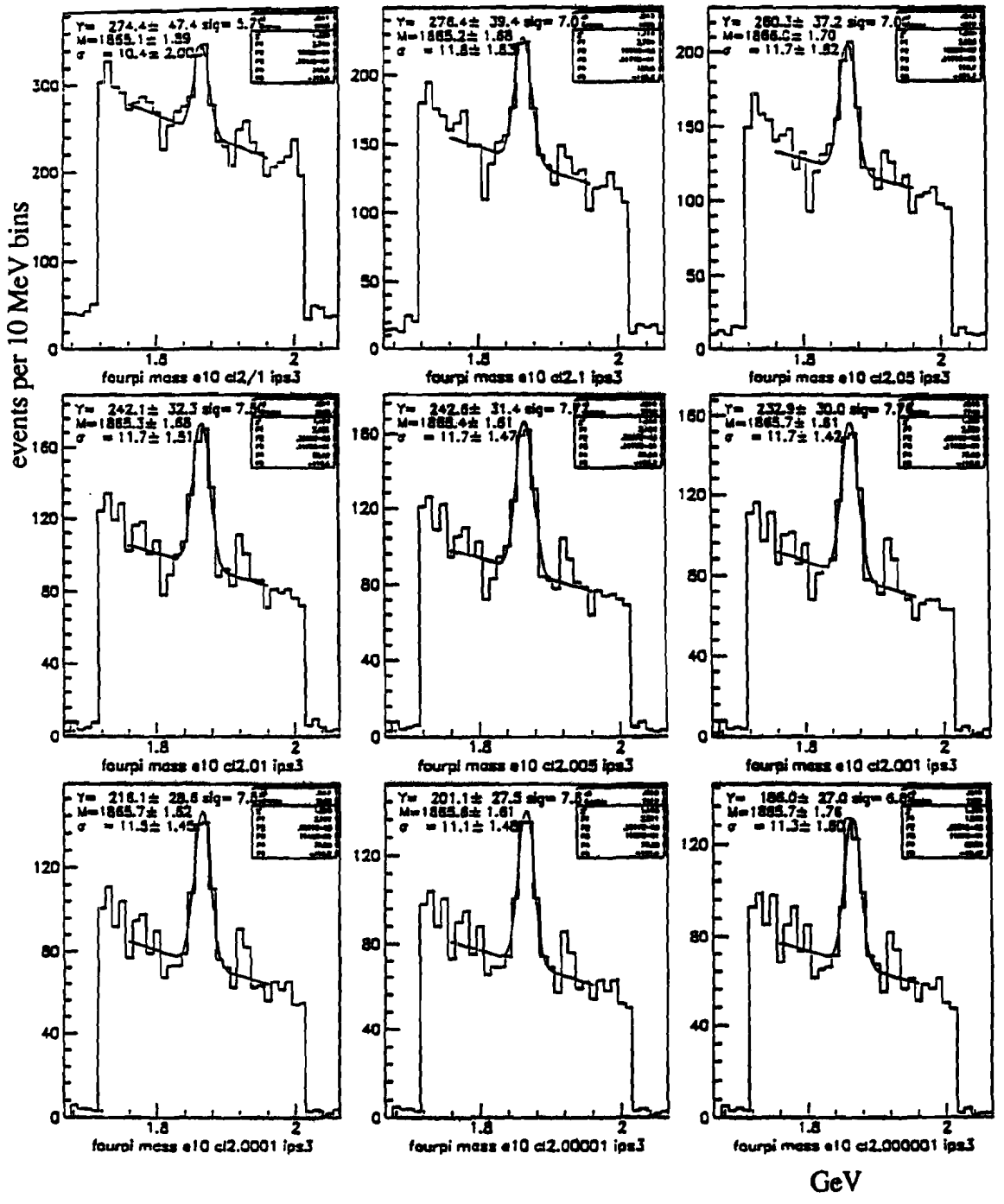

Figure 3.57: Mass plots for systematic study of CL2 for D ->ππππ decay tight Cerenkov definition

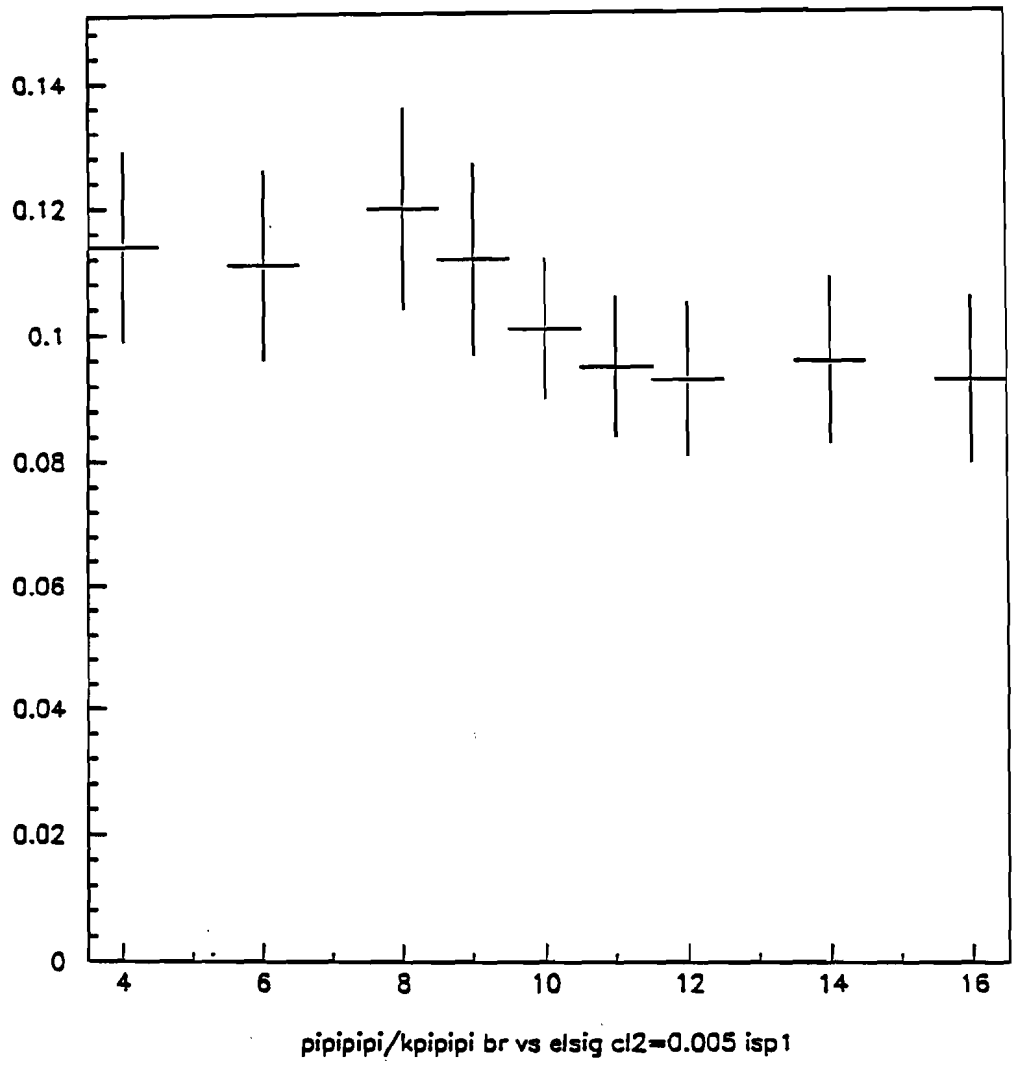

Figure 3.58: Relative branching ratio as a function of L/σ cut for the D ->ππππ decay, loose Cerenkov definition

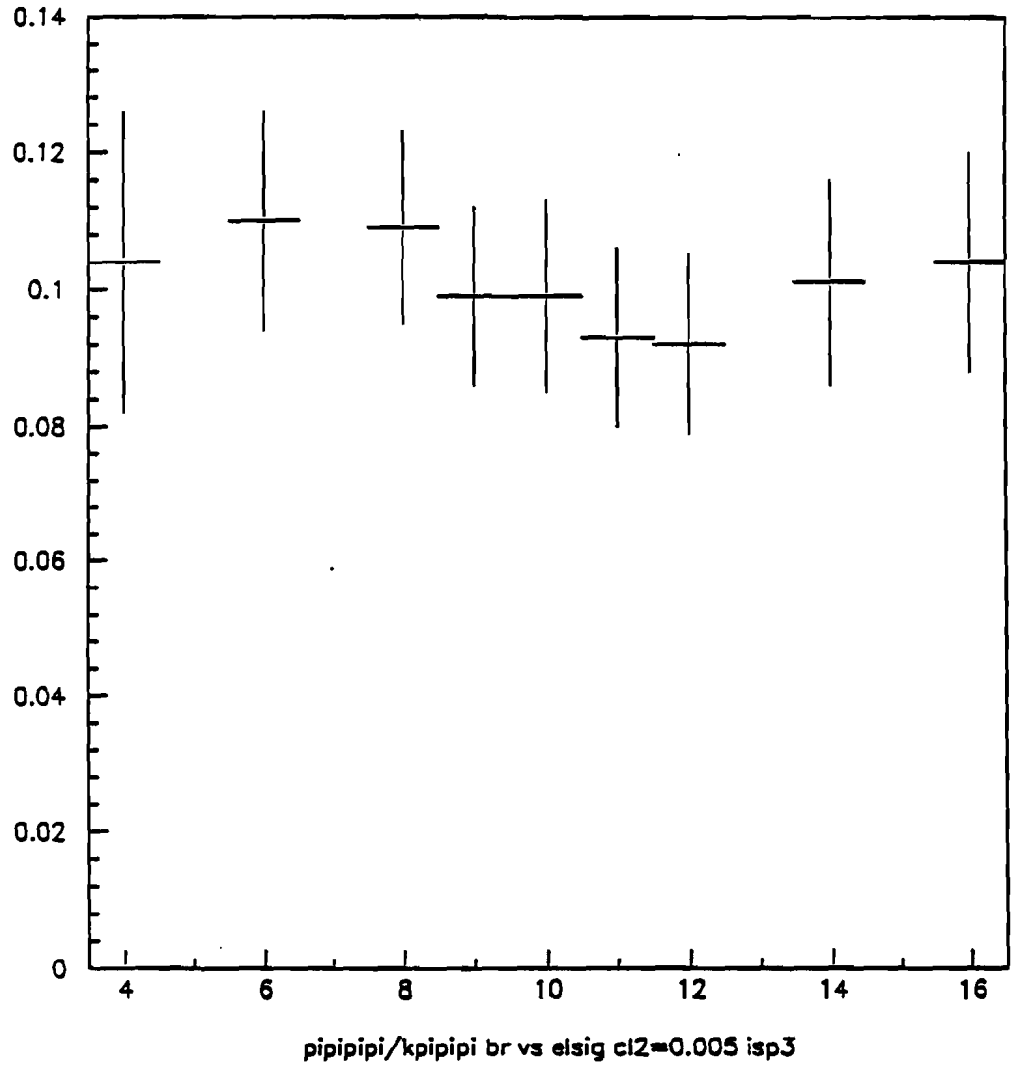

Figure 3.59: Relative branching ratio as a function of L/σ cut for the D ->ππππ decay, tight Cerenkov definition

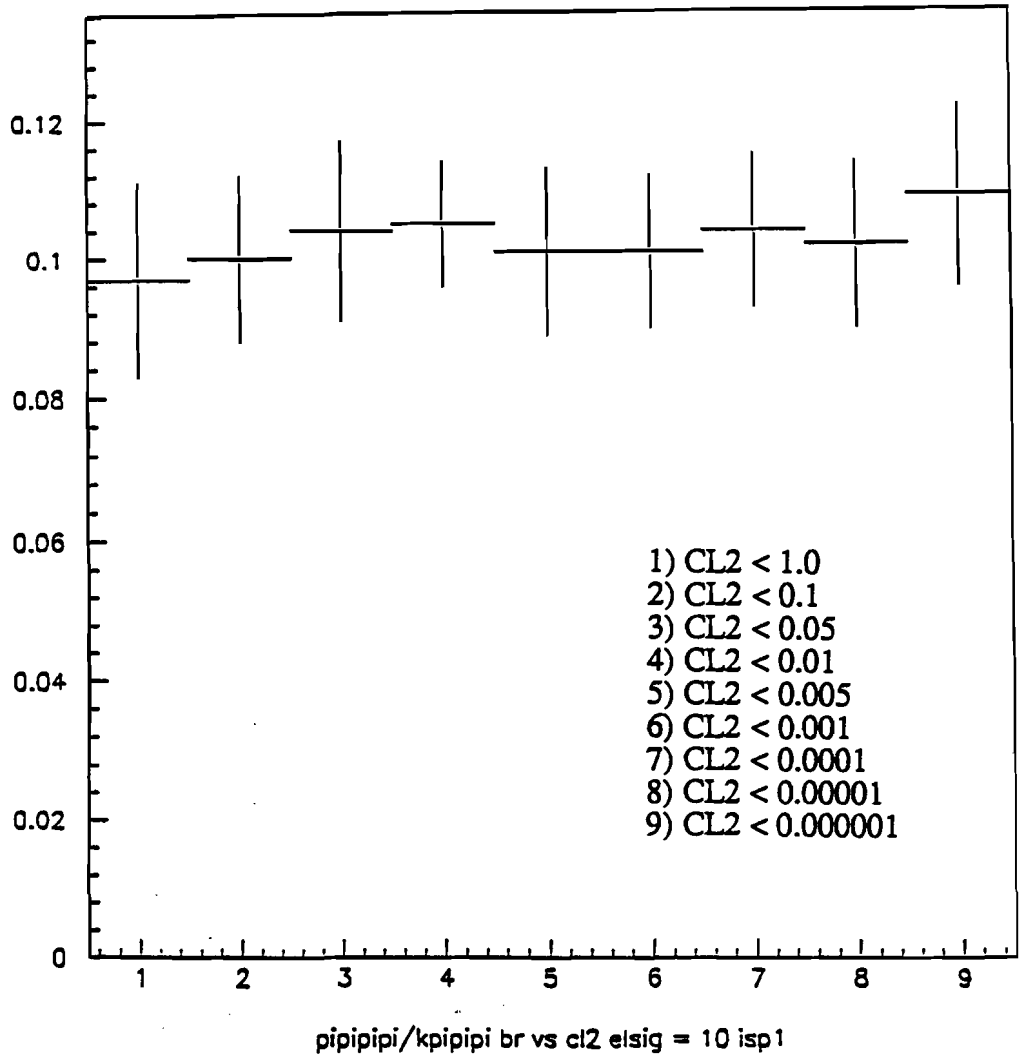

Figure 3.60: Relative branching ratio as a function of CL2 cut for the D ->ππππ decay, loose Cerenkov definition

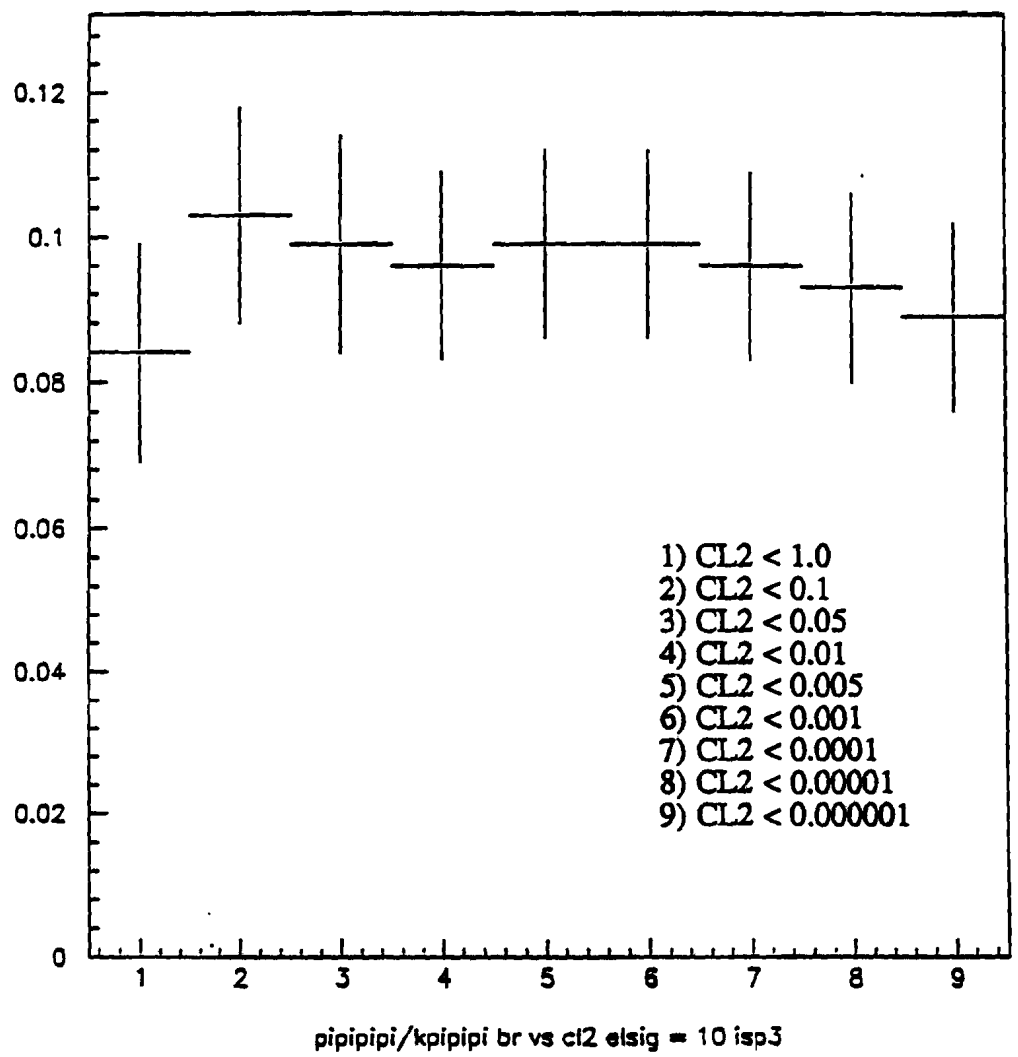

Figure 3.61: Relative branching ratio as a function of CL2 cut for the D ->ππππ decay, tight Cerenkov definition

Table 3.19

cut on CL2	Efficiency with reconstruction cuts	Efficiency with analysis cuts and loose ISTATP definitons	Efficiency with analysis cuts and medium ISTATP definitons	Efficiency with analysis cuts and tight ISTATP definitons
CL2<1	9.57%	5.29%	2.73%	1.50%
CL2<0.1	7.71%	4.33%	2.24%	1.22%
CL2<0.5	6.32%	4.22%	2.19%	1.19%
CL2<0.05	5.75%	4.03%	2.09%	1.14%
CL2<0.01	5.29%	3.93%	2.05%	1.11%
CL2<0.001	4.86%	3.78%	1.97%	1.07%
CL2<1×10^{-3}	4.50%	3.61%	1.89%	1.01%
CL2<1×10^{-4}	3.77%	3.49%	1.83%	0.98%
CL2<1×10^{-5}	3.21%	3.38%	1.77%	0.95%

available energy. As a result we a dealing with a decay mode with a highly restricted phase space. This low Q value also makes measurement of the state very difficult due to the rapidly rising background. The cuts that proved useful in establishing the signal were a tight Cerenkov cut on the pion, defined as ISTATP equals 2 or 3 (pion definite or pion / electron ambiguous), an elsig cut of 6, and an isolation cut on the downstream vertex of less than 0.001. The efficiency of these cuts are presented in Tables 3.20 and 3.21.

Table 3.20

cut on elsig	Efficiencis with reconstruction cuts	Efficiency with analysis cuts and loose ISTATP definitions	Efficiency with analysis cuts and loose ISTATP definitions	Efficiency with analysis cuts and loose ISTATP definitions
elsig>2	7.0%	4.8%	4.45%	2.60%
elsig>3	5.7%	3.9%	3.65%	2.21%
elsig>4	4.7%	3.2%	3.02%	1.85%
elsig>5	3.9%	2.7%	2.54%	1.58%
elsig>6	3.3%	4.3%	2.14%	1.35%
elsig>7	2.7%	1.9%	1.80%	1.15%
elsig>8	2.3%	1.6%	1.51%	0.98%
elsig>9	2.0%	1.4%	1.28%	0.85%
elsig>10	1.7%	1.2%	1.10%	0.73%

Table 3.21

cut on CL2	Efficiency with reconstruction cuts	Efficiency with analysis cuts and loose ISTATP definitions	Efficiency with analysis cuts and loose ISTATP definitions	Efficiency with analysis cuts and loose ISTATP definitions
CL2<1	7.05%	3.25%	3.02%	1.91%
CL2<0.1	5.95%	2.72%	2.54%	1.59%
CL2<0.5	5.70%	2.64%	2.46%	1.55%
CL2<0.01	5.02%	2.46%	2.29%	1.45%
CL2<0.05	5.00%	2.40%	2.24%	2.41%
CL2<0.001	4.75%	2.28%	2.13%	1.35%
CL2<0.0001	4.36%	2.14%	2.01%	2.27%
CL2<1×10^{-4}	4.12%	2.05%	1.92%	1.41%
CL2<1×10^{-5}	3.92%	1.98%	1.85%	1.16%

These cuts gave a signal of 11.6 ± 4.12 events for a branching ratio of 0.0047 ± 0.0017. I then looked at varying the cuts to determine the systematic errors (fig 3.62, 3.63, 3.64, 3.65). I found that for the elsig cut (fig 3.66) there was a systematic error of approximately 0.0005, for the cl2 (fig3.67) cut an error of 0.0004 and for the Cerenkov cuts a rather large systematic error of 0.0015 for a combined systematic error of 0.00174.

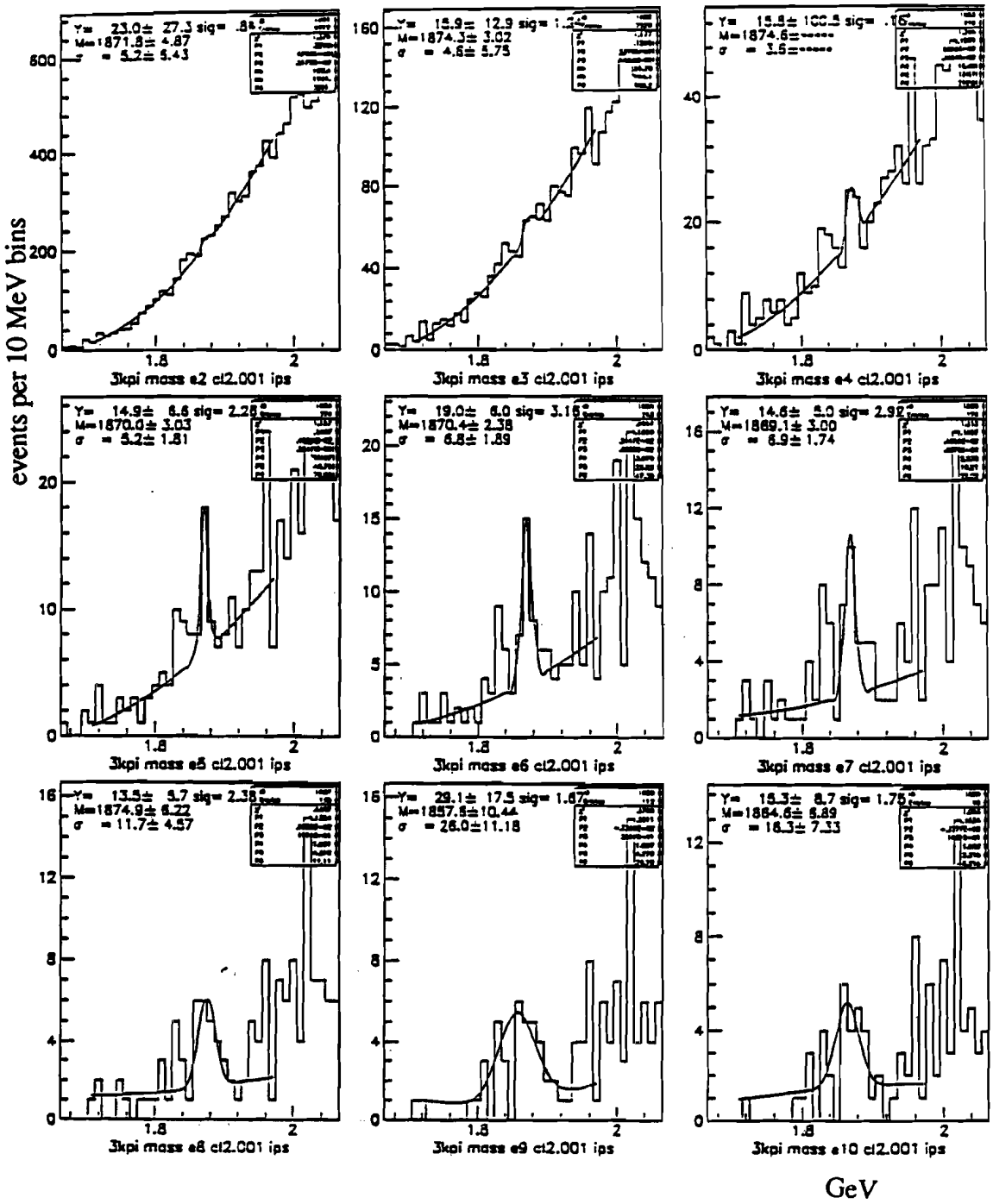

Figure 3.62: Mass plots for systematic study of L/σ for D -> KKKπ decay loose Cerenkov definition

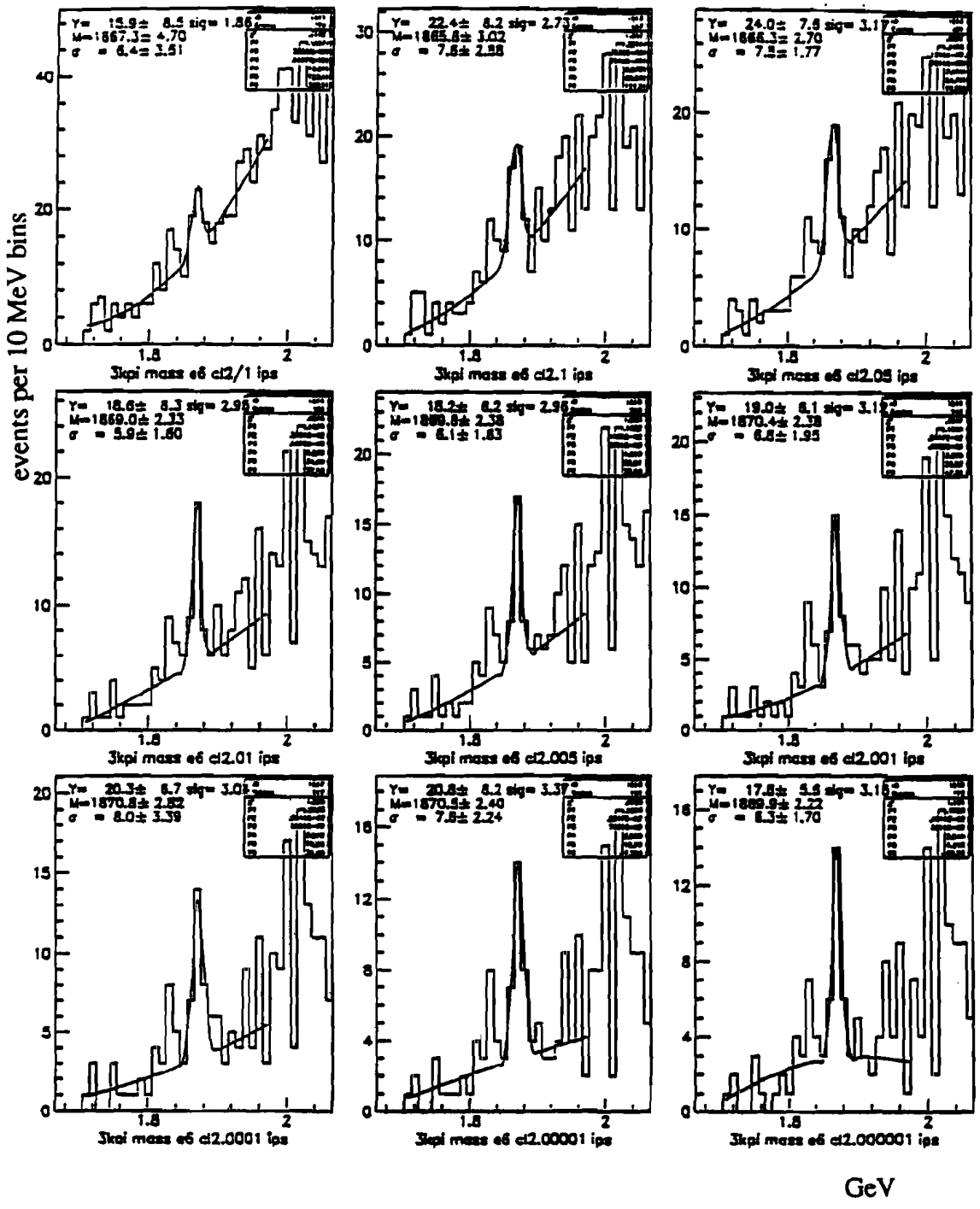

Figure 3.63: Mass plots for systematic study of CL2 for D -> KKKπ decay loose Cerenkov definition

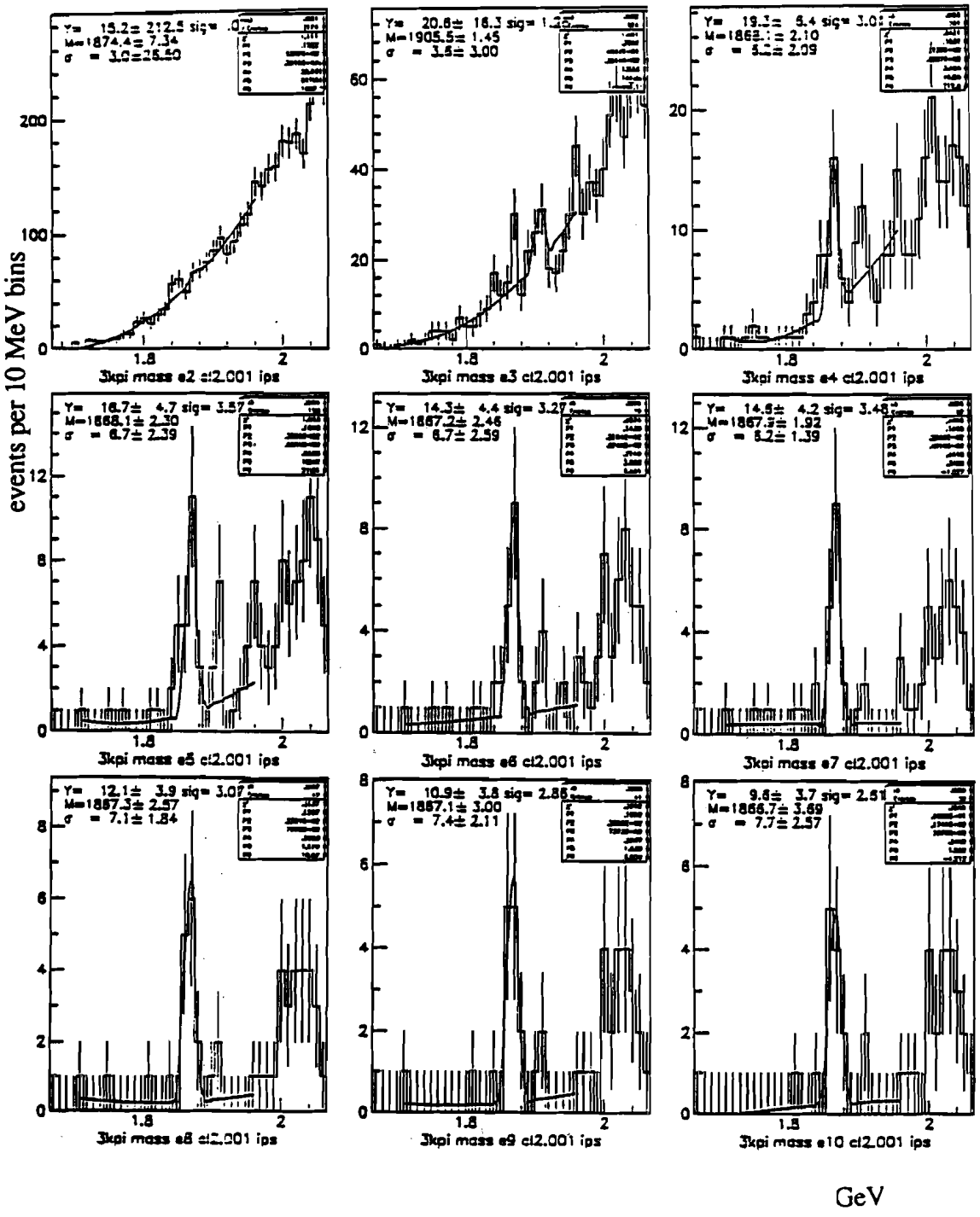

Figure 3.64: Mass plots for systematic study of L/σ for D -> KKKπ decay tight Cerenkov definition

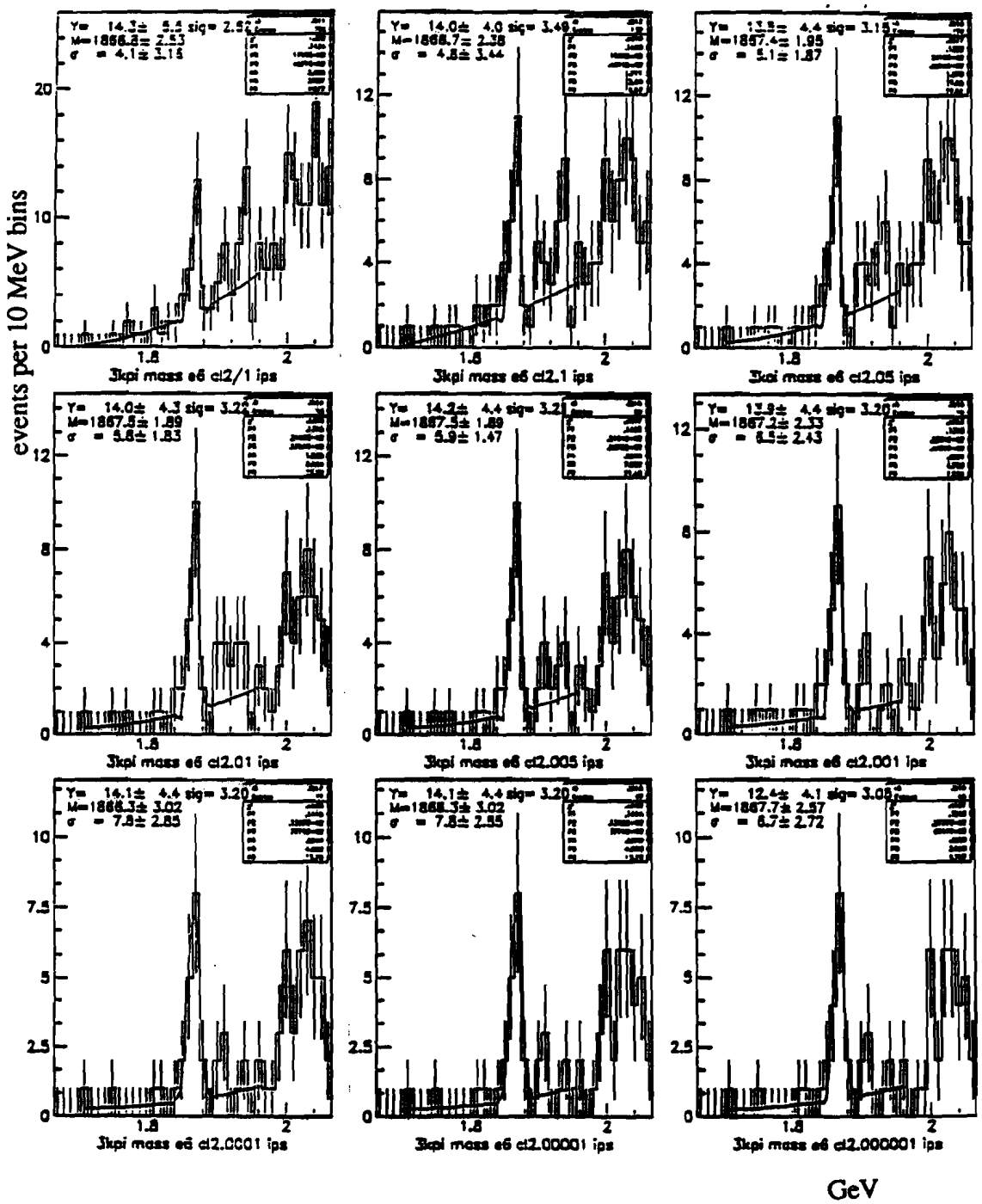

Figure 3.65: Mass plots for systematic study of CL2 for D -> KKKπ decay tight Cerenkov definition

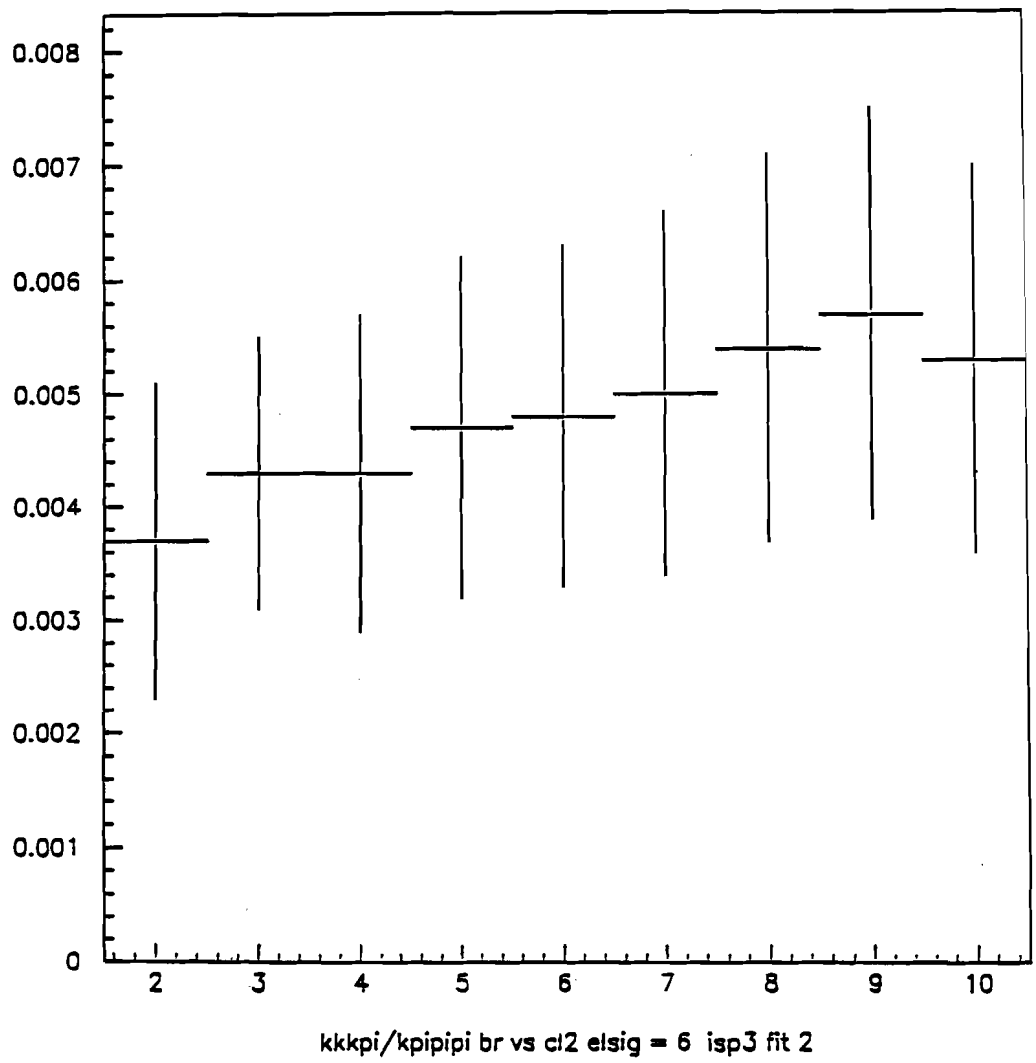

Figure 3.66: Relative branching ratio as a function of L/σ cut for the D ->KKKπ decay,tight Cerenkov definition

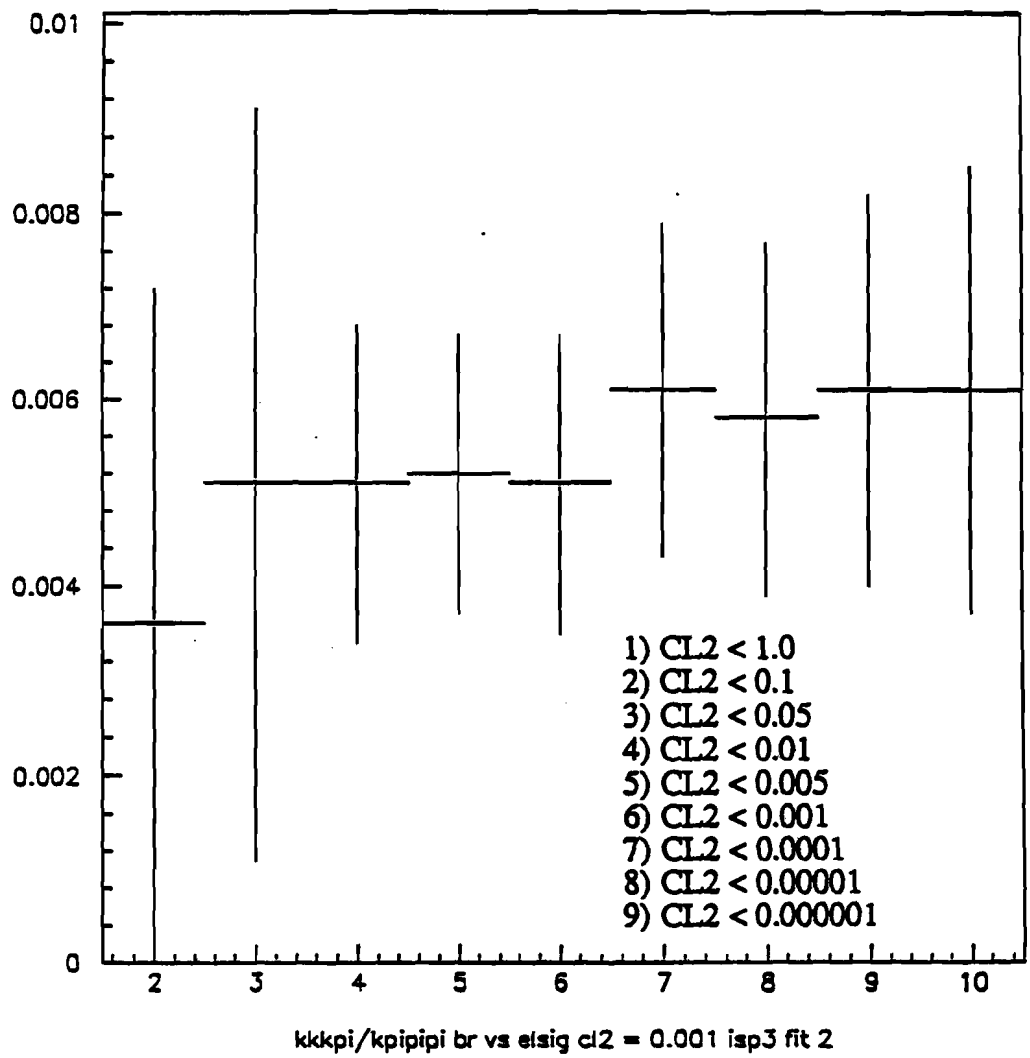

Figure 3.67: Relative branching ratio as a function of CL2 cut for the D ->KKKπ decay,tight Cerenkov definition

CHAPTER 4:

RESULTS AND CONCLUSIONS

As discussed in the last chapter, this analysis involved the measurement of five branching ratios of decay modes of the neutral D meson. These measurements, based on a common data set and analysis are useful for theoretical comparison. Before we compare the data with theoretical expectations we first compare it to the current world average values [4] (Table 4.1) and other experimental results in the following sections.

Table 4.1

Decay Ratio	This Analysis	World Average
$D^o \to \pi\pi / K\pi$	$0.0456 \pm .008 \pm .008$	$0.045 \pm .005$
$D^o \to K K / K\pi$	$0.104 \pm .0075 \pm .0045$	$0.113 \pm .007$
$D^o \to \pi\pi\pi\pi / K\pi\pi\pi$	$0.103 \pm .0114 \pm .013$	$0.100 \pm .011$
$D^o \to K K\pi\pi / K\pi\pi\pi$	$0.034 \pm .0043 \pm .0032$	$0.032 \pm .005$
$D^0 \to K KK\pi / K\pi\pi\pi$	$0.0047 \pm .00167 \pm .00174$	Not Measured

$D^o \to \pi^+ \pi^- / D^o \to K^- \pi^+$

This branching ratio, along with the KK final state were the first Cabibbo suppressed charm meson decays to be measured. This relative branching ratio was found by Mark II [8] to be 0.033 ± 0.015. Since then it has been measured and published in five other experiments [9] [23] [24] [25] [26], all of which have good agreement of the value with respect to each other. The total world sample before this measurement was 326 events. This measurement

increases that sample by about 50%. A summary of these measurements are given in Table 4.2. A graphical representation of branching ratio comparison is also given in figure 4.1

Table 4.2

Experiment	value	# events	type of experiment	
MRK II	0.033 ± 0.015		$e^+ e^-$	3.77GeV
MRK III	0.033 ± 0.010	39	$e^+ e^-$	3.77GeV
CLEO	0.050.± 0.007	110	$e^+ e^-$	10.5 GeV
ARGUS	0.040 ± 0.007	57	$e^+ e^-$	10 GeV
E691	0.055 ± 0.008	120	photoproduction	
WA82	0.048 ± 0.013			
World Average	0.045 ± 0.005	326		
This Analysis	0.046 ± 0.007	151	photoproduction	

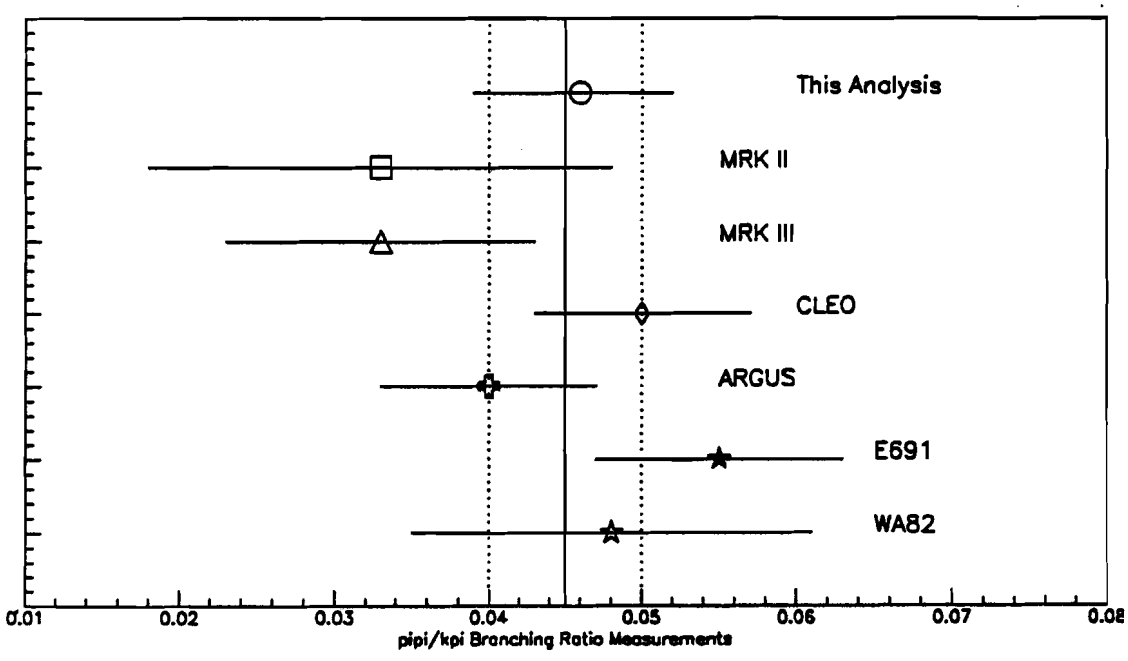

Figure 4.1: Comparison of $\pi\pi$ relative branching ratio to previous measurements

$D^o \to K^+ K^- / D^o \to K^- \pi^+$

This relative branching ratio was found by Mark II to be 0.113 ± 0.030. Since then it has been measured and published by eight other experiments, the six that measured the $\pi\pi$

branching ratio above and CERN experiment NA14 []and it was measured in the first run of E687 [27] The total world sample before this measurement was 880 events. This new measurement of 611 events increases the total by about 75% A summary of these measurements are given in Table 4.3. The graphical comparison of these measurements also given. (fig 4.2)

Table 4.3

Experiment	value	# events	type of experiment	
MRK 2	0.113 ± 0.030		$e^+ e^-$	3.77GeV
MRK 3	0.122 ± 0.018	118	$e^+ e^-$	3.77GeV
CLEO	0.117 ± 0.010	249	$e^+ e^-$	10.5 GeV
ARGUS	0.10 ± 0.02	131	$e^+ e^-$	10 GeV
E691	0.107 ± 0.009	193	photoproduction	
NA14	0.16 ± 0.05	34	photoproduction	
WA82	0.107 ± 0.029			
E687 (87-88)	0.138 ± 0.027	155	photoproduction	
World Average	0.113 ± 0.007	880		
This Analysis	0.104 ± 0.0075	611	photoproduction	

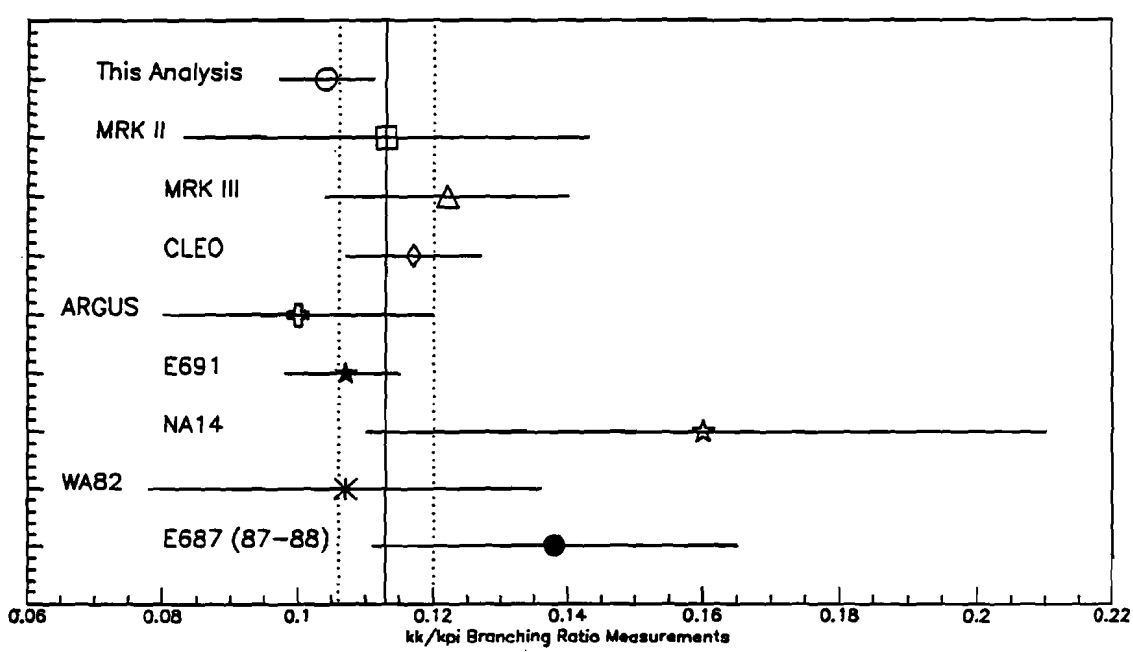

Figure 4.2: Comparison of KK relative branching ratio to previous measurements

$D^0 \to \pi^+\pi^+\pi^-\pi^-$ / $D^0 \to K^-\pi^+\pi^+\pi^-$

Although the absolute branching ratio of D^0 to four pions has been measured by Mark III [28], Hybrid [29], and ACCMOR [30], all of these measurements have been of very low statistical significance. The relative branching ratios by E691 [31] CLEO [32], E687, and WA82 have been much more precise. The experimental values of the relative branching ratios as well as the world average are presented in Table 4.4. A graphical comparison of these relative branching ratios is also presented. (fig 4.3)

Table 4.4

Experiment	value	# events	type of experiment
CLEO	0.102.± 0.013	345	$e^+ e^-$ 10.5 GeV
E691	0.096 ± 0.018	66	photoproduction
WA82	0.115 ± 0.023		
E687 (87-88)	0.108 ± 0.024	79	
World Average	0.100.± 0.011	490	
This Analysis	0.103.± 0.011	1106	photoproduction

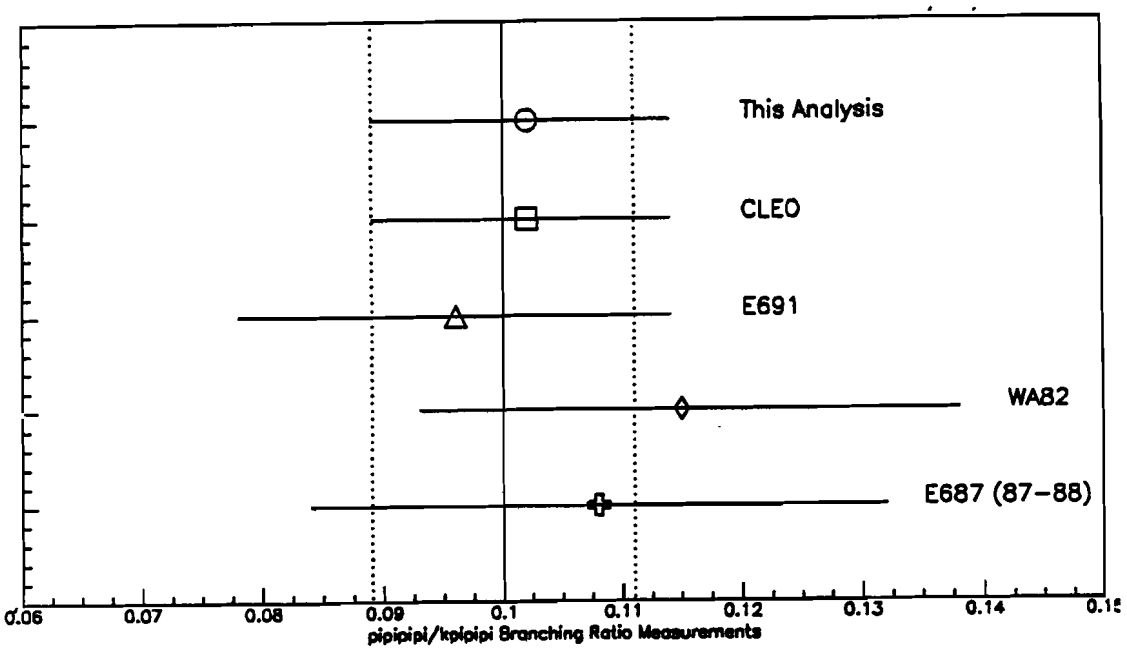

Figure 4.3: Comparison of $\pi\pi\pi\pi$ relative branching ratio to previous measurements

$D^o \to K^+ K^- \pi^+ \pi^- / D^o \to K^- \pi^+ \pi^+ \pi^-$

As with the four pion relative branching ratio above, CLEO and E691, are the only prior experiments to publish results for the $D^o \to K^+ K^- \pi^+ \pi^-$ relative branching ratio. ACCMOR [29] has published an absolute branching ratio of 0.0028 ± 0.0009. Using the world average of 0.075 ± 0.006 for the $D^o \to K^- \pi^+ \pi^+ \pi^-$ we get a value of 0.037 ± 0.012 for the relative branching ratio. We will include this number in our table for completeness. The branching ratios from Table 4.5, as well as the relative number derived from the ACCMOR absolute branching ratio are also presented graphically. (fig 4.4)

Table 4.5

Experiment	value	# events	type of experiment
CLEO	0.0314 ± 0.010	89	$e^+ e^-$ 10.5 GeV
E691	0.028 ± 0.008		photoproduction
ACCMOR	$0.037. \pm 0.012$		
World Average	$0.029. \pm 0.006$		
World Fit	0.032 ± 0.005		
This Analysis	0.034 ± 0.0043	243	photoproduction

$D^o \to K^+ K^- K^- \pi^+ / D^o \to K^- \pi^+ \pi^+ \pi^-$

No prior experiment has published a branching ratio measurement, relative or absolute, for this decay mode. The number we report here is of relatively low statistics and significant additional work needs to be done. Currently, a follow up experiment to E687, E831, has been approved for the next fixed target run at Fermi lab. This state should be a good candidate for further exploration due to the obvious improvements that can be made with higher statistics.

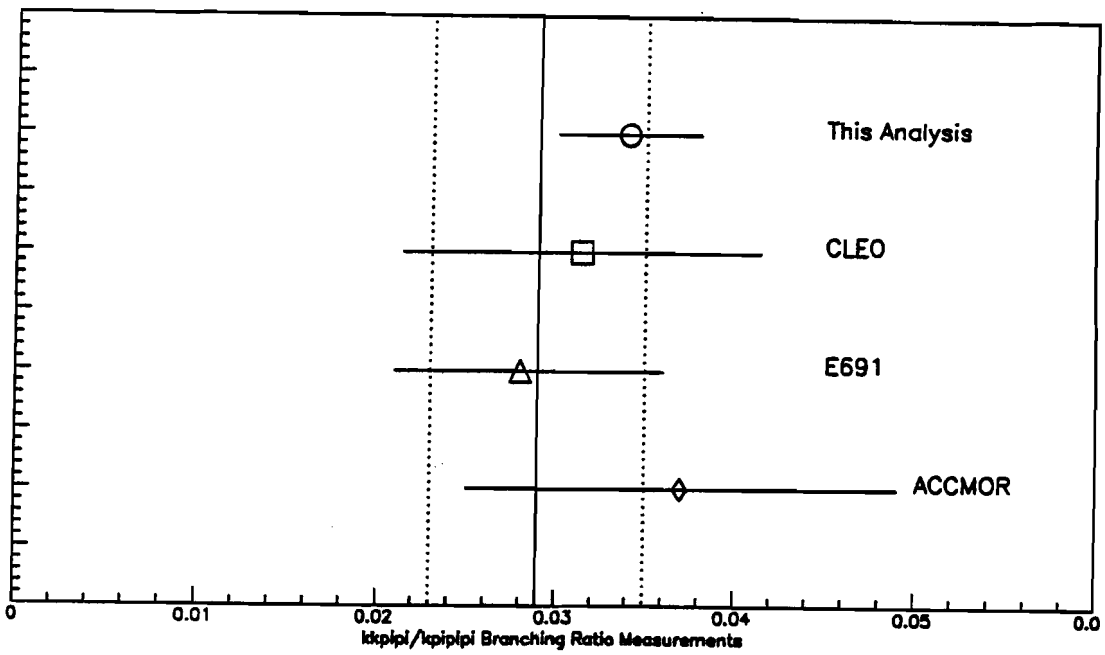

Figure 4.4: Comparison of $KK\pi\pi$ relative branching ratio to previous measurements

$D^0 \to K^+ K^- / D^0 \to \pi^+ \pi^-$

This measurement, talked about after the results of Mark II and Mark III, has been of significant theoretical discussion. As I discussed in the first chapter, there are a number of possible mechanisms by which this number might vary from unity, none fully satisfactory. Actual measurements of this number were published by CLEO, ARGUS and E691. There is a significant variance in the results of the three experiments. The results from these experiments, as well as our result are presented in Table 4.6 and graphically (fig 4.5)

Table 4.6

Experiment	value	type of experiment	
CLEO	2.35.$\pm$0.37	$e^+ e^-$	10.5 GeV
ARGUS	2.5 $\pm$0.7	$e^+ e^-$	10 GeV
E691	1.95 $\pm$0.34	photoproduction	
WA82	2.23 $\pm$0.81		
This Analysis	2.28 $\pm$0.38	photoproduction	

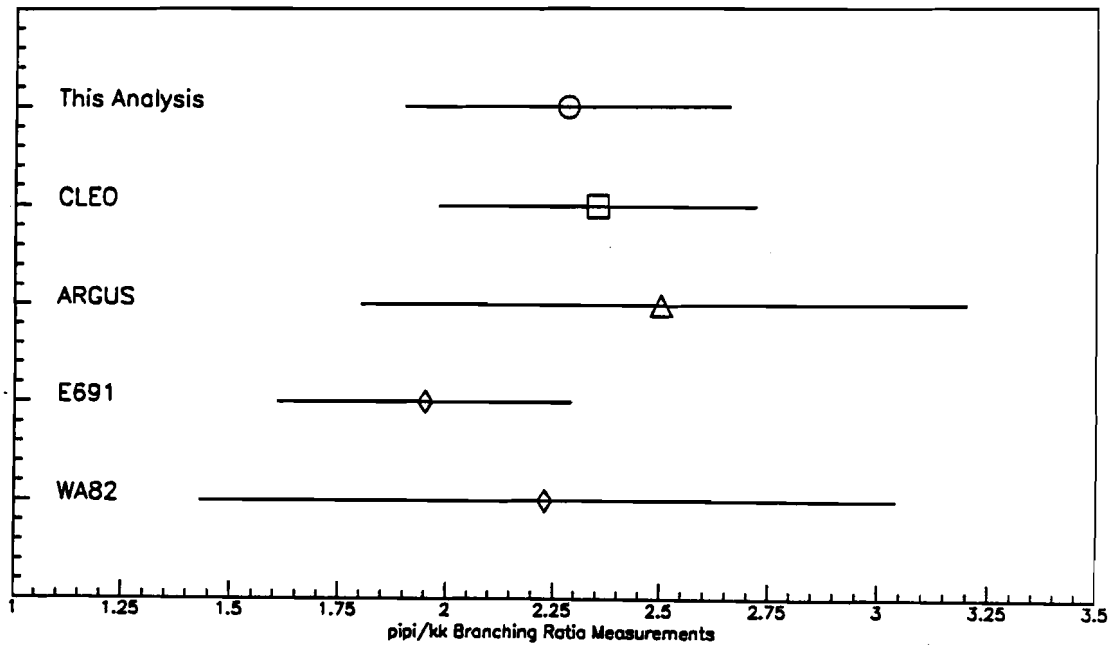

Figure 4.5: Comparison of KK / $\pi\pi$ relative branching ratio to previous measurements

Conclusions

This analysis should be useful in expanding the range of theoretical predictions for the charm meson states. With a large data set there is obviously a great deal of additional analysis that can be performed. The first would be a cp. violation measurement using the D^* tagged D^0 -> K^+K^- sample. In addition there are a variety of resonance substructure measurements that can be implemented on the four body states that were measured for this analysis. Significant advances have been accomplished by E687 due to its tracking, vertex detection and particle identification. As stated above, E831 has been approved for the next fixed target run at Fermi Lab. The expectation if that there will be an order of magnitude improvement in statistics as well as a significant increase in the detection capabilities of the spectrometer.. One interesting measurement is,

$$BR\left(\frac{D^0 \to K^+ + K^- + X}{D^0 \to pi^+ + pi^- + X}\right) .$$

Where X is any combination of charged or neutral pions, charged or neutral kaons. The initial results from this analysis, while far from conclusive, are consistent with the idea the KK/ $\pi\pi$ branching ratio number is not unity simply because the $\pi\pi$ decay state has more available energy to 'pull quark/anti-quark pairs out of the vacuum'. Thus even though the two Cabibbo suppressed decays may go at the same rate the $\pi\pi$ decay is simply more likely to have additional particles. As one can see, there is a significant amount of work left to be done before the mechanisms of charm meson decays are understood. This will surely afford continued and interesting analysis opportunities.

APPENDIX 1:

THE R-CUT

As stated in the main text of this dissertation the R cut is a fractional momentum cut on two body decay states. The general form of the R cut is,

$$cut_{low} < \frac{p_1}{p_1 + p_2} < cut_{high}$$

where cut_{high} is 1-cut_{low} and the cut is usually just expressed by denoting the high cut but understanding that this is actually a symmetric cut.

In discussing this cut we will look at two levels of justification. The first is the empirical level. Namely, this variable acts substantially different for signal events than it does for background events. Since we are able to achieve a relatively clean invariant mass distribution for the Kpi decay of the D^0 meson with out imposing an R cut we will use this signal to examine the behavior of the R variable. The signal that is used was achieved by imposing a significance of detachment cut of greater than 8, an isolation of the primary vertex of less than five percent and an isolation of the secondary vertex cut of less than one percent. The invariant mass is presented in figure A1. Next we can define the signal region as between 1.850 and 1.880 GeV/c^2 and the background region as less than 1.815 and greater than 1.915 GeV/c^2. If we now look at the distribution of the R variable for these two regions (fig. A2),

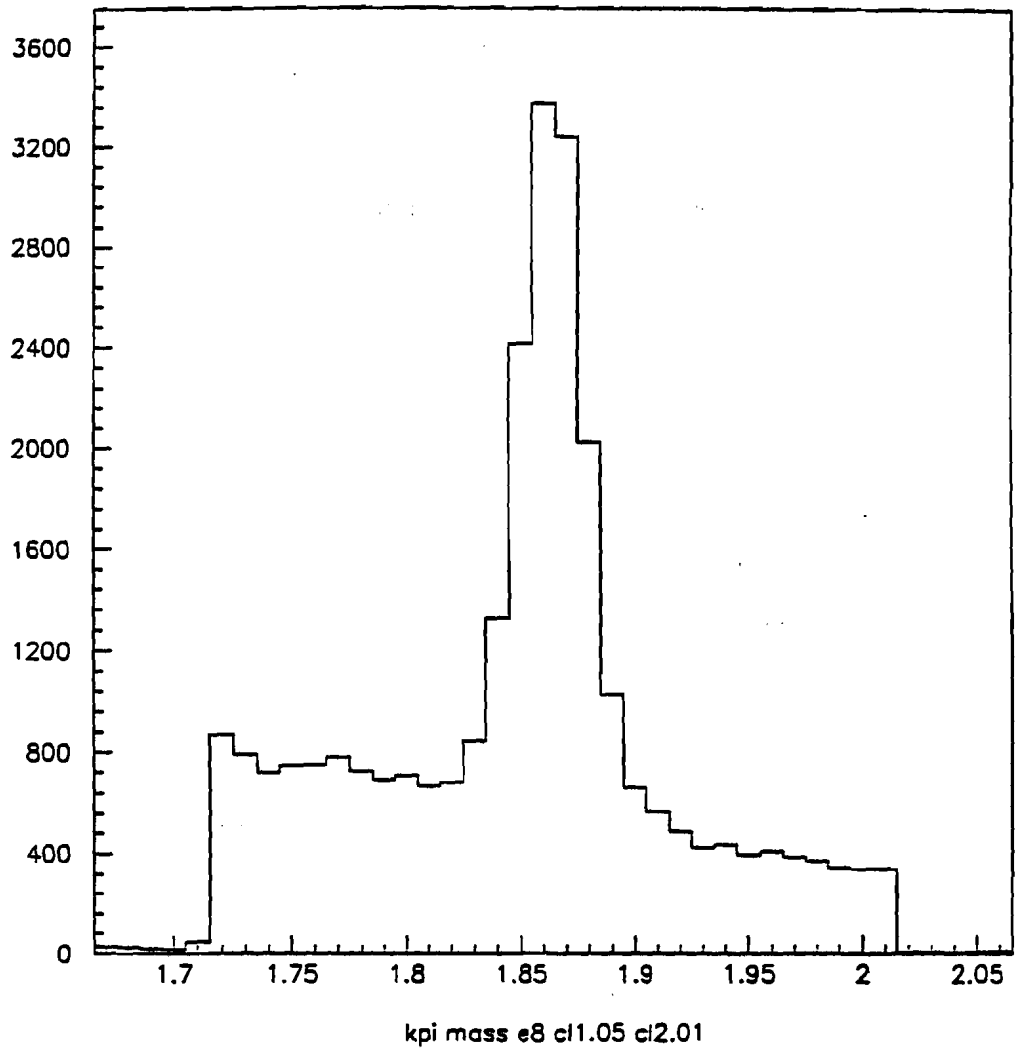

Figure A1: Invariant Mass plot used for R variable studies

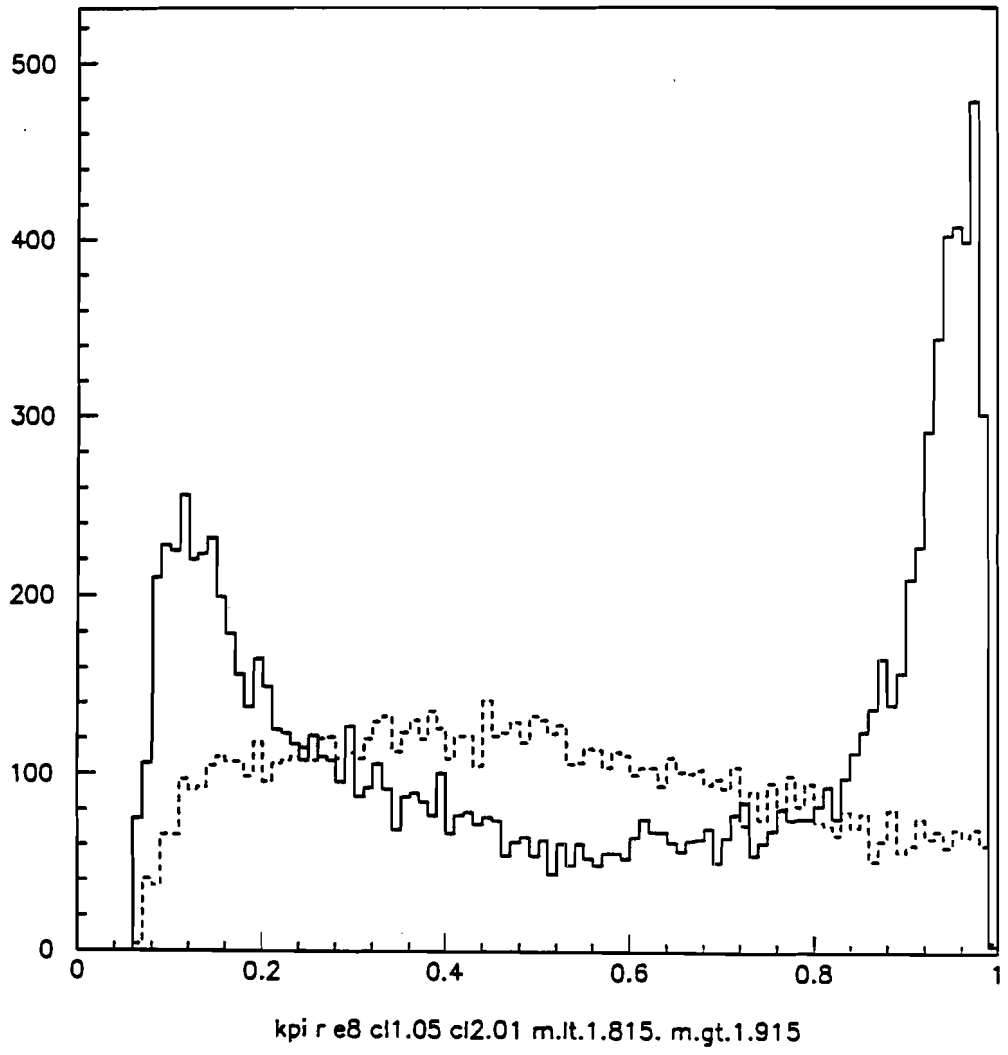

Figure A2: R distribution for background (solid line) and signal (dotted line)

where the background region is represented with the solid line and the signal region is represented with the dotted line, we see that the behavior is in fact very different between the two regions. The background region is highly peaked at high and low values of R and the signal region is relatively flat over the range of R with a slight peaking in the middle. Although this difference is enough to draw our attention to the variable we generally would not like to use a variable without understanding the reason for its behavior.

We will first look at the behavior of the signal region. It was hypothesized that the signal region may be comparatively flat due to the nature of the decay. In our case a pseudo scalar decaying into two other pseudo scalars. It is known that this particular type of decay will generate an isotropic distribution in the rest frame of the parent particle. Obviously if the decay is isotropic in the center of mass we can look at the distribution about any axis we choose. The two main axis of choice would either be the direction of parent particle or the direction of the incident beam particle, in our case the photon. Measuring from these axis gives the "Helicity" angle and the "Jackson Theta" angle respectively. It is know that the cosine of each of these angle is flat for an isotropic distribution. Since our experiment has a large lorentz boost the helicity and Jackson Theta angles are very close. For ease of calculation I chose the Jackson theta angle. The cosine of the Jackson theta angle for the background and signal regions are presented in figure A3, the background region is represented by the solid line and the signal region by the dotted line. Noticing the similarities in the shapes between the R variable and the cos Jackson theta variable I decided to do a scatter plot for the background and signal regions. These scatter plots are figures A4 and A5 respectively. As one can see there is an approximate linear transformation between the cos Jackson theta and the R variable. This explains the flatness of the signal region. The next task is to explain the peaking of the background region.

To explain the peaking of the background region we will start with the equation for the relativistic invariant mass,

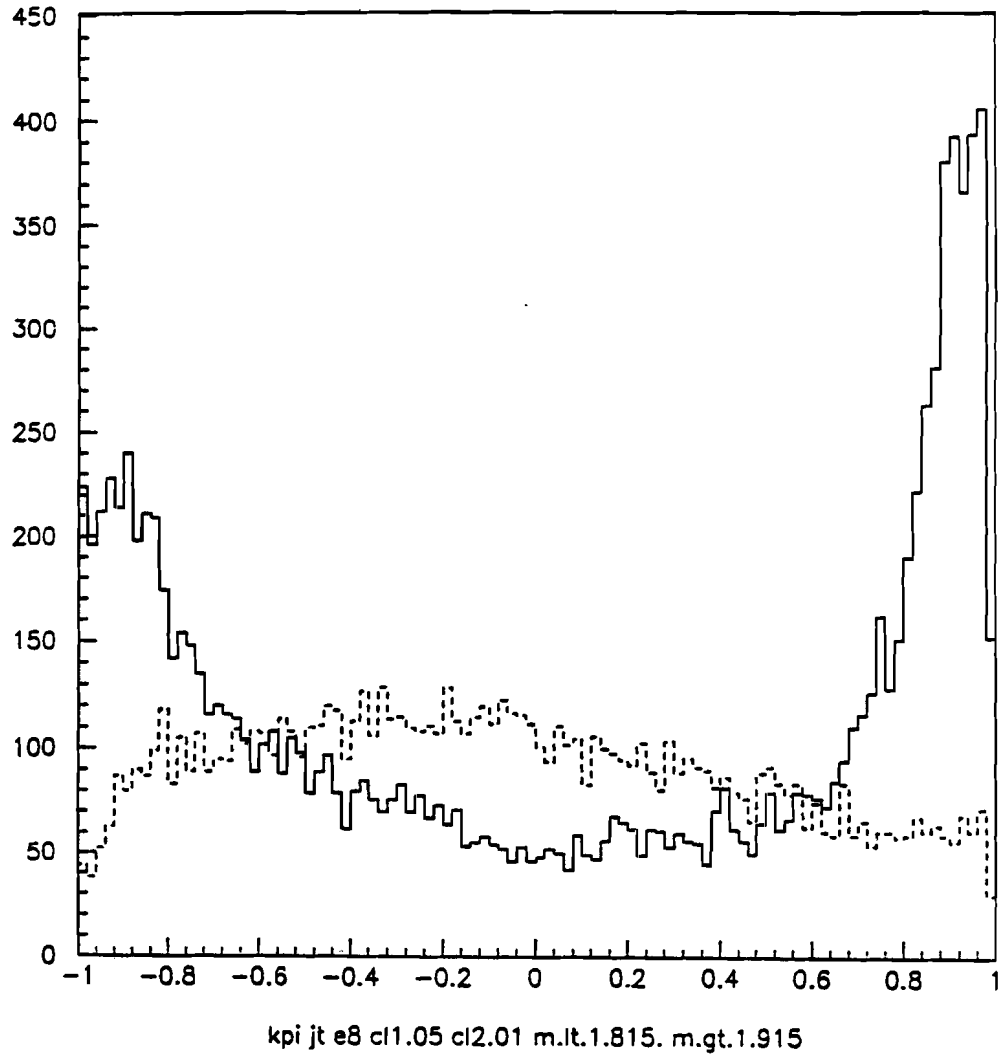

Figure A3: Cosine Jackson Theta Distribution for background (solid line) and signal (dotted line)

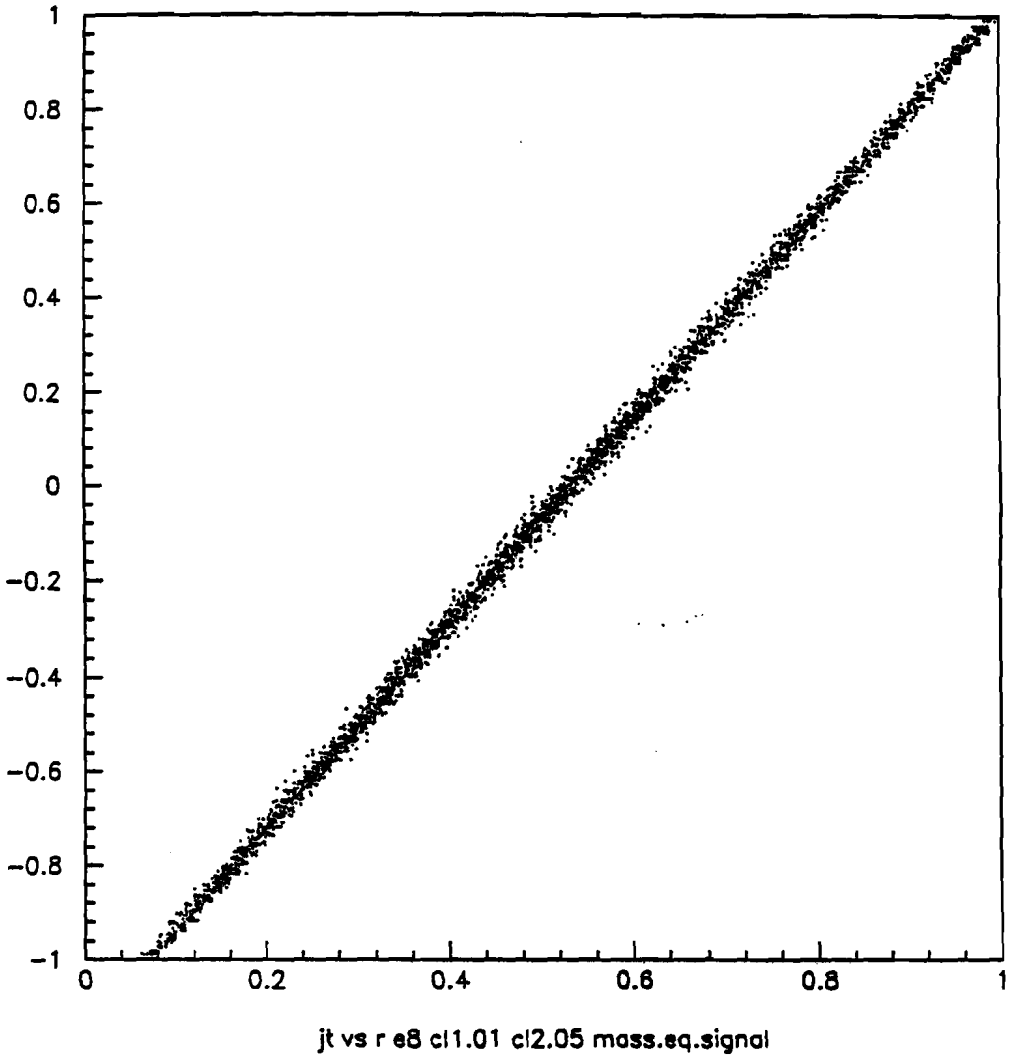

Figure A4: Scatter plot of Cosine Jackson Theta versus R for the signal region

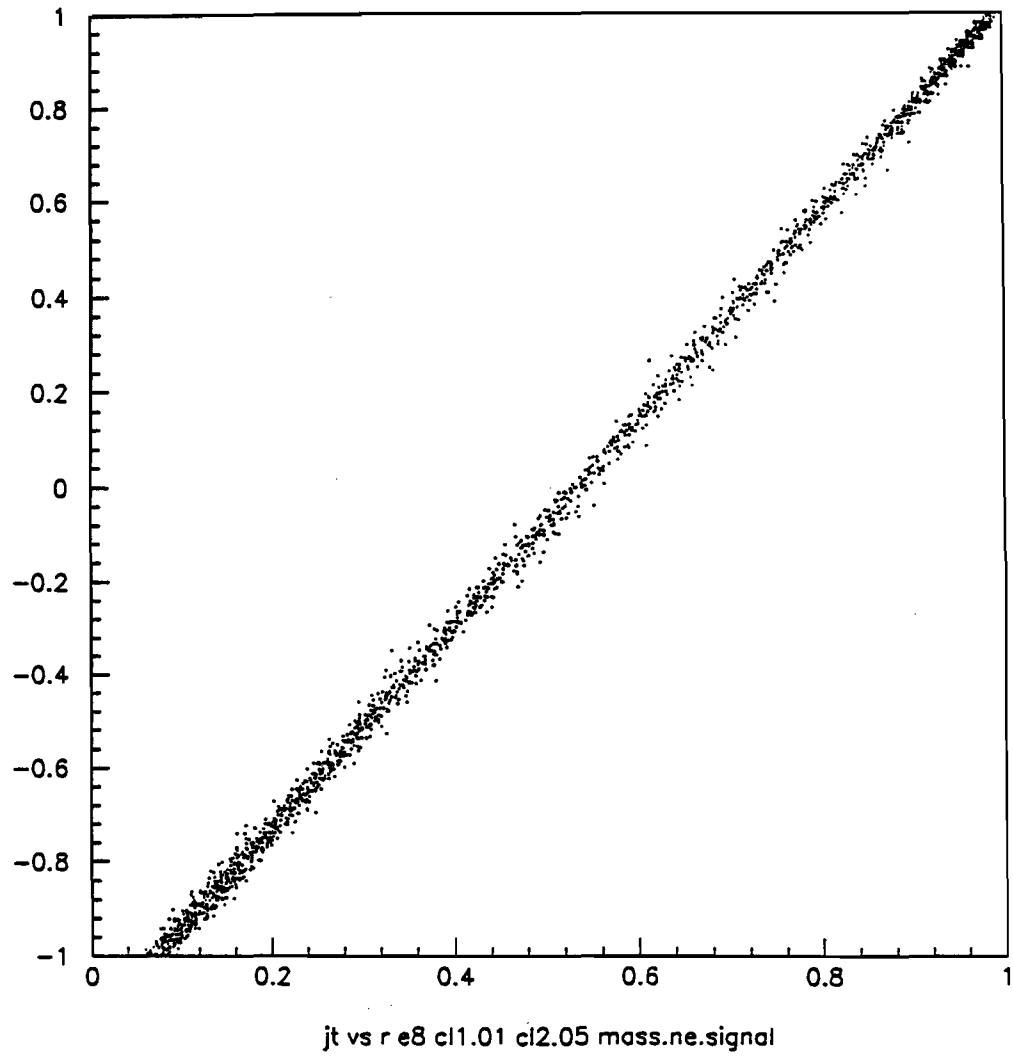

A5: Scatter plot of Cosine Jackson theta versus R for the background region

$$m_{D^o}^2 = \left(E_{D^o}, \overrightarrow{P_{D^o}}\right)^2$$

Since we are constraining this discussion to two body decay states this equation is easily represented as,

$$m_{D^o}^2 = \left(E_1 + E_2 , \vec{P_1} + \vec{P_2}\right)^2$$

where E_1, E_2,P_1 and P_2 are the energy and momentum of the decay products. Expanding this equation we get,

$$m_{D^o}^2 = (E_1 + E_2)^2 - \left(P_1^2 + P_2^2 + 2P_1P_2\cos\theta\right)$$

which can be reorganized to get,

$$m_{D^o}^2 = E_1^2 + E_2^2 + 2E_1E_2 - P_1^2 - P_2^2 - 2P_1P_2\cos\theta \quad .$$

We can rewrite this as,

$$m_{D^o}^2 = E_1^2 - P_1^2 + E_2^2 - P_2^2 + 2E_1E_2 - 2P_1P_2\cos\theta \quad .$$

Knowing the relativistic relations between Energy, momentum and Mass we can rewrite this as,

$$m_{D^o}^2 = m_1^2 + m_2^2 + 2\sqrt{P_1^2 + m_1^2}\,\sqrt{P_2^2 + m_2^2} - 2P_1P_2\cos\theta \quad .$$

Isolating the effects of the momentum we get,

$$m_{D^0}^2 = m_1^2 + m_2^2 + 2P_1P_2\left(\sqrt{1+\frac{m_1^2}{P_1^2}}\sqrt{1+\frac{m_2^2}{P_2^2}} - \cos\theta\right)$$

If we do an expansion on the portions of this equation that are square roots we get,

$$m_{D^0}^2 = m_1^2 + m_2^2 + 2P_1P_2\left(\left(1+\frac{m_1^2}{2P_1^2}\right)\left(1+\frac{m_2^2}{2P_2^2}\right) - \cos\theta_{app}\right)$$

multiplying out we get,

$$m_{D^0}^2 = m_1^2 + m_2^2 + 2P_1P_2\left(\frac{m_1^2m_2^2}{4P_1^2P_2^2} + \frac{m_1^2}{2P_1^2} + \frac{m_2^2}{2P_2^2} + 1 - \cos\theta_{app}\right)$$

Since the first term inside of the parenthesis is much smaller than the others it can be neglected. Therefor multiplying through by the momentum we get,

$$m_{D^0}^2 = \frac{P_1\,m_1^2}{P_1} + \frac{P_2\,m_2^2}{P_2} + \frac{m_1^2\,P_2}{P_1} + \frac{m_2^2\,P_1}{P_2} + 2\,P_1\,P_2\left(1-\cos\theta_{app}\right) \quad .$$

Rearranging the equation we get,

$$m_{D^0}^2 = \frac{(P_1+P_2)\,m_1^2}{P_1} + \frac{(P_1+P_2)\,m_2^2}{P_2} + 2\,P_1\,P_2\left(1-\cos\theta_{app}\right)$$

Since out definition of the R variable is give by:

$$R = \frac{P_1}{P_1 + P_2}$$

we can replace our momenta in the first two terms of the equation with R and 1-R. Doing this we get,

$$m_{D^0}^2 = \frac{m_1^2}{R} + \frac{m_2^2}{1-R} + 2\,P_1\,P_2\left(1 - \cos\theta_{app}\right)$$

This approximation of the invariant mass equation indicates that we have the ability to create high invariant mass states for high and low values of R, as expressed by the first two terms. Since the momentum distribution of the signal is determined by the isotropic nature of the decay in the rest frame of the D^0 meson, as discusssed above, we do not expect that R or theta are infact free variables. The background, being uncorrelated tracks, will have R and theta distributions that are more determined by the single particle momentum distribution (fig A6). Since the single particle momentum distribution peaks at low momentum we expect that the majority of random combinations will have a low momentum particle. These low momentum particles can combine to form a high invariant mass if there is a large disparity in the lab momentum for the pair of particles chosen, thus the peaking at high and low R values.

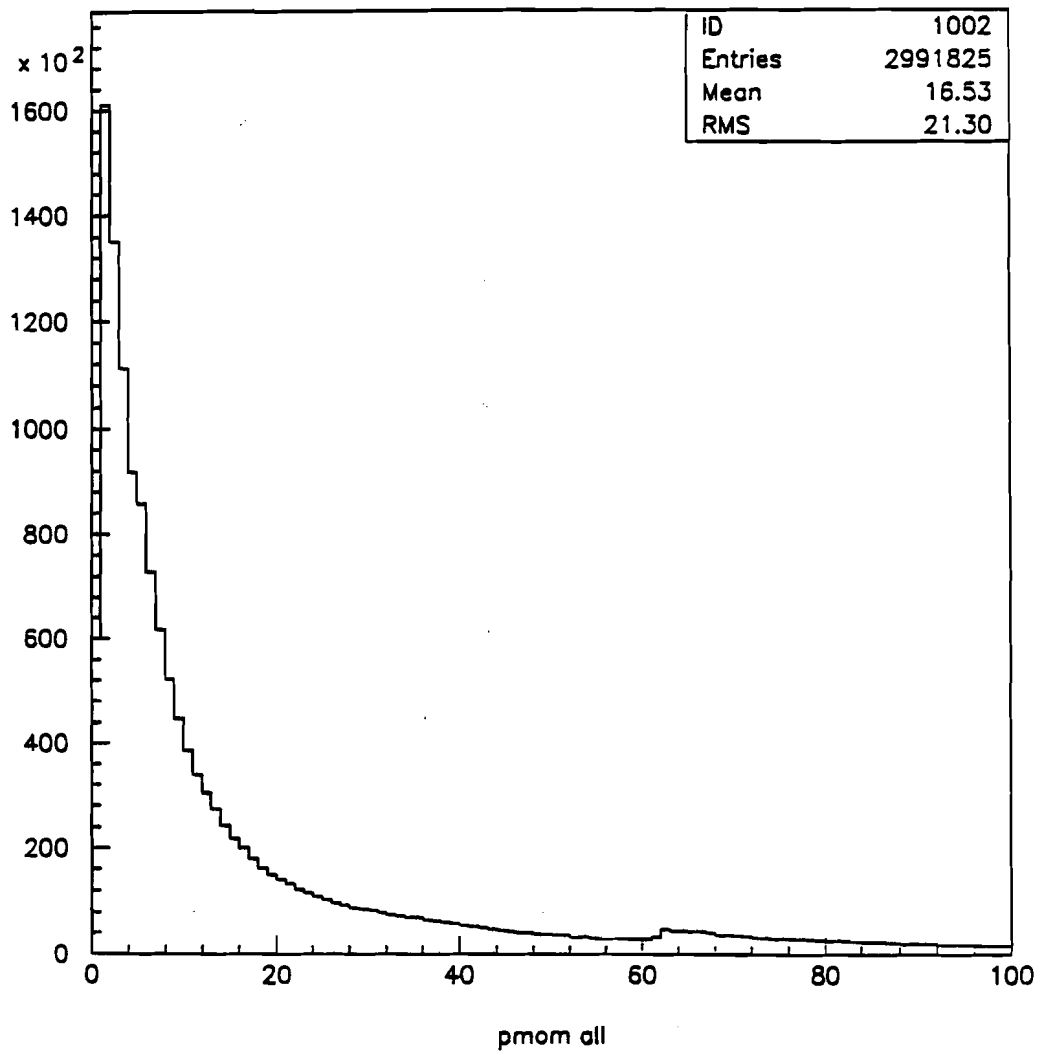

Figure A6: Single particle momentum distribution for the E687 experiment

BIBLIOGRAPHY

[1] J.J. Sakurai, Ann. Phys. 11, 1 (1960)

[2] L.M. Jones and H.W. Wyld, Phys. Rev. D17, 759 (1987)

[3] I.I. Bigi, Nucl. Phys. Rev. B7A (Proc. Suppl.), 318 (1989)

[4] Particle Properties Data Group, "Review of Particle Properties", Phys. Rev. D45 11, (1992)

[5] N. Cabibbo, Phys. Rev. Lett. 10, 531 (1963)

[6] M. Kobayashi and T. Maskawa, Prog. Theor. Phys. 49, 652 (1973)

[7] J. J. Aubert et. al., Phys. Rev. Lett. 33, 1404 (1974)

[8] Abrams et. al., (MARK II), Phys. Rev. Lett. 43, 481

[9] R.M. Baltrusaitus et. al. (MARK III) Phys. Rev. Lett. 55, 150 (1985)

[10] I.I. Bigi, personal discussion

[11] J. Cumalat et. al.," High Energy Photoproduction of States Containing Heavy Flavors and Other Rare Phonomena", FERMILAB experimental proposal

[12] J. Butler et. al., "Design for a New Wide Band Beam ro the Tevatron." FERMILAB note TM-963, 1980

[13] G. Alimonte et. al., "Beam Tagging Performance", E687 Memo, 21 Nov, 1991

[14] P.L. Frabettti et.al., "Discription and Performance of the Fermilab E687 Spectrometer" FERMILAB-PUB-90-258-E (1990). Submitted to Nucl. Instr. and Meth.

[15] D. Petravick et. al. (Fermilab Online and Data Acquition Software Groups), "The PAN-DA Data Acquisition System", Fermilab Compution Department Note

[16]J. Wiss, "Calculation Related to Fitting and Linking", E687 Memo, 16 Nov 1988

[17]K Lingel, "Charm Skim Based in Global Vertex Chi-Squared", E687 Memo, 20 April 1989

[18] R. Culbertson, "Vertexing in the 90's", E687 Memo, 5 June 1991

[19] G Jaross, PhD Thesis, University of Illinois, 1990 (Unpublished)

[20] R. Yoshida, PhD Thesis, Northwestern University, 1990 (Unpublished)

[21] G Jaross, "Skimadee", E687 Memo, 15 Feb. 1990

[22] K. Lingel, PhD Thesis, University of Illinois, 1990 (Unpublished)

[23] J. Alexander et. al. (CLEO), Phys. Rev. Lett. 65, 1184 (1990)

[24] H. Albrecht et. al. (ARGUS), Zeit. Phys C46, 9 (1990)

[25] J. Anjos et. al.(E691), Phys. Rev. D44, 3371 (1991)

[26] M. Adamovich et. al. (WA82), Phys. Lett. B280, 163 (1992)

[27] M. P. Alvarez et. al. (NA14), Zeit. Phys. C50, 11 (1991)

[28] P.L. Frabetti et. al. (E687), Phys Rev. Lett. 55, 150 (1985)

[29] R.M. Baltrusaitis et. al. (MARK III), Phys. Rev. Lett. 55, 150 (1985)

[30] M. Aguilar-Benitez et. al. (Hybrid), Zeit. Phys., C36, 559 (1987)

[31] S. Barlog et. al. (ACCMOR), Zeit. Phys., C48, 29 (1990)

[32] J. Anjos et. al. (E691), Phys. Rev., D43, R635 (1991)

[33] R. Ammar et. al. (CLEO), Phys. Rev., D44, 3383 (1991)